

[REDACTED]
[REDACTED]
WADC TECHNICAL REPORT 55-334

ASTIA DOCUMENT NO. AD 110555

(UNCLASSIFIED TITLE)

✓ FLUTTER TESTS OF LARGE STRAIGHT WING MODELS
AT HIGH SUBSONIC SPEEDS (9)

✓
Richard P. White, Jr.

Cornell Aeronautical Laboratory, Inc.

December 1955

[REDACTED]
[REDACTED]
[REDACTED]
[REDACTED]

[REDACTED]

Aircraft Laboratory
Contract No. AF 33(038)-9734
Project No. 1370

MAY 7 1957

2114 Wright Air Development Center/
Air Research and Development Command
United States Air Force
Wright-Patterson Air Force Base, Ohio

[REDACTED]
[REDACTED]

56WCLS-9981

[REDACTED]

[REDACTED]

FOREWORD

The reserach and development work described in this report was accomplished by the Cornell Aeronautical Laboratory, Inc., Buffalo, New York, for the Aircraft Laboratory, Wright Air Development Center, Wright-Patterson Air Force Base, Ohio. The research was conducted under Air Force Contract No. AF 33(038)-9734, Project No. 1370, (UNCLASSIFIED TITLE) "Aeroelasticity, Vibration and Noise," and Task No. 13473. Mr. Walter J. Mykytow was task engineer. This work is part of a continuing program of aircraft flutter research.

The author is indebted to Mr. Walter P. Targoff for his stimulating supervision and constructive criticism, and to Mr. Stephen R. King who contributed greatly to the successful design, construction, and testing of the models. Appreciation is also extended to Mr. John C. Balcerak and Miss Jean M. Herrmann who conducted most of the detailed analysis work reported herein.

This document is classified CONFIDENTIAL in its entirety (excepting the title) because the results of flutter model tests in the high subsonic speed region are presented. These data have application in the form of flutter prevention design criteria.

[REDACTED]

ABSTRACT

Large rectangular straight wing flutter models were designed, constructed, and flutter tested at high subsonic speeds in a wind tunnel in order to determine:

1. The effects of rigid body degrees of freedom.
2. The effects of compressibility.
3. The effects of an unbalanced spring-restrained aileron mounted on a cantilevered wing.
4. The agreement between theoretical analyses and experimental results.

The models were of NACA 65-006 section with a constant two-foot chord and six-foot semi-span. An effective full-span aerodynamic aspect ratio of six was realized with the semi-span models as the models were mounted from the tunnel ceiling, which acted as a reflection plane. The spring-restrained aileron occupied the aft 20% of the wing chord and the outer 50% of the wing semi-span. The suspension system provided a rigid root for cantilever flutter tests, freedom in pitch and translation for symmetric flutter tests, and freedom in roll for antisymmetric flutter tests.

Flutter analyses were conducted for all plain wing configurations tested (wings without ailerons), and for two representative wing-aileron configurations.

All phases of this project were conducted at Cornell Aeronautical Laboratory, Inc., Buffalo, New York. The wind tunnel tests were performed in the Laboratory's 8½ x 12 ft. Variable Density Tunnel.

PUBLICATION REVIEW

This report has been reviewed and is approved.

FOR THE COMMANDER:

E. Schwartz
for DANIEL D. McKEE
Colonel, USAF
Chief, Aircraft Laboratory

[REDACTED]

SUMMARY

This report presents the results of an experimental research program that was conducted to determine the effects of compressibility, rigid body degrees of freedom, and a non-irreversible mass unbalanced aileron on the flutter characteristics of unswept cantilevered rectangular models in the high subsonic speed regime up to $M = 0.93$.


The models were of a semi-span type, hung vertically from a suspension system in the tunnel ceiling. The wing chord was two feet and the semi-span six feet which gives a full-span aspect ratio of 6.0. The elastic axis position, the bending-torsion frequency ratio ω_h/ω_{α} and all other non-dimensional flutter parameters were kept constant for all plain wing models (models without aileron). The wing-aileron models were obtained by modifying the plain wings to incorporate the aileron which occupied the aft 20% of the wing chord and the outboard 50% of the wing semi-span. No mass balance was provided and, as the aileron was hinged at its leading edge, neither was any aerodynamic balance present.

Since a high level of turbulence existed in the wind tunnel airstream, it was necessary to design the models not only on the basis of rigidity and weight requirements, but also on the basis of a stress-deflection relationship so that large buffeting amplitudes could be withstood without producing a high oscillatory stress level in the dural skins.

The suspension system which provided freedom in roll, pitch, and translation at the root of the model, was a modification of a system designed for low speed flutter tests of models carrying large tip pods (Ref. 1). The elastic deformation of the various suspension components affected the vibratory modes of the models, and it became necessary to include the elastic rigidities of the suspension system in the theoretical correlative analyses to obtain the measured coupled-mode frequencies and nodal lines.

The primary results of this research program may be summarized as follows:

1. The flutter tests with the symmetric degrees of freedom gave results nearly the same as those obtained with the cantilever degrees of freedom. It should be noted that the symmetric modes and frequencies were very similar to the corresponding cantilever values.
2. The flutter tests with the antisymmetric degrees of freedom yield flutter speeds higher than the ones obtained with the cantilever degrees of freedom. However, the severity of flutter motion was reduced.
3. No large effects of compressibility on the flutter speed in the Mach number range for 0.65 to 0.93 were noticed in the experimental phase of the contract.

- 
4. Reductions to 30% of the cantilever flutter speed were obtained at a frequency ratio $\omega_{\alpha} / \omega_{\alpha_1}$ of approximately 0.80 with the addition of the unbalanced spring-restrained half-span aileron.
 5. A second wing-aileron flutter mode was obtained below the cantilever bending-torsion flutter speed when the ratio of aileron rotational frequency to first wing torsional frequency was one or above. Minimum flutter velocities in this higher mode of flutter were obtained when the aileron rotational frequency was about 80% of the zero air speed frequency of the mode corresponding to the flutter mode.
 6. If an unfavorable wing mass distribution is present, wing-aileron flutter in the higher frequency modes can be obtained at a speed below the cantilever flutter speed even if the frequency of the aileron is sufficient to preclude conventional flutter in the lower frequency wing-aileron modes.
 7. Incompressible, infinite aspect ratio flutter analyses predicted the experimental results within a few percent.
 8. Theoretical calculations indicate that for these models the flutter speed and frequency are lowered by compressibility.
 9. To estimate the effects of finite span, the Biot-Wasserman method (Refs. 6 and 7) was superior to a modified Reissner-Stevenson method (Refs. 5 and 8). In all cases unconservative results were predicated in using these finite span corrections.
 10. If possible, high speed flutter models should be inexpensive and of simple construction so that they are expendable and therefore the difficulties associated with the use of flutter locks at these speeds would be avoided. An example of this type of construction is reported in Refs. 16 and 17.

[REDACTED]

TABLE OF CONTENTS

	<u>Page</u>
List of Figures	vii
List of Tables	xii
List of Symbols	xiii
Introduction	1
I Description of Models and Equipment.	3
II Preliminary Tests.	7
III Tunnel Tests	42
IV Vibration Analyses	47
V Flutter Analyses	50
VI Discussion and Results	71
VII Conclusions and Recommendations.	81
VIII Bibliography	83
Appendix I Design and Construction Details of Models, Suspension System, and Flutter Lock	85
Appendix II Tabular Summaries of; Vibration Analyses Results, Vibration Test Results, Wind Tunnel Test Results, and Model Mass Data, Listing of Flutter Determinant Elements.	123

[REDACTED]

LIST OF FIGURES

<u>Figure</u>		<u>Page</u>
1	Wing-Aileron Model Mounted in Tunnel with Flutter Lock Actuated - Looking Upstream	4
2	Static Test Setup to Obtain Bending Rigidities	8
3	Static Test Setup to Obtain Torsional Rigidities	9
4	Test Setup to Obtain Vibratory Modes of the Models	10
5-13	Experimental and Theoretical Node Lines for M = 0.65, 0.75, and 0.85 Models in the Cantilever, Symmetric, and Antisymmetric Configurations	13-21
14	Experimental Wing-Aileron Node Lines M = 0.65 Model $\omega_\beta = 15.0$ CPS $\omega_\beta / \omega_{\alpha 1} = 0.45$	23
15	Experimental Wing-Aileron Node Lines M = 0.65 Model $\omega_\beta = 25.9$ CPS $\omega_\beta / \omega_{\alpha 1} = 0.78$	24
16	Experimental and Theoretical Wing-Aileron Node Lines M = 0.65 Model $\omega_\beta = 33.1$ CPS $\omega_\beta / \omega_{\alpha 1} = 1.00$	25
17	Experimental Wing-Aileron Node Lines M = 0.65 Model $\omega_\beta = 39.9$ CPS $\omega_\beta / \omega_{\alpha 1} = 1.21$	26
18	Experimental Wing-Aileron Node Lines M = 0.65 Model $\omega_\beta = 42.0$ CPS $\omega_\beta / \omega_{\alpha 1} = 1.27$	27
19	Experimental and Theoretical Wing-Aileron Node Lines M = 0.65 Model $\omega_\beta = 47.9$ CPS $\omega_\beta / \omega_{\alpha 1} = 1.45$	28
20	Experimental Wing-Aileron Node Lines M = 0.65 Model $\omega_\beta = 54.4$ CPS $\omega_\beta / \omega_{\alpha 1} = 1.65$	29
21	Experimental Wing-Aileron Node Lines M = 0.65 Model $\omega_\beta = 61.6$ CPS $\omega_\beta / \omega_{\alpha 1} = 1.86$	30
22	Experimental Wing-Aileron Node Lines M = 0.75 Model $\omega_\beta = 22.8$ CPS $\omega_\beta / \omega_{\alpha 1} = 0.56$	31
23	Experimental Wing-Aileron Node Lines M = 0.75 Model $\omega_\beta = 33.1$ CPS $\omega_\beta / \omega_{\alpha 1} = 0.81$	32

<u>Figure</u>		<u>Page</u>
24	Experimental Wing-Aileron Node Lines M = 0.75 Model $\omega_\beta = 39.9$ CPS $\omega_\beta / \omega_{\alpha_1} = 0.97$	33
25	Experimental Wing-Aileron Node Lines M = 0.75 Model $\omega_\beta = 44.6$ CPS $\omega_\beta / \omega_{\alpha_1} = 1.09$	34
26	Experimental Wing-Aileron Node Lines M = 0.75 Model $\omega_\beta = 49.7$ CPS $\omega_\beta / \omega_{\alpha_1} = 1.21$	35
27	Experimental Wing-Aileron Node Lines M = 0.75 Model $\omega_\beta = 54.4$ CPS $\omega_\beta / \omega_{\alpha_1} = 1.33$	36
28	Experimental Wing-Aileron Node Lines M = 0.85 Model $\omega_\beta = 22.8$ CPS $\omega_\beta / \omega_{\alpha_1} = 0.51$	37
29	Experimental Wing-Aileron Node Lines M = 0.85 Model $\omega_\beta = 36.0$ CPS $\omega_\beta / \omega_{\alpha_1} = 0.80$	38
30	Experimental Wing-Aileron Node Lines M = 0.85 Model $\omega_\beta = 44.6$ CPS $\omega_\beta / \omega_{\alpha_1} = 0.99$	39
31	Experimental Wing-Aileron Node Lines M = 0.85 Model $\omega_\beta = 49.7$ CPS $\omega_\beta / \omega_{\alpha_1} = 1.10$	40
32	Test Setup for Conducting Dynamic Fatigue Test on Model Specimen	41
33	Three-Exposure Picture Showing Model Specimen Deflected ± 5.0 Inches	43
34	Typical Flutter Records	44
35	$v/b \omega_{\alpha_1}$ vs. $\omega_\beta / \omega_{\alpha_1}$ Wing-Aileron Flutter Test Results	48
36	$v/b \omega_\alpha$ vs. ω_h / ω_α M = 0.65 Cantilever Model $\rho = 0.001127$ slugs/ft ³	52
37	$v/b \omega_\alpha$ vs. ω_h / ω_α M = 0.75 Cantilever Model $\rho = 0.001138$ slugs/ft ³	53
38	$v/b \omega_\alpha$ vs. ω_h / ω_α M = 0.85 Cantilever Model $\rho = 0.001120$ slugs/ft ³	54
39	$v/b \omega_\alpha$ vs. ω_h / ω_α M = 0.65 Cantilever Model $\rho = 0.000850$ slugs/ft ³	55

<u>Figure</u>		<u>Page</u>
40	$v/b\omega_\alpha$ vs. ω_h/ω_α $M = 0.75$ Cantilever Model $\rho = 0.000830$ slugs/ft ³	56
41	$v/b\omega_\alpha$ vs. ω_h/ω_α $M = 0.85$ Cantilever Model $\rho = 0.000830$ slugs/ft ³	57
42	$v/b\omega_\alpha$ vs. ω_h/ω_α $M = 0.65$ Symmetric Model $\rho = 0.001120$ slugs/ft ³	59
43	$v/b\omega_\alpha$ vs. ω_h/ω_α $M = 0.75$ Symmetric Model $\rho = 0.001130$ slugs/ft ³	60
44	$v/b\omega_\alpha$ vs. ω_h/ω_α $M = 0.85$ Symmetric Model $\rho = 0.001100$ slugs/ft ³	61
45	$v/b\omega_\alpha$ vs. ω_h/ω_α $M = 0.65$ Antisymmetric Model $\rho = 0.001139$ slugs/ft ³	62
46	$v/b\omega_\alpha$ vs. ω_h/ω_α $M = 0.75$ Antisymmetric Model $\rho = 0.001131$ slugs/ft ³	63
47	$v/b\omega_\alpha$ vs. ω_h/ω_α $M = 0.85$ Antisymmetric Model $\rho = 0.001114$ slugs/ft ³	64
48	$v/b\omega_\alpha$ vs. ω_h/ω_α Comparison of Two and Three Degree Analyses for $M = 0.85$ Cantilever Model $\rho = 0.001120$ slugs/ft ³	65
49	$v/b\omega_\alpha$ vs. ω_h/ω_α Comparison of Compressible and Incompressible Analyses for $M = 0.65$ Cantilever Model $\rho = 0.001127$ slugs/ft ³	66
50	$v/b\omega_\alpha$ vs. ω_h/ω_α Comparison of Compressible and Incompressible Analyses for $M = 0.65$ Antisymmetric Model $\rho = 0.001139$ slugs/ft ³	67
51	$v/b\omega_\alpha$ vs. ω_h/ω_α Comparison of Various Methods of Finite Span Analyses for $M = 0.65$ Cantilever Model $\rho = 0.001127$ slugs/ft ³	68
52	$v/b\omega_\alpha$ vs. ω_h/ω_α Comparison of Various Methods of Finite Span Analyses for $M = 0.65$ Antisymmetric Model $\rho = 0.001139$ slugs/ft ³	69
53	$v/b\omega_{\alpha 1}$ vs. $\omega_p/\omega_{\alpha 1}$ Comparison of Theoretical and Experimental Results Obtained with $M = 0.65$ Wing- Aileron Model	70



<u>Figure</u>		<u>Page</u>
54	An Exploded View of the Wing Framework of a High Speed Flutter Model	87
55	An Assembled Wing Framework of a High Speed Flutter Model	88
56	Interchangeable Skin Units of a High Speed Flutter Model	89
57	Root Fitting for the Flutter Models	90
58	An Assembled High Speed Flutter Model Mounted in the Wind Tunnel	91
59	An Exploded View of a Composite Styrofoam-Balsa Core	93
60	A Completed Core	94
61	Exploded View of Skin-Doubler Unit	96
62	A Completed Model Ready for Installation in the Tunnel	97
63	An Exploded View of the Aileron	99
64	A Complete Aileron	100
65	Details of Aileron Springs and Flexure Pivot	102
66	A Wing-Aileron Model	103
67	Schematic Views of Suspension Configurations	104
68	Picture of Basic Suspension System	105
69	Cutaway View of Model Suspension Head	107
70	Suspension Pitch Frequency System and Angle of Attack Control	108
71	Placement of Translational Stops and Springs	109
72	Placement of Translational Damper	110
73	Installation of Pitch Damper	111
74	Suspension System in Cantilever Configuration	113





<u>Figure</u>		<u>Page</u>
75	Suspension System in Antisymmetric Configuration	114
76	Flutter Lock Mounted in Tunnel	118
77	Picture of Lock Clamping Model in the Tunnel	119
78	Pneumatic Actuating System for Lock	121
79	Locking Sequence of Flutter Brake	122



[REDACTED]

LIST OF TABLES

<u>Table</u>		<u>Page</u>
I	Summary of Measured Coupled Mode Vibratory Frequencies for Plain Wings	12
II	Summary of Measured Coupled Mode Frequencies for all Wing-Aileron Configurations Tested (Wing Root Cantilevered)	22
III	Summary of Experimental Flutter Results for Plain Wings	45
IV	Summary of Experimental Flutter Results for Wing-Aileron Models (Wing Root Cantilevered)	46
V	Summary of Calculated Uncoupled and Coupled Mode Frequencies	49
VI	Summary of Calculated Flutter Results for Plain Wing Configurations	51
VII	Comparison Summary of Calculated and Experimental Vibration Results	128-129
VIII	Comparison of Calculated and Experimental Flutter Results	130
IX	Mass Properties of Various Plain Wing Models	131-132
X	Mass Properties of Various Wing-Aileron Models	133
XI	Numerical Values of Aerodynamic Summations	134

[REDACTED]

LIST OF SYMBOLS

- a Location of the wing elastic axis measured from the wing mid-chord point, as a fraction of the wing semi-chord (positive when aft of the wing mid-chord).
- b Wing semi-chord (in.).
- b_r Reference semi-chord (in.) (12 in.).
- c Location of the aileron hinge axis measured from the wing mid-chord point as a fraction of the wing semi-chord (positive when aft of the wing mid-chord).
- $\xi_{h_1}, \xi_{\alpha_1}, \xi_{h_0}, \xi_{\alpha_0}, \xi_{\beta}$ Structural damping coefficients in the wing bending, wing torsion, wing translation, wing pitch, and aileron degrees of freedom, respectively.
- h_i Bending displacement of the elastic axis in a direction perpendicular to the undisturbed direction of the airflow (in.) (positive when down) $i = 1, 2$ refer to the first and second uncoupled bending modes respectively.
- h_{0i} Rigid body bending displacement of the elastic axis (positive when down) when $i = r$ refers to rigid body roll; $i = t$ refers to rigid body translation (in.).
- J $\sqrt{-I}$
- I_R Weight rolling moment of inertia of the fuselage (lbs.-in.²).
- I_{α} Weight moment of inertia of wing per bay about the elastic axis (lbs.-in.²).
- I_{β} Weight moment of inertia of aileron per bay about the aileron hinge axis (lbs.-in.²).
- L Wing semi-span (in.).
- L_h Aerodynamic wing lift coefficient due to bending oscillations of the wing.
- L_{α} Aerodynamic wing lift coefficient due to torsional oscillations of the wing about its quarter-chord.
- L_{β} Aerodynamic wing lift coefficient due to oscillations of the aileron about its leading edge.
- M Mach number.

- [REDACTED]
- M_e Experimental Mach number.
- M_h Aerodynamic moment coefficient about the wing quarter-chord point due to bending oscillations of the wing.
- M_α Aerodynamic moment coefficient about the wing quarter-chord point due to torsional oscillations of the wing about the quarter chord.
- M_β Aerodynamic moment coefficient about the wing quarter-chord point due to oscillations of the aileron about its leading edge.
- S_α Static weight unbalance of wing per bay about the elastic axis (lbs.-in.) (positive when tail heavy).
- S_β Static weight unbalance of aileron per bay about the aileron hinge line (lbs.-in.) (positive when tail heavy).
- T_h Aerodynamic moment coefficient about the aileron leading edge due to bending oscillations of the wing.
- T_α Aerodynamic moment coefficient about the aileron leading edge due to torsional oscillations of the wing about the quarter-chord.
- T_β Aerodynamic moment coefficient about the aileron leading edge due to oscillations of the aileron about its leading edge.
- v Wind tunnel velocity (ft./sec.).
- W Weight of wing per bay (lbs.).
- α_1 Torsional deflection about the elastic axis (radians). (positive for increasing angle of attack). $i = 1, 2$ refer to the first and second uncoupled torsion modes respectively.
- α_0 Rigid body pitch displacement about the elastic axis (radians) (positive for increasing angle of attack).
- β Rotation of the aileron about its hinge line (radians) (positive for increasing angle of attack).
- Δx Spanwise bay length (in.).
- π 3.141593 .

- [REDACTED]
- ϕ_i Bending slope of wing at the root, $i = 0$ refers to rigid body roll mode and $i = 1$ refers to first antisymmetric bending mode (rad./in.) (positive for a negative bending deflection).
- ρ Air density (slugs/ft.³).
- ω Flutter frequency of wing (rad./sec.).
- ω_h Uncoupled wing bending frequency (rad./sec.).
- ω_{h_0} Uncoupled translation frequency of wing (rad./sec.).
- ω_α Uncoupled torsion frequency of wing (rad./sec.).
- ω_{d_0} Uncoupled pitch frequency of wing (rad./sec.).
- ω_{d_1} First uncoupled torsion frequency of wing (rad./sec.).
- ω_β Rotational frequency of aileron about its hinge line (rad./sec.).
- $v/b\omega_\alpha$ Flutter speed coefficient.
- μ Non-dimensional mass ratio = $\frac{W_{3/4}}{\pi \rho b_r^2 \Delta x}$.

[REDACTED]

[REDACTED]



INTRODUCTION

Prediction of the flutter characteristics of a given aerodynamic surface is difficult primarily because of the oscillatory aerodynamic forces. At low speeds, where the aerodynamic forces acting on the oscillating airfoil are well-established theoretically, the computation of the flutter speed and other flutter characteristics for straight wings of moderate to high aspect ratio can be determined fairly accurately if sufficient effort is put into the analysis. However, at high subsonic and transonic speeds, the oscillatory aerodynamic forces are not as well-established theoretically and, therefore, the computation of the flutter characteristics for a given surface is an approximation at best. Since present-day aircraft are flying in the high subsonic and transonic speed ranges and their flutter characteristics must be determined, experimental flutter tests of dynamic models have been required to obtain the desired information. Reference 10, which is a compilation of experimental flutter tests conducted in this country since 1947, indicates the substantial effort that has been expended since that year in order to determine some of the flutter characteristics in this speed range for various configurations. This test data has been accumulated using free-falling bombs or rocket-propelled missiles (Ref. 14), a wing flow method (Ref. 12), and by means of wind tunnel tests using flexible cantilever models (Refs. 13 and 15) or semi-rigid models (Ref. 11).

The research program reported herein, had a somewhat broader scope than those conducted in the past in that the symmetric and antisymmetric flutter modes were investigated in the high subsonic speed regime by the inclusion in these degrees of freedom of properly scaled fuselage mass parameters. Specifically, the purposes for which this flutter research program was initiated are as follows:

To determine in the high subsonic speed regime,

1. The effects of rigid body degrees of freedom.
2. The effects of compressibility.
3. The effects of a mass unbalanced spring-restrained aileron.
4. The agreement between theoretical analyses and experimental results.

Manuscript released by the author December 1955 for publication as a WADC Technical Report.

[REDACTED]

Since the purpose of this project was to determine the general flutter characteristics of straight wings flying at high subsonic speeds, no effort was made to simulate a particular type of airplane wing planform or dynamic characteristics. Instead, to facilitate construction and analyses methods, a non-tapered, uniform wing was chosen as the basic model planform. However, the rectangular shape of the wing planform accentuated the undesirable effects of tunnel turbulence, and it became necessary during the experimental phase of this contract to undertake a model development program to evolve a model design satisfactory for high speed testing of the large flutter models in the wind tunnel. Since it is felt that the results of this development program contributed to the art of designing high speed flutter models of all sizes, there is considerable discussion allotted in Appendix I to the difficulties that were encountered and the design methods used to solve them.

In addition to presenting the flutter test results obtained during the experimental phase of this contract, this report also presents the results of the zero airspeed vibration tests, and the correlative flutter analyses that were conducted.

I. DESCRIPTION OF MODELS AND EQUIPMENT

A. Models

Since the purpose of this project was to determine the general flutter characteristics of straight wings flying at high subsonic speeds, no effort was made to simulate a particular type of airplane wing planform or dynamic characteristics. Instead, to facilitate construction and analysis methods, a non-tapered, uniform wing was chosen as the basic model planform.

The wings were of the semi-span type, hung vertically from a suspension system in the tunnel ceiling. The wing chord was two feet and the semi-span six feet. The elastic axis position, frequency ratio ω_h/ω_α , and all other non-dimensional flutter parameters were kept constant for all plain wing models (models without ailerons). Different flutter speeds were obtained by constructing the models with different values of torsional rigidity. For the wing-aileron models, the aileron occupied 20% of the wing chord and 50% of the wing semi-span. The aileron was located in the outboard section of the wing. (See Fig. 1.) The aileron hinge line was at the leading edge of the aileron so no aerodynamic or mass balance was obtained. All flutter parameters except ω_p/ω_α were kept constant for all wing-aileron models and the flutter speed was changed on each model by varying the aileron rotational frequency.

The models not incorporating ailerons consisted of large structural torque boxes formed to the outside contour of the wing and occupying approximately 70% of the chord, and non-structural spruce-balsa leading and trailing edge sections. The dural skins of the torque box were prevented from buckling by a solid composite core of balsa and Styrofoam to which the dural skins were bonded.

The wing-aileron models were constructed exactly as the plain wing models except that the balsa trailing edge sections of the models were cut out to accommodate the aileron which was constructed of thin dural skins bonded to a solid Strux core formed to the proper contour.

A complete description of the model construction is presented in Appendix I.

Mass, unbalance, and inertial distributions for the various plain wings are tabulated in Table IX, Appendix II, and for the wing-aileron models in Table X, Appendix II.

B. Suspension System

The suspension system which provided freedom in roll, pitch, and translation at the fuselage of the model, was a modified version of the system designed under Contract No. AF 33(038)-3551 (Ref. 1). Associated with each

~~CONFIDENTIAL~~

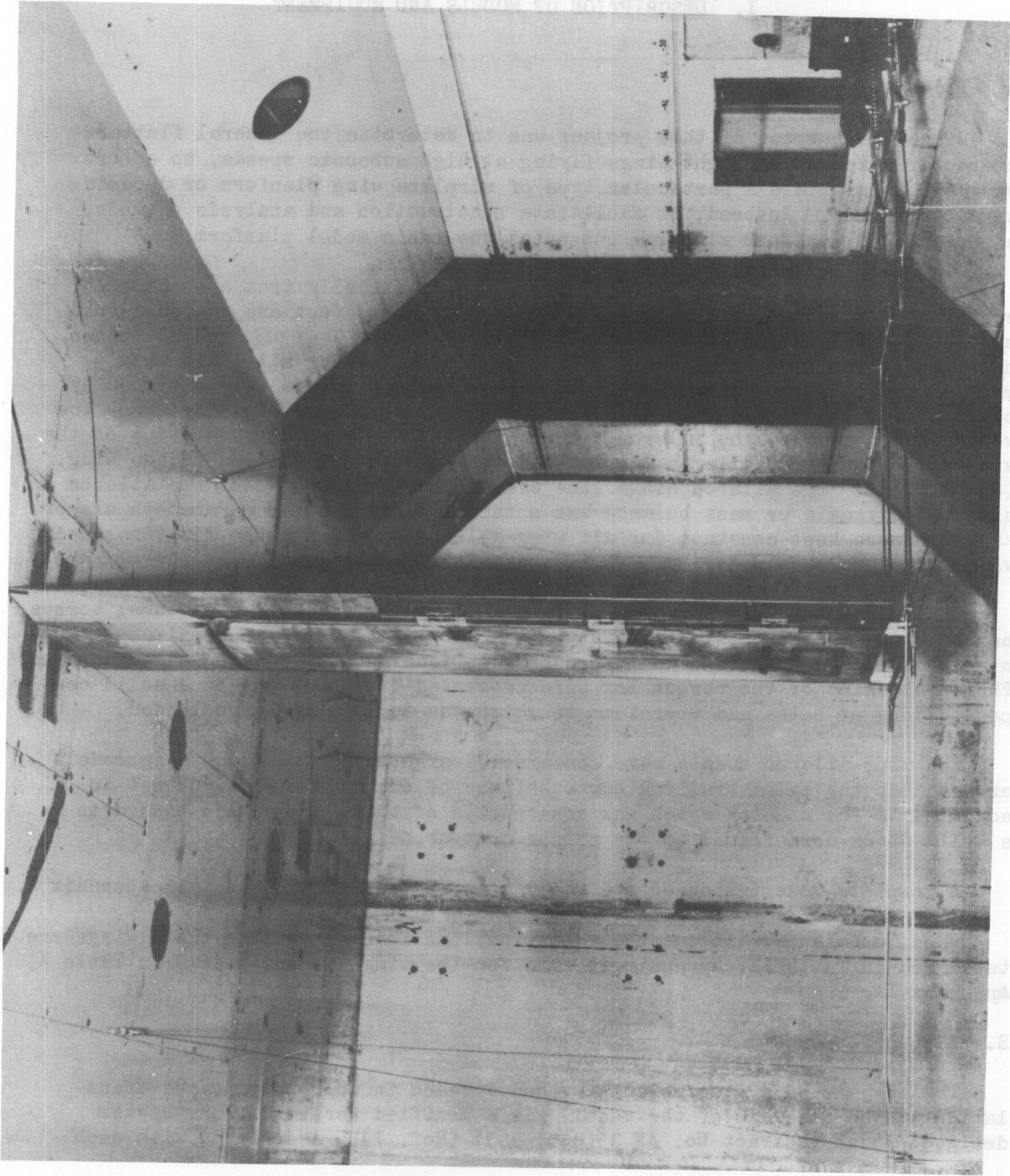


FIGURE 1 WING-AILERON MODEL MOUNTED IN TUNNEL WITH FLUTTER LOCK ACTUATED - LOOKING UPSTREAM

~~CONFIDENTIAL~~

[REDACTED]

degree of freedom, there was a lock which was capable of reducing that motion to zero. By the proper combination of these freedoms, either symmetric, anti-symmetric, or cantilever root conditions were obtained. Means were provided for obtaining proper values of fuselage roll inertia in the antisymmetric case, and fuselage weight, static unbalance, and pitching inertia in the symmetric case. The dynamic and static stability inherent in an airplane was produced by the proper arrangement of springs and dampers in the suspension system. A detailed description of the suspension system is given in Appendix I. A full discussion of the kinematics and dynamics of the suspension system is given in Ref. 1.

C. Flutter Lock

The flutter lock used in this program restrained only the tip of the wing. The lock consisted of two endless run-around cables to which locking bars were attached at similar points on each cable. The sequence of events as the lock closed was first centering and then clamping of the model. The locking bars, besides clamping the model, acted as motion limiters or stops at the wing tip when the lock was in the open position. The distance between the locking bars when in the open position could be varied so that free motion of the wing tip from ± 1.00 in. to ± 5.00 in. was obtainable. The locking system was electronically controlled and pneumatically operated to obtain minimum closing time.

For the aileron models, a flutter brake for the aileron was used in addition to the main lock. The brake consisted of a thin cable enclosed in a rubber tube which was held downstream from the model by the drag force of the airflow in the tunnel. When operated (manually) the rubber tubing was brought in contact with the trailing edge of the aileron and the friction force so obtained effectively attached the aileron to the cable and stopped the flutter motion.

A detailed description of the main wing lock and its development is presented in Appendix I. A photograph showing the lock mounted in the tunnel is presented in Fig. 1.

D. Instrumentation

When conducting wind tunnel flutter tests, it is desirable to record the model deformations at several wing locations so that the flutter mode shape can be determined in addition to the frequency and critical speed. During the course of the test program, two distinct types of instrumentation were used to measure the model elastic deformations. Descriptions of both types used in the course of the test program are given in the following paragraphs.

[REDACTED]

(1) Instrumentation Using Accelerometers

Two types of accelerometers were used for this setup, (a) Consolidated Type 4-104, and (b) Martin Type B. Both types of accelerometers gave equally satisfactory results, but the Martin Type B were considerably lighter and were, therefore, placed in the outboard portions of the wing where weight considerations were important.

Consolidated Engineering Corporation 1000 cps carrier-type system was used in conjunction with the Consolidated and Martin accelerometers to demodulate, amplify, and to twice integrate the accelerometer signals. Therefore, the signals recorded by the oscillograph presented a time history of the wing displacement at the various stations. Satisfactory results were obtained using this arrangement, but due to loss of models, and consequent destruction of the accelerometers, this type of instrumentation had to be abandoned.

(2) Instrumentation Using Strain Gages

Pairs of bending and of torsional gages were mounted at three and two spanwise locations of the torque box respectively. (See Fig. 62, p.97.) Due to the many high frequency components picked up by the strain gages, a low pass L-C type filter was used on all strain gage circuits to eliminate the high frequency hash. Typical records showing the type of traces obtained on the oscillograph are shown in Fig. 34, p. 44. To measure the aileron motion relative to the wing, a pair of strain gages was mounted back-to-back on one of the steel flexure pivots, Fig. 65, p.102.

To obtain the deflections of the wing from the strain variations recorded by the strain gages, a relationship between the strain and corresponding deflections was first determined. This was accomplished by means of influence coefficients where the influence coefficients relating strain to applied load and the corresponding deflection to applied load were experimentally determined. The influence coefficients for the bending degree of freedom were measured at three spanwise stations and for the torsional degree of freedom at two of the same spanwise stations. The influence coefficients for the deflection and strain matrices were experimentally obtained in the usual manner by placing a load at one spanwise station and measuring the strain and deflection at all three spanwise stations. The point of load application was then moved to one of the other spanwise stations and the procedure repeated. This process was repeated until the point of load application had been placed at all three spanwise reference stations. The resulting two matrix equations, one relating deflection to applied load, and the other relating strain to applied load, were then combined to yield a single matrix equation relating deflection to the corresponding strain.

To obtain the characteristic deflections along the wing span while the wing was vibrating, the strain variations recorded as trace deflections on an oscillograph were determined and then substituted into the matrix equation.

[REDACTED]

(3) Measurement of Fuselage Motion

Rigid body translation and pitch motions, present in the symmetric flutter mode, were measured by autosyns. The fuselage roll motion, in the antisymmetric flutter mode, was measured using a Shaevitz differential transformer.

II. PRELIMINARY TESTS

Prior to wind tunnel testing, each model was subjected to a test program to determine its elastic and dynamic properties. In addition to these routine tests conducted on all wind tunnel models, one model was subjected to an extensive fatigue and limit load test. To ensure that the root fixities present during the wind tunnel tests would also be present during the static and dynamic tests, all preliminary testing was conducted with the wings mounted from the suspension system in the tunnel cart ceiling.

A. Static Tests

Figure 2 shows the arrangement of equipment used to obtain the flexural rigidities of the various models. In order to separate the rigidities of the root fitting, support, and wing, loading positions at different spanwise stations were used. Since the wing had a smooth exterior, the bending loads were applied to the wing through a contoured loading bar which could be clamped to the wing at any spanwise station. The deflections resulting from the application of the bending loads at the 40% chordline were measured by mechanical dial gages located at six spanwise stations.

The static test setup to obtain the torsional rigidities of the various wings is shown in Fig. 3. A torsional couple was applied to the wing at various spanwise locations by simultaneously placing equal and opposite loads at two locations on the loading bar equally distant from the 40% chordline. The resulting deflections were again measured by mechanical dial gages placed in pairs at three spanwise locations. The data obtained from these tests indicated that the elastic axis was within $\pm 1.0\%$ of the 40% chord station which was the design elastic axis.

B. Dynamic Tests

Figure 4 shows the equipment and model arrangement used for conducting the vibration tests of the plain wings. Excitation of the model was obtained by two electromagnetic Bozak shakers mounted at the tip of the wing. The shakers were electrically connected through a switching arrangement so that

~~CONFIDENTIAL~~

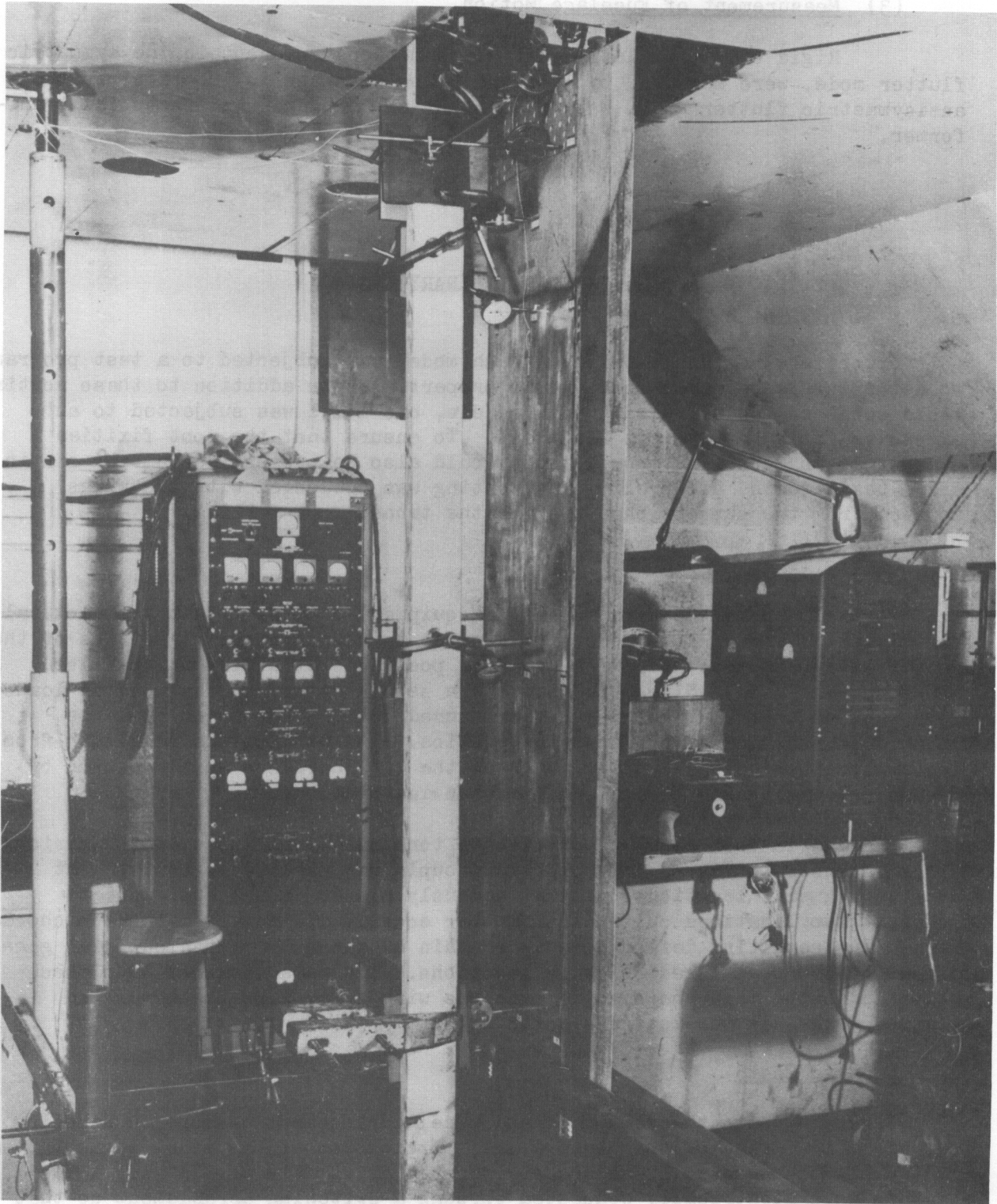


FIGURE 2 STATIC TEST SETUP TO OBTAIN BENDING RIGIDITIES

~~CONFIDENTIAL~~

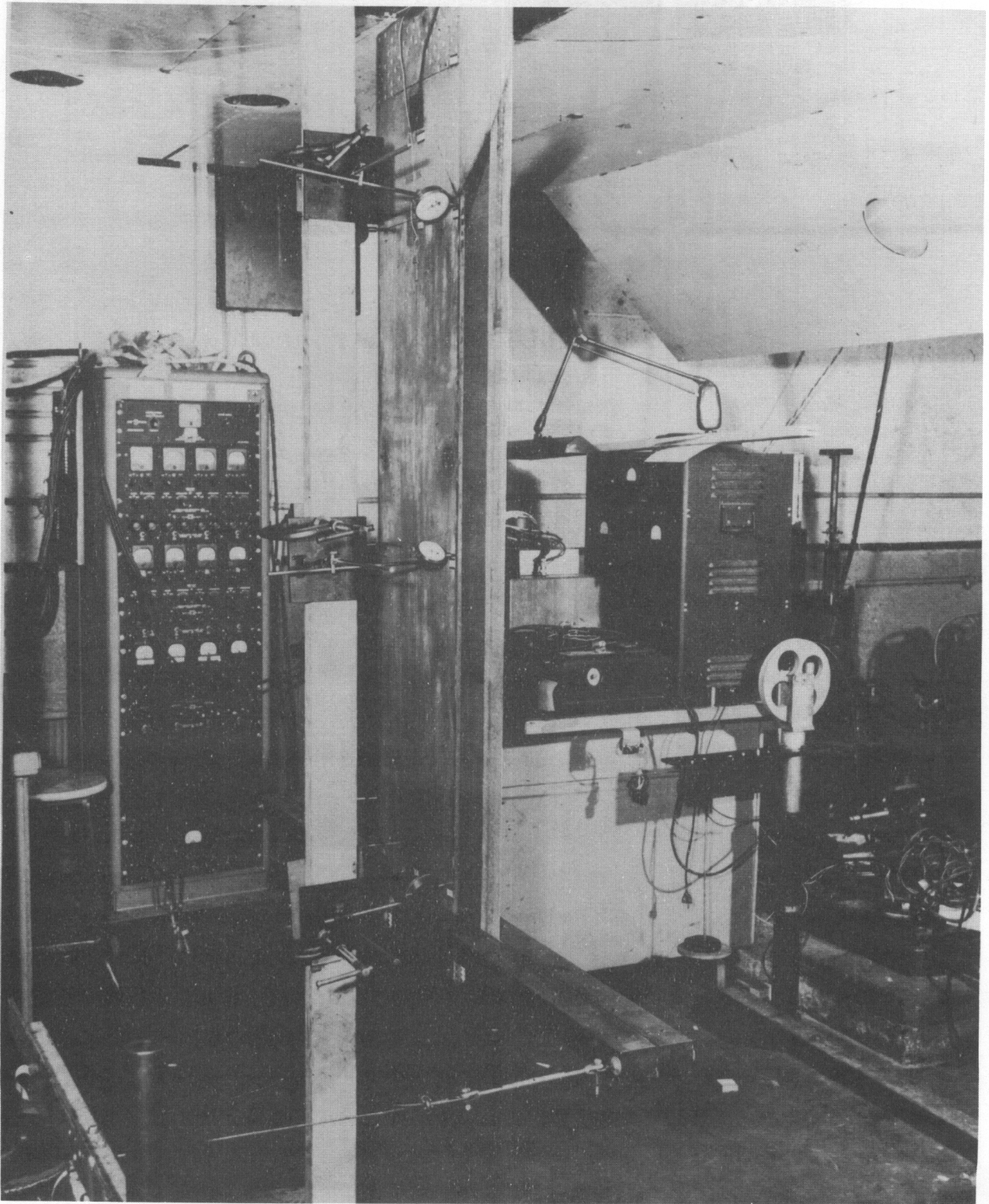


FIGURE 3 STATIC TEST SETUP TO OBTAIN TORSIONAL RIGIDITIES

CONFIDENTIAL

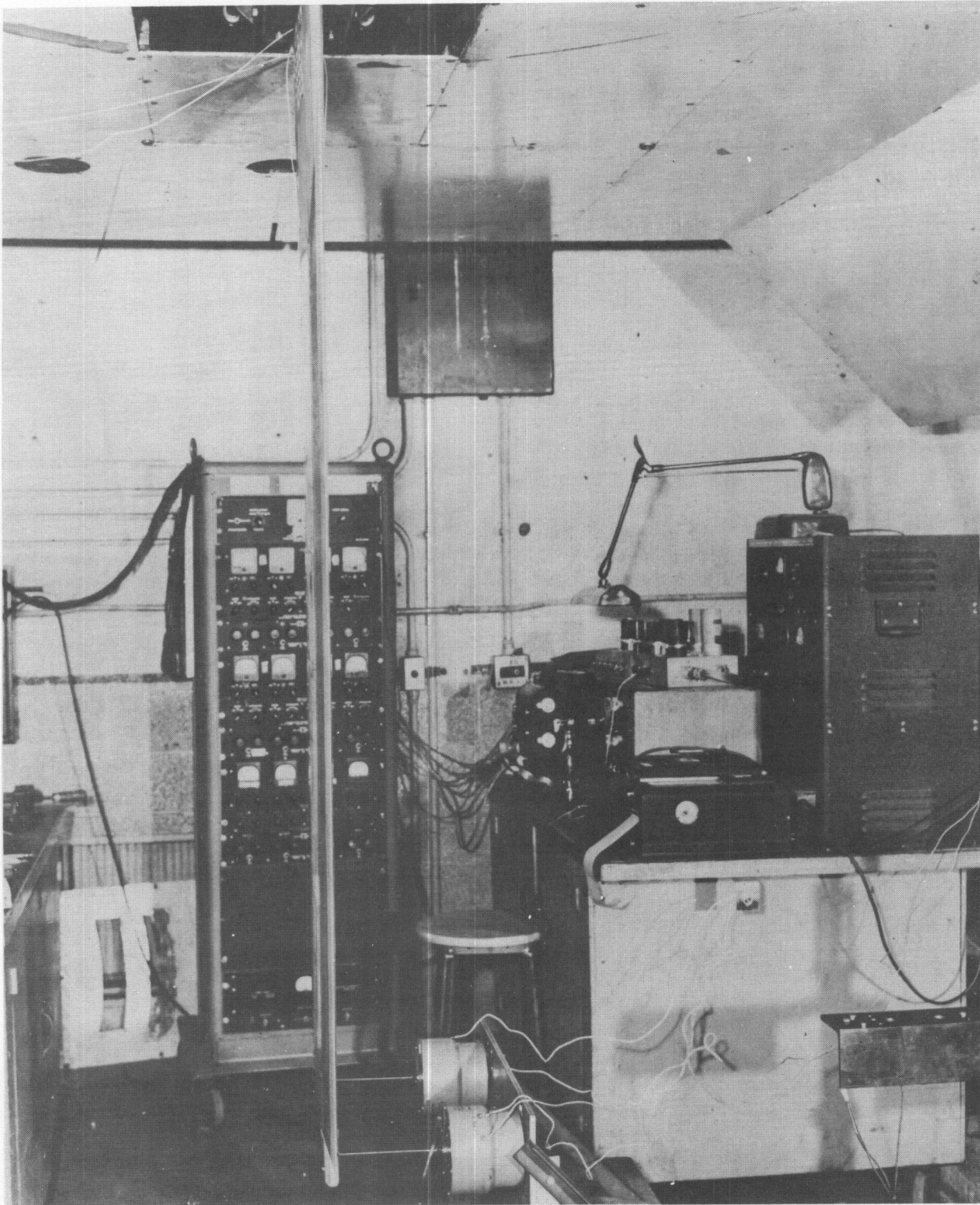


FIGURE 4 TEST SETUP TO OBTAIN VIBRATORY MODES OF THE MODELS

CONFIDENTIAL

[REDACTED]

the oscillatory shaking forces could be applied either in phase, or 180° out of phase with each other. The mass and elastic effects of the shakers were minute on the second and third coupled modes of vibration but were pronounced on the first coupled mode. Therefore, primary bending was determined by means of a "bang" test to eliminate the restraining effects of the shakers. For every plain wing, the first three coupled modes were determined for each of the cantilever, symmetric, and antisymmetric configurations. The node lines were determined from visual observation and the frequencies from the corresponding recorded oscillograph traces. Figures 5 through 13, pp. 13 through 21, present the measured coupled mode frequencies and node lines for the three plain wings. Table 1 lists the measured coupled mode frequencies for the various plain wings in the cantilever, symmetric, and antisymmetric configurations.

The wing-aileron models were dynamically tested the same way as the wings without ailerons, i.e., primary bending was determined by means of a "bang" test and all higher modes were found using electromagnetic shakers. The aileron uncoupled rotational frequencies were determined by mounting the aileron with its associated springs to a heavy dural bar which was firmly anchored to fixed structure. Figures 14 through 31, pp. 23 through 40, present the measured coupled mode frequencies and the associated node lines of the wing-aileron models for all values of the uncoupled aileron rotational frequency tested in the wind tunnel. Table 2 lists the coupled mode frequencies obtained for the different wing-aileron models for the various values of ω_β used.

C. Fatigue and Proof Load Tests

Due to the loss of a model of an early design from large bending oscillations caused by random disturbances in the tunnel, a fatigue and proof test was conducted on an exact duplicate of the load-carrying torque box section used in the final model design.

The fatigue test of the model consisted of vibrating the wing for an extended period of time through an amplitude corresponding to the buffeting amplitude expected in the tunnel. For the test model, a tip amplitude of $1\frac{1}{2}$ in. was maintained at the frequency of the first bending mode for sixteen hours. At the end of this time, approximately 520,000 stress reversals had been applied. Comparison of data obtained from static and dynamic tests conducted before and after the fatigue test, indicated that there were no changes in the model properties. A photograph showing the equipment setup used to conduct this test is shown in Fig. 32.

A proof test of the model was then conducted to determine the maximum deflection obtainable with this type of construction. However, before testing to limit deflection, the wing was flexed ± 5.0 in. for twelve cycles to insure that the model would not fail in the tunnel if deflected the maximum amount allowed by the flutter brake stops. Comparison of results obtained



TABLE I
SUMMARY OF MEASURED COUPLED MODE
VIBRATORY FREQUENCIES FOR PLAIN WINGS

Wing (Designated by Design Mach No.)	1st Coupled Mode (CPS)	2nd Coupled Mode (CPS)	$\frac{\omega_2}{\omega_1}$	3rd Coupled Mode (CPS)	$\frac{\omega_3}{\omega_1}$
CANTILEVER					
0.65	7.3	31.2	4.27	39.2	5.37
0.75	8.5	36.9	4.34	44.8	5.27
0.85	9.0	39.2	4.36	48.6	5.40
SYMMETRIC*					
0.65	7.6	31.3	4.12	39.0	5.13
0.75	8.9	38.3	4.30	45.5	5.11
0.85	9.5	40.0	4.21	47.5	5.00
ANTISYMMETRIC**					
0.65	17.1	33.9	1.98	41.8	2.44
0.75	19.8	41.7	2.11	45.3	2.29
0.85	21.4	45.0	2.10	48.0	2.24

* Translation Frequency = 1.0 CPS

Pitch Frequency = 1.6 CPS

** Roll Frequency = 2.7 CPS



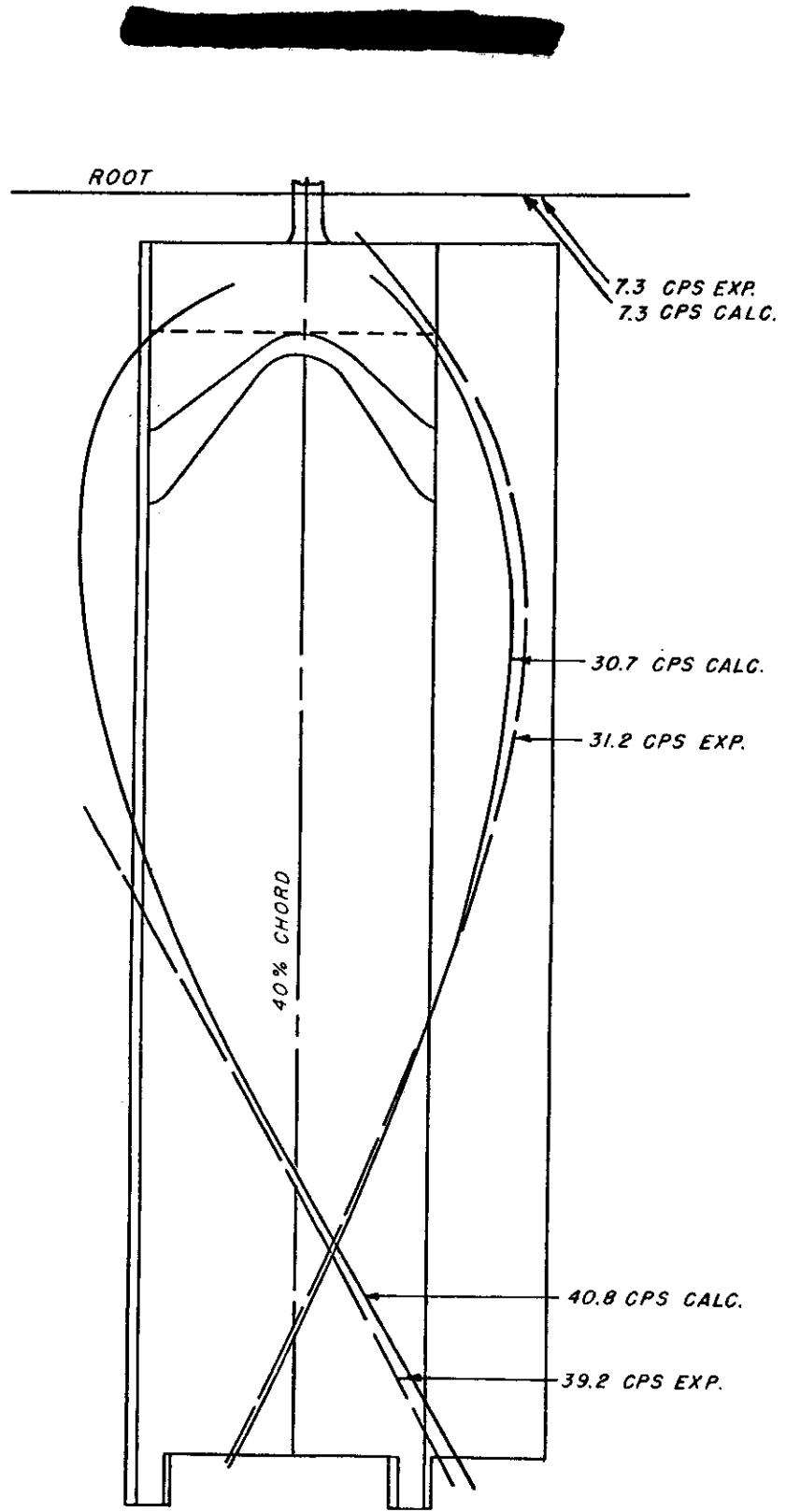


FIGURE 5 $M = 0.65$ MODEL
EXPERIMENTAL AND THEORETICAL CANTILEVER NODE LINES

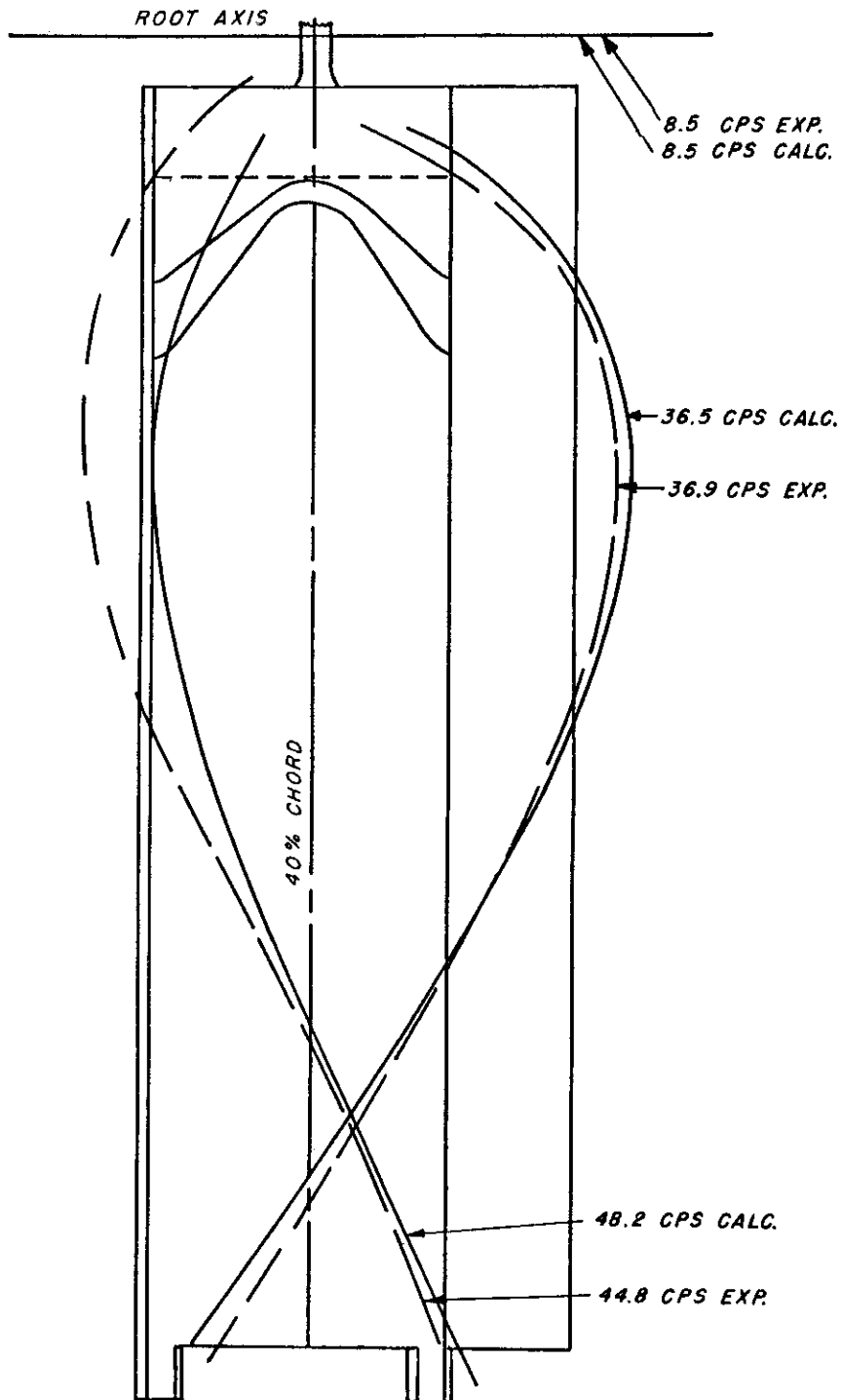


FIGURE 6 $M = 0.75$ MODEL
EXPERIMENTAL AND THEORETICAL CANTILEVER NODE LINES

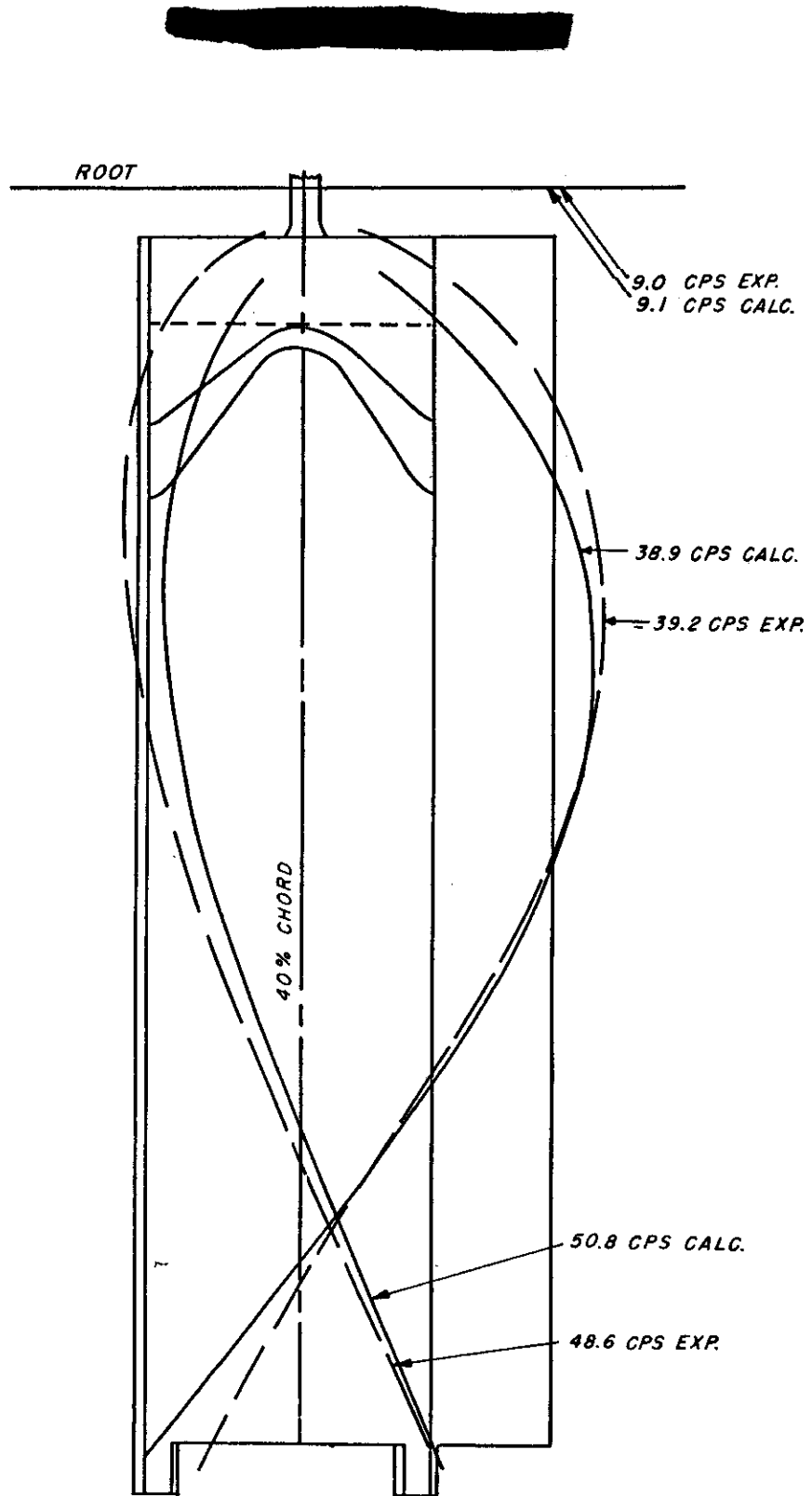


FIGURE 7 $M = 0.85$ MODEL
EXPERIMENTAL AND THEORETICAL CANTILEVER NODE LINES

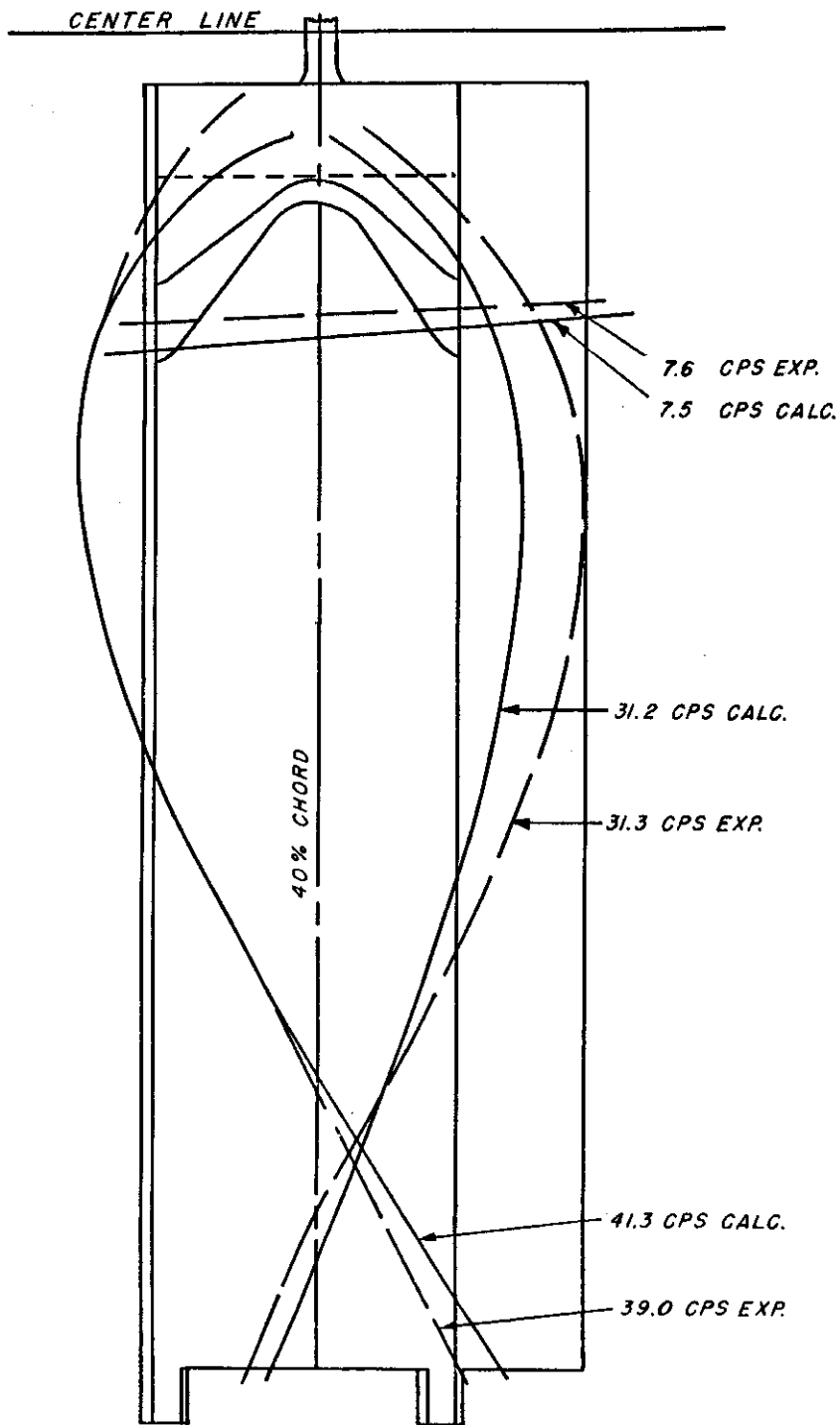


FIGURE 8 $M = 0.65$ MODEL
EXPERIMENTAL AND THEORETICAL SYMMETRIC NODE LINES

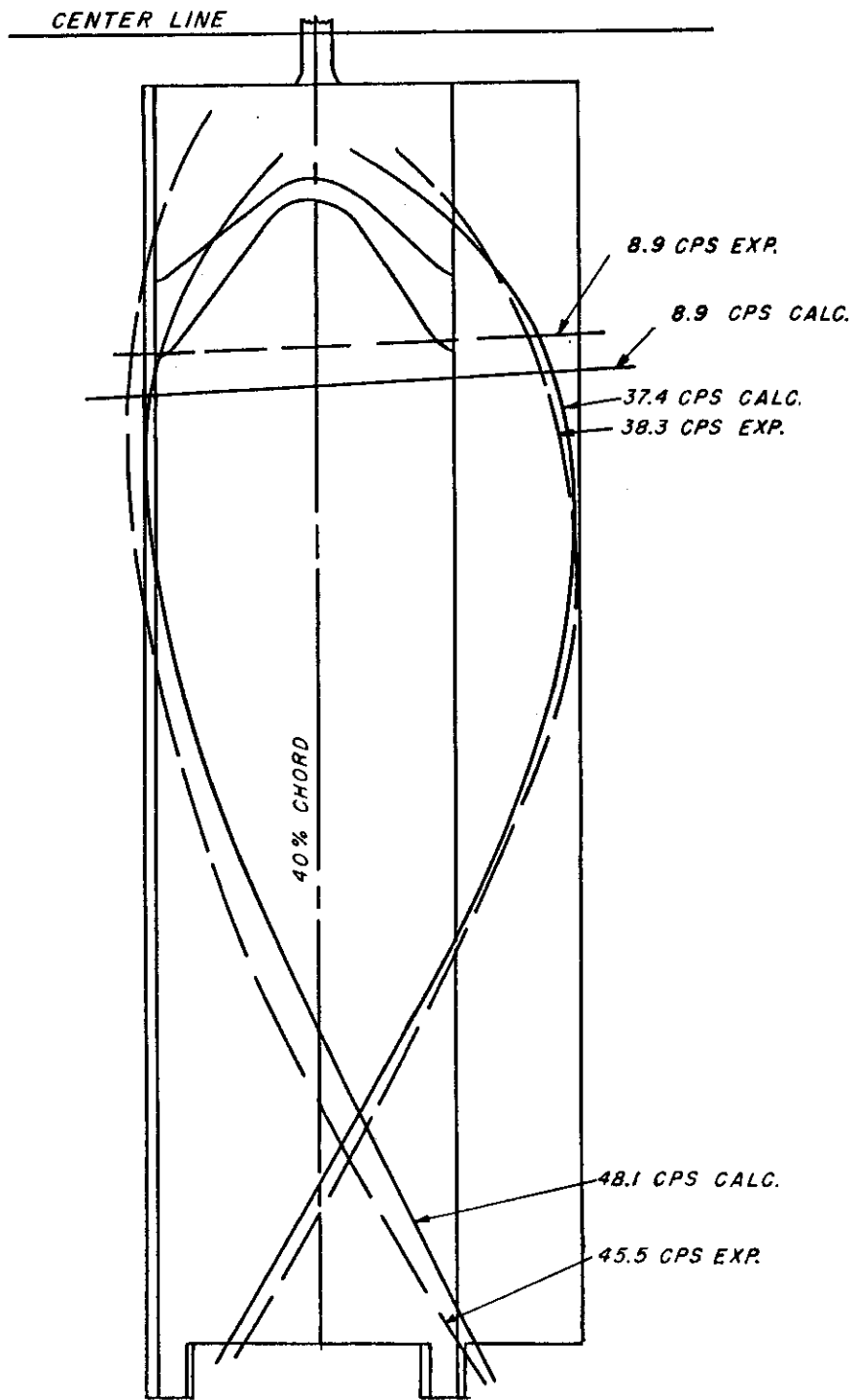


FIGURE 9 $M = 0.75$ MODEL
EXPERIMENTAL AND THEORETICAL SYMMETRIC NODE LINES

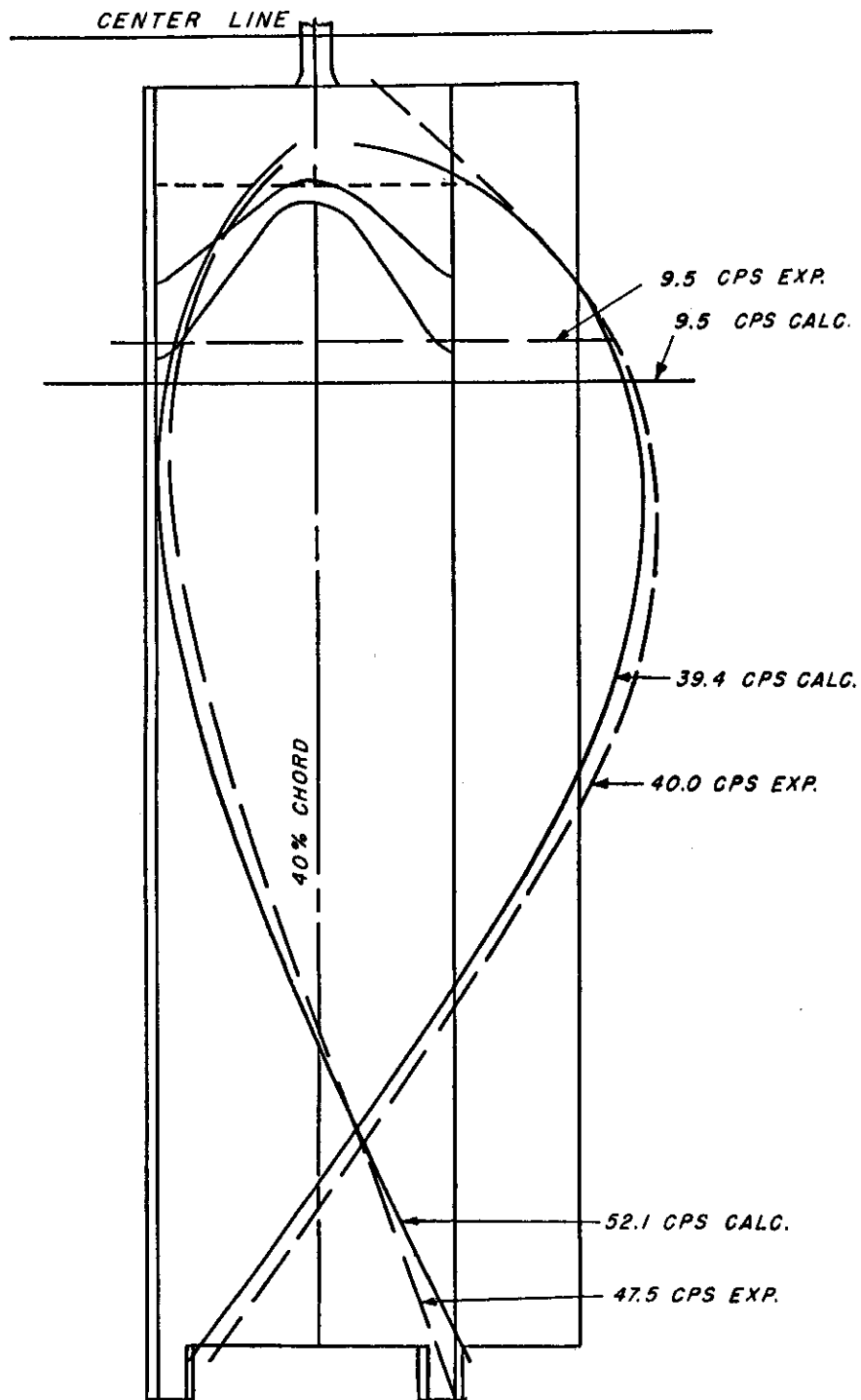


FIGURE 10 $M = 0.85$ MODEL
EXPERIMENTAL AND THEORETICAL SYMMETRIC NODE LINES

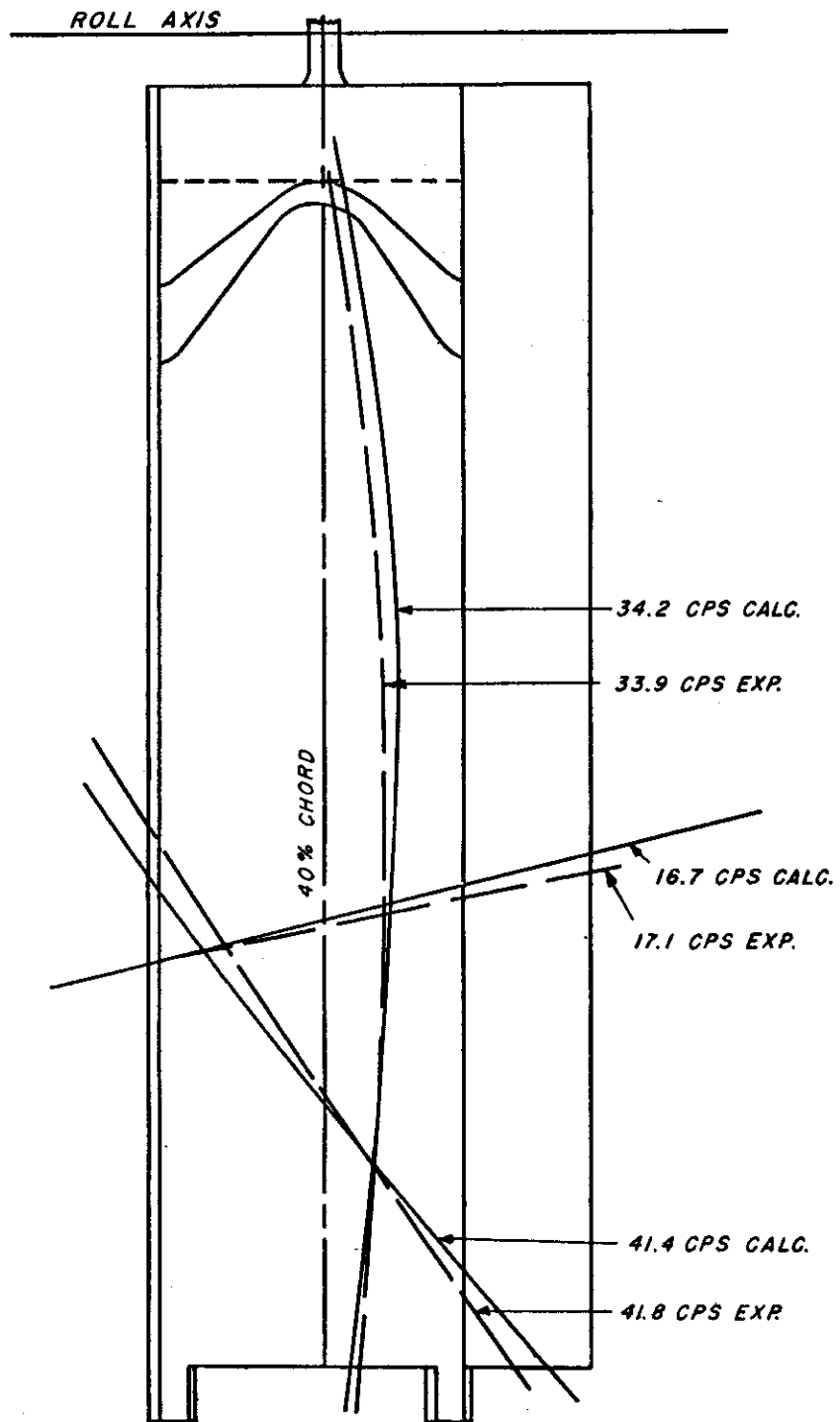


FIGURE 11 $M = 0.65$ MODEL
EXPERIMENTAL AND THEORETICAL ANTISYMMETRIC NODE LINES

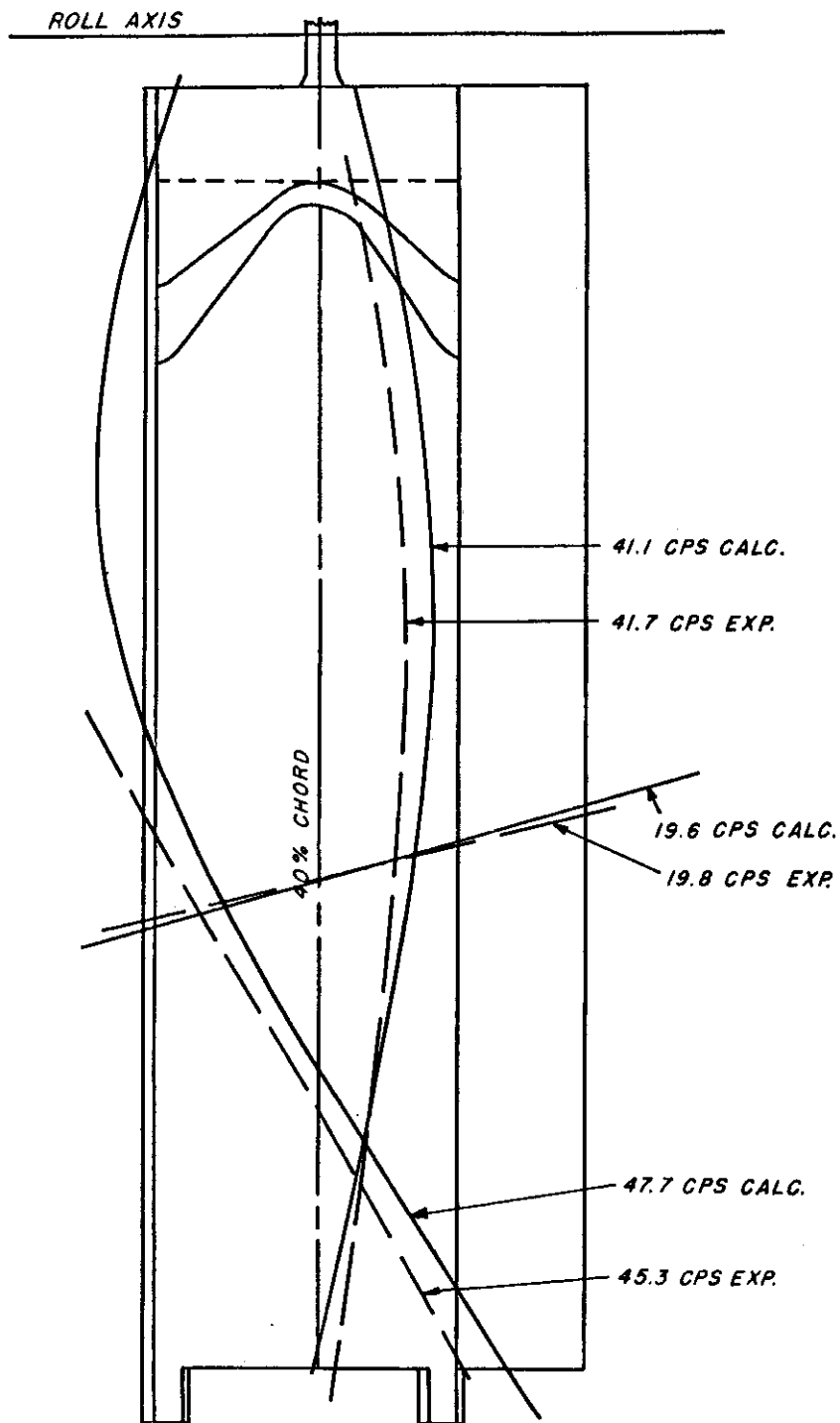


FIGURE 12 $M = 0.75$ MODEL
 EXPERIMENTAL AND THEORETICAL ANTISYMMETRIC NODE LINES

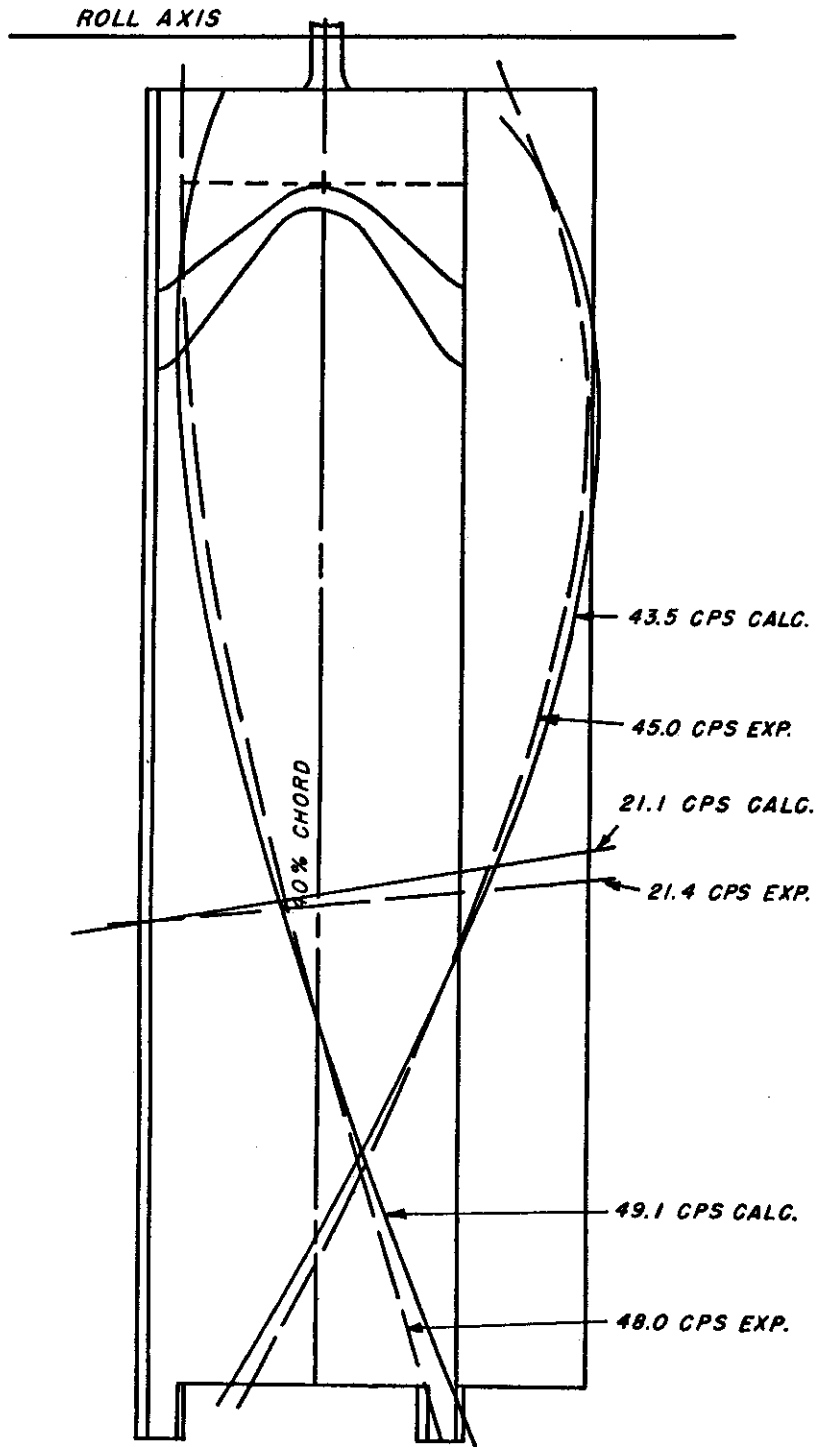


FIGURE 13 $M = 0.85$ MODEL
EXPERIMENTAL AND THEORETICAL ANTISYMMETRIC NODE LINES

TABLE II

SUMMARY OF MEASURED COUPLED MODE FREQUENCIES
FOR ALL WING-AILERON CONFIGURATIONS TESTED
(WING ROOT CANTILEVERED)

Model	ω_β (GPs)	$\omega_\beta/\omega_{\alpha_1}$	COUPLED MODE FREQUENCIES (GPs)				
			1st Mode	2nd Mode	3rd Mode	4th Mode	5th Mode
0.65	15.0	0.45	7.2	14.6	30.0	40.2	----
0.65	25.9	0.78	7.2	24.3	30.9	40.5	----
0.65	33.1	1.00	7.2	29.4	32.1	41.9	----
0.65	39.9	1.21	7.2	30.2	34.9	45.3	70.0
0.65	42.0	1.27	7.2	29.6	35.1	45.5	70.0
0.65	47.9	1.45	7.2	29.7	36.1	50.0	70.0
0.65	54.5	1.65	7.2	29.9	36.7	55.6	70.8
0.65	61.6	1.86	7.2	30.0	37.1	59.7	72.0
0.75	22.8	0.56	8.4	22.4	36.4	45.7	----
0.75	33.1	0.81	8.4	31.0	36.4	46.5	----
0.75	39.9	0.97	8.4	34.8	37.5	48.7	----
0.75	44.6	1.09	8.4	35.3	38.5	49.5	81.2
0.75	49.7	1.21	8.4	35.7	40.3	52.6	81.5
0.75	54.4	1.33	8.4	35.7	41.7	57.3	82.4
0.85	22.8	0.51	8.9	23.2	37.5	48.9	----
0.85	36.0	0.80	8.9	33.3	38.7	49.2	----
0.85	44.6	0.99	8.9	37.5	40.7	52.2	88.9
0.85	49.7	1.10	8.9	37.7	42.3	54.3	88.9

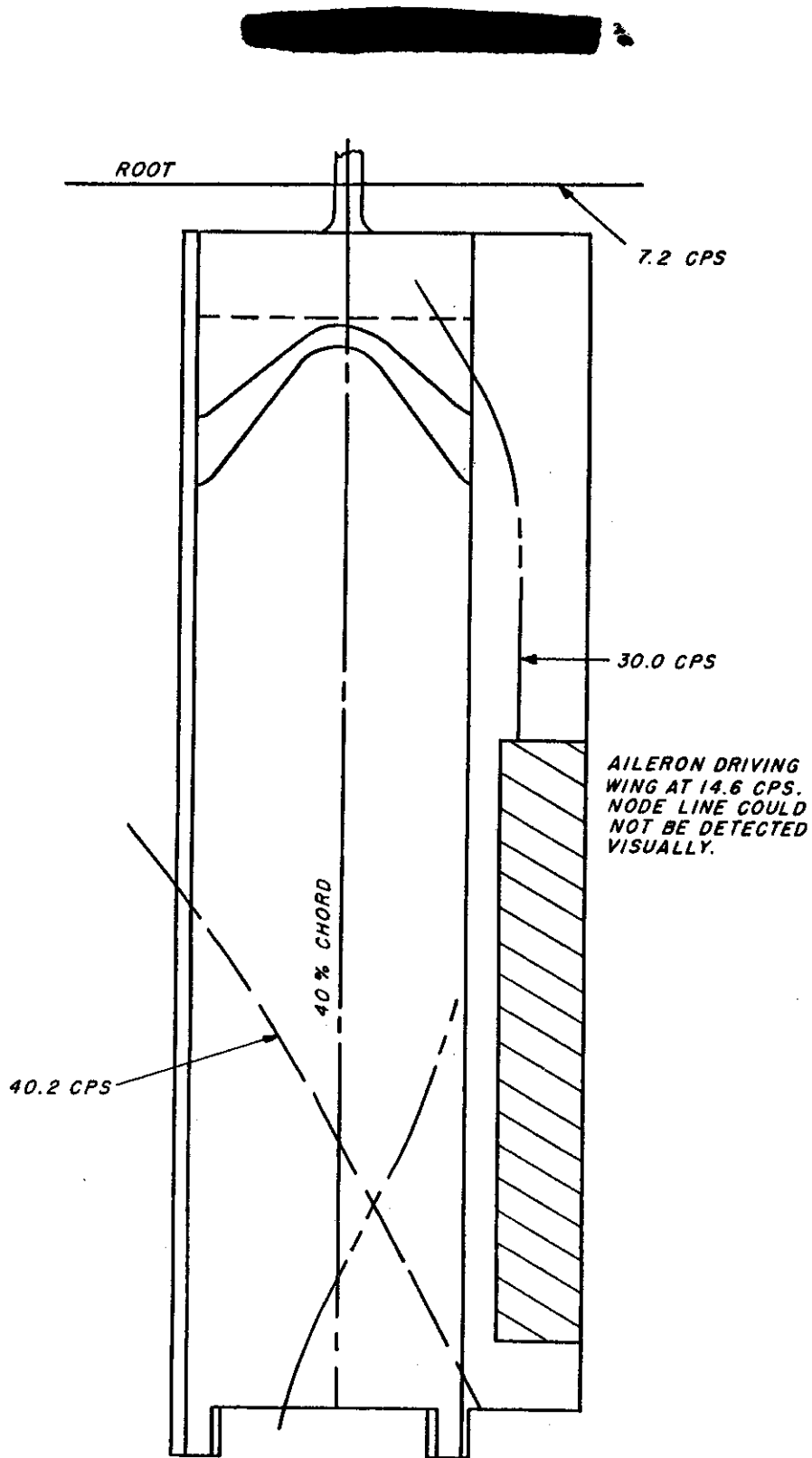


FIGURE 14 EXPERIMENTAL WING-AILERON NODE LINES

$M = 0.65$ MODEL $\omega_2 = 15.0$ CPS $\frac{\omega_2}{\omega_1} = 0.45$

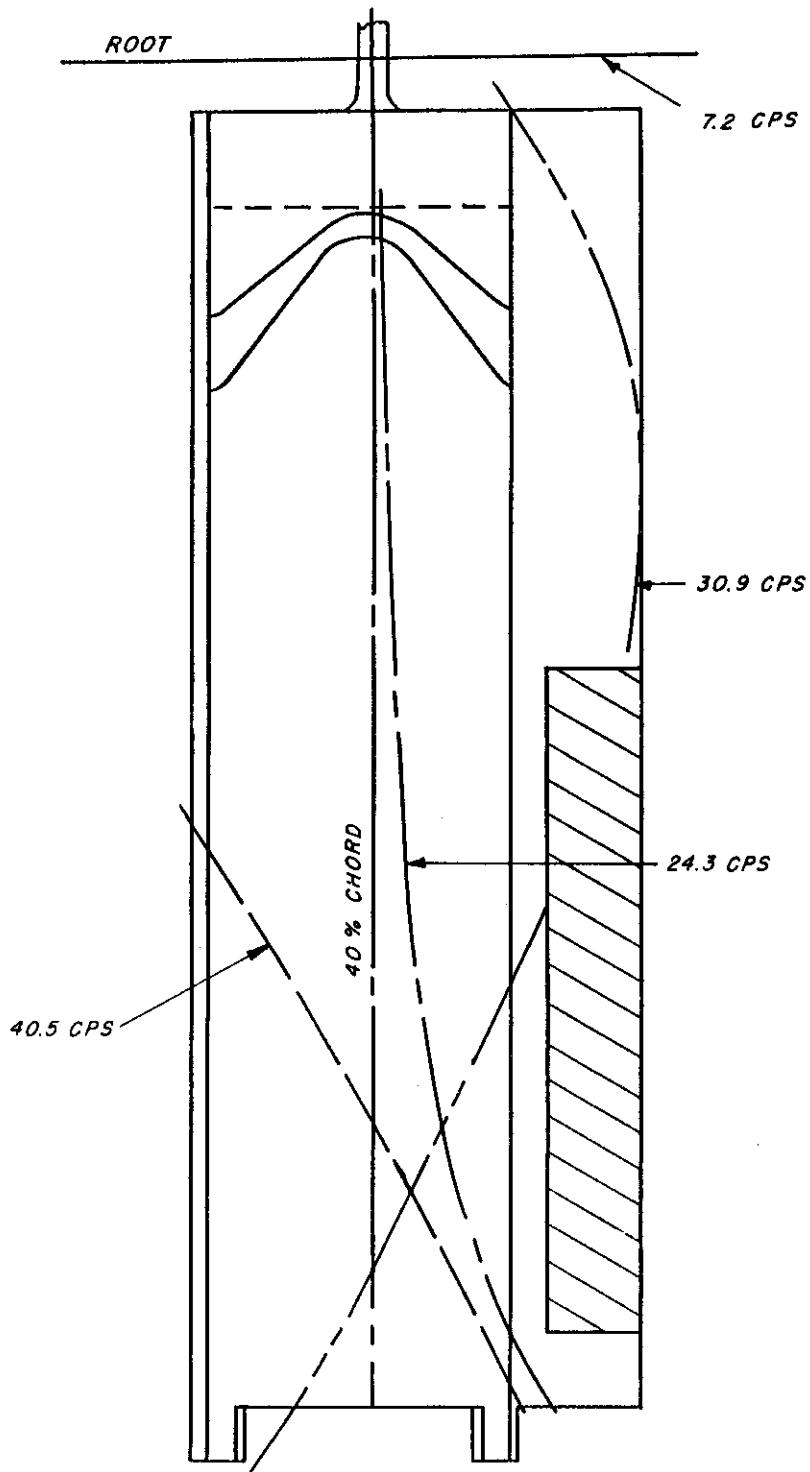


FIGURE 15 EXPERIMENTAL WING-AILERON NODE LINES

$M = 0.65$ MODEL $\omega_0 = 25.9$ CPS

$$\frac{\omega_2}{\omega_1} = 0.78$$

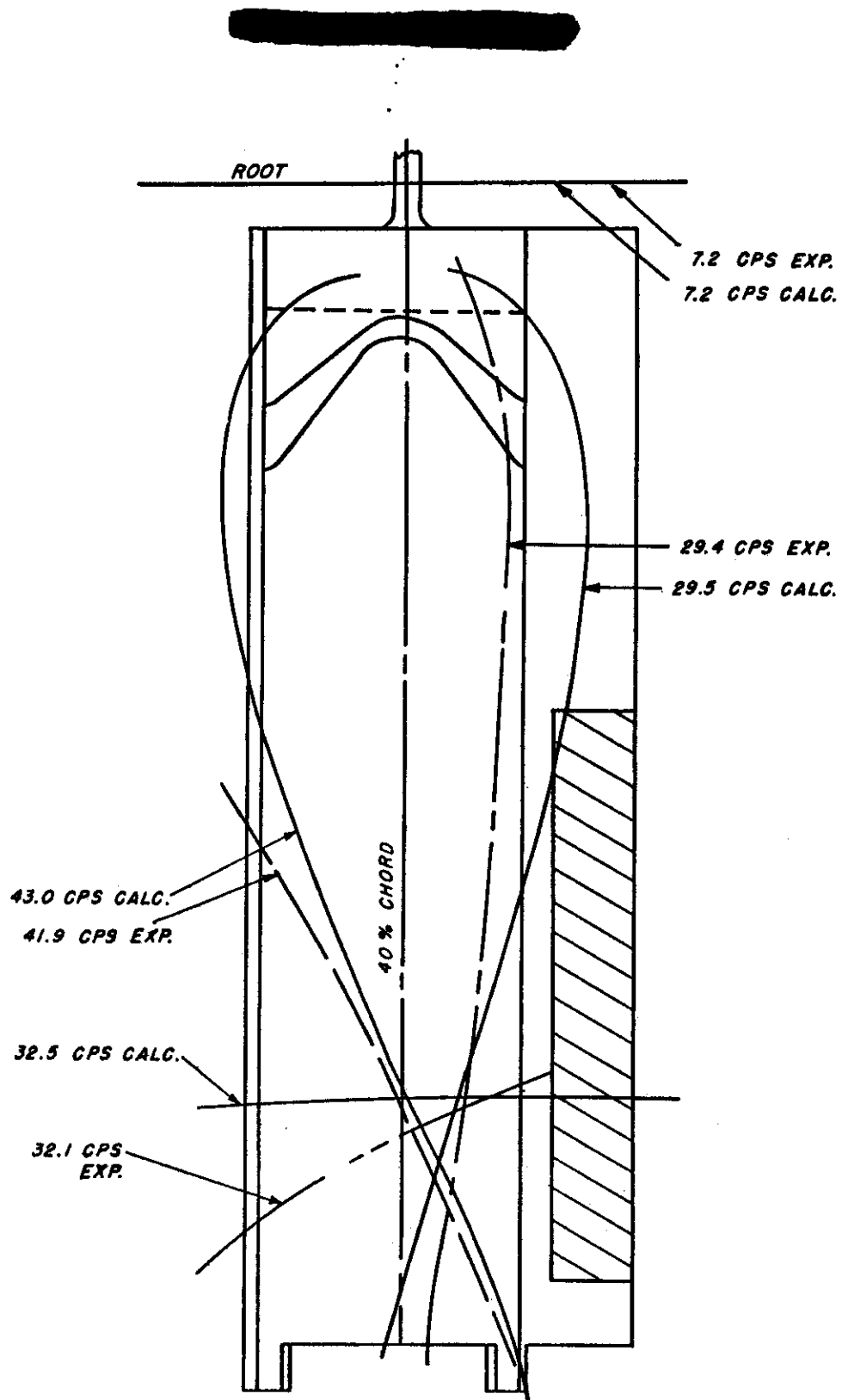


FIGURE 16 EXPERIMENTAL AND THEORETICAL WING-AILERON NODE LINES
 $H = 0.65$ MODEL $\omega_B = 33.1$ CPS $\frac{\omega_A}{\omega_{\alpha,1}} = 1.00$

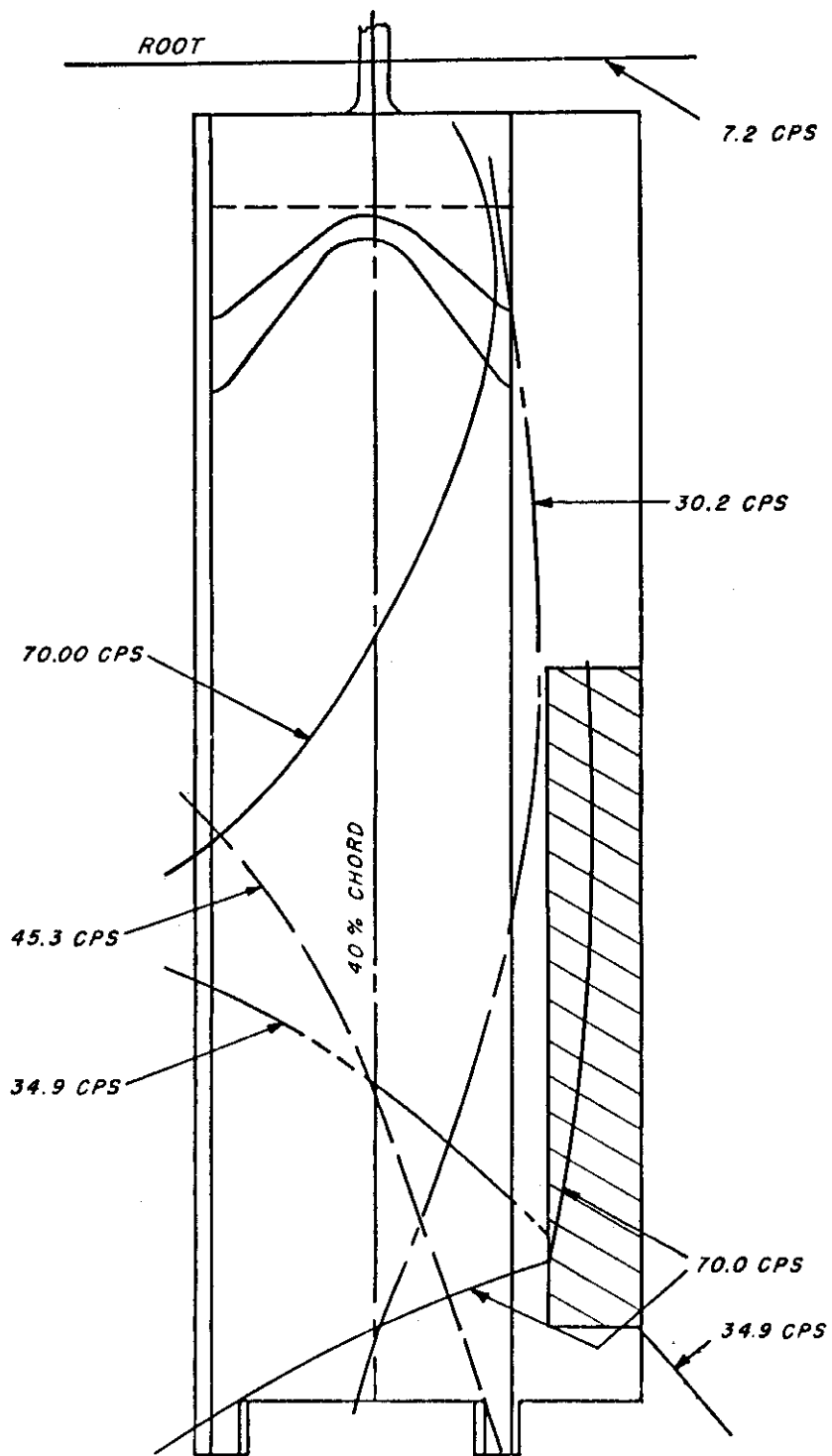


FIGURE 17 EXPERIMENTAL WING-AILERON NODE LINES
 $M = 0.65$ MODEL $\omega_B = 39.9$ CPS $\frac{\omega_B}{\omega_{\omega_1}} = 1.21$

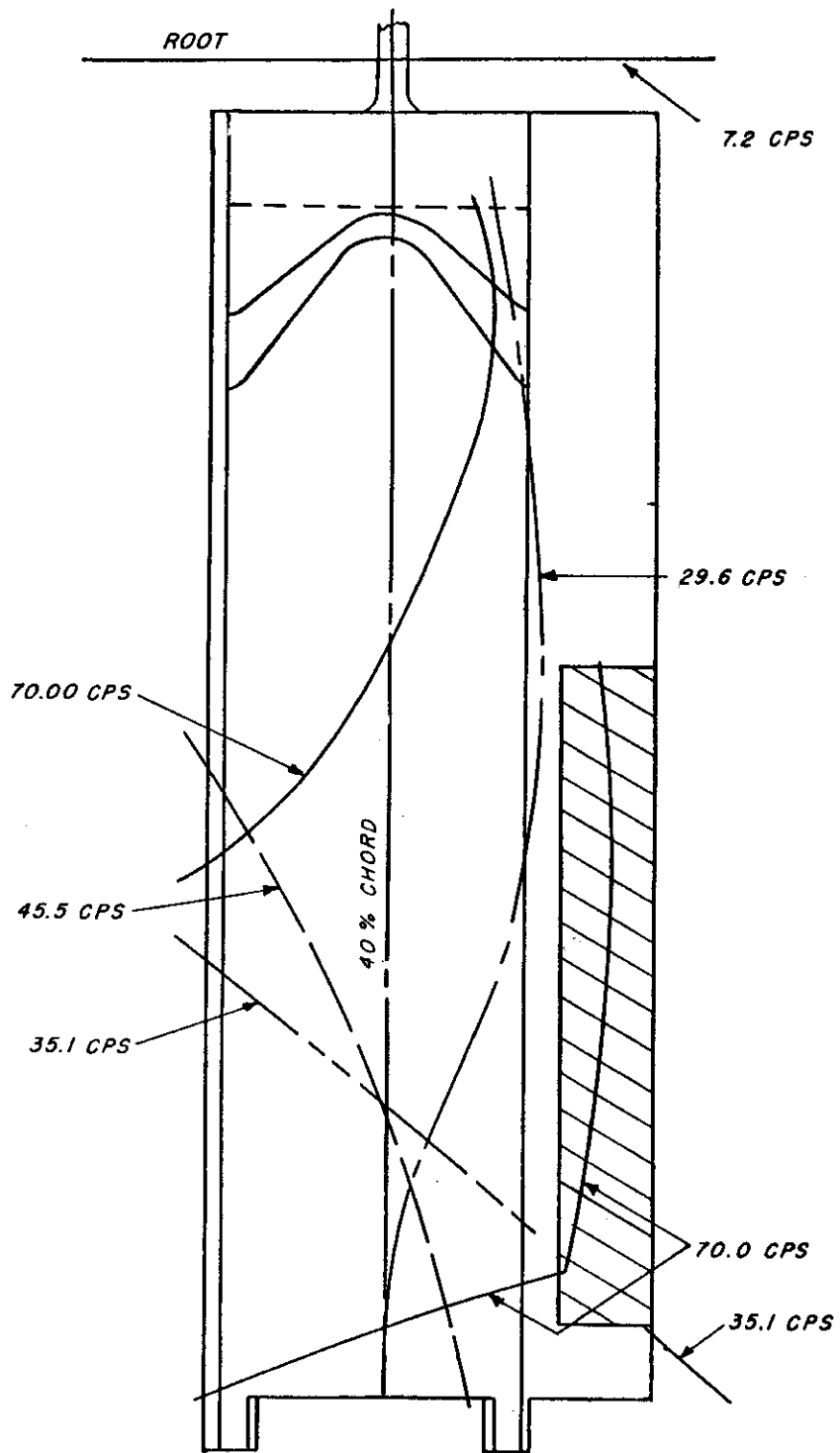


FIGURE 18 EXPERIMENTAL WING-AILERON NODE LINES
 $M = 0.65$ MODEL $\omega_B = 42.0$ CPS $\frac{\omega_B}{\omega_{\infty 1}} = 1.27$

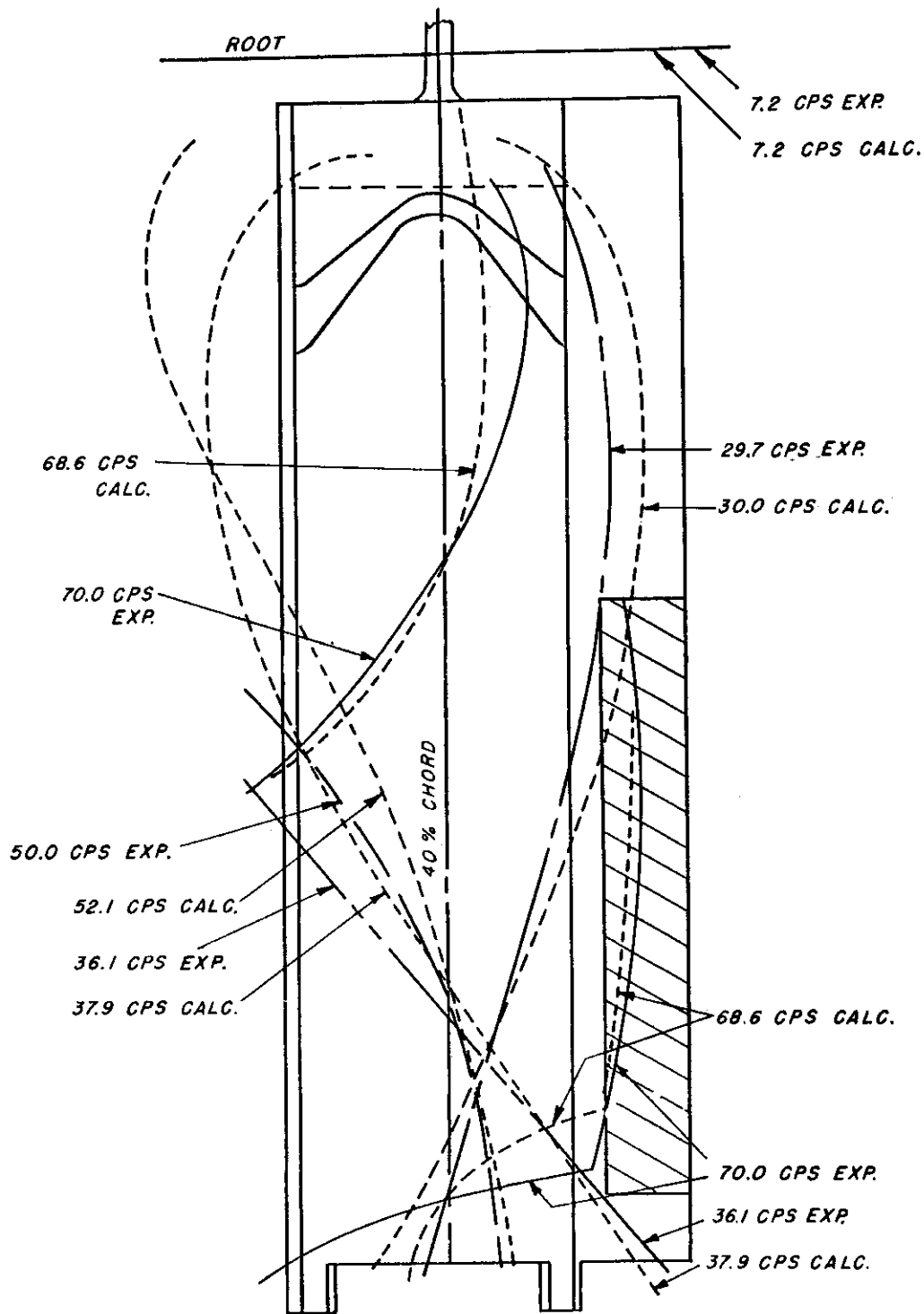


FIGURE 19 EXPERIMENTAL AND THEORETICAL WING-AILERON NODE LINES

$M = 0.65$ MODEL $\omega_B = 47.9$ CPS $\frac{\omega_B}{\omega_{\infty}} = 1.45$

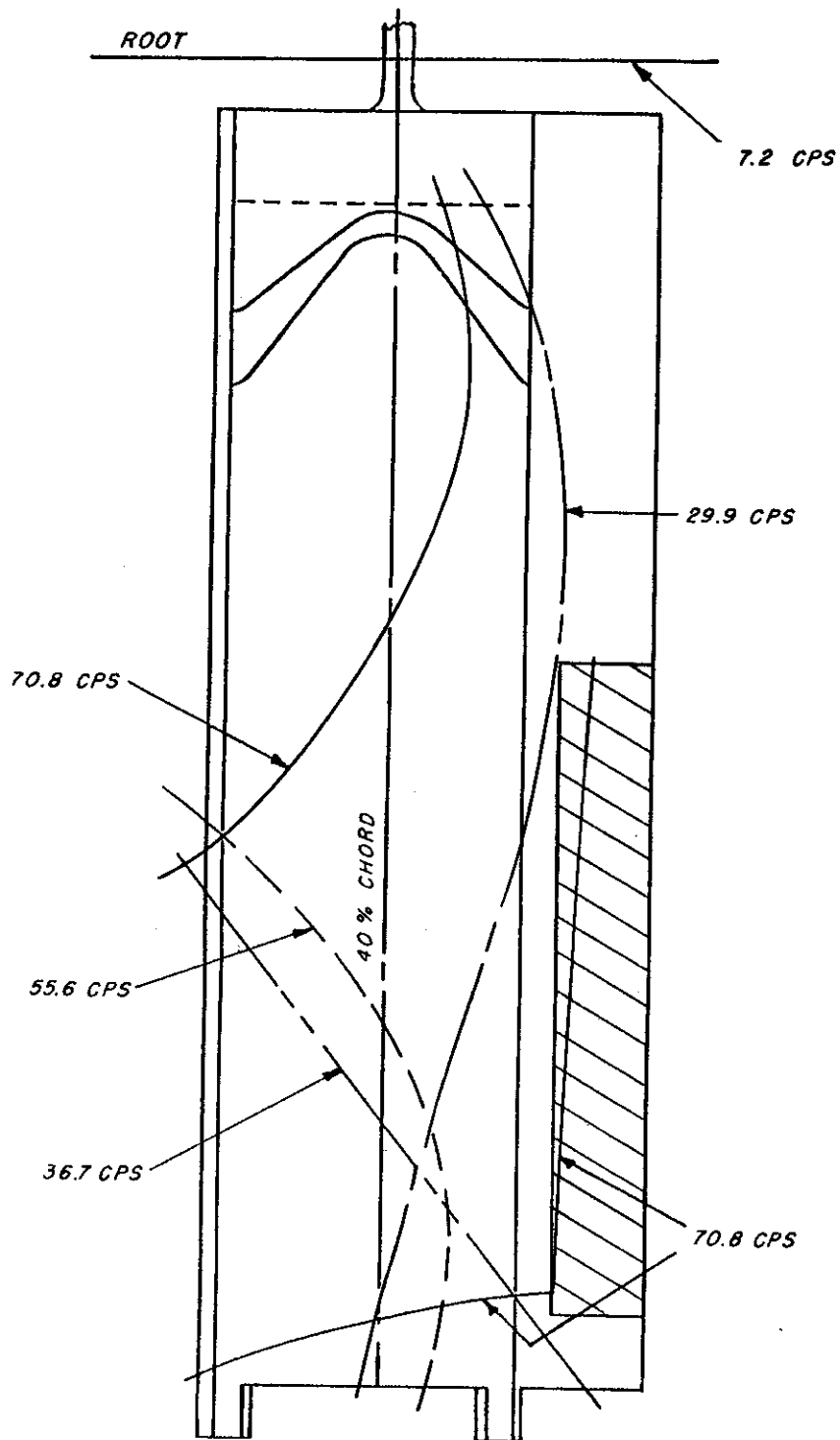


FIGURE 20 EXPERIMENTAL WING-AILERON NODE LINES
 $M = 0.65$ MODEL $\omega_B = 54.4$ CPS $\frac{\omega_B}{\omega_{\omega_1}} = 1.65$

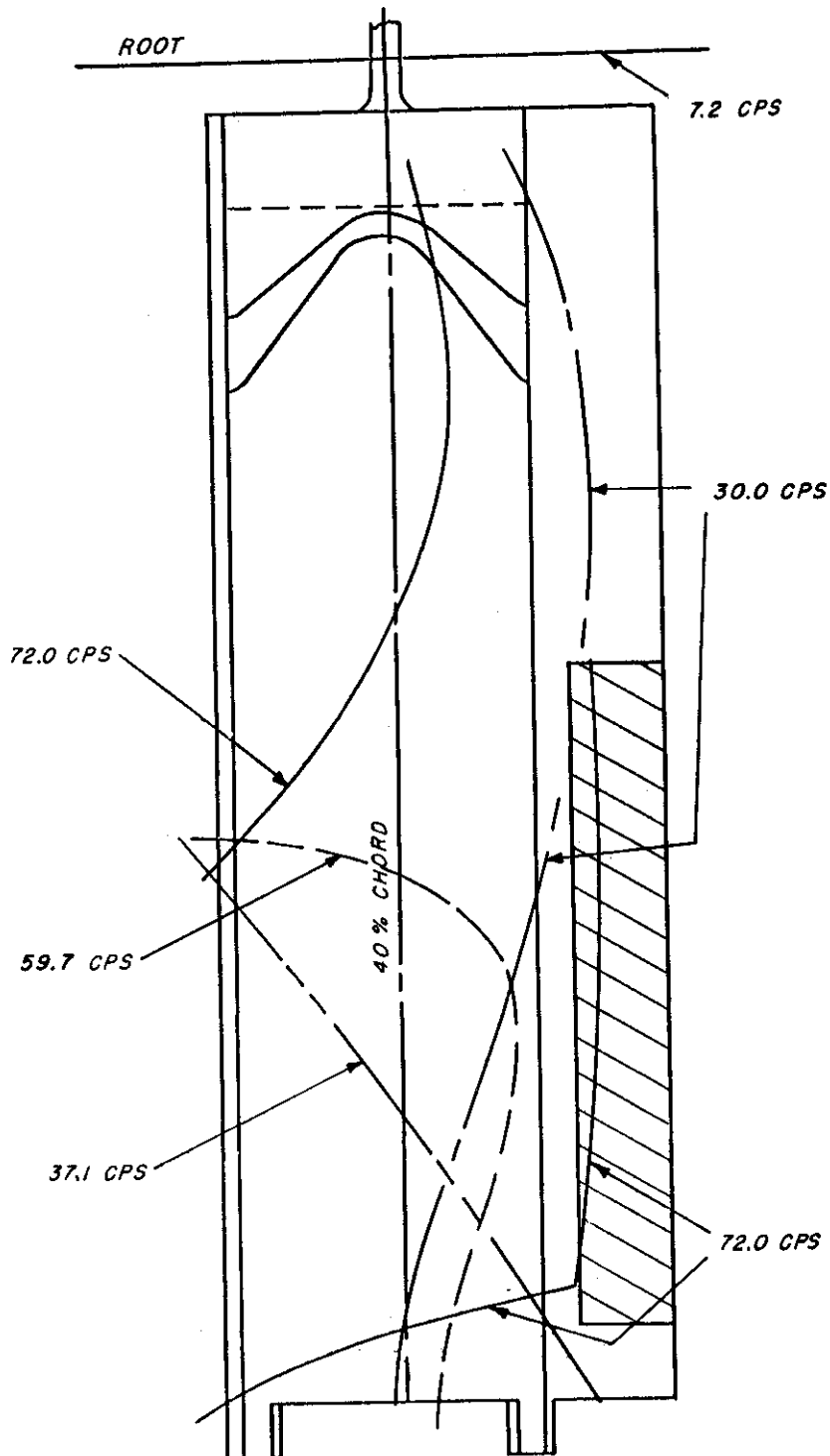


FIGURE 21 EXPERIMENTAL WING-AILERON NODE LINES
 $M = 0.65$ MODEL $\omega_B = 61.6$ CPS $\frac{\omega_B}{\omega_{W1}} = 1.86$

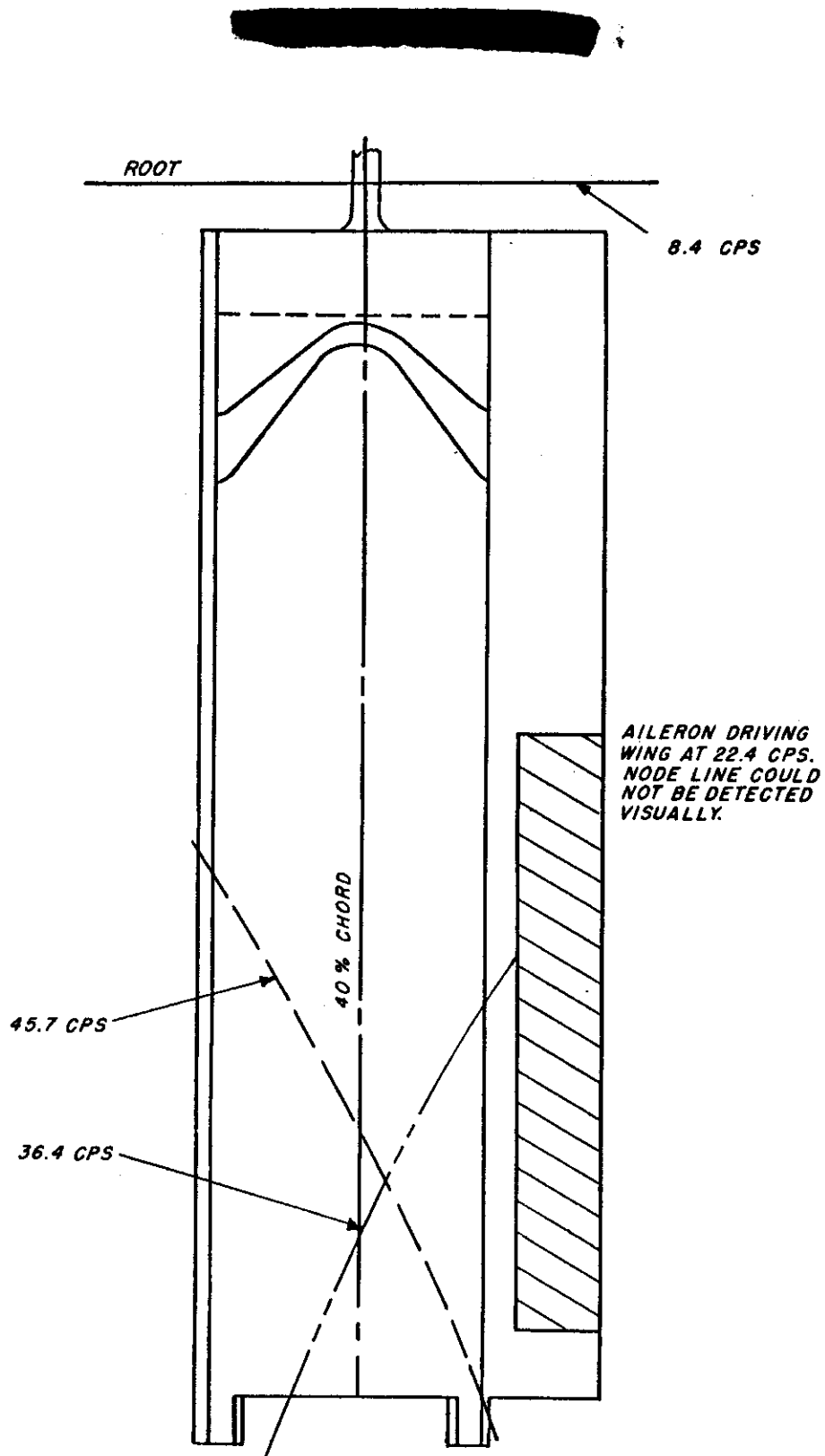


FIGURE 22 EXPERIMENTAL WING-AILERON NODE LINES

$M = 0.75$ MODEL

$\omega_2 = 22.8$ CPS

$\frac{\omega_2}{\omega_1} = 0.56$

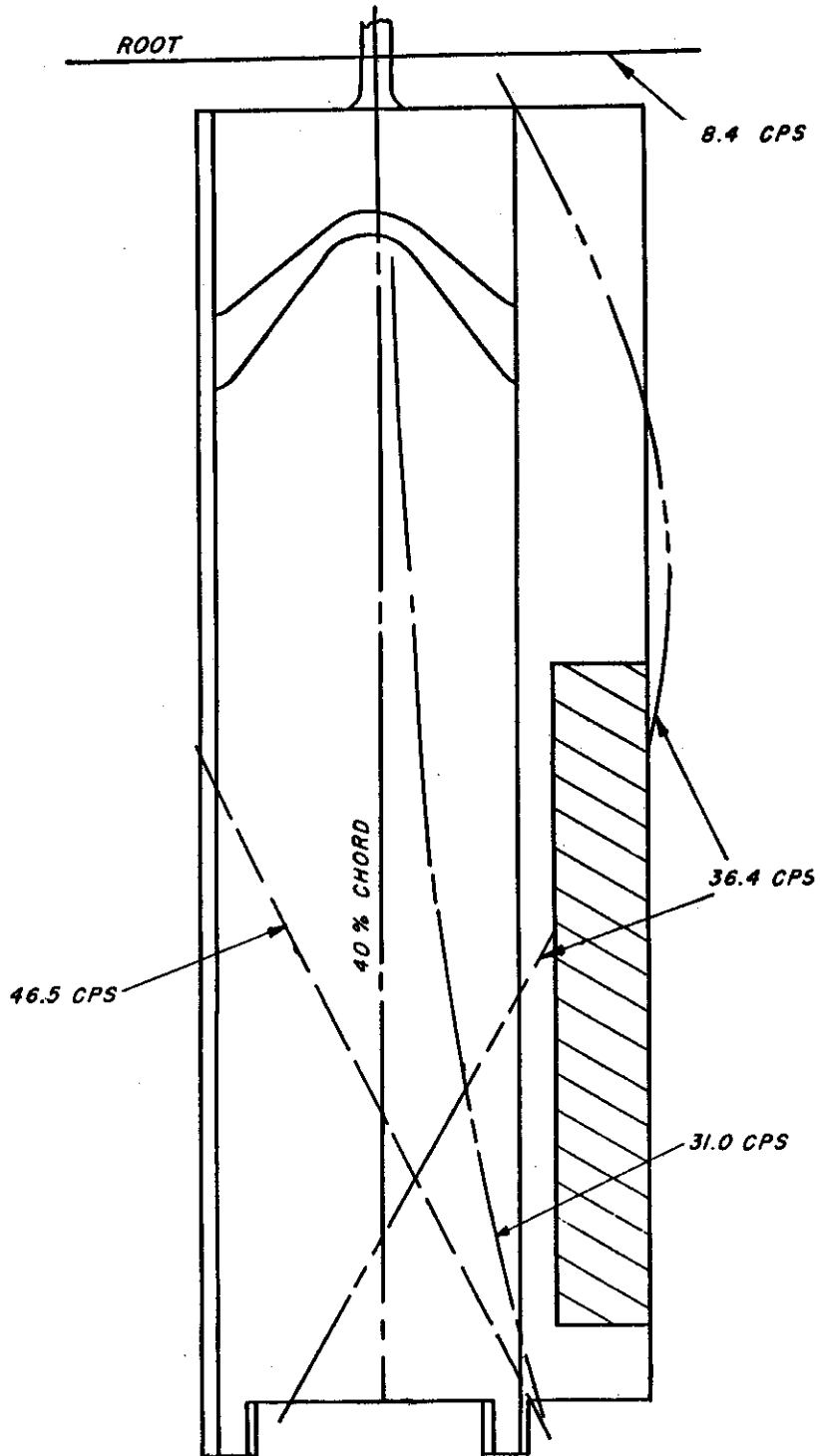


FIGURE 23 EXPERIMENTAL WING-AILERON NODE LINES

$M = 0.75$ MODEL

$\omega_B = 33.1$ CPS

$\frac{\omega_B}{\omega_{W1}} = 0.81$

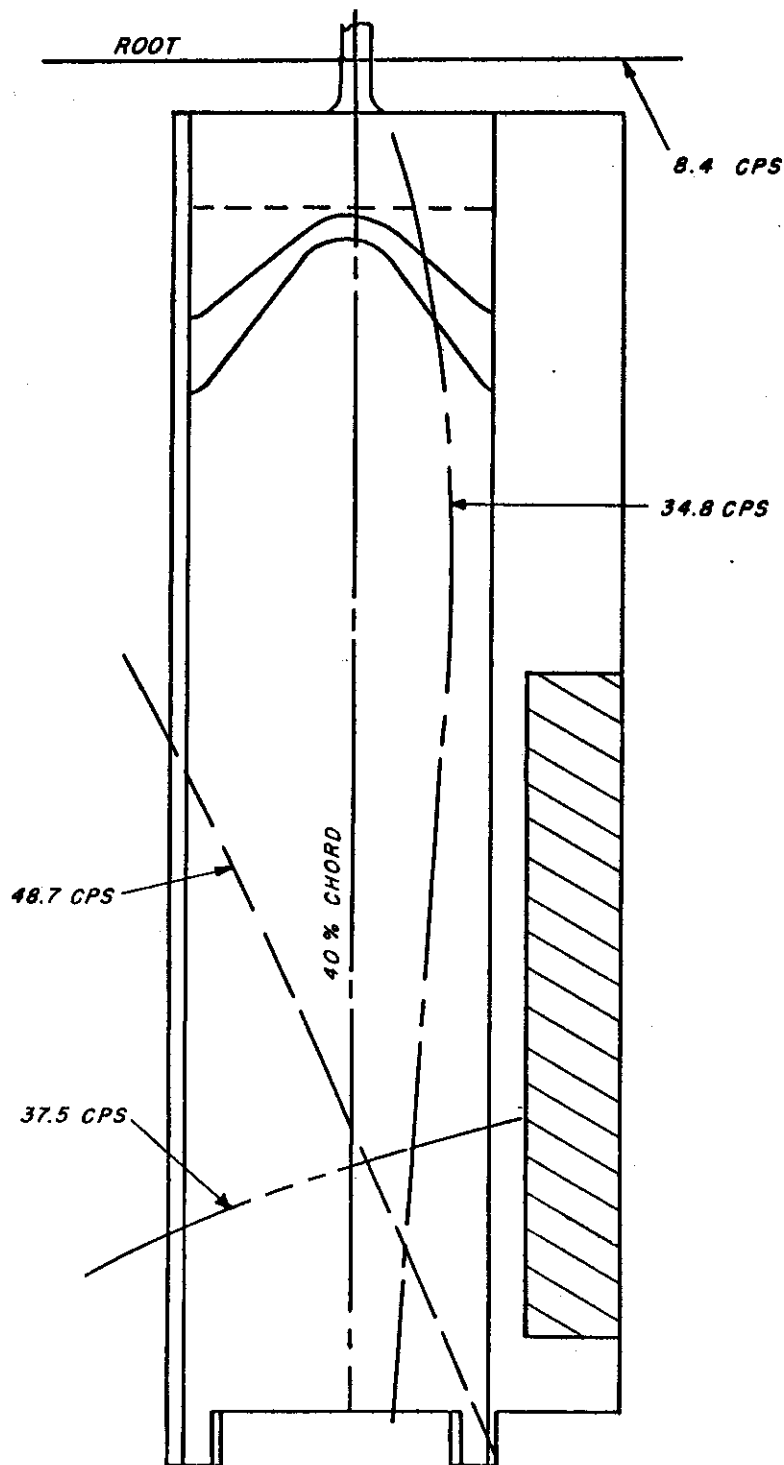


FIGURE 24 EXPERIMENTAL WING-AILERON NODE LINES
 $M = 0.75$ MODEL $\omega_3 = 39.9$ CPS $\frac{\omega_3}{\omega_{\alpha_1}} = 0.97$

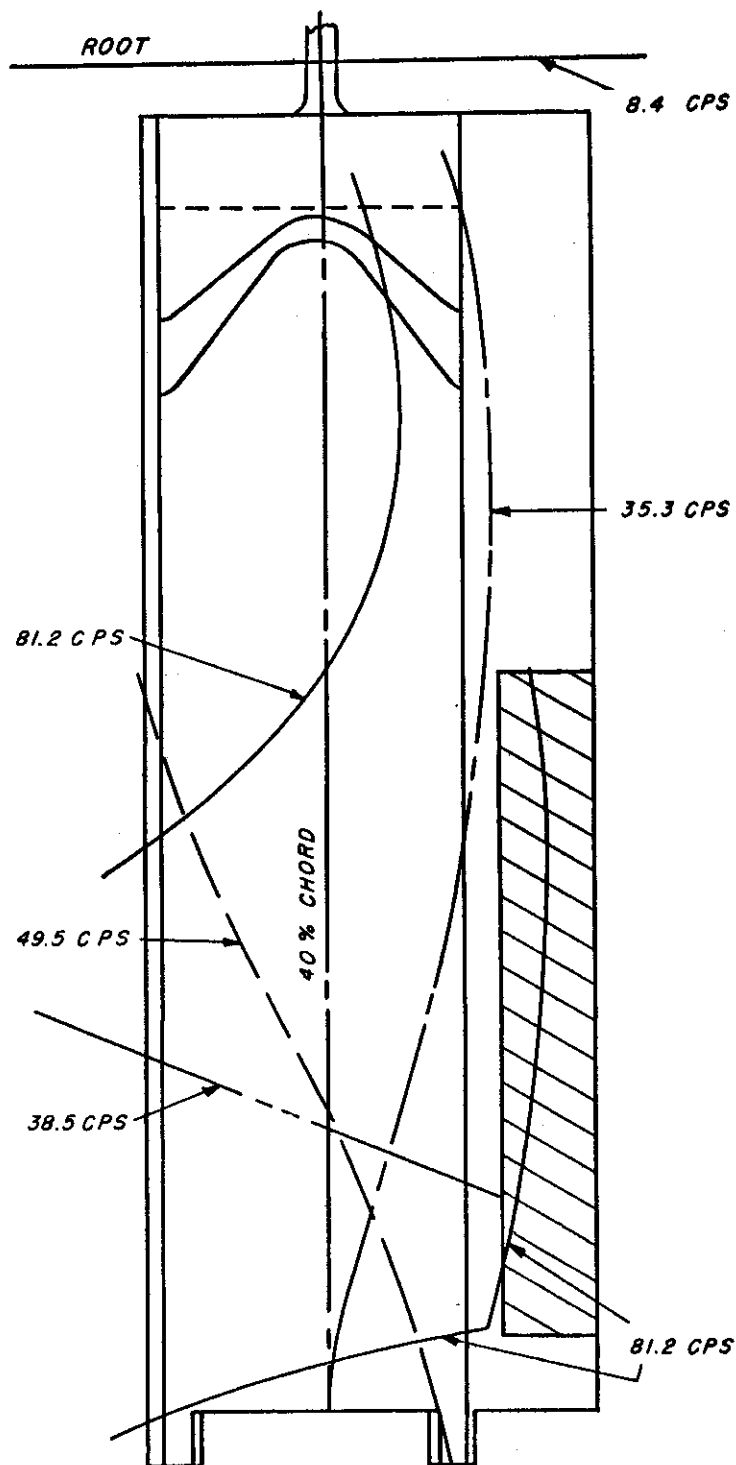


FIGURE 25 EXPERIMENTAL WING-AILERON NODE LINES

$M = 0.75$ MODEL $\omega_B = 44.6$ CPS

$$\frac{\omega_B}{\omega_{\alpha_1}} = 1.09$$



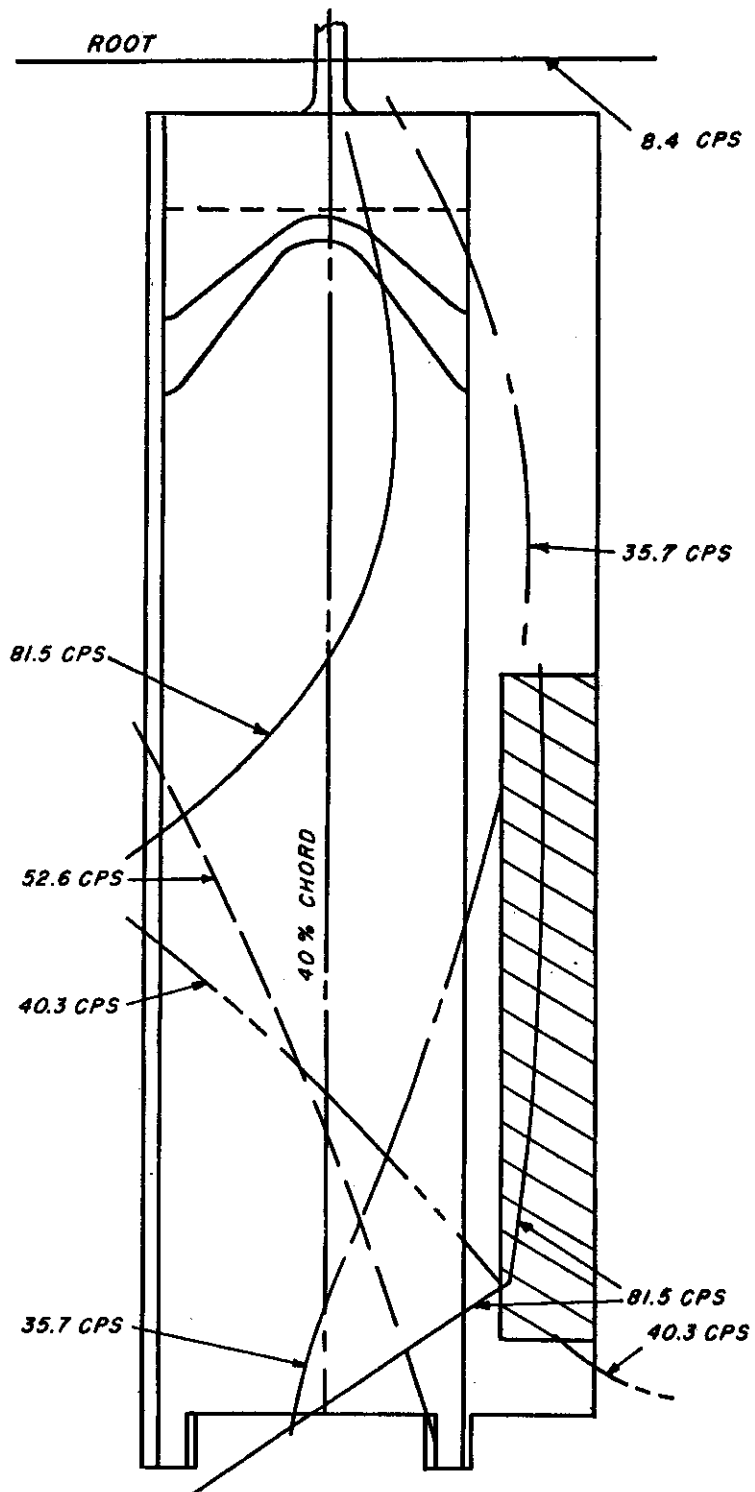


FIGURE 26 EXPERIMENTAL WING-AILERON NODE LINES
 $M = 0.75$ MODEL $\omega_B = 49.7$ CPS $\frac{\omega_B}{\omega_{a1}} = 1.21$

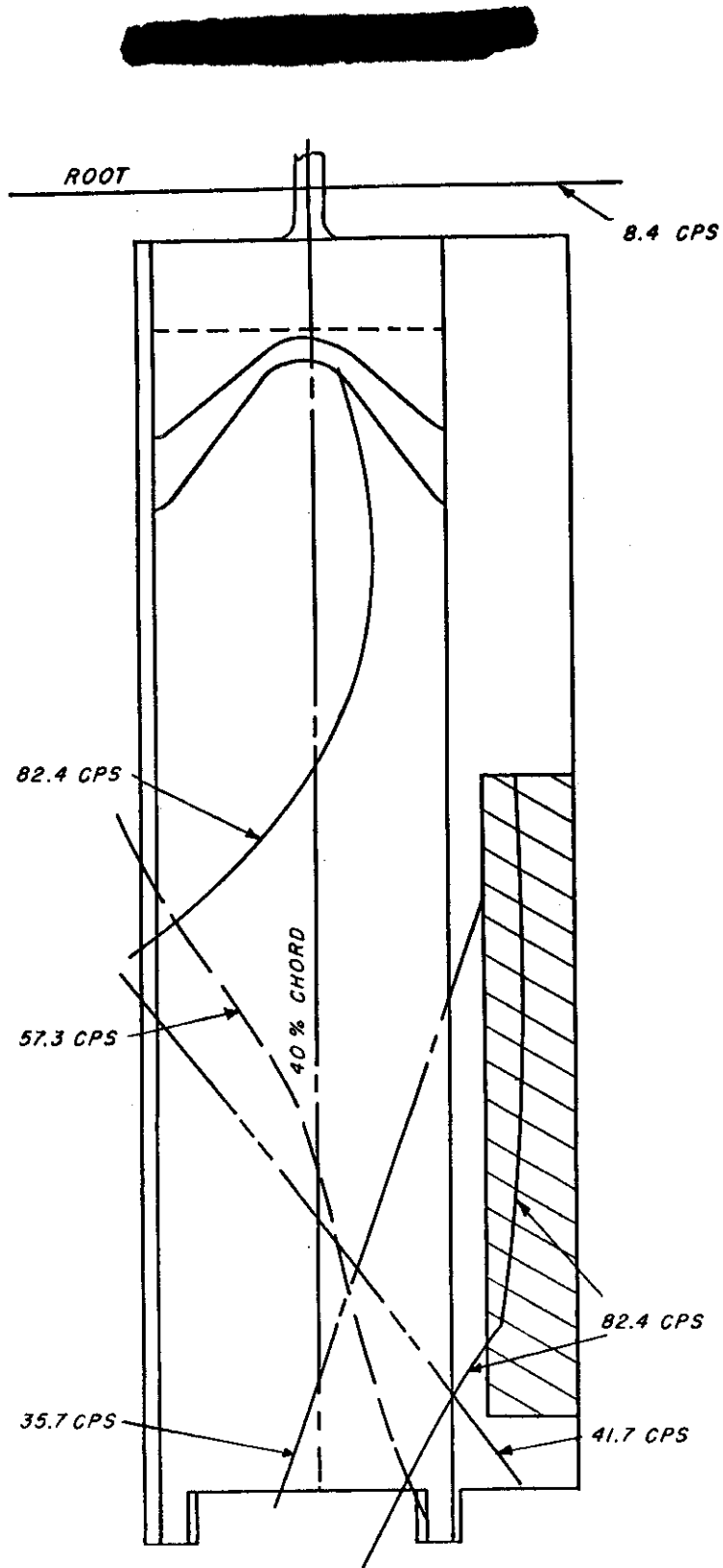


FIGURE 27 EXPERIMENTAL WING-AILERON NODE LINES

$M = 0.75$ MODEL $\omega_B = 54.4$ CPS

$$\frac{\omega_B}{\omega_{\alpha 1}} = 1.33$$

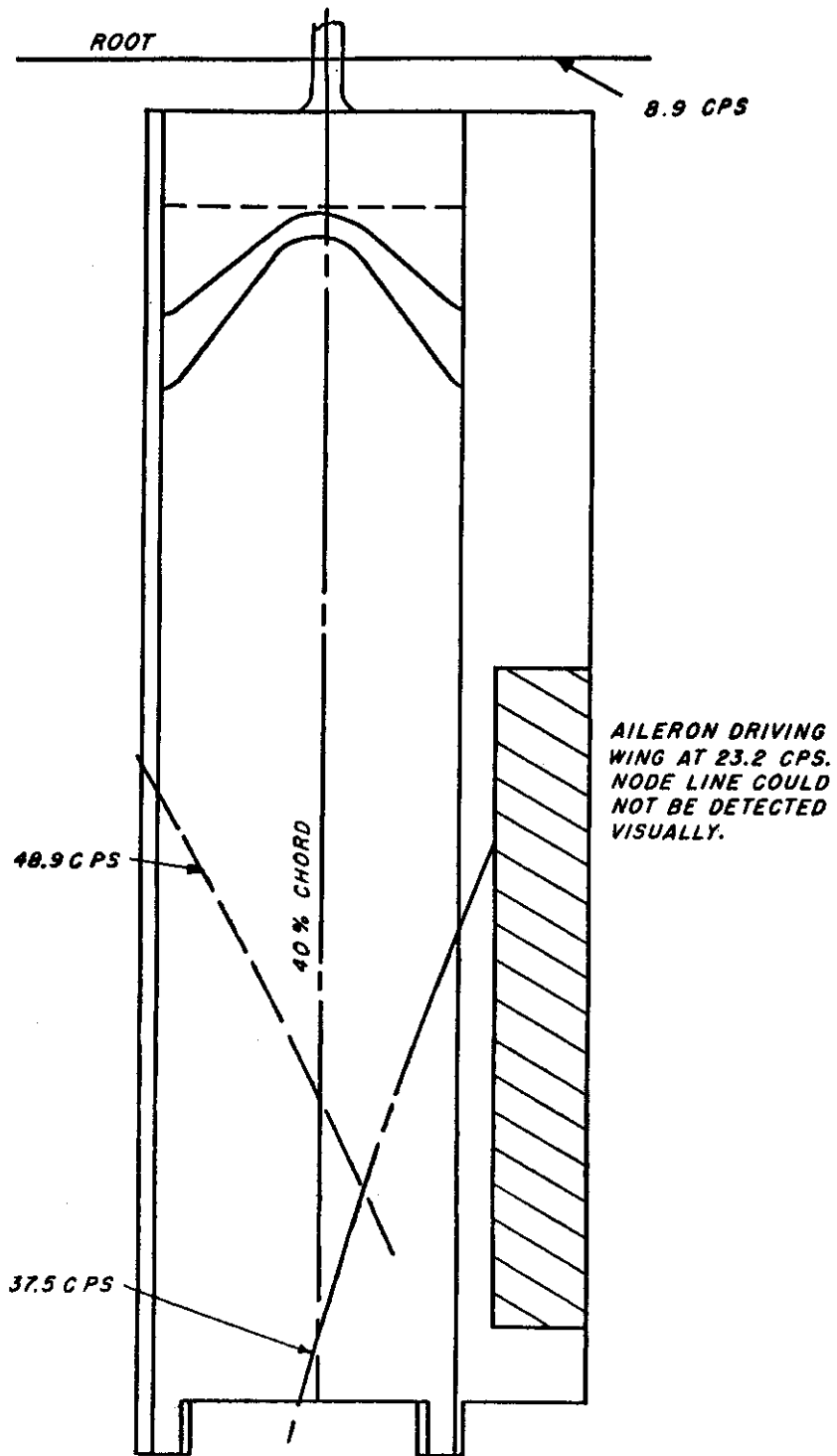


FIGURE 28 EXPERIMENTAL WING-AILERON NODE LINES

$M = 0.85$ MODEL

$\omega_B = 22.8$ CPS

$\frac{\omega_A}{\omega_{\alpha_1}} = 0.51$

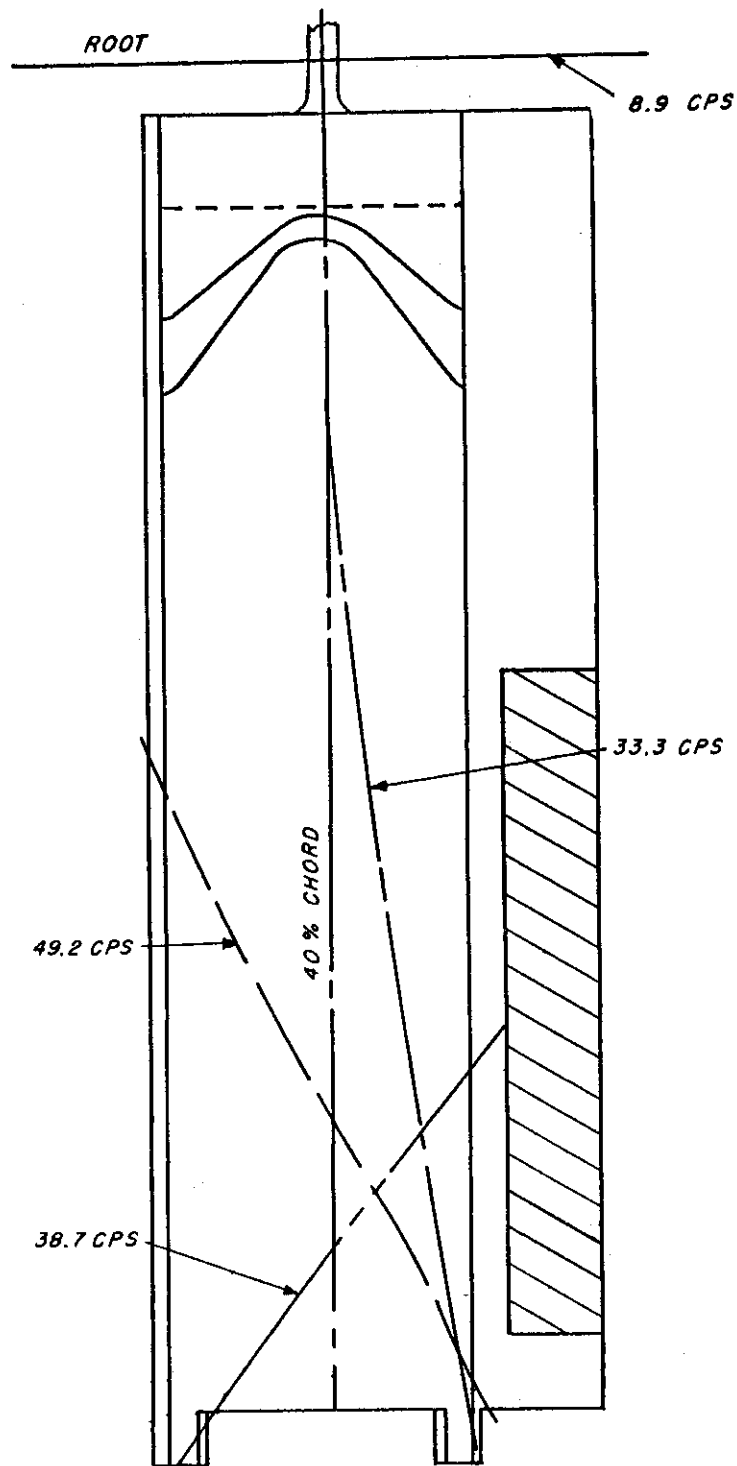


FIGURE 29 EXPERIMENTAL WING-AILERON NODE LINES
 $M = 0.85$ MODEL $\omega_B = 36.0$ CPS $\frac{\omega_B}{\omega_{B1}} = 0.80$

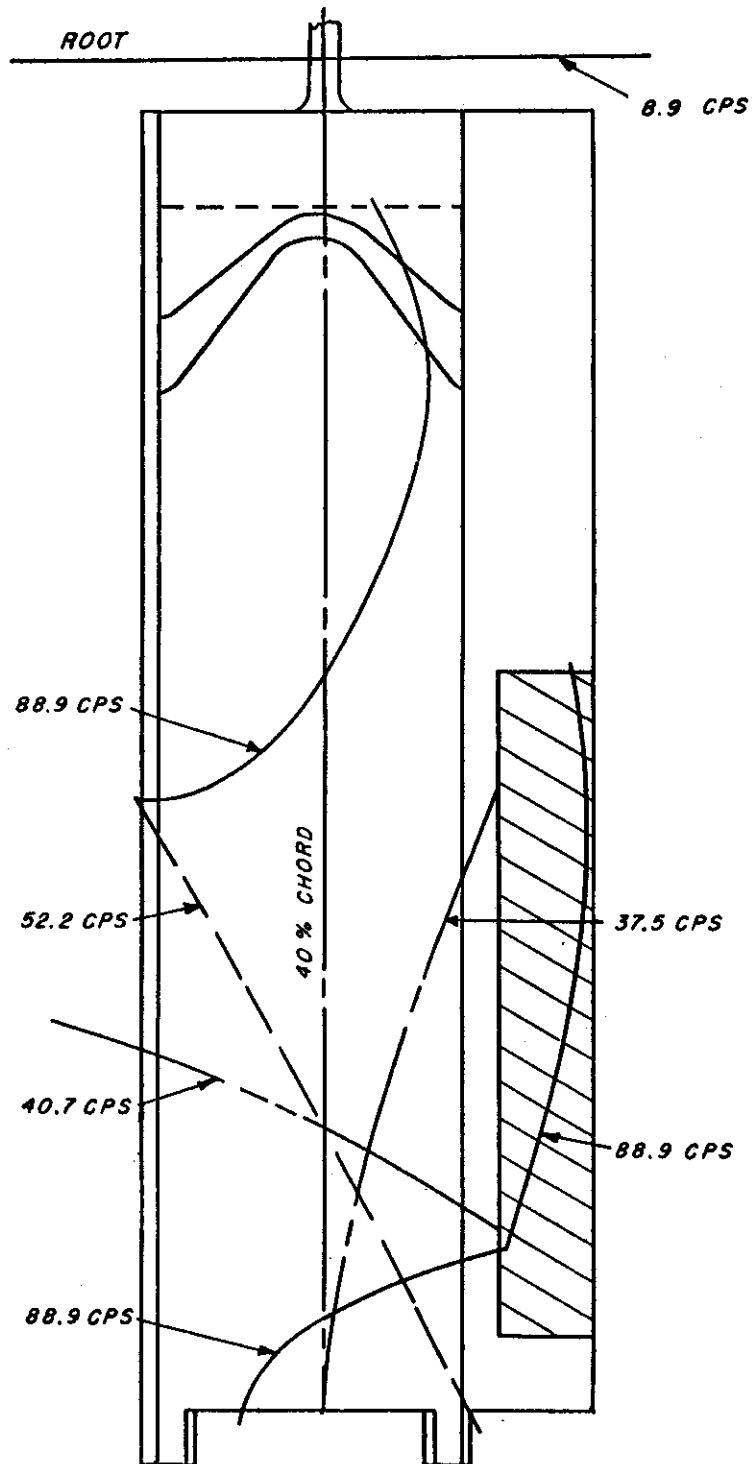


FIGURE 30 EXPERIMENTAL WING-AILERON NODE LINES

$M = 0.85$ MODEL $\omega_B = 44.6$ CPS $\frac{\omega_B}{\omega_{\alpha_1}} = 0.99$

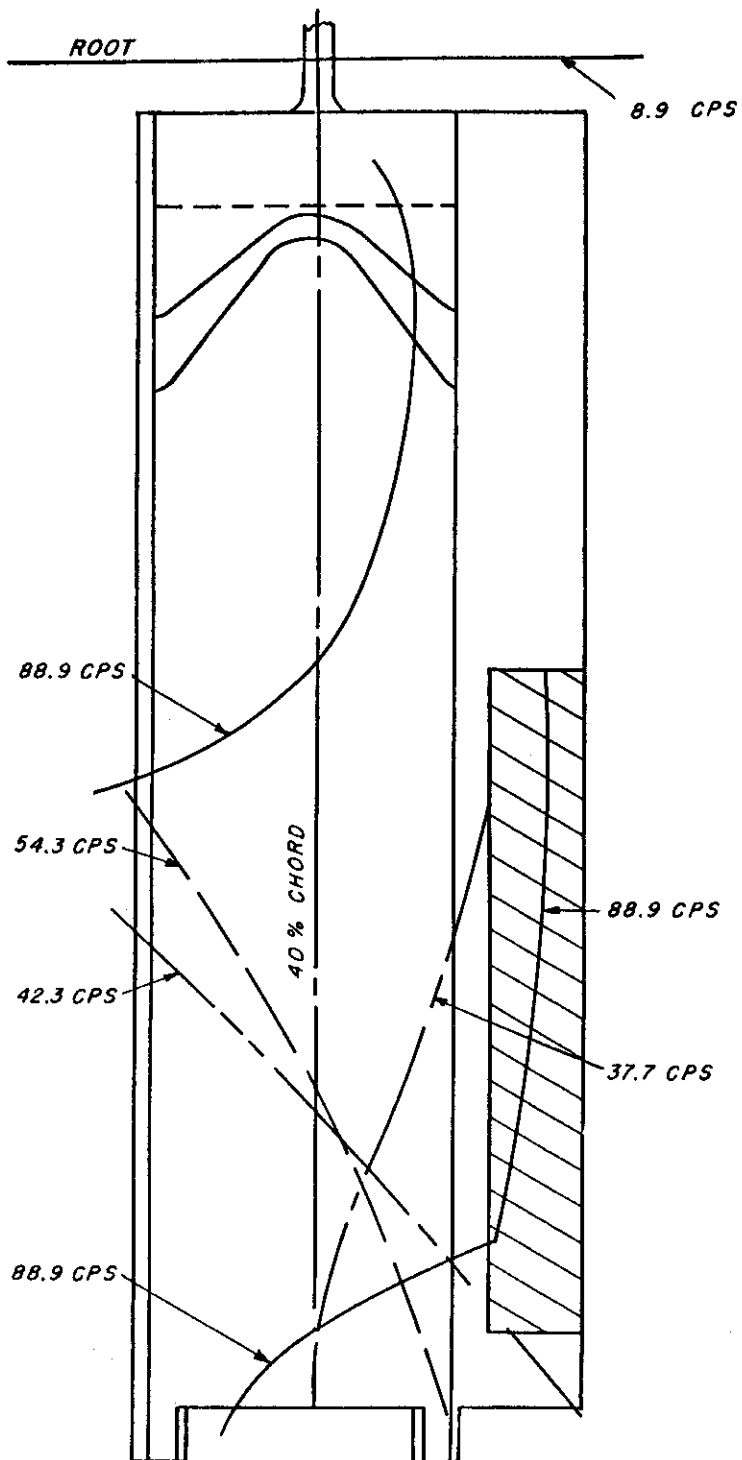


FIGURE 31 EXPERIMENTAL WING-AILERON NODE LINES

$M = 0.85$ MODEL $\omega_B = 49.7$ CPS

$\frac{\omega_B}{\omega_{\text{ref}}} = 1.10$

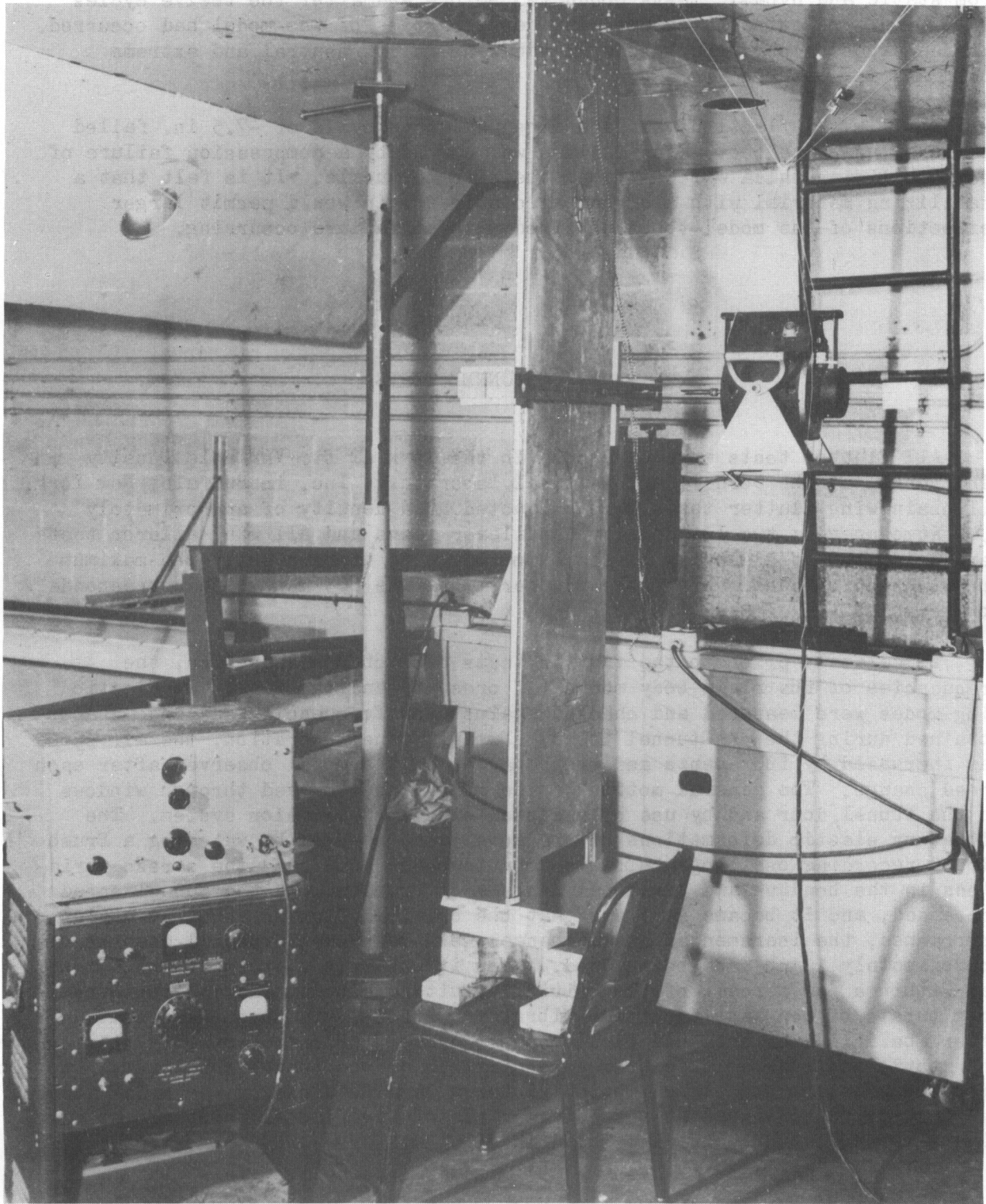


FIGURE 32 TEST SETUP FOR CONDUCTING DYNAMIC FATIGUE TEST ON MODEL SPECIME

[REDACTED]

from static and dynamic tests conducted before and after the twelve cycles of ± 5.0 in. indicated no changes in the properties of the model had occurred. A three-exposure photograph showing the wing in its neutral and extreme positions is given in Fig. 33.

The limit deflection was determined when one cycle of ± 7.5 in. failed the model near the root. The failure was caused by a compression failure of the stabilizing balsa which allowed the skin to buckle. It is felt that a stabilizing material with a higher allowable strain would permit larger deflections of the model to be obtained without failure occurring.

III. TUNNEL TESTS

All flutter tests were conducted in the $8\frac{1}{2}$ x 12 ft. Variable Density Wind Tunnel at the Cornell Aeronautical Laboratory, Inc. in Buffalo, New York. All plain wing flutter tests were conducted at a density of approximately 0.47 atmospheres; two low density cantilever tests and all wing-aileron tests were conducted at a density of approximately 0.36 atmospheres. The maximum tunnel speed obtained during the flutter tests was 695 mph which corresponds to a Mach number of 0.92.

Immediately prior to the flutter tests of each configuration, the frequencies of the rigid body modes (if present) and the first two elastic wing modes were measured and checked against the frequencies and mode shapes obtained during the pre-tunnel tests. During tunnel operation, the air speed was increased by increments and the behavior of the model observed after each speed change. The general motion of the model was observed through windows in the tunnel door and by use of a closed circuit television system. The vibratory elastic deformations of the model were checked by watching a Brush direct recording oscillograph, which continuously monitored the stress variations in the bending and torsional degrees of freedom. As the tunnel speed increased, and it became apparent that the critical flutter speed was being approached, the incremental speed changes were made smaller until changes of approximately 2 mph were being used. When it was felt that the tunnel speed was within a few percent of the critical flutter velocity (as indicated by long bursts of constant amplitude vibratory motion), the tunnel was shut down after the following data had first been recorded; air speed, density, temperature, and static and dynamic pressures. In addition to the tunnel conditions, oscillograph records and high-speed motion pictures were obtained of the model motion. Typical records obtained at a cantilever plain wing flutter point and at a wing-aileron flutter point are shown in Fig. 34.

[REDACTED]

TYPICAL CANTILEVER FLUTTER RECORD

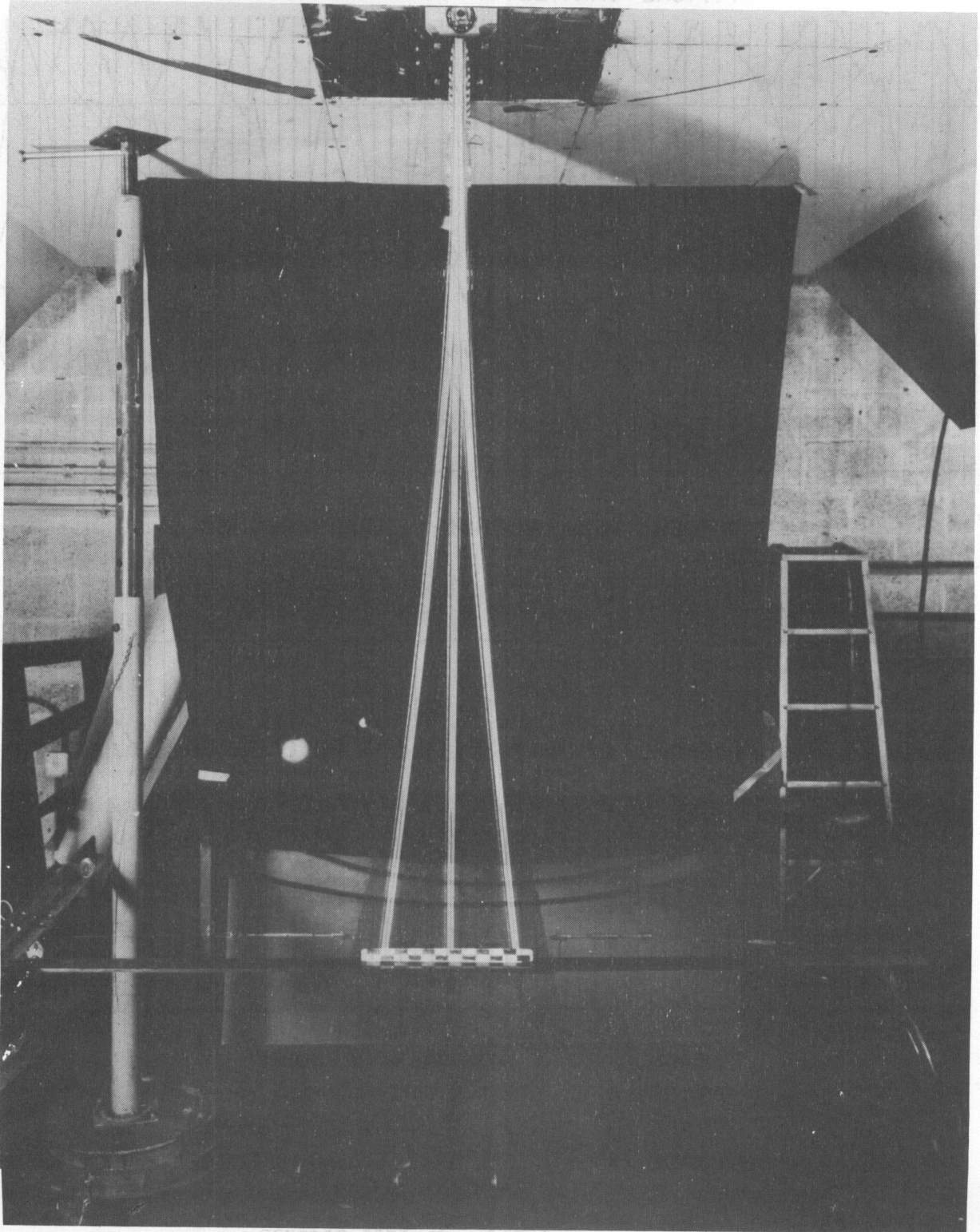
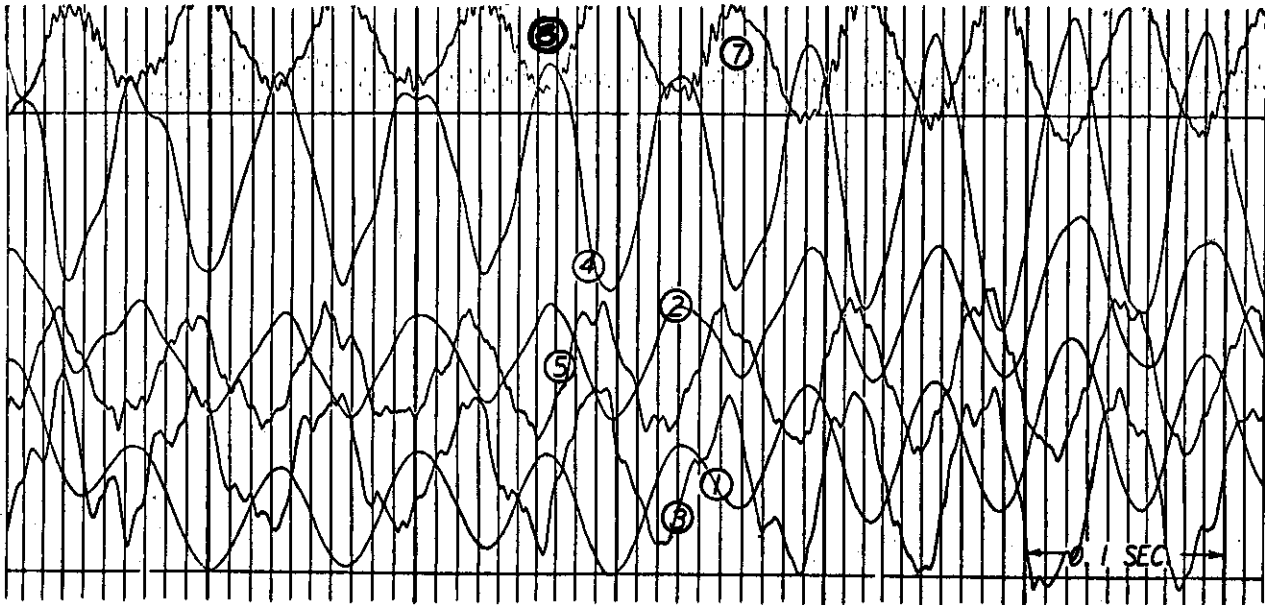


FIGURE 33 TYPICAL FLUTTER RECORDS

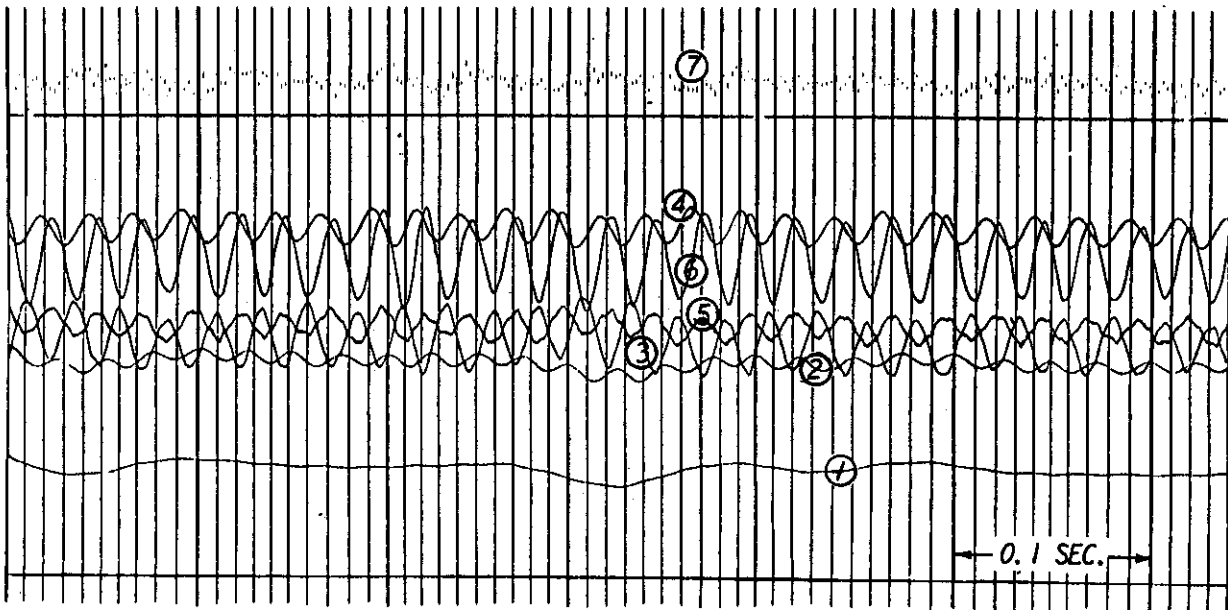
FIGURE 33 THREE-EXPOSURE PICTURE SHOWING MODEL SPECIMEN DEFLECTED 5.0 INCHES

[REDACTED]

TYPICAL CANTILEVER FLUTTER RECORD



TYPICAL WING-AILERON FLUTTER RECORD



TRACES 1 TO 3 WING BENDING GAGES
TRACES 4 & 5 WING TORSION GAGES
TRACE 6 AILERON ROTATION GAGE
TRACE 7 CALIBRATED TIMING TRACE

FIGURE 34 TYPICAL FLUTTER RECORDS

TABLE III

SUMMARY OF EXPERIMENTAL FLUTTER RESULTS
FOR PLAIN WINGS

Wing (Identified by Design Mach No.)	Root Condition	Flutter Speed (mph)	Flutter Mach. No.	Flutter Freq. (CPS)	$\frac{\omega}{\omega_A}$	$\frac{V}{b\omega}$	$\frac{V^{***}}{b\omega_A}$	$\frac{V}{b\omega\sqrt{\mu}}$	Density ρ (slugs/ ft. ³)
0.65	Cantilever	493*	0.653	22	0.665	5.25	3.47	0.721	.001127
		532***	0.691	17	0.514	7.25	3.81	0.794	.001133
		592*	0.785	22	0.536	6.78	3.37	0.720	.001138
0.75	Cantilever	639**	0.831	15	0.366	9.71	3.84	0.773	.001122
		652*	0.852	27	0.600	5.64	3.38	0.716	.001120
0.65	Cantilever	566	0.751	19	0.574	6.95	3.95	0.714	.000850
0.75	Cantilever	695	0.920	25	0.610	6.51	3.95	0.721	.000830
0.85	Cantilever	---	---	---	---	---	---	---	---
0.65	Symmetric	523	0.683	22	0.663	5.55	3.68	0.763	.001120
		584	0.767	26	0.634	5.25	3.33	0.710	.001130
		663	0.863	28	0.622	5.52	3.44	0.723	.001100
0.65	Antisymmetric	502	0.665	16	0.483	7.32	3.56	0.746	.001139
0.75	Antisymmetric	613	0.811	19	0.463	7.51	3.49	0.744	.001131
0.85	Antisymmetric	654	0.866	21	0.467	7.26	3.39	0.717	.001114

* Mild flutter

** Violent flutter

*** Based on calculated uncoupled torsion frequency

TABLE IV

SUMMARY OF EXPERIMENTAL FLUTTER RESULTS FOR WING-AILERON MODELS (WING ROOT CANTILEVERED)

Model	Aileron Frequency ω_{β} (CPS)	Frequency Ratio $\omega_{\beta}/\omega_{\alpha_1}$	Flutter Frequency (CPS)	Flutter Speed (ft./sec.)	Flutter Mach No.	ρ ($\frac{\text{slugs}}{\text{ft}^3}$)
0.65	15.0	0.45	39.6	272	.240	.000866
0.65	25.9	0.78	40.4	232	.206	.000963
0.65	25.9	0.78	40.4	247	.218	.000862
0.65	33.1	1.00	41.4	283	.252	.000890
0.65	39.9	1.21	42.0	438	.390	.000867
0.65	42.0	1.27	68.0	499	.447	.000877
0.65	47.9	1.45	69.2	479	.422	.000843
0.65	54.4	1.65	69.6	464	.410	.000865
0.65	61.6	1.86	70.4	491	.434	.000873
0.75	22.8	0.56	46.3	301	.267	.000860
0.75	33.1	0.81	47.4	295	.261	.000860
0.75	39.9	0.97	48.0	393	.351	.000870
0.75	44.6	1.09	48.4	514	.460	.000875
0.75	49.7	1.21	79.0	517	.465	.000888
0.75	54.4	1.33	79.2	507	.455	.000894
0.85	22.8	0.51	48.9	332	.296	.000879
0.85	36.0	0.80	50.0	339	.302	.000874
0.85	44.6	0.99	51.3	489	.439	.000877
0.85	49.7	1.10	75.0	605	.542	.000869

[REDACTED]

Table III summarizes the experimental flutter data accumulated during the tests of the plain straight wings and Table IV summarizes the experimental flutter data accumulated during the tests of the wing-aileron models. Fig. 35 presents plots of $v/b\omega_{\alpha 1}$ vs. $\omega_{\beta}/\omega_{\alpha 1}$ for the three wing-aileron models tested.

IV. VIBRATION ANALYSES

Vibration analyses were performed for all the plain wing configurations tested. For the wing-aileron models, vibration analyses were conducted for only two of the configurations tested. The method described in Ref. 2 was used to calculate the first three uncoupled bending mode shapes and frequencies and a Holzer analysis was used to calculate the first two torsional mode shapes and frequencies. The coupled mode shapes and frequencies were then calculated by standard means using the uncoupled modes as generalized coordinates. Elastic coupling between the modes due to flexibility in the suspension system had to be considered as it was discovered that the suspension system had insufficient rigidity to permit ignoring its effects on the higher frequency modes of the wing.

The elastic-mass coupling between the wing and suspension was sufficient to alter the coupled mode shapes from one wing to another due to the different ratios of wing rigidity to suspension rigidity. While the differences are small, they are still noticeable when comparing the node lines for the $M = 0.65$ and $M = 0.85$ models. The node lines of the various calculated coupled modes for the different plain wing configurations are compared with the measured node lines in Figs. 5 through 13, pp. 13 through 21.

The wing-aileron node lines and frequencies were calculated by the same methods as used for the plain wing models except that more uncoupled modes were considered when determining the coupled mode characteristics. The calculated wing-aileron node lines for the two values of ω_{β} considered are compared with the measured data in Figs. 16 and 19. A tabular listing of the calculated uncoupled and coupled mode frequencies for the plain wings and wing-aileron models is given in Table V.

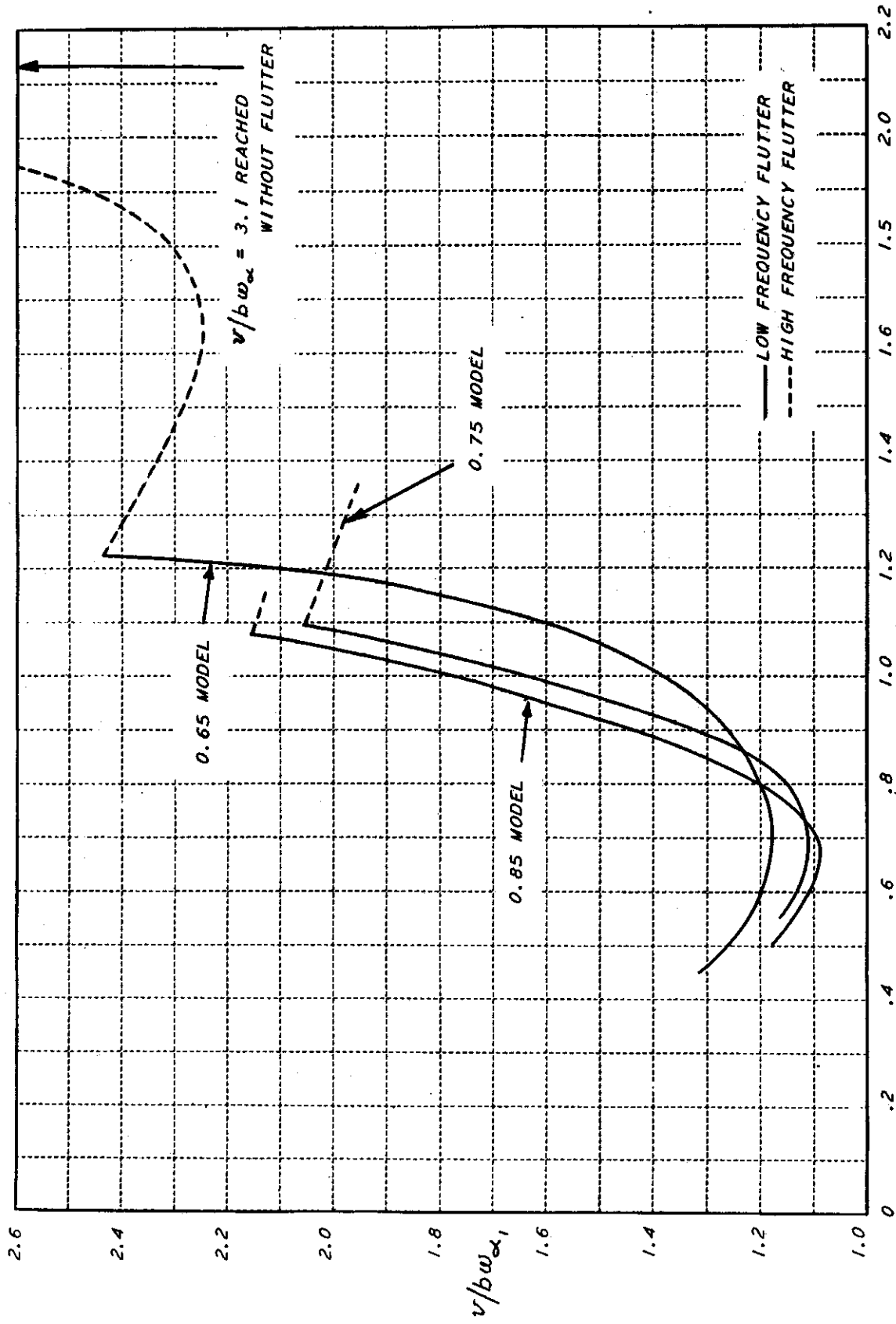


FIGURE 35 $v/b\omega_{\alpha_1}$ VS. $\omega_{\beta}/\omega_{\alpha_1}$
WING-AILERON FLUTTER TEST RESULTS

TABLE V

SUMMARY OF CALCULATED UNCOUPLED AND COUPLED
MODE FREQUENCIES

PLAIN MODELS

Model	Root Condition	Uncoupled Mode Frequency (CPS)			Coupled Mode Frequency (CPS)		
		First Bending	First Torsion	Second Bending	First Mode	Second Mode	Third Mode
0.65	Cantilever	7.3	33.1	35.0	7.3	30.7	40.8
0.75	Cantilever	8.5	41.0	40.0	8.5	36.5	48.2
0.85	Cantilever	9.1	45.0	43.0	9.1	38.9	50.8
0.65	Symmetric	7.5	33.2	36.0	7.5	31.2	41.3
0.75	Symmetric	8.9	41.0	40.0	8.9	37.4	48.1
0.85	Symmetric	9.5	45.0	43.0	9.5	39.4	52.1
0.65	Antisymmetric	16.9	32.9	40.0	16.7	34.2	41.4
0.75	Antisymmetric	20.0	41.0	50.0	19.6	41.1	47.7
0.85	Antisymmetric	21.3	45.0	51.0	21.1	43.5	49.1

WING-AILERON MODELS

Model	Root Condition	Uncoupled Mode Frequency (CPS)				Coupled Mode Frequency (CPS)				
		First Bending	First Torsion	Second Bending	Second Torsion	First Mode	Second Mode	Third Mode	Fourth Mode	Fifth Mode
0.65 $\omega_p/\omega_{\alpha_1} = 1.0$	Cantilever	7.2	32.5	34.0	70.0	7.2	29.5	32.5	43.0	-----
0.65 $\omega_p/\omega_{\alpha_1} = 1.445$	Cantilever	7.2	32.5	34.0	70.0	7.2	30.0	37.9	52.1	68.6



V. FLUTTER ANALYSES

A. Configurations Without Ailerons

Flutter analyses were conducted for all cantilever, symmetric, and anti-symmetric configurations tested. The analyses were three-dimensional, using strip theory, with aerodynamic coefficients based on incompressible air, obtained from Ref. 3. Each analysis was conducted at the density present in the tunnel at the time flutter was obtained, and the structural damping coefficient used in each degree of freedom corresponded to the measured value obtained during the zero air speed vibration tests. A tabular summary of all calculated flutter results is presented in Table VI.

(1) Cantilever Flutter Analyses

The cantilever flutter analyses were two degrees of freedom analyses using the first uncoupled cantilever bending and the first uncoupled cantilever torsion modes as the generalized coordinates. The results of these theoretical analyses are shown in Figs. 36 to 41.

To check the effect of the second bending mode on the flutter speed, a three-degree analysis was conducted using first uncoupled cantilever bending, first uncoupled cantilever torsion, and second uncoupled cantilever bending modes as the generalized coordinates. The results of this analysis, presented in comparison with the two-degree analysis, are shown in Fig. 48.

In order to obtain an indication of the effects of compressible air, a two-degree analysis was conducted using the compressible unsteady aerodynamic coefficients listed for $M = 0.70$ in Ref. 4. The results of this analysis, shown in comparison with the same two degrees of freedom used in an analysis with incompressible aerodynamic coefficients, are presented in Fig. 49.

To determine the correlative agreement between experimental results and flutter analyses including the effects of finite span, two different methods of including finite span effects were used. The first method used the procedure of Ref. 6. This involves the determination of the static three-dimensional circulations on the wing corresponding to the various vibration mode shapes. On the basis of the ratio of the three-dimensional to the two-dimensional static circulations on each wing strip, an equivalent aspect ratio was computed and then reference was made to Ref. 7, from which aerodynamic coefficients were chosen based on this calculated equivalent aspect ratio. The second method used the static circulation ratios in lieu of the dynamic circulation ratio in Eq. 6 of Ref. 8. This second method was found to give quite satisfactory results when applied to the flutter models discussed in Ref. 5. The results of both of these analyses are shown in Fig. 51, where they are compared with the results obtained from a two-degree of freedom analysis without finite span effects included, and also with the experimental result. The determinant elements used in the cantilever flutter determinant are presented in Appendix II.

TABLE VI
 SUMMARY OF CALCULATED FLUTTER RESULTS
 FOR PLAIN WING CONFIGURATIONS

Model	Root Condition	Flutter Speed (mph)	Flutter Frequency (CPS)	$\frac{\omega}{\omega_c}$	$\frac{v}{b\omega}$	$\frac{v}{b\omega_c}$	$\frac{v}{b\omega_c \mu}$	Density ρ ($\frac{\text{slugs}}{\text{ft.}^3}$)	Type of Analysis (Method Used)
0.65	Cantilever	472	18.7	0.565	5.90	3.34	0.694	0.001127	Incompressible, Infinite AR (Ref. 3)
0.65	Cantilever	430	15.4	0.465	6.55	3.05	0.634	0.001127	Compressible, Infinite AR (Ref. 3 and 4)
0.65	Cantilever	594	15.4	0.465	9.00	4.20	0.873	0.001127	Incompressible, Finite AR (Ref. 5 and 8)
0.65	Cantilever	556	20.8	0.628	6.25	3.93	0.817	0.001127	Incompressible, Finite AR (Ref. 6 and 7)
0.65	Cantilever	540	18.1	0.547	6.97	3.82	0.691	0.00085	Incompressible, Infinite AR (Ref. 3)
0.75	Cantilever	600	21.9	0.534	6.40	3.42	0.731	0.001138	Incompressible, Infinite AR (Ref. 3)
0.75	Cantilever	676	22.1	0.539	7.14	3.85	0.702	0.00083	Incompressible, Infinite AR (Ref. 3)
0.85	Cantilever	655	24.7	0.549	6.20	3.40	0.720	0.001120	Incompressible, Infinite AR (Ref. 3)
0.85	Cantilever	645	23.4	0.520	6.45	3.35	0.710	0.001120	Includes Effects of Second Bending (Ref. 3)
0.85	Cantilever	740	23.0	0.511	7.50	3.84	0.699	0.00083	Incompressible, Infinite AR (Ref. 3)
0.65	Symmetric	481	18.7	0.563	6.00	3.38	0.701	0.001120	Incompressible, Infinite AR (Ref. 3)
0.75	Symmetric	590	23.3	0.568	5.90	3.36	0.716	0.001130	Incompressible, Infinite AR (Ref. 3)
0.85	Symmetric	665	25.0	0.556	6.20	3.45	0.725	0.001100	Incompressible, Infinite AR (Ref. 3)
0.65	Antisymmetric	467	19.6	0.592	5.55	3.30	0.692	0.001139	Incompressible, Infinite AR (Ref. 3)
0.65	Antisymmetric	438	18.3	0.553	5.60	3.10	0.650	0.001139	Compressible, Finite AR (Ref. 3 and 4)
0.65	Antisymmetric	565	22.0	0.665	6.00	4.00	0.838	0.001139	Incompressible, Finite AR (Ref. 6 and 7)
0.75	Antisymmetric	583	24.3	0.593	5.60	3.32	0.708	0.001131	Incompressible, Infinite AR (Ref. 3)
0.85	Antisymmetric	651	26.7	0.593	5.70	3.38	0.714	0.001114	Incompressible, Infinite AR (Ref. 3)

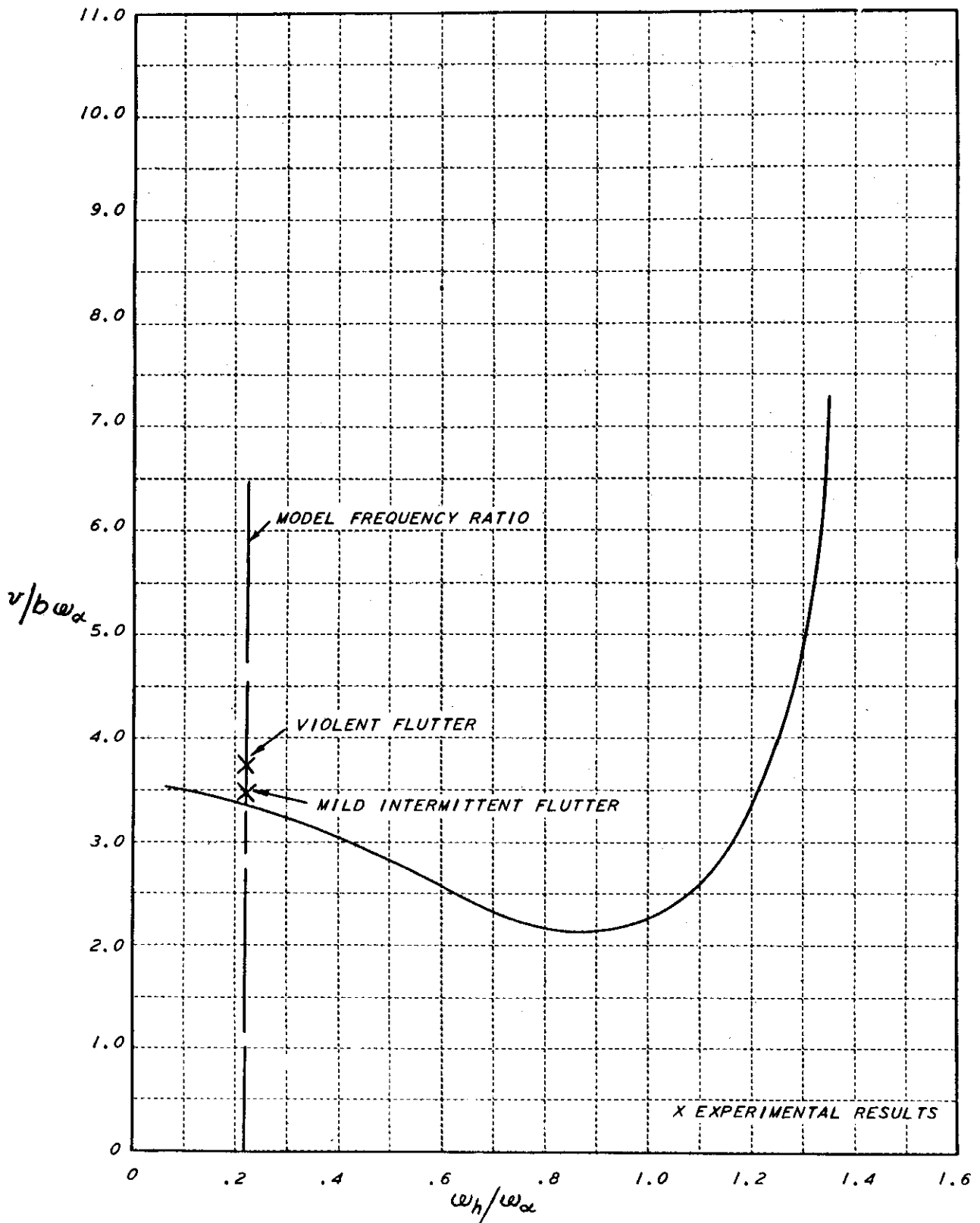


FIGURE 36 $v/b\omega_\alpha$ VS. ω_h/ω_α
 $M = 0.65$ CANTILEVER MODEL - $\rho = 0.001127$ SLUGS/FT³

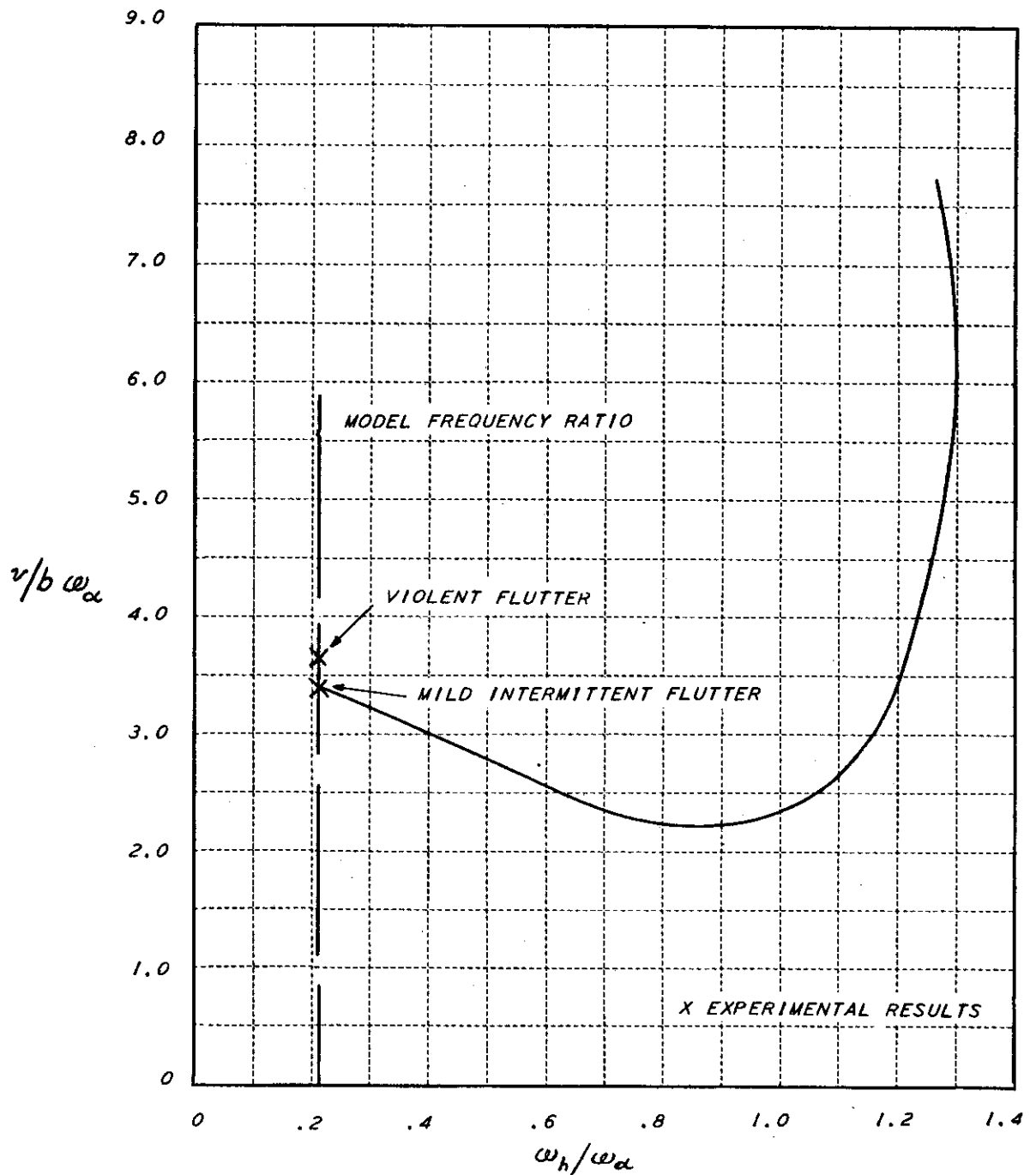


FIGURE 37 $r/b\omega_\alpha$ VS. ω_h/ω_α
 $M = 0.75$ CANTILEVER MODEL - $\rho = 0.001138$ SLUGS/FT³

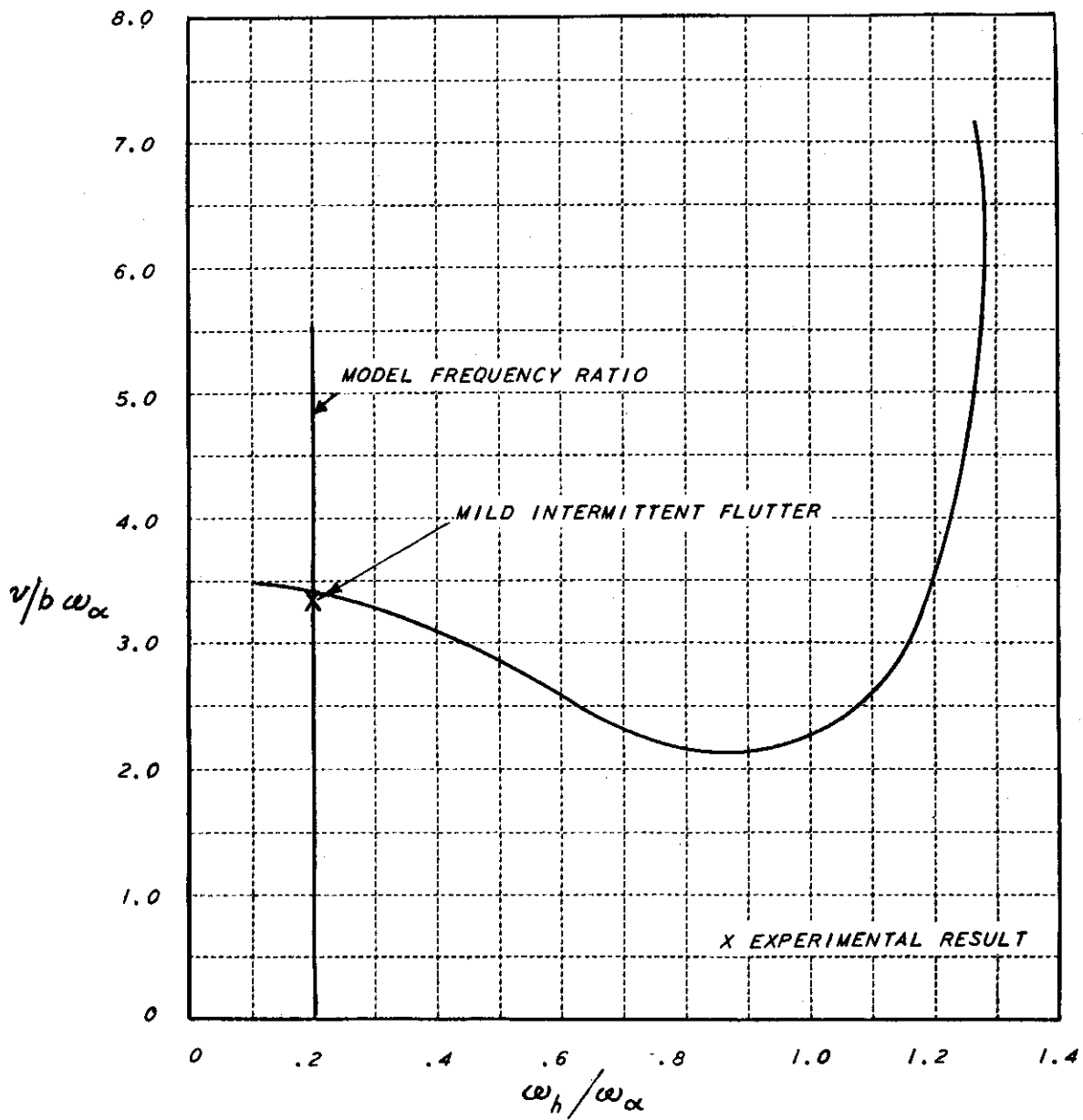


FIGURE 38 $v/b\omega_\alpha$ VS. ω_h/ω_α
 $M = 0.85$ CANTILEVER MODEL - $\rho = 0.001120$ SLUGS/FT³

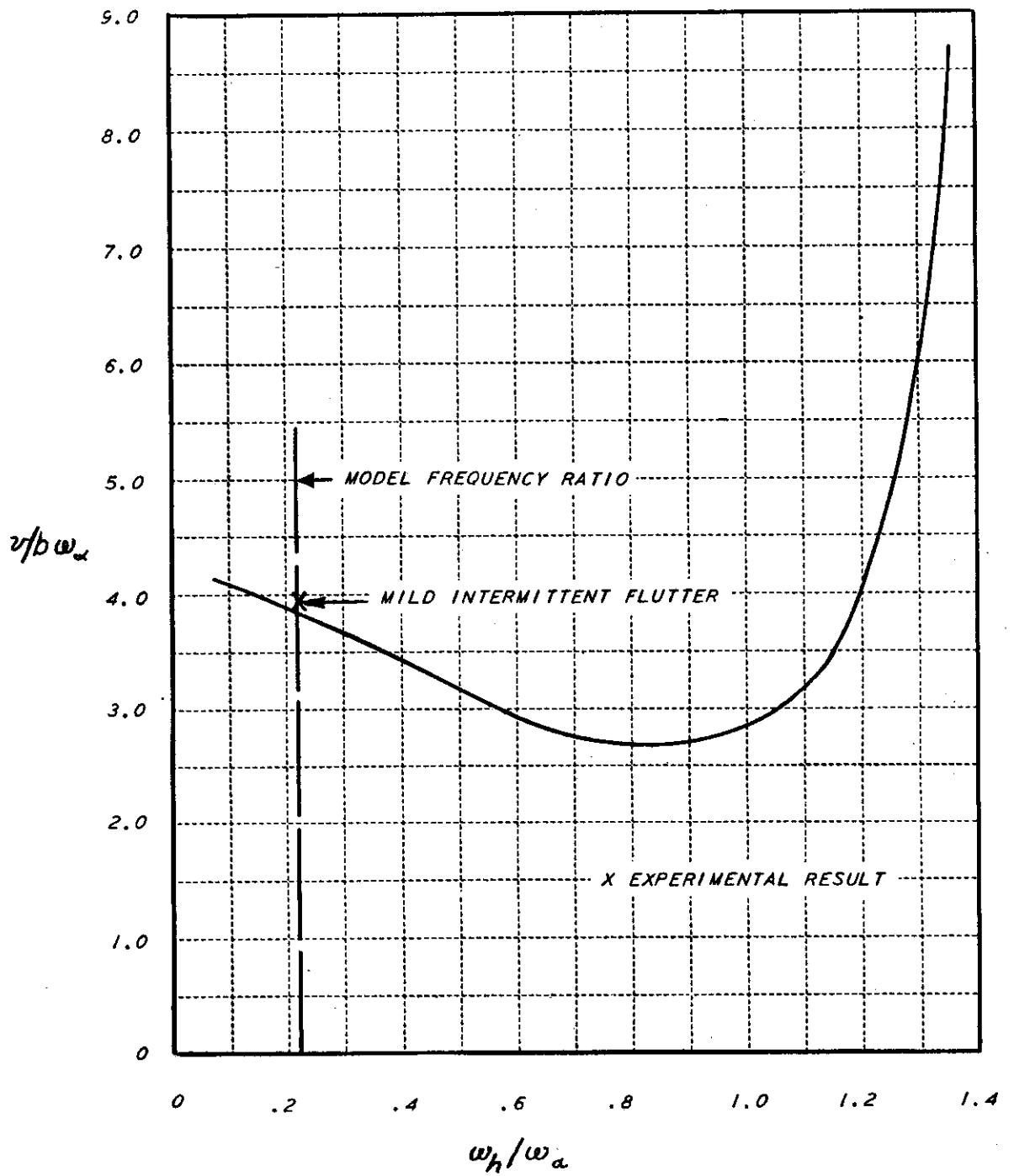


FIGURE 39 $v/b\omega_\alpha$ VS. ω_h/ω_α
 $M = 0.65$ CANTILEVER MODEL - $\rho = 0.000850$ SLUGS/FT³

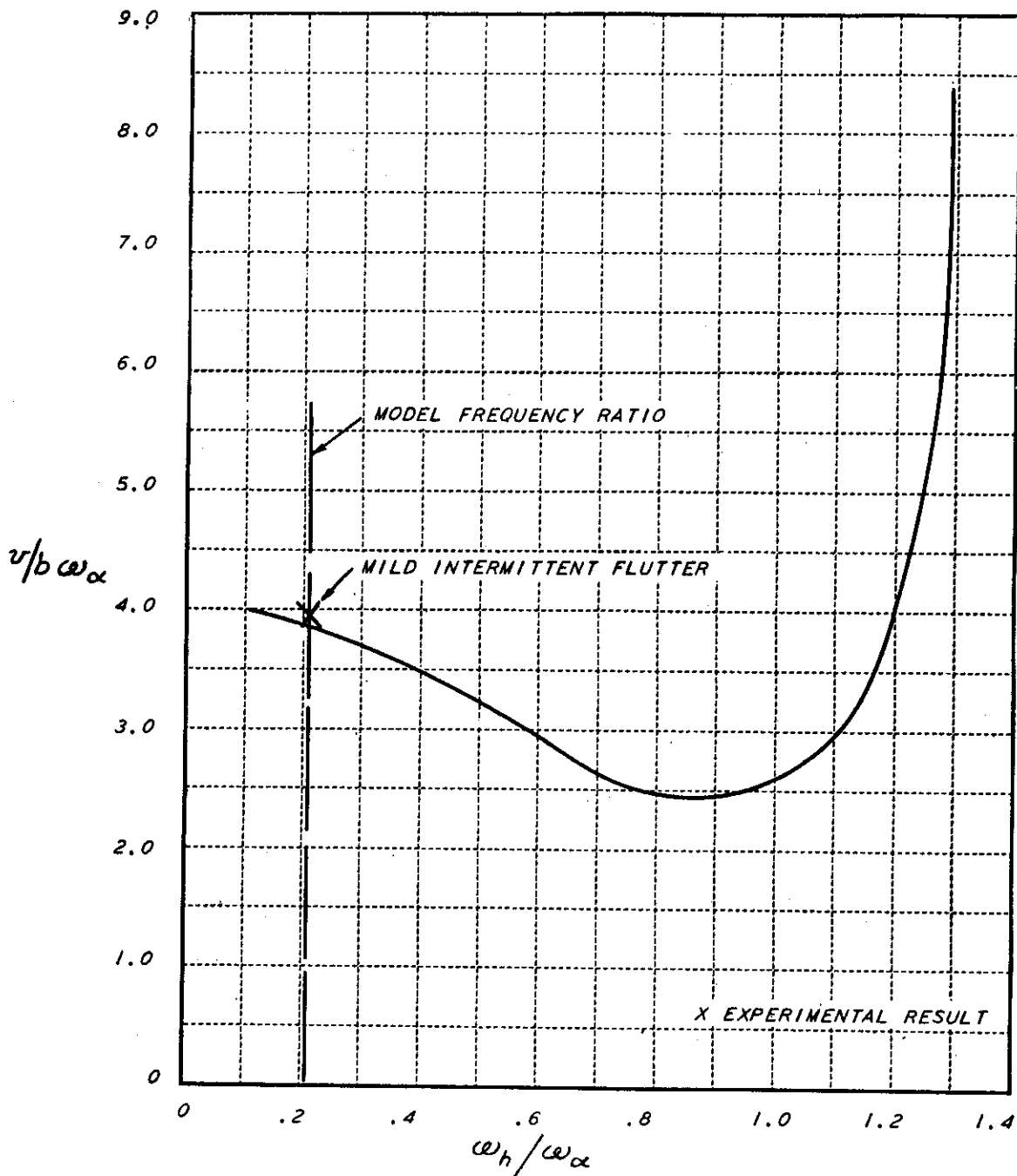


FIGURE 40 $v/b\omega_\alpha$ VS. ω_h/ω_α
 $M = 0.75$ CANTILEVER MODEL - $\rho = 0.000830$ SLUGS/FT³

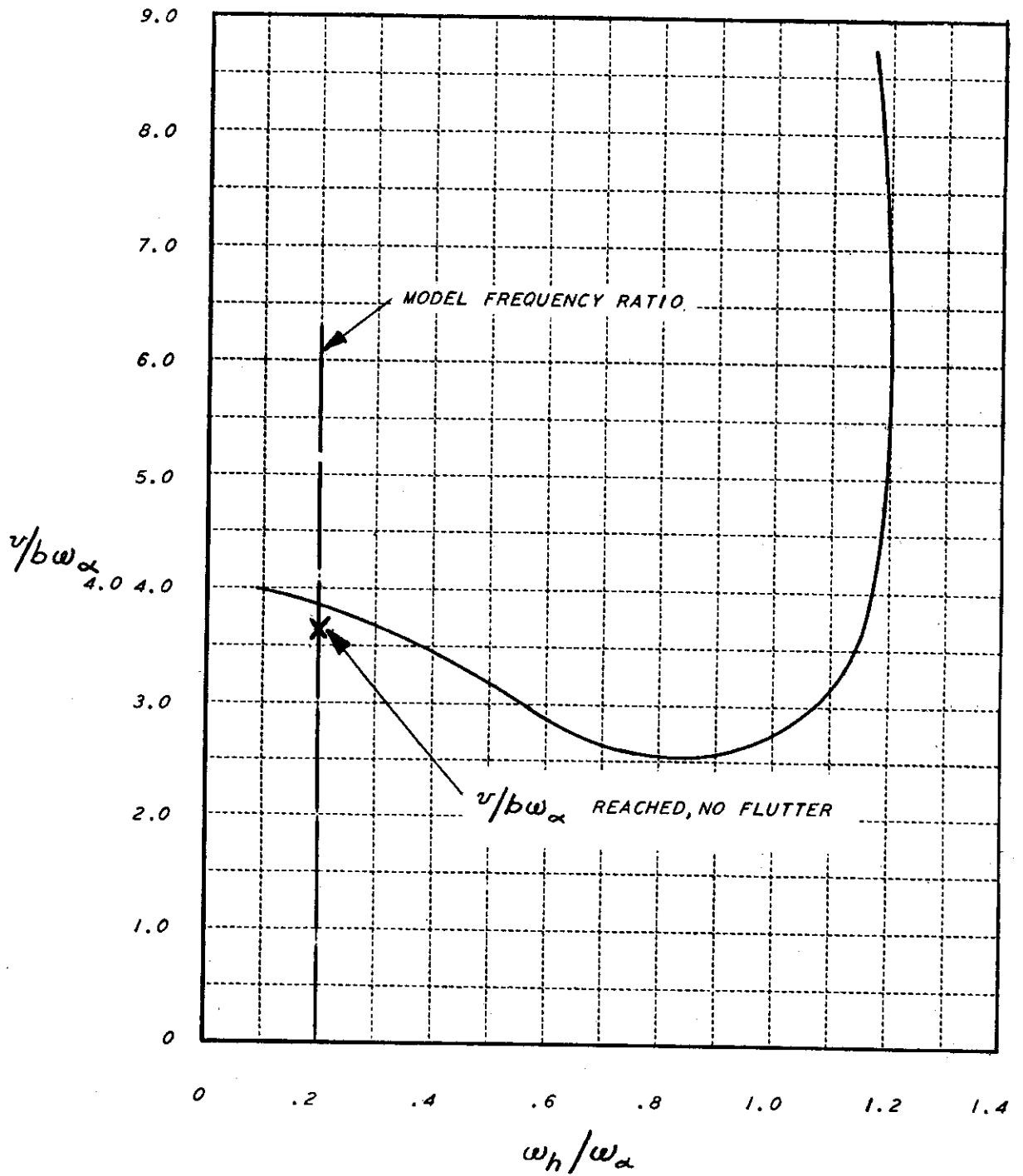


FIGURE 41 $v/b\omega_\alpha$ VS. ω_h/ω_α
 $M = 0.85$ CANTILEVER MODEL - $\rho = 0.000830$ SLUGS/FT³

[REDACTED]

(2) Symmetric Flutter Analyses

All the symmetric analyses conducted were four-degree-of-freedom analyses with pitch, translation, first uncoupled symmetric bending, and first uncoupled symmetric torsion modes as the generalized coordinates. The results of these calculations are given in Figs. 42 to 44. The effects of compressibility, finite span, or higher modes were not included in any of the symmetric flutter analyses. The determinant elements present in the symmetric flutter determinant are listed in Appendix II.

(3) Antisymmetric Flutter Analyses

All the antisymmetric flutter analyses were three-degree-of-freedom analyses with roll, first uncoupled antisymmetric bending and first uncoupled antisymmetric torsion modes as the generalized coordinates. The results of these calculations are shown in Figs. 45 to 47. The effects of compressible air and finite span were included in the analyses in the same manner as in the cantilever calculations and the results are shown in comparison with the calculated results without these effects in Figs. 50 and 52 respectively. The determinant elements of the antisymmetric flutter determinant are listed in Appendix II.

B. Configurations with Ailerons

Flutter analyses for one wing-aileron combination were conducted for all frequency ratios ($\omega_p/\omega_{\alpha 1}$) tested. The analyses were three-dimensional, by means of strip theory, and the aerodynamic coefficients listed in Ref. 3 were used. In an attempt to obtain better correlation between theoretical and experimental results, the values of T_{β} , the oscillatory aileron hinge moment coefficient, as experimentally determined in Ref. 9, were used in lieu of the two-dimensional values listed in Ref. 3.

In the experimental phase of the program, two distinct wing-aileron flutter modes were observed depending upon the frequency ratio $\omega_p/\omega_{\alpha 1}$. One was a flutter mode whose frequency closely corresponded to the fourth wing-aileron coupled mode and the other, a flutter mode whose frequency closely corresponded to the fifth wing-aileron coupled mode. Therefore, for the correlative calculations for each of these flutter modes, the uncoupled wing and aileron modes which were of importance in obtaining the coupled mode which corresponded to the flutter mode were used as generalized coordinates in the corresponding flutter analyses. A short description of each set of analyses is given below.

(1) Low Frequency Wing-Aileron Flutter Mode

These analyses were four-degree analyses with the following degrees of freedom used as generalized coordinates:

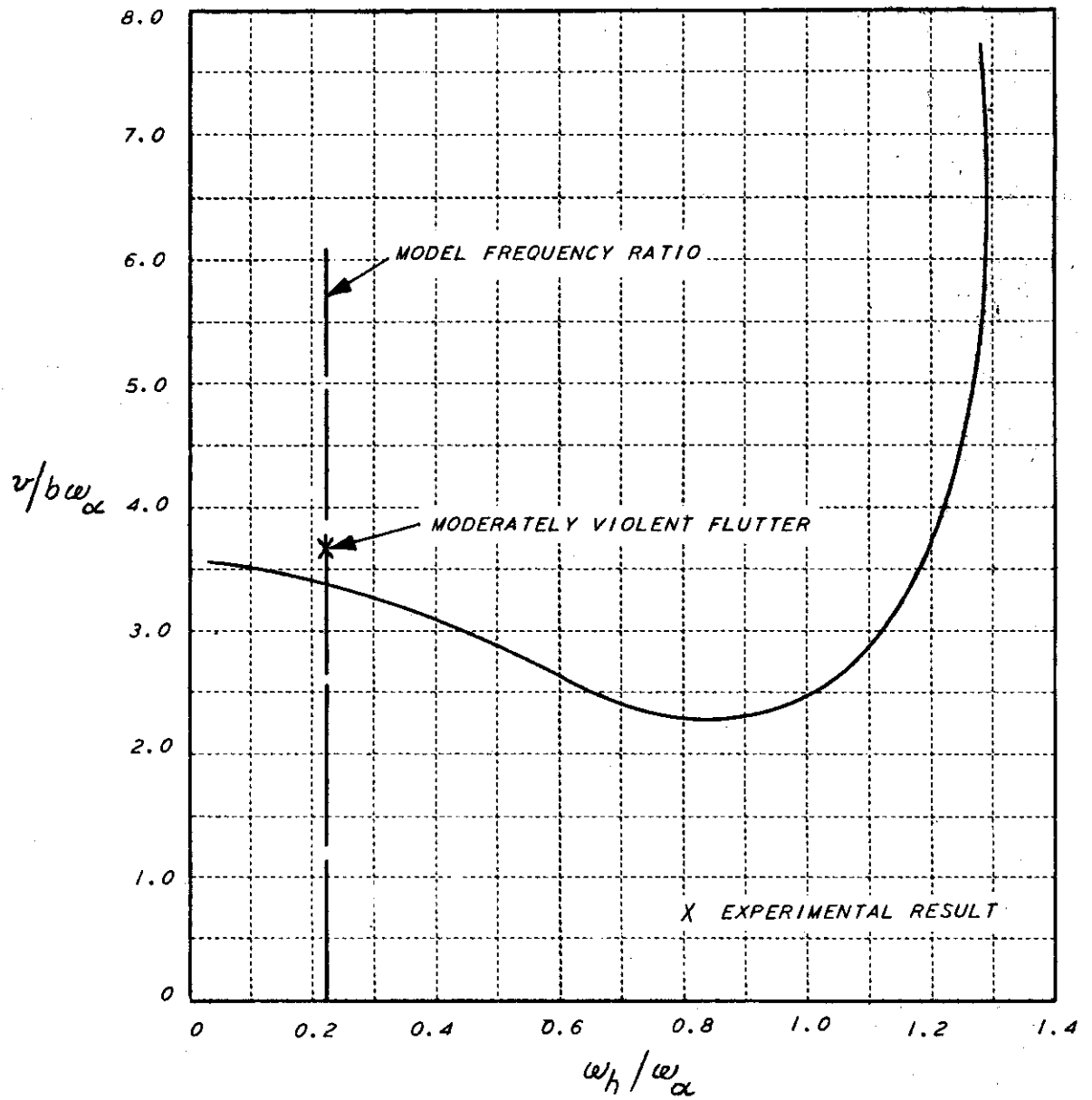


FIGURE 42 $v/b\omega_\alpha$ VS. ω_h/ω_α
 M = 0.65 SYMMETRIC MODEL - $\rho = 0.001120$ SLUGS/FT³

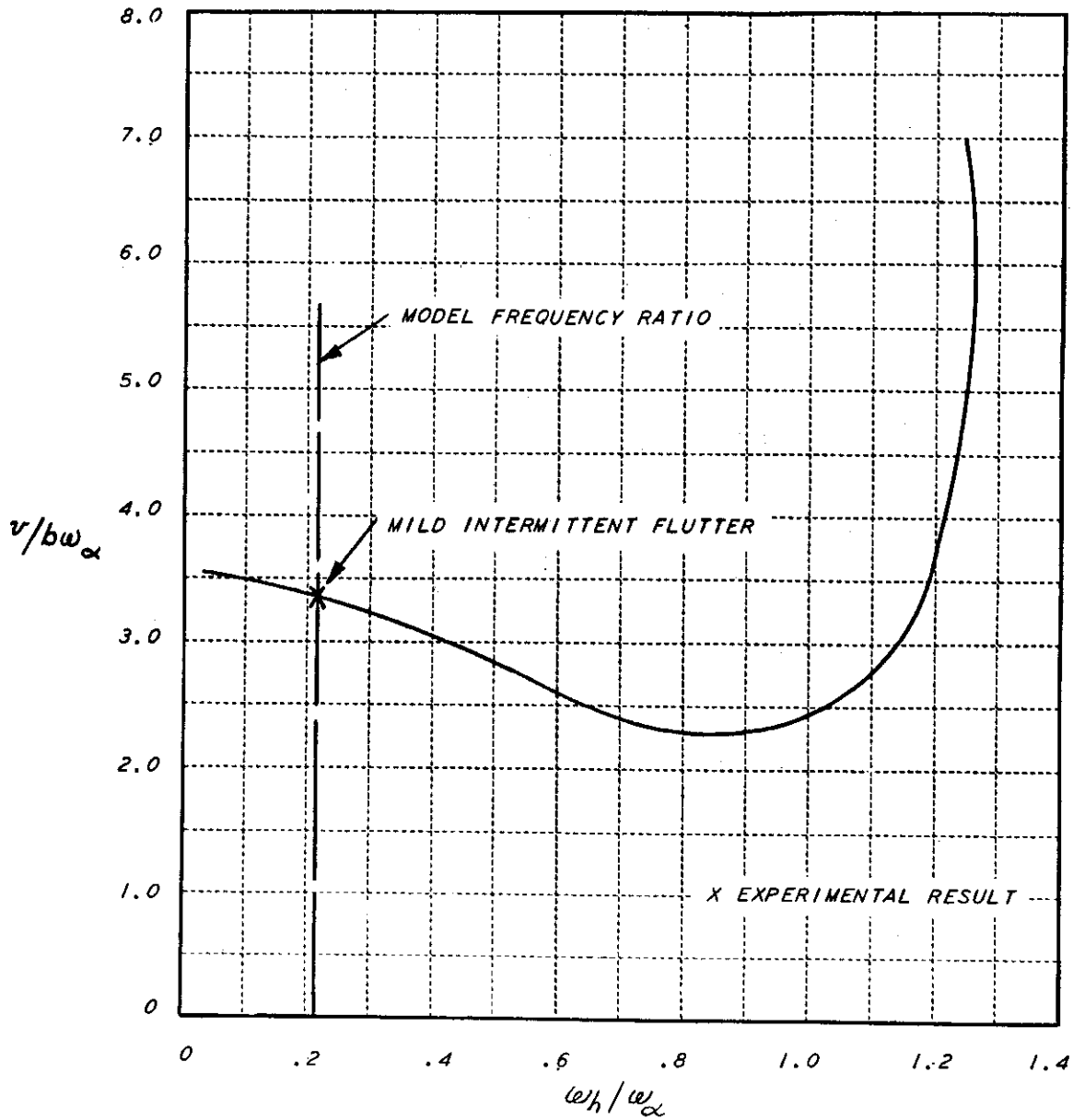


FIGURE 43 $v/b\omega_\alpha$ VS. ω_h/ω_α
 $M = 0.75$ SYMMETRIC MODEL - $\rho = 0.001130$ SLUGS/FT³

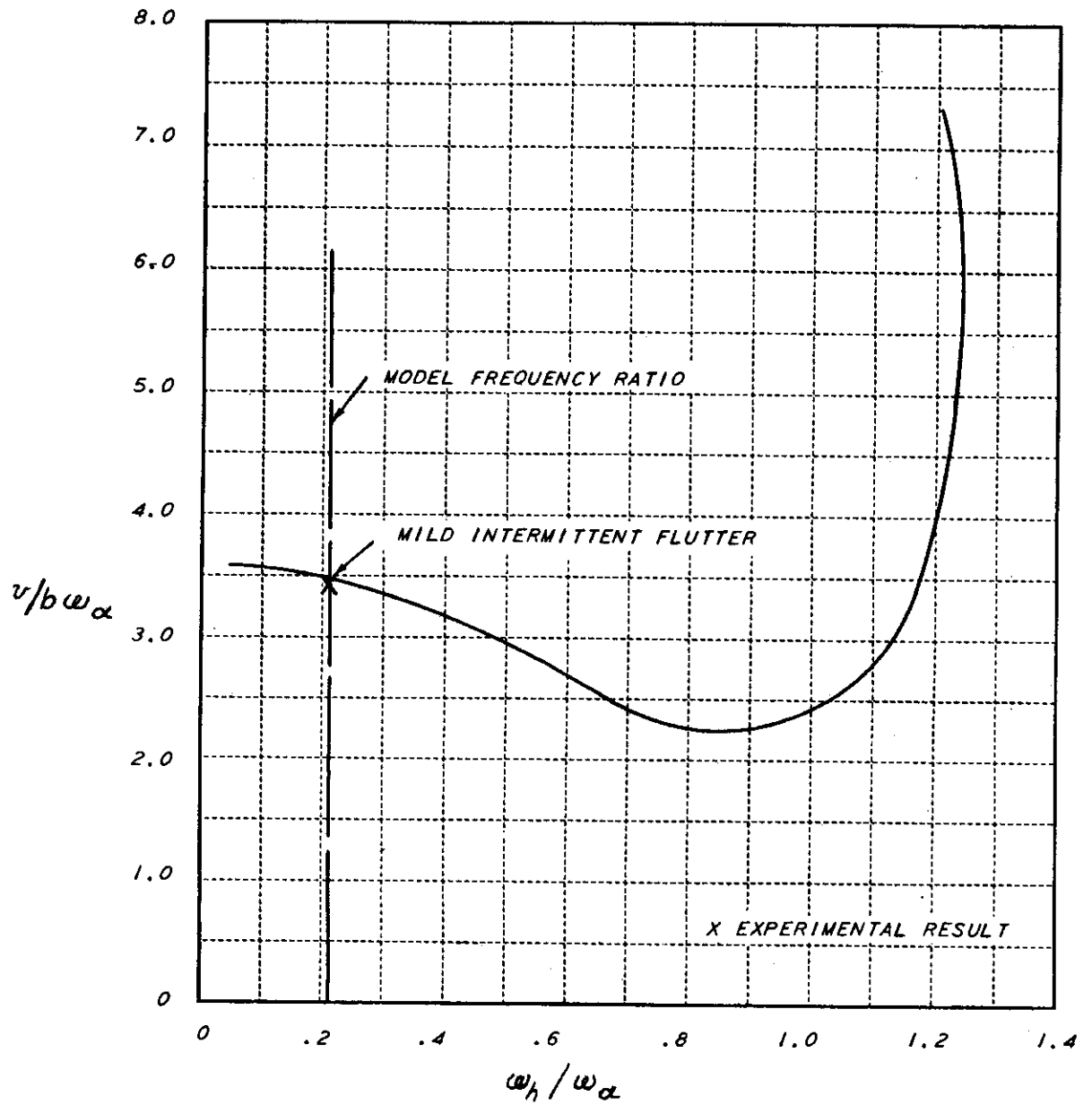


FIGURE 44 $v/b\omega_\alpha$ VS. ω_h/ω_α
 $M = 0.85$ SYMMETRIC MODEL - $\rho = 0.001100$ SLUGS/FT³

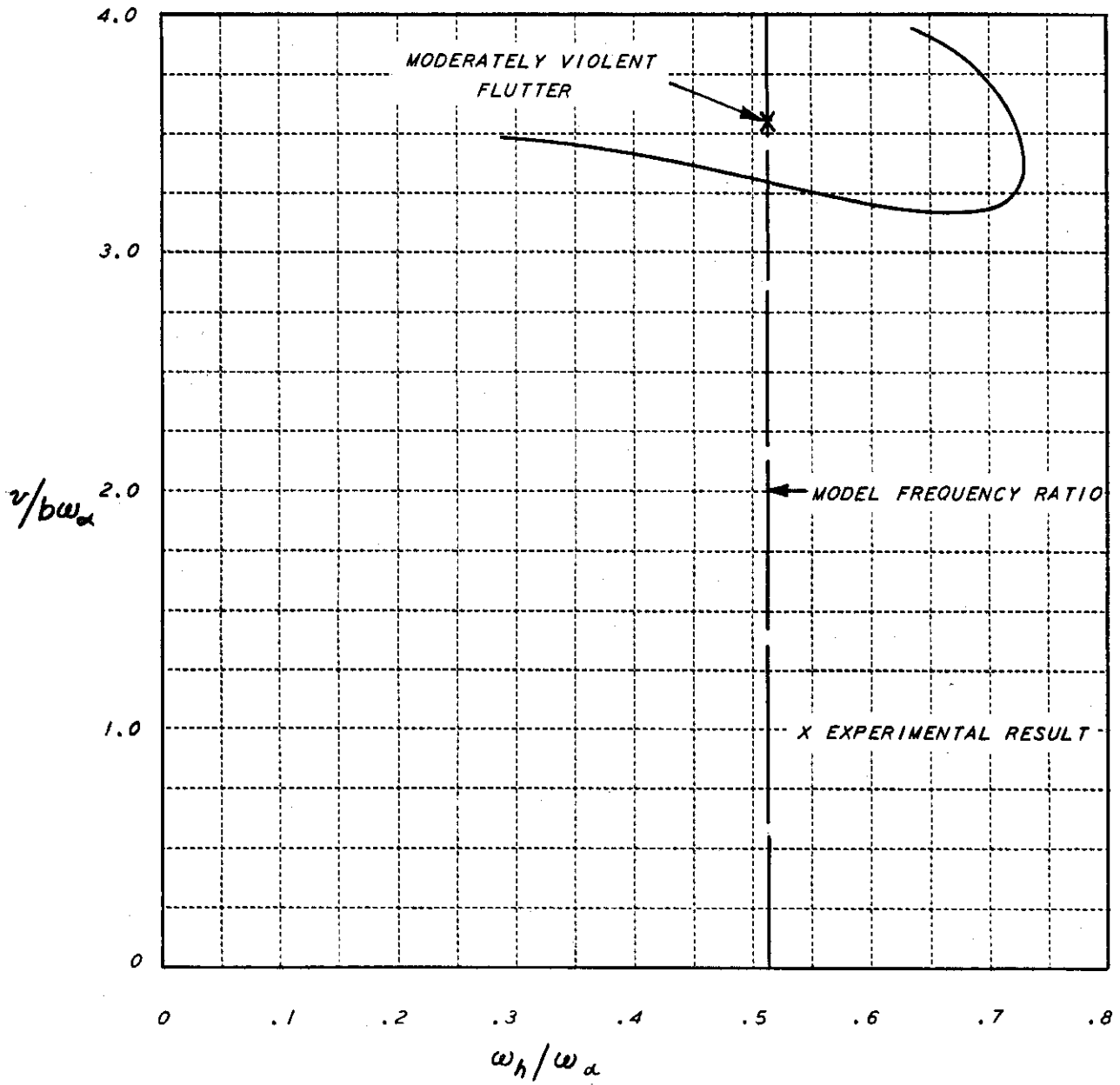


FIGURE 45 $v/b\omega_\alpha$ VS. ω_h/ω_α
 $M = 0.65$ ANTISYMMETRIC MODEL - $\rho = 0.001139$ SLUGS/FT³

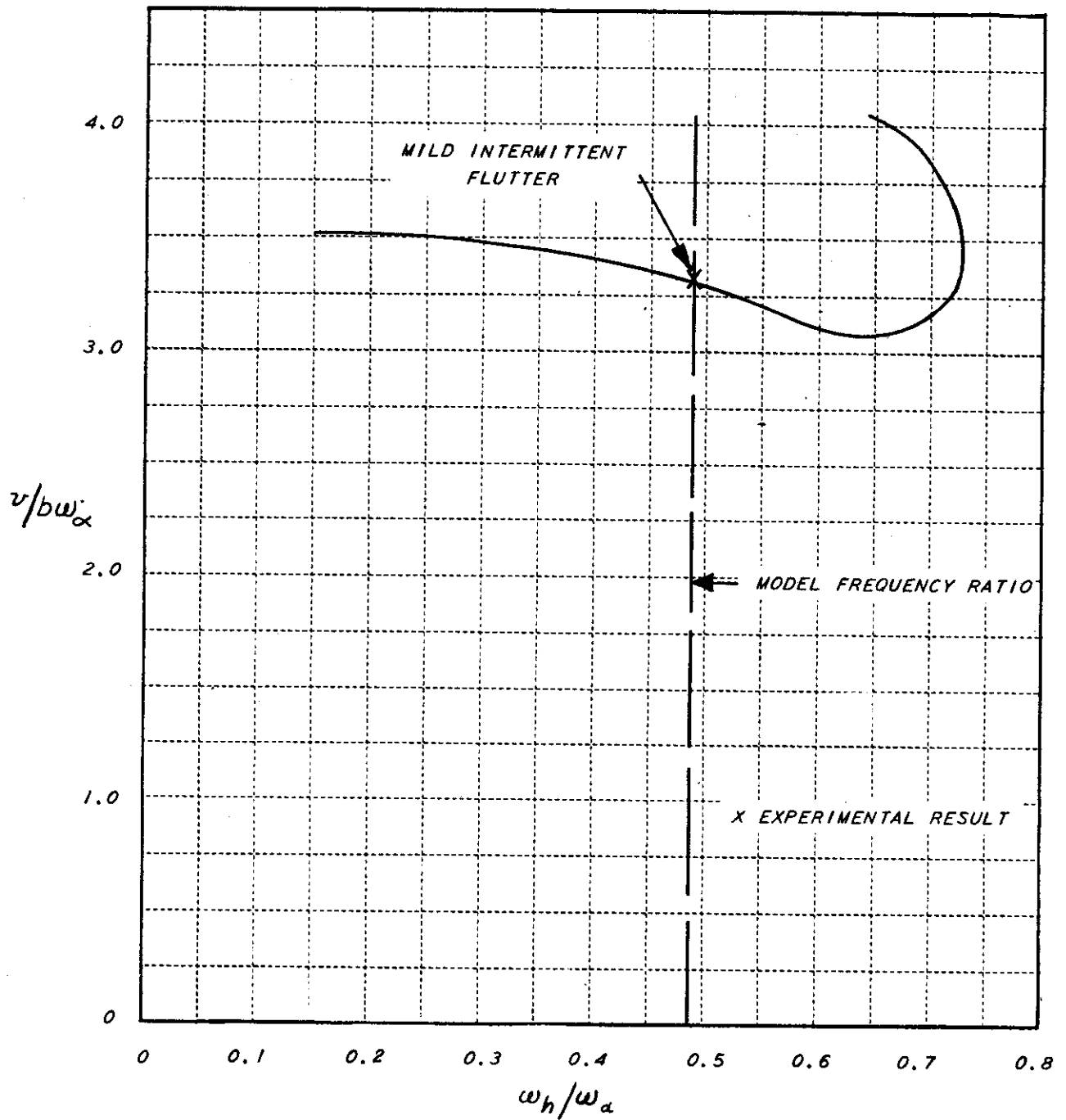


FIGURE 46 $v/b\omega_\alpha$ VS. ω_h/ω_α
 $M = 0.75$ ANTISYMMETRIC MODEL - $\rho = 0.001131$ SLUGS/FT³

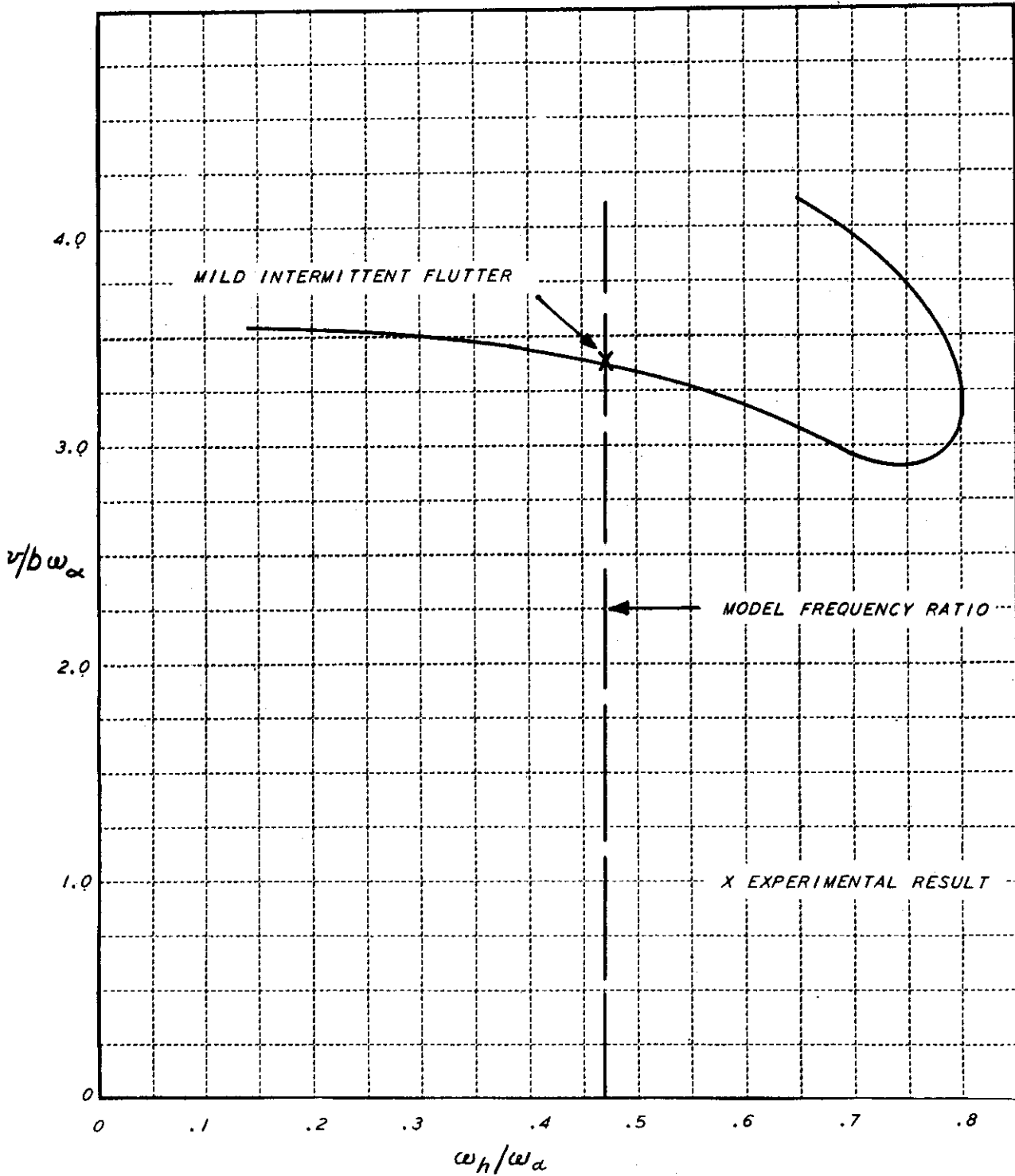


FIGURE 47 $v/b\omega_\alpha$ VS. ω_h/ω_α
 $M=0.85$ ANTISYMMETRIC MODEL - $\rho=0.001114$ SLUGS/FT³

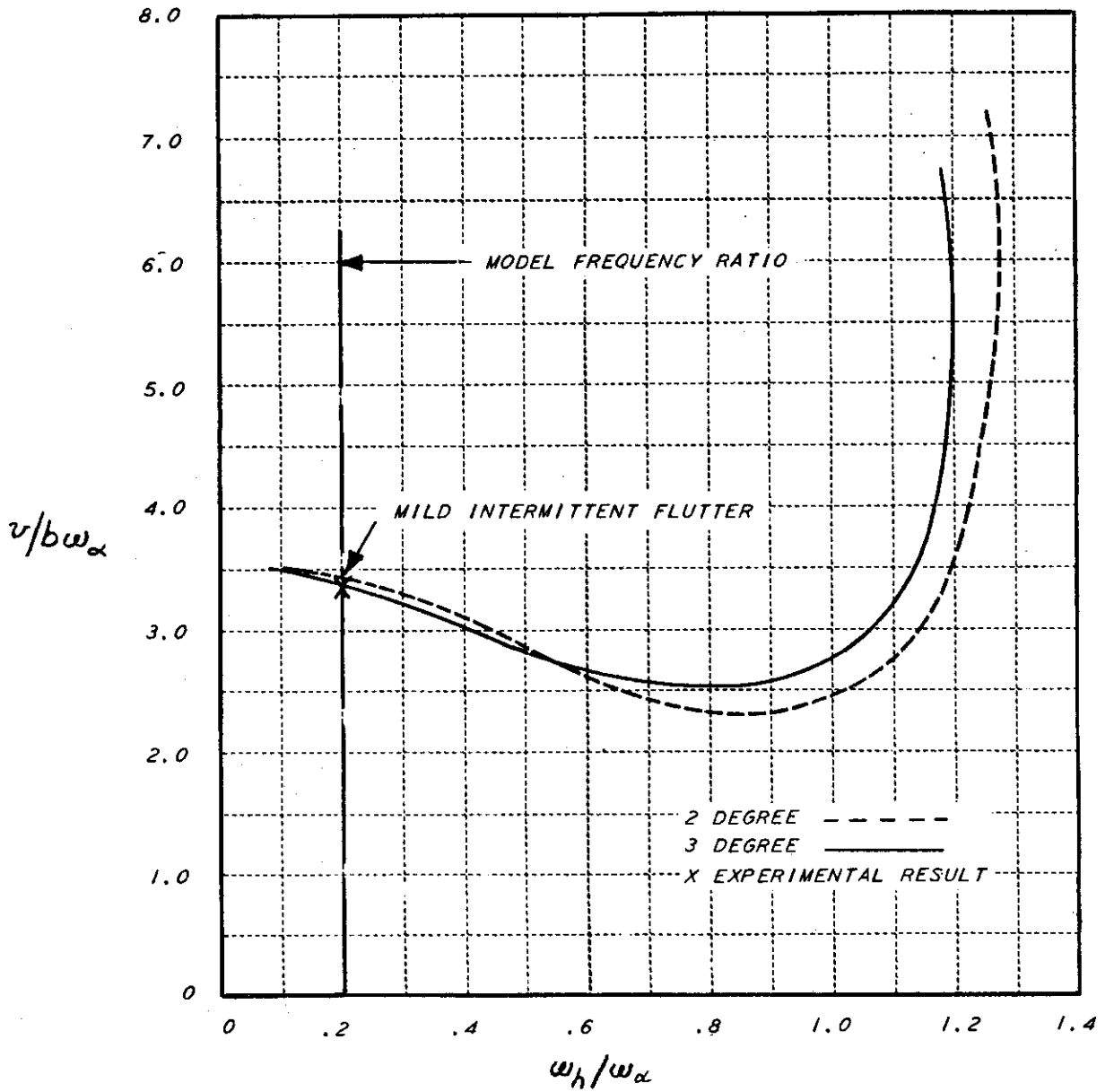


FIGURE 48 $v/b\omega_\alpha$ VS. ω_h/ω_α
 COMPARISON OF TWO AND THREE DEGREE ANALYSES OF $M = 0.85$ CANTILEVER
 MODEL $\rho = 0.001120$ SLUGS/FT³

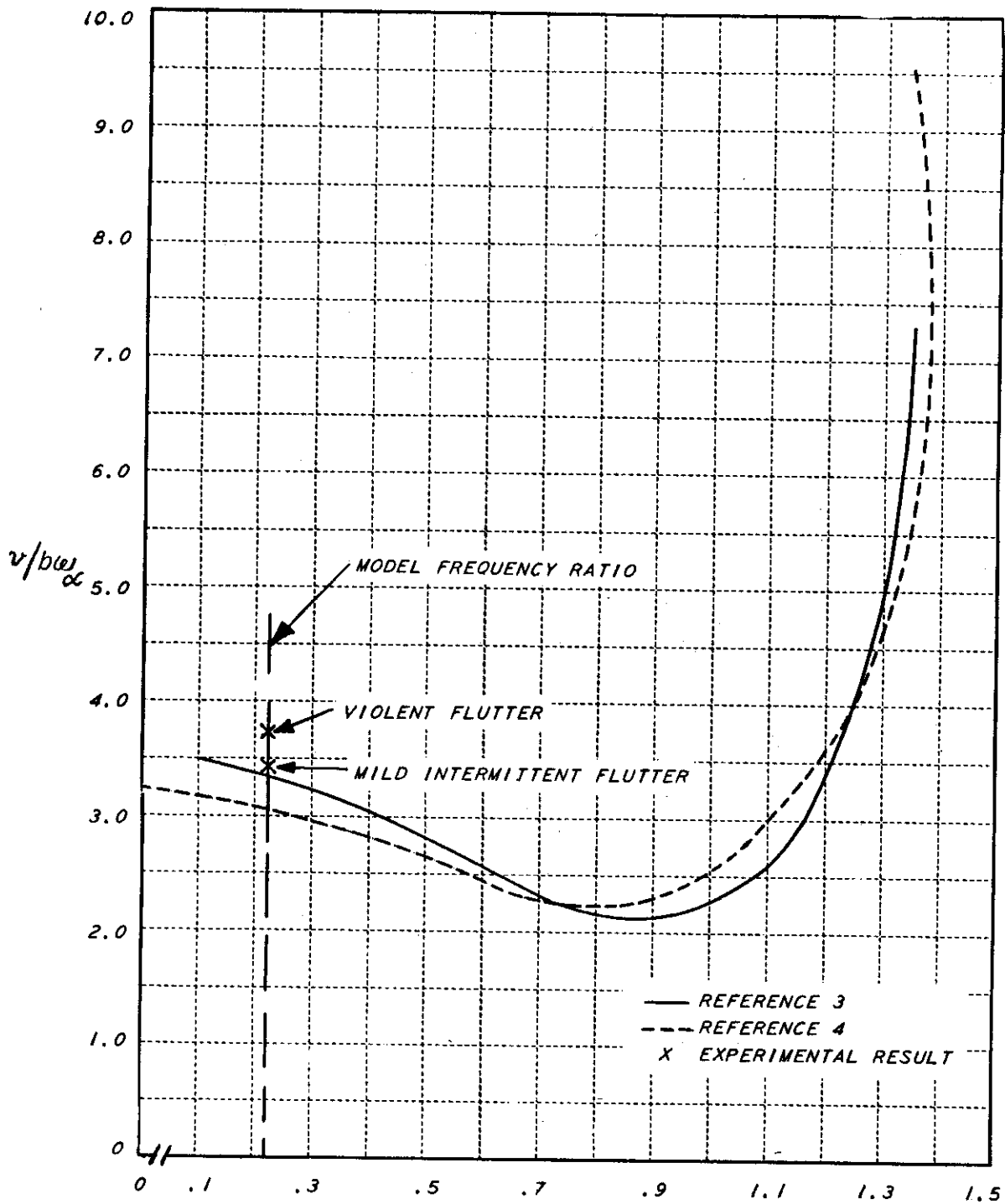


FIGURE 49 $v/b\omega_\alpha$ VS. ω_h/ω_α
 COMPARISON OF COMPRESSIBLE AND INCOMPRESSIBLE ANALYSES
 FOR $M = 0.65$ CANTILEVER MODEL - $\rho = 0.001127$ SLUGS/FT³

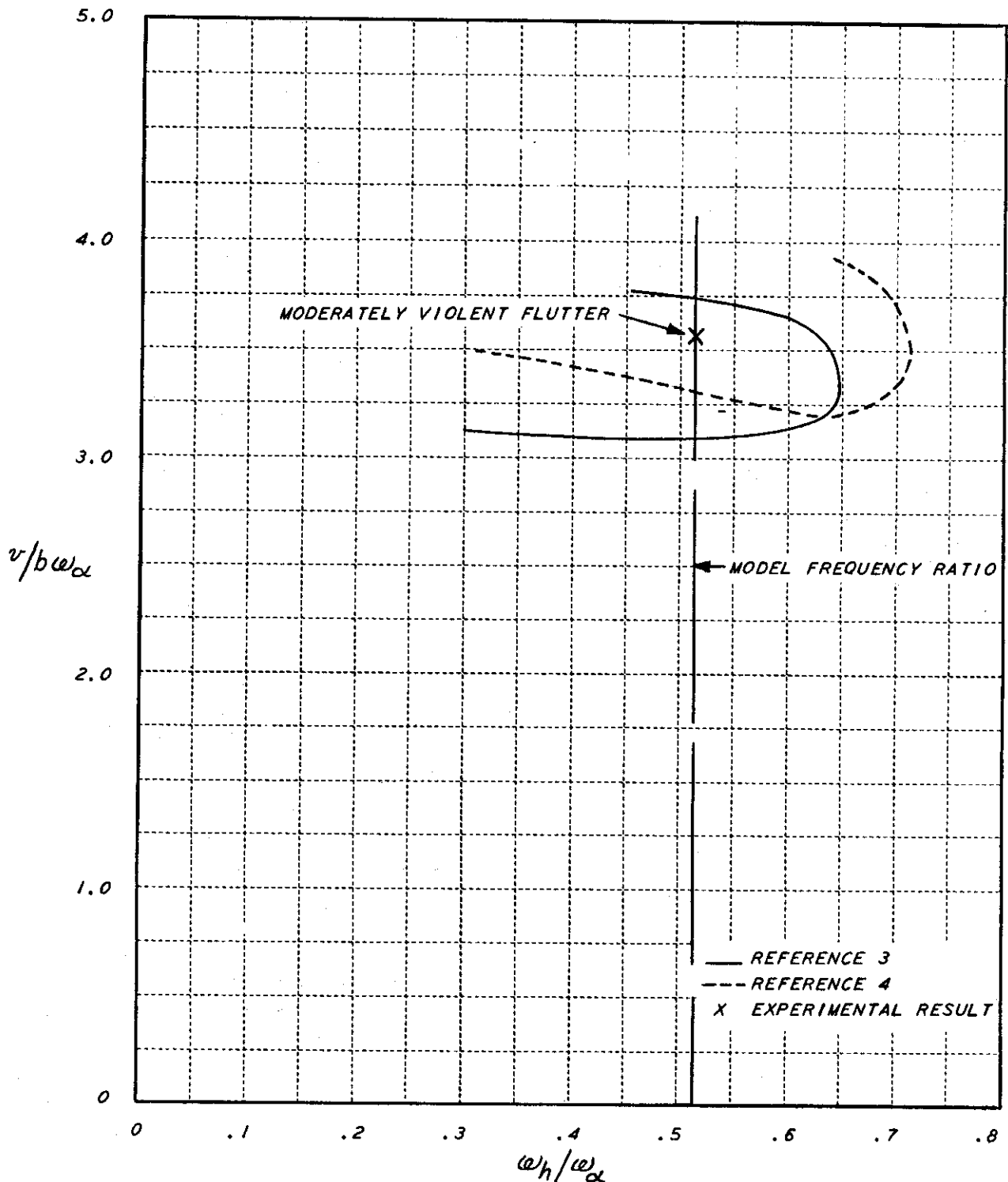


FIGURE 50 $v/b\omega_\alpha$ VS. ω_h/ω_α
 COMPARISON OF COMPRESSIBLE AND INCOMPRESSIBLE ANALYSES
 FOR $M = 0.65$ ANTISYMMETRIC MODEL - $\rho = 0.001139$ SLUGS/FT³

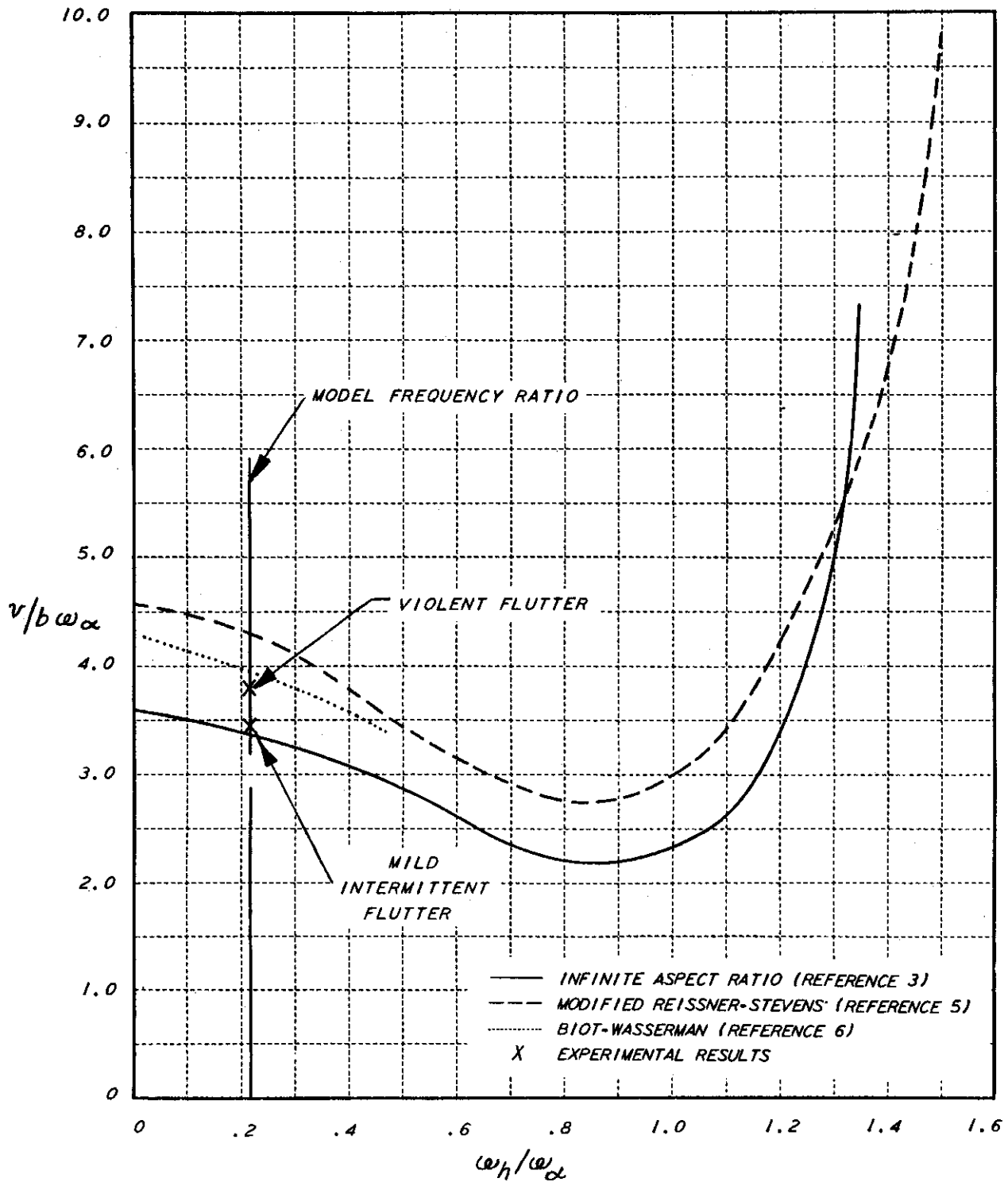
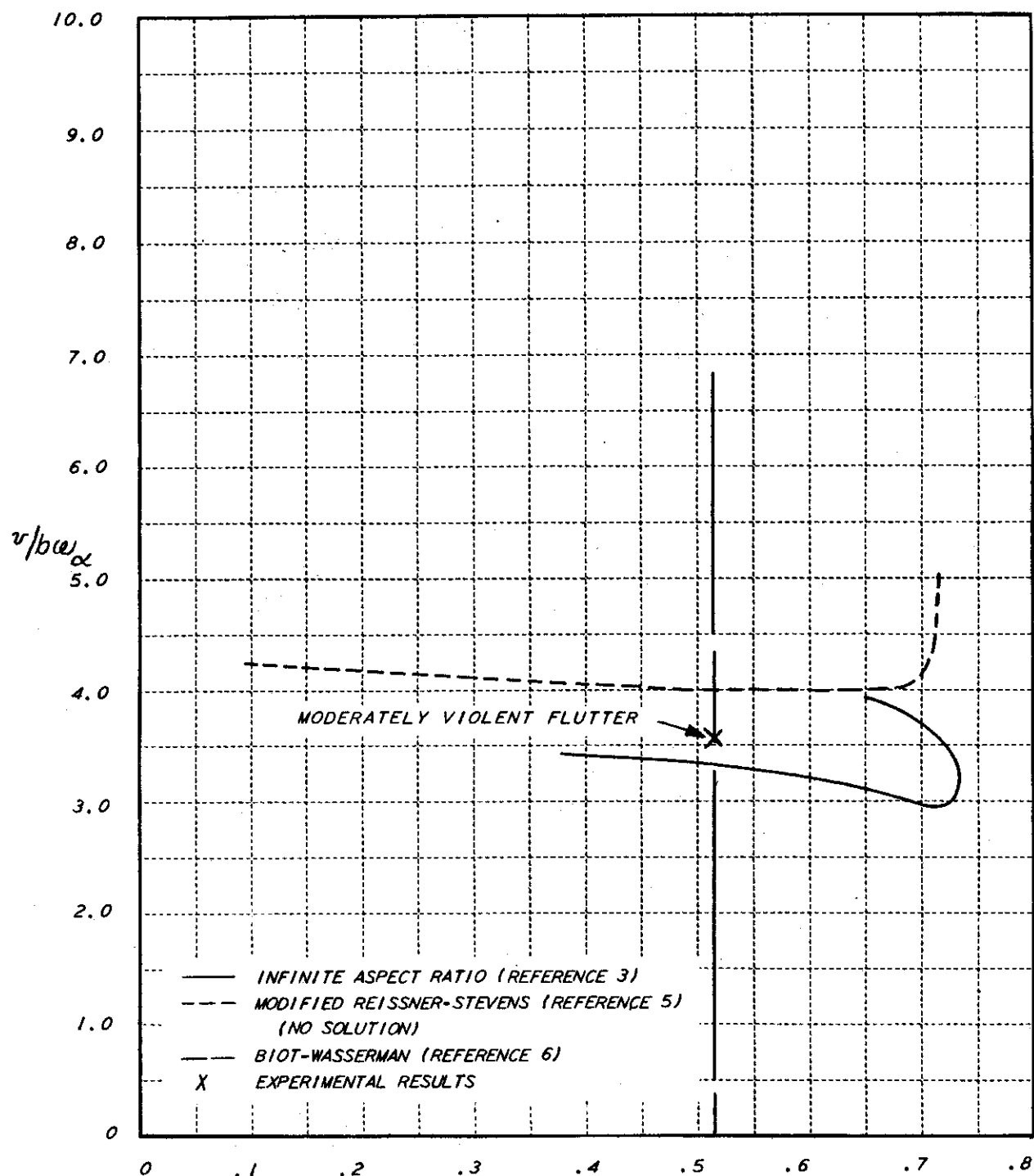


FIGURE 51 $v/b\omega_\alpha$ VS. ω_h/ω_α
 COMPARISON OF VARIOUS METHODS OF FINITE SPAN ANALYSES
 FOR $M = 0.65$ CANTILEVER MODEL - $\rho = 0.001127$ SLUGS/FT³



ω_h/ω_α
 FIGURE 52 $v/b\omega_\alpha$ VS. ω_h/ω_α
 COMPARISON OF VARIOUS METHODS OF FINITE SPAN ANALYSES
 FOR $M = 0.65$ ANTISYMMETRIC MODEL $\rho = 0.001139$ SLUGS/FT³

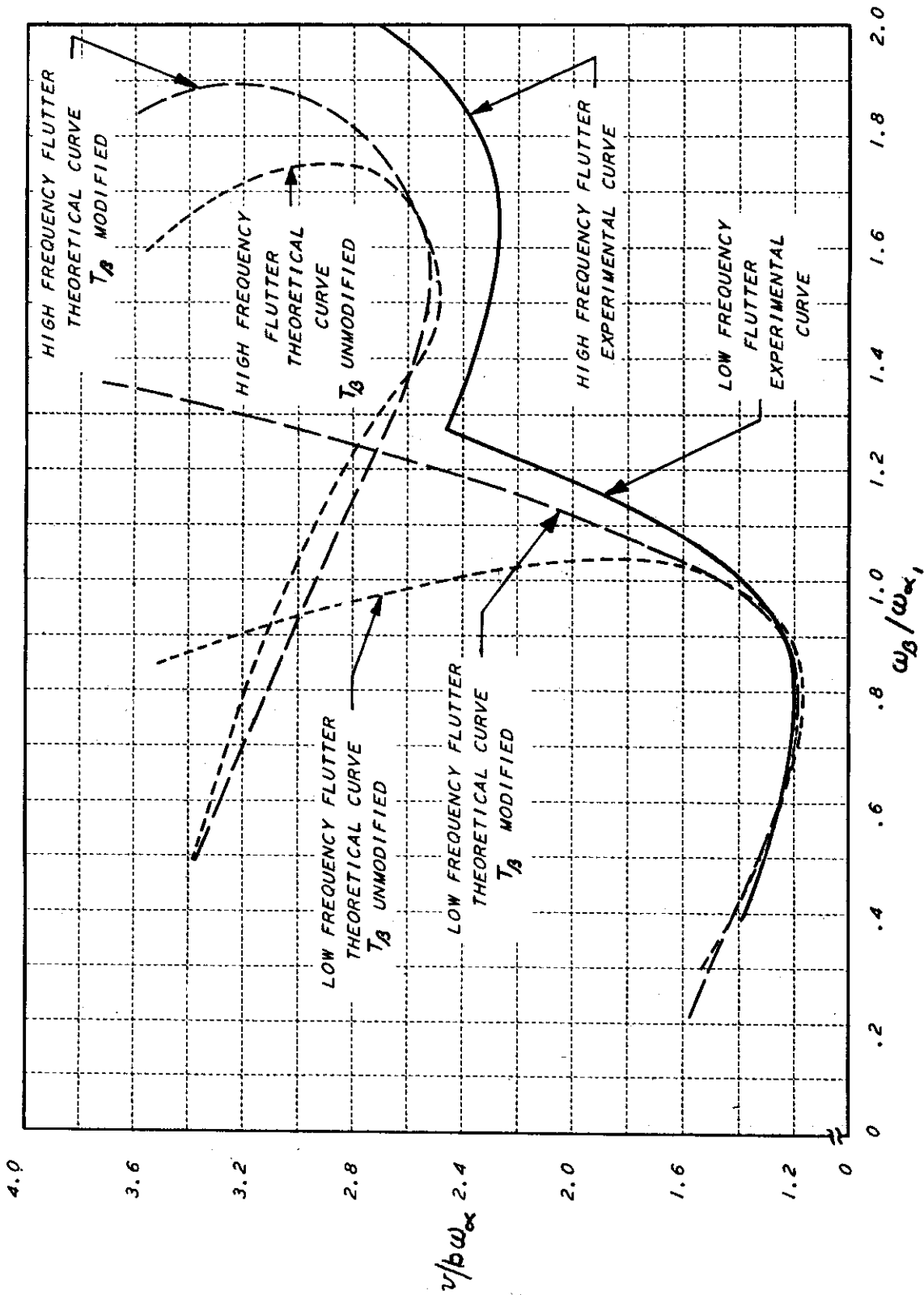



FIGURE 53 $v/b\omega_\alpha$ VS. $\omega_\beta/\omega_\alpha$,
 COMPARISON OF THEORETICAL AND EXPERIMENTAL RESULTS
 OBTAINED WITH $M = 0.65$ WING-AILERON MODEL

- 
- (a) First uncoupled wing cantilever bending.
 - (b) First uncoupled wing cantilever torsion.
 - (c) Second uncoupled wing cantilever bending.
 - (d) Aileron rotation.

The results of these analyses, with and without $T\beta$ modified, are shown in Fig. 53 in comparison with the experimental results for all values of the frequency ratio $\omega\beta/\omega\alpha_1$ tested. The determinant elements are listed in Appendix II.

(2) High Frequency Wing-Aileron Flutter Mode

These analyses were five-degree analyses with the following degrees of freedom used as generalized coordinates:

- (a) First uncoupled wing cantilever bending.
- (b) Second uncoupled wing cantilever bending.
- (c) Third uncoupled wing cantilever bending.
- (d) Second uncoupled wing cantilever torsion.
- (e) Aileron rotation.

The results of these analyses, with and without $T\beta$ modified, are shown in Fig. 53 in comparison with the experimental results.

VI. DISCUSSION AND RESULTS

A. Models and Associated Equipment

(1) Plain Wing Models

At the inception of this program, many problems associated with testing flexible flutter models at high subsonic Mach numbers were unknown and only estimates as to the severity of wind tunnel turbulence, Mach number effects, etc., could be made. It was realized that the large size and rectangular shape of the flutter models would tend to accentuate any random gust energy present in the wind tunnel but this was not considered a serious

[REDACTED]

problem due to past experience with other large flutter models tested in the wind tunnel. These models, while tested at relatively low speeds, indicated the tunnel flow was smooth and it was expected that no large deviations from this condition would result as the tunnel speed was increased. However, this was not found to be the case and the magnitude of the random gust loadings on the models due to increased tunnel turbulence at high subsonic Mach numbers was much higher than had been anticipated. The result of the increased tunnel turbulence was the loss of the first model tested when large oscillations caused by the unsteady air flow buckled the wing near the root. This problem, plus others that arose during tunnel testing, resulted in a flutter model development program to obtain a successful model construction. Appendix I presents a detailed description of this development program from which the following conclusions were drawn:

- (a) The models should be constructed as simply as possible. Due to the high probability of model loss, it is better to build more models of a simple inexpensive design to effect parameter variations than to construct a few expensive models whereby means of parameter variations are an integral part of the model.
- (b) If item (a) can be accomplished to a high degree, it is desirable to make the models expendable so that the problems associated with a flutter lock can be neglected. It was found that some ideal characteristics of the flutter models were compromised in this program in order to successfully incorporate the flutter lock and thus save the expensive models and prevent damage to the wind tunnel.
- (c) It is insufficient to design for proper elastic rigidity only. The design must be based on a stress-deflection relationship and not a stress-load criterion. This is particularly true when it is expected that large amounts of random gust energy are present, as the large bending deflections which these loads can induce will sometimes stress the model to levels beyond those present in a steady state flutter mode.
- (d) Since the models can be highly stressed due to random gusts, care should be taken to insure that no stress concentrations are present in the model construction to prevent a model failure due to causes other than destructive flutter.

[REDACTED]


(2) Wing-Aileron Models

Since the wing-aileron models were essentially the same as the plain wing models, most of the conclusions and design criteria obtained for those models also apply to the wing-aileron models. The aileron construction, using a Strux core with a 0.004 in. dural skin bonded to the outside contour, satisfactorily duplicated a rigid aileron with the specified non-dimensional mass parameters. The aileron frequency system, consisting of fixed springs and steel flexure pivots, satisfactorily provided a suitable range of linear aileron rotational rigidities with a minimum amount of damping.

(3) Flutter Lock

The large size of the flutter models and the speeds to which they were to be tested in this program indicated that a successful flutter lock had to be obtained if the loss of expensive models and damage to the wind tunnel were to be prevented. It was found from experience gained during wind tunnel testing and from theoretical checks of possible locking devices that a simple locking system to provide fast-acting, positive action without imposing a series weight penalty could not be constructed, and thus, the lock that was finally used successfully was a system of electronic, pneumatic, and mechanical equipment. A detailed summary of the development program required to design this locking system is presented in Appendix I. During the development program undertaken for this project, it was found that certain basic design criteria must be followed to successfully build a flutter lock for high speed flutter testing. The following are felt to be basic criteria but do not necessarily include all the factors which might have to be considered due to the peculiarities of a specific design requirement:

- (a) The lock must be fast-acting. It is felt that to save the model, only a few cycles of pronounced flutter can be allowed. For any specific configuration, this criterion can vary due to the type of flutter mode expected and the severity of the flutter motion obtained.
- (b) In conjunction with (a), stops should be provided to limit divergent oscillations due to flutter or rigid body instability so that an excessively large oscillation will not destroy the model before the lock is actuated.
- (c) Since high flutter frequencies are usually associated with flutter at high speeds, the human reaction time is too slow to actuate the lock quickly and, therefore, electronic sensing devices should be used.

- 
- (d) The model should be locked at zero angle of attack and at zero bending deflection. The dynamic motions that are induced by the static loads applied when the model is locked off-center might prove disastrous when the model is unlocked.
 - (e) Since any positive lock would restrain the torsional motion of the model, it is important that the lock disengage uniformly along the chord so that divergence problems associated with the lock providing an aft pivot point on the wing are avoided.
 - (f) It is insufficient to design for proper elastic rigidity of the lock to prevent flutter in the locked position as it is possible for a fluttering wing to destroy the lock before it entirely clamps the model.
 - (g) For flutter tests which involve rigid body degrees of freedom, the lock should also be capable of locking out any rigid body instability which might occur.

The lock used for the flutter tests, described in detail in Appendix I of this report, included all of the above features as well as others which were included to account for conditions peculiar to the subject model construction and testing techniques. The lock used in this series of tests consisted of cables and locking pads placed adjacent to the tip of the wing. Aerodynamic tufts placed on the wing over the outboard portions of the span indicated that the lock did not affect the flow characteristics over the wing.

(4) Suspension System

The suspension system used for these tests was a modification of the suspension used for low speed flutter model testing reported in Ref. 1 to provide freedom in translation, pitch, and roll for the symmetric and anti-symmetric configurations respectively. Cantilever conditions were obtained by locking out all root motions. The suspension system successfully provided rigid body translation, pitch, and roll for the low speed, low frequency flutter tests described in Ref. 1. However, when used in conjunction with the present models, whose frequencies were considerably higher than those of Ref. 1, it was found that the small amount of slop present in the four-bar linkage, in addition to the elastic deformation of the various suspension components, markedly affected the vibratory modes of the models. It, therefore, became necessary to modify the suspension system in order to eliminate, as far as was possible, all slop and elastic deformations in the component parts. The modifications to the suspension system effectively eliminated slop but could not completely prevent elastic deformations of the supporting members.

[REDACTED]

The elastic rigidities of the suspension system were included in the theoretical correlative analyses to obtain the measured coupled mode frequencies and node lines. Figures 5 through 13, pp. 13 through 21 indicate the magnitude of this effect by the shift of node lines as the rigidities of the models were increased. A complete description of the suspension, as modified for this project, is given in Appendix I.

(5) Instrumentation

The instrumentation used for this project was generally unsatisfactory. Two types of model instrumentation were used, accelerometers and strain gages. Accelerometer signals were integrated twice to yield a continuous displacement reading at six wing stations. Reasonable correlative checks of node lines were obtained but loss of models and subsequent destruction of accelerometers required that other means of recording model motions be used.

The strain gage instrumentation used in place of the accelerometers is fully discussed in the instrumentation section in the body of this report. The method did not give very satisfactory results in that the mode shapes could not be predicted to any great degree of accuracy from the data obtained from the strain gage traces. However, it is felt that the method has great potential and further investigation into the methods of calibration and strain gage placement would make this system very satisfactory.

B. Vibration Tests

The vibration tests of the models were conducted with the wings mounted in the suspension system attached to the wind tunnel cart ceiling. The wings were vibrated with two electromagnetic vibrators mounted at the tip. Node lines obtained by visual observation at the various coupled mode frequencies are presented in Figs. 5 through 13 for the plain wings. Figures 14 through 31 present the node lines of the coupled modes for the wing-aileron models. The node lines associated with the higher coupled mode frequencies for the various wings differed somewhat from one another. It was found that this difference can be attributed to the flexibility of the suspension system. While negligible for the lower frequencies, it becomes more pronounced with increasing model frequency.

C. Vibration Analyses

Correlative vibration analyses were conducted for all plain wing configurations tested. Two representative wing-aileron configurations were analyzed. Coupled modes were obtained by a standard mass elastic coupling of the uncoupled bending and torsional modes. It was found that the elastic properties of the suspension system had to be included in the coupled mode analyses to obtain good agreement with the measured coupled modes. In general, good agreement between measured and calculated mode shapes and frequencies were obtained. Table V summarizes the calculated uncoupled and coupled mode

[REDACTED]

frequencies. Comparison of the calculated node lines with the measured ones are presented in Figs. 5 through 13 for all the plain wing configurations. Figures 16 and 19 present the comparisons for the two wing-aileron configurations analyzed.

D. Flutter Tests

(1) Plain Wing Models

In actual experimental investigations, it is often difficult to obtain the constant amplitude, steady oscillations which theoretically exist at that air speed corresponding exactly to the flutter stability boundary. Under ideal conditions, where speeds are low and a sinusoidal driving force can be used to start the motion, the exact flutter boundary can be obtained relatively easily. However, in the present series of tests, these ideal conditions were not present as the speeds were high, the models large, and the random frequency gust energy present excited the model. In the symmetric and antisymmetric configurations, electromagnetic shakers were attached to the suspension system in an attempt to excite the model with a sinusoidal driving force. However, the magnitude of the random energy imposed on the large exposed model surface was much greater than the output of the electromagnetic shakers and the system was, therefore, abandoned.

Since a series of expensive flutter models had been lost while attempting to obtain a constant amplitude steady-state flutter condition at these high speeds, it was decided to stop the tests when it appeared that the speed obtained was very close to the critical flutter speed as exemplified by bursts of large constant amplitude motion. Under this type of testing procedure, the speed at which the flutter boundary is said to exist, is based on the experience and judgment of the experimenters in interpreting visual observations of the model motion and the outputs of the instrumentation. It was felt that in using this testing procedure, the purposes of the flutter tests would be satisfied, i.e., a critical flutter speed would be obtained for specific configurations, and the flutter motion would not start at a relatively high initial energy level and thus produce the uncontrollable flutter that previously had been obtained. It is felt that the velocity data accumulated using this testing technique is within a few percent of data that would be obtained if constant amplitude steady-state flutter could have been produced safely. This estimate is based on the results of two cantilever tests that were conducted using this testing technique and then tested to speeds where extremely violent motion was obtained and damage to the models resulted. It was found, however, that the frequency of the flutter motion changed very rapidly as violent flutter was approached and different frequency results, as compared to the previous tests, were obtained.

[REDACTED]

The effects of finite span, theoretically determined for one cantilever and one antisymmetric configuration, are shown in comparison for the infinite aspect ratio solutions in Figs. 51 and 52 respectively. In general, the finite span effects, as predicted using the Biot-Wasserman method (Ref. 6 and Ref. 7), were in much better agreement with the experimental results than were the effects predicted by a modified Reissner-Stevens method (Ref. 5 and Ref. 8). For the cantilever case investigated, the Biot-Wasserman method (Ref. 6 and Ref. 7), predicted an increase in flutter velocity of approximately 17% whereas the modified Reissner-Stevens method (Ref. 5 and Ref. 8), predicted an increase of approximately 28%. For the antisymmetric case, the Biot-Wasserman method predicted an increase of approximately 20% whereas no solutions were obtained using the modified Reissner-Stevens method. For the cantilever case investigated, the Biot-Wasserman method yielded a flutter speed approximately 6% unconservative whereas the modified Reissner-Stevens method yielded a flutter speed approximately 14% unconservative. Since for the antisymmetric case investigated the modified Reissner-Stevens method did not yield any solutions, a comparison with experimental results can only be made for the Biot-Wasserman method which yielded results approximately 12% unconservative.

Since the second uncoupled bending mode frequency was equal to, or slightly below the first uncoupled torsion mode frequency, and was very important in obtaining the correct coupled mode shapes and frequencies, it was decided to find its effect on the flutter characteristics of a cantilever wing. The results of the analysis are shown in Fig. 48 where it can be seen that the inclusion of the second bending mode reduced the flutter speed by only $1\frac{1}{2}\%$. The inclusion of the second bending mode also reduced the flutter frequency by approximately 5%.

(2) Wing-Aileron Models

The results of the wing-aileron flutter analyses are shown in Fig. 53. In general, the results of the theoretical analyses predicted the trend of experimental data obtained. To obtain better correlation with the experimental results, it became necessary to modify the T_{β} term, the oscillatory aileron hinge moment coefficient, in the flutter analyses. This was accomplished by using the experimental values reported in Ref. 9, which are generally lower than the two dimensional values listed in Ref. 3. The analyses indicated that both the high and low frequency flutter modes exist for this model and that neither is a single degree of freedom instability. It is felt that the reason the high frequency flutter mode does not agree as well with the experimental results as the low frequency flutter mode may be that all of the higher frequency vibration modes that are of importance in completely defining the flutter motion were not included in the analyses. However, the analyses predicted the correct trend and flutter frequency for the frequency ratios of interest.

Details of Experimental Results

(a) Cantilever Flutter Tests

Three sets of cantilever flutter tests were conducted; (1) flutter tests of the $M = 0.65$, $M = 0.75$, and $M = 0.85$ models at the design density, (2) flutter tests of the $M = 0.65$ and $M = 0.75$ wings at a density lower than the design density so that higher Mach numbers at flutter could be obtained, (3) flutter tests of the $M = 0.65$ and $M = 0.75$ wings at the design density to determine the velocity increment that would have to be applied to the results of the first series of tests to obtain extremely violent flutter.

The results of these tests are tabulated in Table III and plotted in comparison with the theoretical results in Figs. 36 through 41, pp. 52 through 57. On the basis of the results obtained in the first and third series of tests, it appears that the test results obtained for the $M = 0.85$ wing are somewhat low. It is felt, however, that the flutter speed is within 5% of the speed where destructive flutter would occur. Due to blockage in the tunnel, this model could not be tested to higher speeds so that a comparison similar to that conducted with the $M = 0.65$ and $M = 0.75$ models could not be made.

The tests conducted under sets (1) and (3) indicated that the velocities obtained in the first set of tests were only 5% to 6% lower than the velocities obtained when violent flutter resulted in damage to the models. The flutter frequencies that were obtained from the two sets of tests, however, were substantially different, with the violent flutter tests producing lower flutter frequencies. The flutter frequency obtained for the $M = 0.75$ wing in the violent test was lower than the corresponding flutter frequency of the $M = 0.65$ wing indicating that compressibility effects were markedly affecting the flutter frequency. An indication of this was also noticed in the mild flutter tests where the flutter frequencies of the $M = 0.65$ and $M = 0.75$ models were the same for flutter oscillations of approximately the same magnitude and duration. It is felt that the elastic effects of the suspension system which changed the coupled mode shapes of the $M = 0.65$ and $M = 0.75$ models did not cause this drop in flutter frequency. This conclusion was reached when theoretical analyses showed that the fuselage flexibilities primarily affected only the second uncoupled bending mode which had very little effect on the flutter mode. (See Fig. 48, p. 65.)

(b) Symmetric Flutter Tests

For the symmetric flutter tests, viscous damping had to be placed in both the pitch and translational degrees of freedom to produce a dynamically stable system within the confines of allowed rigid body motion. The magnitude of the damping in the pitch and translational degrees of freedom was 100% of the critical value but there was sufficient slop placed in the system so that the damping, frequencies, and mode shapes of the symmetric

[REDACTED]

modes of vibration were unaffected. The flutter results of these tests are tabulated in Table III and plotted in comparison with theoretical results in Figs. 42 through 44. In general, the flutter motion was rather mild but the response to gusts was rather violent and, consequently, difficulty was experienced in flying the model between the motion limiters which were placed ± 4.0 in. from the center line of the model.

(c) Antisymmetric Flutter Tests

The antisymmetric flutter tests were mild and, therefore, sustained oscillations for 15 to 20 cycles were obtained at the flutter points. The dynamic stability of the models in these configurations was very good and no difficulty was experienced in flying the model between the motion limiters which were placed ± 3.0 in. from the tip of the wing. The results of the flutter tests are tabulated in Table III and plotted in comparison with the theoretical results in Figs. 45 through 47.

(2) Wing-Aileron Models

The wing-aileron configurations yielded rather low speed results and, therefore, the random energy present in the tunnel was at a low level. This fact, plus a slow approach to flutter, enabled the attainment of constant amplitude steady-state flutter for all configurations tested.

As indicated in Fig. 53, two discrete wing-aileron flutter modes were obtained for the range of the parameter $\omega_\beta/\omega_{\alpha 1}$ used. Both flutter modes had frequencies close to still air coupled mode frequencies of the wing-aileron combination and the flutter frequency increased as the coupled mode frequency increased. At the frequency ratio where the envelopes of the two flutter modes intersected, the flutter was very violent. As this intersection point was approached by increasing air speed at a constant value of $\omega_\beta/\omega_{\alpha 1}$, instability in the lower frequency mode became more pronounced. However, near the critical value, a slight change in velocity caused the high frequency flutter mode to come in very violently.

Wing-aileron flutter was obtained in the low frequency flutter mode at speeds as low as 30% of the wing-alone critical speeds. The lowest speeds were obtained at a frequency ratio ($\omega_\beta/\omega_{\alpha 1}$) of 0.65 to 0.80 depending on the wing considered. The change from the low to high frequency flutter mode occurred at different ($\omega_\beta/\omega_{\alpha 1}$) ratios for the various wings but all occurred in the range of ($\omega_\beta/\omega_{\alpha 1}$) from 1.05 to 1.25. The flutter frequency of the lower frequency mode followed the fourth coupled mode (see Tables II and IV) which was in turn controlled somewhat by the aileron frequency. The fourth coupled mode appears to be one which is the higher of the two coupled modes involving wing first torsion, second bending, and aileron degrees of freedom. The flutter mode frequency was, in all cases, between 13% and 20% higher than the second uncoupled bending mode frequency.

[REDACTED]

Wing-aileron flutter in the high frequency mode occurred as low as 55% of the critical wing-alone speed. The high frequency mode was obtained at frequency ratios (ω_p / ω_{A1}) from 1.27 to 1.86 in the $M = 0.65$ flutter model and at lower frequency ratios for the $M = 0.75$ and $M = 0.85$ models. With the $M = 0.65$ model, for a frequency ratio of 2.11, a speed of 443 MPH or $M_e = .578$ was obtained without detecting any instability. Speeds higher than this were not obtained due to the difficulty in operating the manual aileron flutter lock. The speed obtained did indicate that the wing-aileron flutter speed was approaching the wing-alone value. The frequency of the high frequency flutter mode followed the fifth coupled mode (see Tables II and IV) whose frequency was, in turn, controlled somewhat by the aileron frequency. The fifth mode is an aileron, second torsion-higher order bending mode and minimum flutter speeds in this mode were obtained when the aileron frequency was approximately 80% of the fifth mode frequency.

E. Flutter Analyses

(1) Plain Wing Models

The three dimensional analyses using strip theory and the two dimensional coefficients listed in Ref. 3, either closely predicted the flutter speed or yielded results that were slightly conservative. For the $M = 0.65$ model in the cantilever, symmetric, and antisymmetric configurations, the analyses were approximately 10% conservative in predicting the critical velocity. However, in all of these configurations, the flutter obtained was rather violent and it is, therefore, possible that this model in the different configurations was carried beyond the critical speed and into the flutter region. These results would, therefore, indicate a higher degree of conservatism than the other models in the similar configurations as it is felt that the flutter boundary was not exceeded in obtaining the results for the $M = 0.75$ and $M = 0.85$ models. The results of the theoretical analyses for the plain wings are presented as flutter loops in Figs. 36 through 47, pp. 52 through 64 and are tabulated in Table VI, p. 51.

To find the effects of compressibility, theoretical analyses using the Possio aerodynamic coefficients listed in Ref. 4 were used to calculate the flutter speed for one cantilever and one antisymmetric configuration. The results of these analyses are shown for the cantilever and antisymmetric configurations in Figs. 49 and 50 respectively and tabulated in Table VI. The calculated flutter speeds were 8.7% and 11.4% lower than the incompressible flutter speeds calculated for the same configurations which indicates that the analyses using compressible aerodynamics yield results approximately 10% more conservative than those using incompressible aerodynamics. The predicted speed reduction due to compressibility was not obtained in the experimental results. However, the compressible analyses did predict lower flutter frequencies than the incompressible analyses and this effect was obtained in the experiments.


[REDACTED]

Since the high frequency wing-aileron flutter mode had not been expected, it was of interest to determine the cause for its existence, i.e., could the flutter mode be expected on any rectangular wing with uniform stiffness properties or was it caused by the particular ballast configuration present in these models? Therefore, a flutter analysis was conducted using the same degrees of freedom used to predict the high frequency flutter mode obtained in the wind tunnel tests but the vibratory modes were determined using constant values of weight, inertia, and unbalance along the span. The results of this analysis indicated that the high frequency wing aileron flutter mode did not exist for the unballasted model. The reason for the existence of this higher order flutter mode in the ballasted model, and not the unballasted model, seems to be two-fold: (1) the ballast weights reduced the frequency of the unstable mode from approximately 97 cps to 68 cps, (2) the sign of the mass coupling terms between the primary modes involved has been changed from the unballasted model to the ballasted model, thus producing a stable flutter condition for the unballasted model and an unstable condition for the ballasted model. An important conclusion that can be derived from these results is that if an unfavorable mass distribution is present, wing-aileron flutter in the higher frequency modes can be obtained at a speed below the cantilever flutter speed even if the frequency of the aileron is sufficient to preclude flutter in the conventional lower frequency wing-aileron modes.

VII. CONCLUSIONS AND RECOMMENDATIONS

It may be concluded that the general objectives of this flutter program were accomplished. On the basis of the experimental tests and theoretical analyses conducted, the following specific conclusions may be drawn:

- (1) The flutter tests with the symmetric degrees of freedom gave results nearly the same as those obtained with the cantilever degrees of freedom. It should be noted that the symmetric modes and frequencies were very similar to the corresponding cantilever values.
- (2) The flutter tests with the antisymmetric degrees of freedom yield flutter speeds higher than the ones obtained with the cantilever degrees of freedom. Furthermore, the severity of the flutter motion was reduced.
- (3) No large effects of compressibility on the flutter speed up to $M = 0.93$ were noticed in the experimental phase of the contract.
- (4) Reductions to 30% of the cantilever flutter speed were obtained at a frequency ratio $\omega_\beta/\omega_{\alpha_1}$ of approximately 0.80 with the addition of the unbalanced spring-restrained half-span aileron.

- 
- (5) A second wing-aileron flutter mode was obtained below the cantilever bending-torsion flutter speed when the ratio of aileron rotational frequency to first wing torsional frequency was 1.1 or above. Minimum flutter velocities in this higher mode of flutter were obtained when the aileron rotational frequency was about 80% of the zero air speed frequency of the mode corresponding to the flutter mode.
 - (6) If an unfavorable mass distribution is present, wing-aileron flutter in the higher frequency modes can be obtained at a speed below the cantilever flutter speed even if the frequency of the aileron is sufficient to preclude conventional flutter in the lower frequency wing-aileron modes.
 - (7) Incompressible, infinite aspect ratio flutter analyses predicted the experimental results within a few percent.
 - (8) Theoretical calculations indicate that the flutter speed and frequency are lowered by compressibility.
 - (9) To estimate the effects of finite span, the Biot-Wasserman method (Refs. 6 and 7) was superior to a modified Reissner-Stevenson method (Refs. 5 and 8). In all cases unconservative results were predicted in using these finite span corrections.
 - (10) If possible, the model should be inexpensive and simply constructed so that they are expendable and therefore the difficulties associated with the use of flutter locks at these speeds would be avoided. An example of this type of construction is reported in Refs. 16 and 17.

It is recommended that:

- (1) Additional flutter tests be conducted with small, inexpensive, expendable models to investigate the effects of compressibility and rigid body degrees of freedom at Mach numbers well into the transonic region.
- (2) Additional flutter tests be conducted with wing-aileron models to determine the critical speeds for spring-restrained ailerons with values of mass unbalance between the fully unbalanced and balanced condition.
- (3) To conduct additional wing flutter tests in the high subsonic and transonic speed regime to determine the effects of the chordwise location of the center of gravity.

VIII. BIBLIOGRAPHY

1. Brady, W. G., Loewy, R. G., and Targoff, W. P., Flutter Model Tests of Wings Carrying Heavy Tip Pods - Part I - Straight Wings. WADC Technical Report 53-161. Wright Air Development Center, Wright-Patterson Air Force Base, Ohio, August 1953. (CONFIDENTIAL report)
2. Targoff, W. P., "The Associated Matrices of Bending and Coupled Bending-Torsion Vibrations." Journal of the Aeronautical Sciences. Vol. 14, No. 8. August 1947.
3. Smilg, B. and Wasserman, L. S., Application of Three-Dimensional Flutter Theory to Aircraft Structures. Air Corps Technical Report No. 4798. Wright Air Development Center, Wright-Patterson Air Force Base, Ohio, July 9, 1942.
4. White, R. P., Tapered-Wing Aerodynamic Coefficients for Compressible Air. Glenn L. Martin Engineering Report No. 3229. The Glenn L. Martin Co., Baltimore, Maryland, June 1949.
5. Andreopoulos, T. C., Chee, C. F., and Targoff, W. P., The Effect of Engine Locations on the Antisymmetric Flutter Mode. Air Force Technical Report No. 6353. Wright Air Development Center, Wright-Patterson Air Force Base, Ohio, August 1951. (CONFIDENTIAL report)
6. Wasserman, L. S., Aspect Ratio Corrections in Flutter Calculations. WADC Memorandum Report No. MCREXA5-4595-8-5. Wright Air Development Center, Wright-Patterson Air Force Base, Ohio, August 26, 1948.
7. Biot, M. A. and Boehnlein, G. T., Aerodynamic Theory of the Oscillating Wing of Finite Span. GALCIT Report No. 5 for the Army Air Forces. Guggenheim Aeronautical Laboratory at California Institute of Technology, Pasadena, California, 1942.
8. Reissner, E. and Stevens, J. E., Effect of Finite Span on the Airload Distributions for Oscillating Wings, II - Methods of Calculations and Examples of Application. NACA Technical Note No. 1195. National Advisory Committee for Aeronautics, Washington, D. C., October 1947.
9. Beals, V., and Targoff, W. P., Control Surface Oscillatory Coefficients Measured on Rectangular Wings of Low Aspect Ratio. WADC Technical Report 53-64. Wright Air Development Center, Wright-Patterson Air Force Base, Ohio, April 1953. (CONFIDENTIAL report)
10. Cunningham, H. J., and Brown, H. H., A Compilation of Experimental Flutter Information. NACA Research Memorandum L53K02a. National Advisory Committee for Aeronautics, Washington, D. C., January 11, 1954. (CONFIDENTIAL report)

- [REDACTED]
11. Flutter Section, Design and Test Results of High Speed Subsonic Flutter Model. Curtiss-Wright Corporation Report No. H-47-3. Curtiss-Wright Corporation, Columbus, Ohio, September 9, 1947. (RESTRICTED report)
 12. D'Ewart, B. B. and Ryken, J. M., Cantilever Wing Flutter Model Tests at Low and Transonic Speeds. WADC Technical Report 53-47. Wright Air Development Center, Wright-Patterson Air Force Base, Ohio, November 1954.
 13. Pratt, G. L., Experimental Flutter Investigation of a Thin Unswept Wing at Transonic Speeds. NACA Research Memorandum L55A18. National Advisory Committee for Aeronautics, Washington, D. C., April 4, 1955. (CONFIDENTIAL report)
 14. Lauten, William T., Jr. and Teitelbaum, J. M., Some Experiments on the Flutter of Wings with Sweepback in the Transonic Speed Range Utilizing Rocket-Propelled Vehicles. NACA Research Memorandum L50C03a. National Advisory Committee for Aeronautics, Washington, D. C., May 18, 1950. (CONFIDENTIAL report)
 15. Barnby, J. G., Cunningham, H. J., and Garrick, I.E., Study of Effects of Sweep on the Flutter of Cantilever Wings. NACA Technical Note 2121. National Advisory Committee for Aeronautics, Washington, D. C., June 1950. (CONFIDENTIAL report)
 16. Maier, H. G. and King, S. R., Special Progress Report The Critical Flutter Mach Number for 45° Sweptback Wings, Transonic Flutter Model Tests. C.A.L. Report No. 70. Cornell Aeronautical Laboratory, Inc., Buffalo, New York, January 1955. (CONFIDENTIAL report)
 17. King, S. R., Lightweight Flutter Models Using Stabilized Aluminum Foil. C.A.L. Report No. 68. Cornell Aeronautical Laboratory, Inc., Buffalo, New York, January 10, 1955.

[REDACTED]

APPENDIX I

DESIGN AND CONSTRUCTION DETAILS

A. Model Design

1. Basic Wing Models

At the outset of the program, it was realized that the design of a successful flutter model would be a difficult task due to the many problems associated with high speed flight. It was realized that the large size of the models would tend to accentuate the undesirable effects of random energy present in the air stream and only estimates, based on previous experience with low speed aeroelastic models, could be made as to its severity. The difficulties associated with testing flexible models to Mach numbers close to, and beyond, the critical Mach number of the airfoil section were not known. The effects of compressibility, which were to be part of the results of the tests, had to be pre-estimated so that proper model design rigidities could be approximated to insure flutter close to the required Mach numbers. Due to the nature of many of these problems, the final design of the flutter models was reached only after a program of design, test, and re-evaluation of a series of flutter models.

At the beginning of the program, three basic types of flutter model construction were considered:

- (a) Remotely-controlled continuous variation of the wing sectional properties.
- (b) A separate model for each test point in which the sectional properties were fixed.
- (c) Manual variation of the wing sectional properties by some suitable means.

Method (a) is a very desirable type of construction as the testing technique involved would be very simple and the construction costs would be greatly reduced since relatively few models would be constructed. However, a feasible design, using this type of construction, and incorporating the mass and elastic properties required for an aeroelastic model, could not be readily found.

Method (b) at this state in the program was not desirable as knowledge of the parameters required to give the desired results were essentially the results sought from the present research program. Thus, to construct models with fixed parameters arrived at by guessing the results of

████████████████████

the flutter program, was considered to be unwise. Therefore, method (c), which was a compromise of methods (a) and (b), was considered to be the best and most economical means of obtaining the desired results.

The model designed and constructed using method (c) is shown in Figs. 54, 55, and 58. The airfoil section chosen for this model was an 8% symmetrical section, NACA Series Number 65-008, which has a critical Mach number of approximately 0.80. The model was constructed of two basic units; (1) a wing framework to specify the spanwise and chordwise wing contour, and (2) a skin unit to provide the required torsional and bending rigidities. When the two basic units were joined together to form the complete wing structure, a torque box was obtained bounded on two sides by the skin units and on the other two sides by the leading and trailing edge sections. The wing frame consisted of a dural structure composed of eight ribs and two spars to which the leading and trailing edges were attached by rivets. The leading edge was a hollow structure of dural formed to the airfoil contour. The trailing edge was a composite structure of a balsa core and dural skins which were bonded together. The trailing edge section also included sufficient lead ballast weight (Fig. 54) distributed along the span to provide the correct mass parameters. The skin units shown in Fig. 56 were a composite structure of dural and balsa formed to the outside contour of the wing. Narrow doubler strips were spot welded around the periphery of the skin units, and also at the rib stations to provide a thicker section so that the screws used to fasten the two units together could be countersunk. The large unsupported skin lengths in this design demanded that some means of stabilizing the dural sheet be provided. Since the skins had to be easily removable, the stabilizing material could not connect the two sheets together as would be done in the ideal situation. It was experimentally verified that a one-half inch thick balsa sheet bonded to the inside of the skin between rib stations (Fig. 56), would effectively stabilize the skin units and prevent buckling when loads, larger than those expected during tunnel tests, were applied. Skin units using dural sheets of thicknesses of 0.012, 0.016, 0.020, 0.025, and 0.032 in. were constructed to provide the various rigidities required. The lead strips shown bonded to the balsa skin backing (Fig. 56) were used to ballast the various skin panels to provide the same mass properties as those of the 0.032 panels.

The root fitting shown in Fig. 57, was constructed of steel. The tapered shaft was welded to the steel box structure which fitted into the torque box section of the wing. Nut plates riveted to the inside of the root fitting received the screws fastening the skin to the root fitting.

An assembled model mounted in the wind tunnel ready for flutter testing is shown in Fig. 58.

Flutter tests of two wings of this design were unsuccessful from the viewpoint of program accomplishment as both models were lost for reasons other than flutter. However, the failures of the models pointed out the unforeseeable

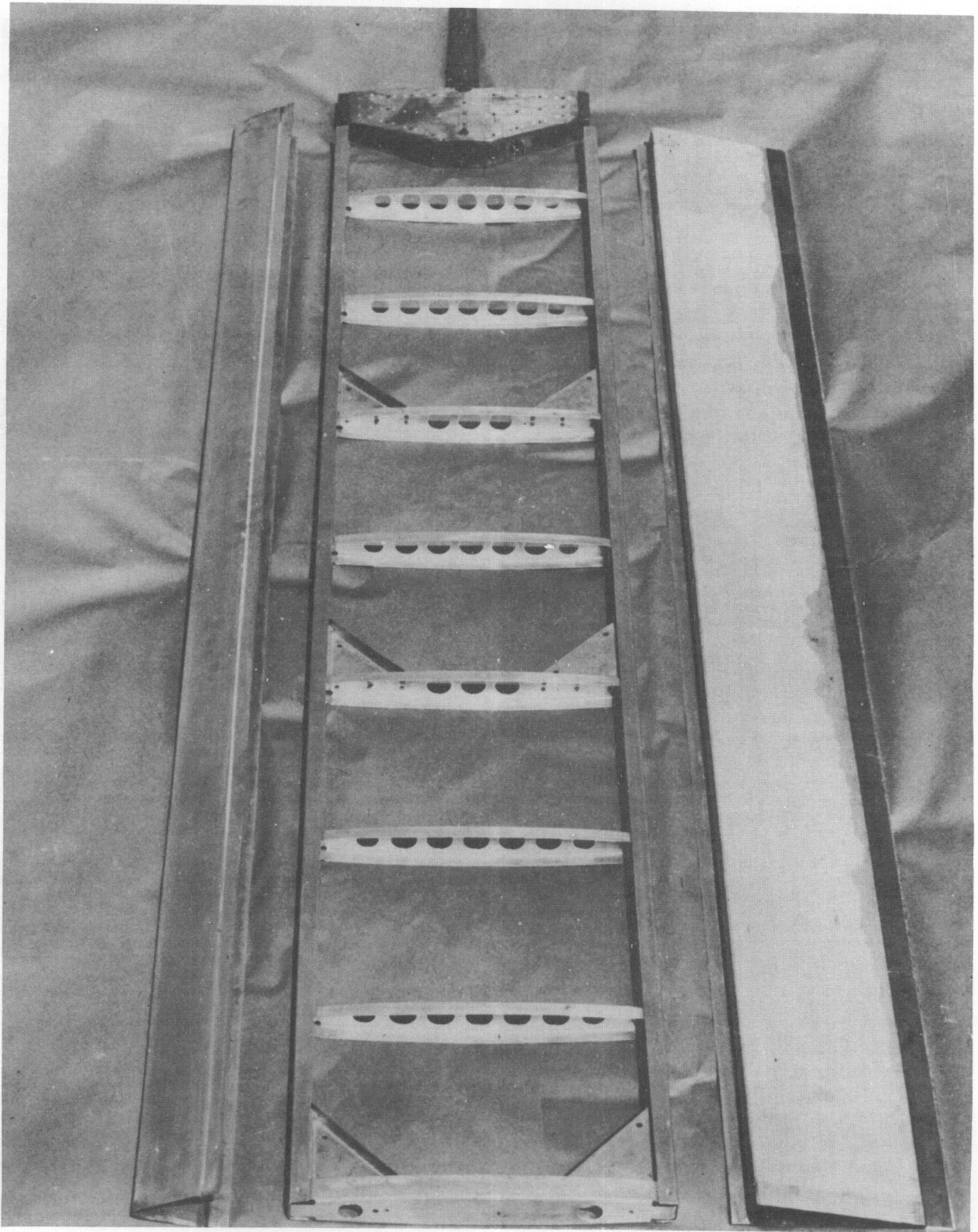


FIGURE 54 AN EXPLODED VIEW OF THE WING FRAMEWORK
OF A HIGH SPEED FLUTTER MODEL

~~CONFIDENTIAL~~

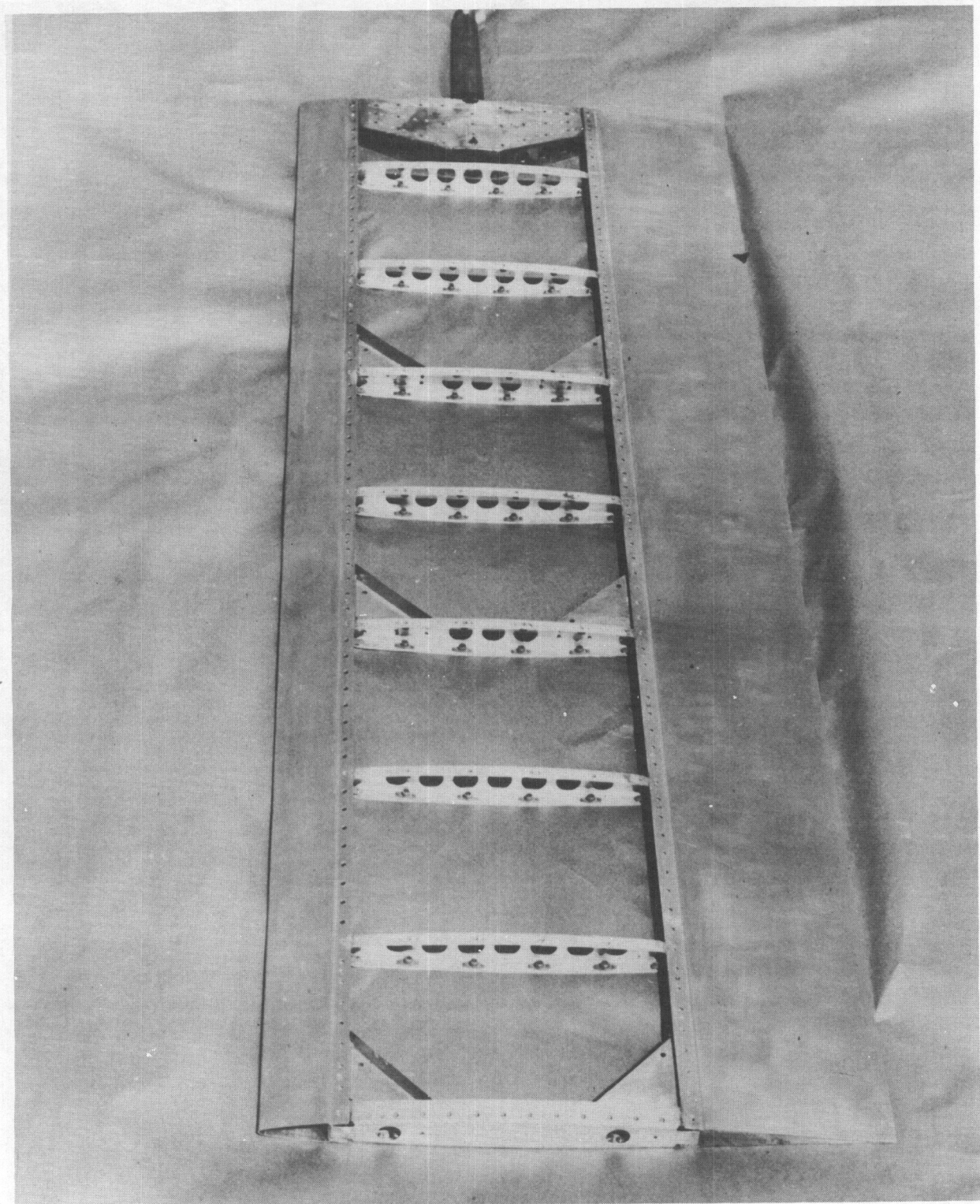


FIGURE 55 AN ASSEMBLED WING FRAMEWORK OF A HIGH SPEED FLUTTER MODEL

WADC TR 55-334

~~CONFIDENTIAL~~

WADC TR 55-334

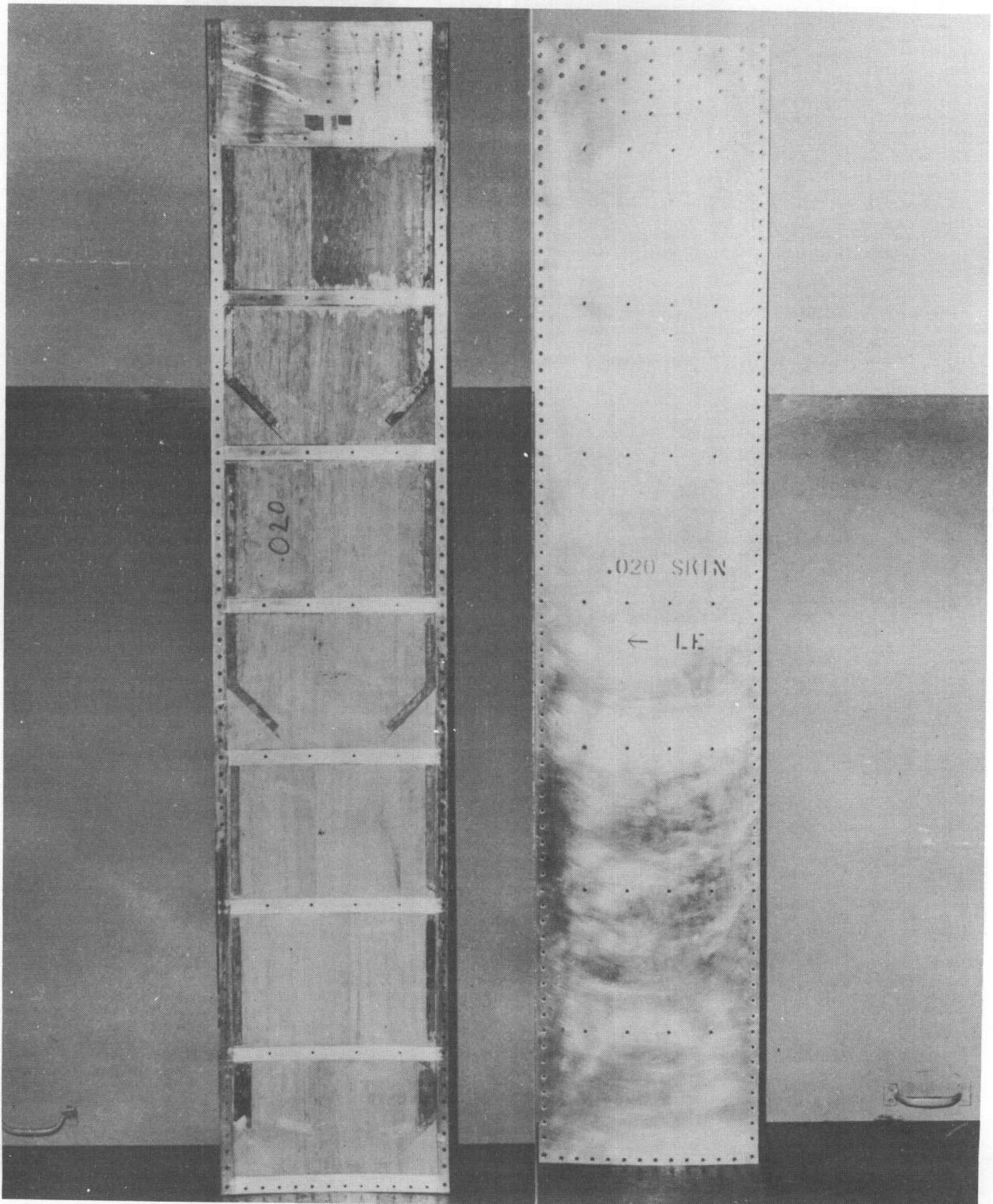


FIGURE 56 INTERCHANGEABLE SKIN UNITS OF A HIGH SPEED FLUTTER MODEL

~~CONFIDENTIAL~~

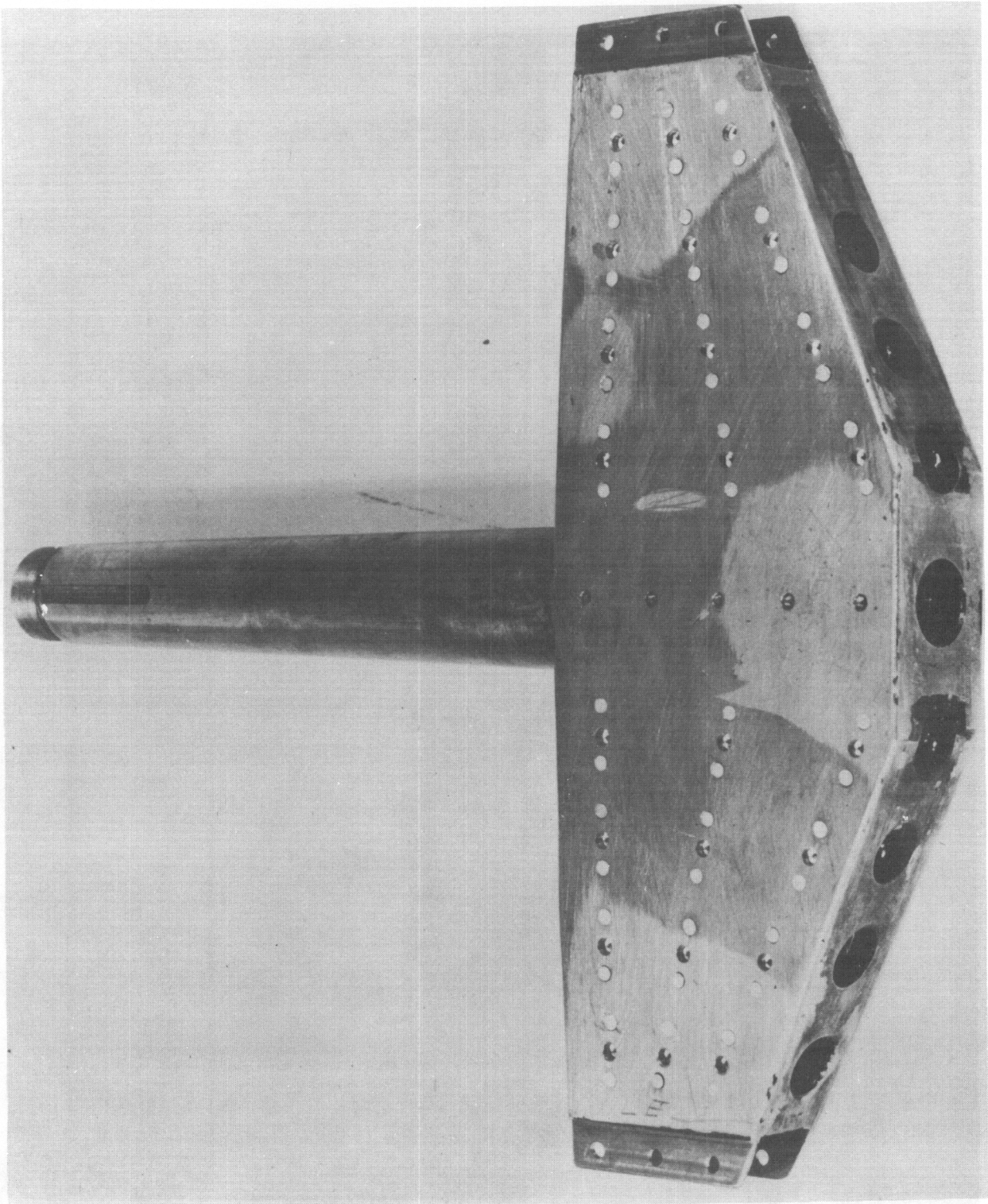


FIGURE 57 ROOT FITTING FOR THE FLUTTER MODELS

WADC TR 55-334

~~CONFIDENTIAL~~

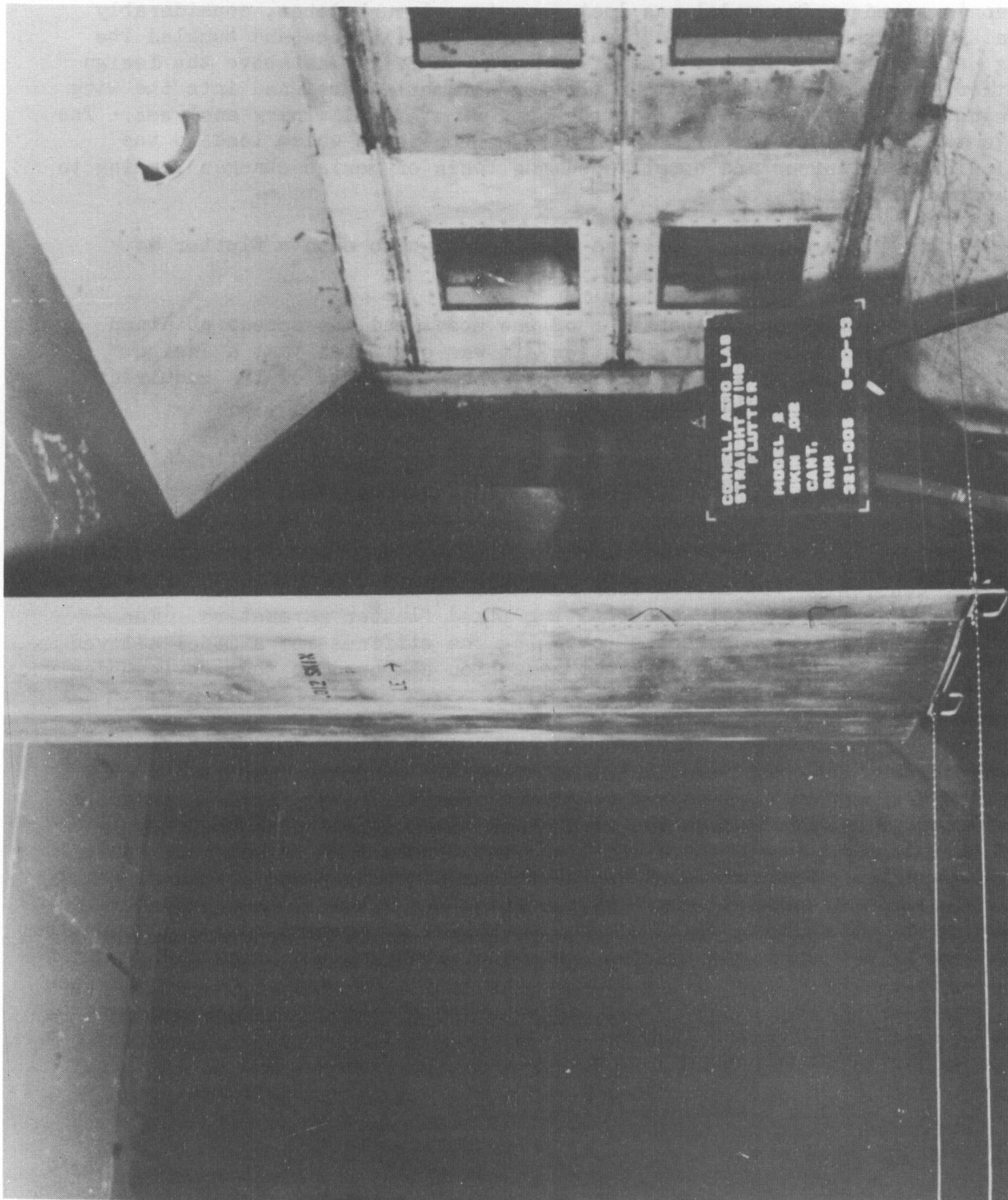


FIGURE 58 AN ASSEMBLED HIGH SPEED FLUTTER MODEL MOUNTED IN THE WIND TUNNEL

[REDACTED]

faults of this type of design and gave more insight as to what could be expected when testing large flexible models in the wind tunnel at high subsonic speeds. One model was lost when tunnel turbulence, considerably greater than had been expected, caused large oscillations and buckled the wing near the root. At the time of failure, the wing was above the design flutter speed indicating that the flutter parameters designed into the wing were not correctly predicted from the approximate preliminary analyses. The above two facts were the primary results of the tests which lead to the following conclusions and established the basis of design changes leading to a successful flutter model:

- (a) The design rigidities were too high to obtain flutter at the design speeds.
- (b) Based on the behavior of the model and the speeds obtained without inducing flutter, it was estimated that a design based on a calculated flutter speed 10% below the required speed would yield a satisfactory model design.
- (c) It is insufficient to design for proper elastic rigidity only, as the failure due to buffeting indicated a design, based on a stress-deflection relationship instead of a stress-load criteria, is required to prevent this type of failure.

Conclusion (b) having been reached, it was decided that it was now reasonable to design a model incorporating fixed flutter parameters. The elimination of the requirement of changing the stiffness of a model allowed realization of a considerable weight reduction compared to the previous design.

The buckling failure of the previous model design, caused by large oscillations due to tunnel turbulence, required that the new model design, if it was to be successful, must allow considerably larger deflections of the model before the critical stress level was reached. Therefore, in order to obtain more flexibility from the models and thus prevent failure due to buffeting in the tunnel, the airfoil was reduced to a 6% symmetrical airfoil which moved the skins in toward the neutral axis and allowed a much larger deflection for an equal stress. Furthermore, the skins of the torque box in the re-designed model could now be stabilized by means of a solid composite Styrofoam-balsa core since the requirement of changing the skins had been eliminated. A thin sheet of balsa was used to present a good bonding surface for the skin-core bond. The bonding agent used for all bonding was a Recorcin formaldehyde cement called Penacolite G11-32. Before bonding the core to the dural skins, the metal was primed with air-drying Bostik #1007 to provide good adhesive properties between the dural skin and the bonding agent. The lead ballast weights used to equalize the mass properties of all wings were bonded into the Styrofoam core. A picture showing the make-up of a complete core is given in Fig. 59. Figure 60 shows a completed core with a large lead ballast weight attached to the leading edge. The need for this ballast weight

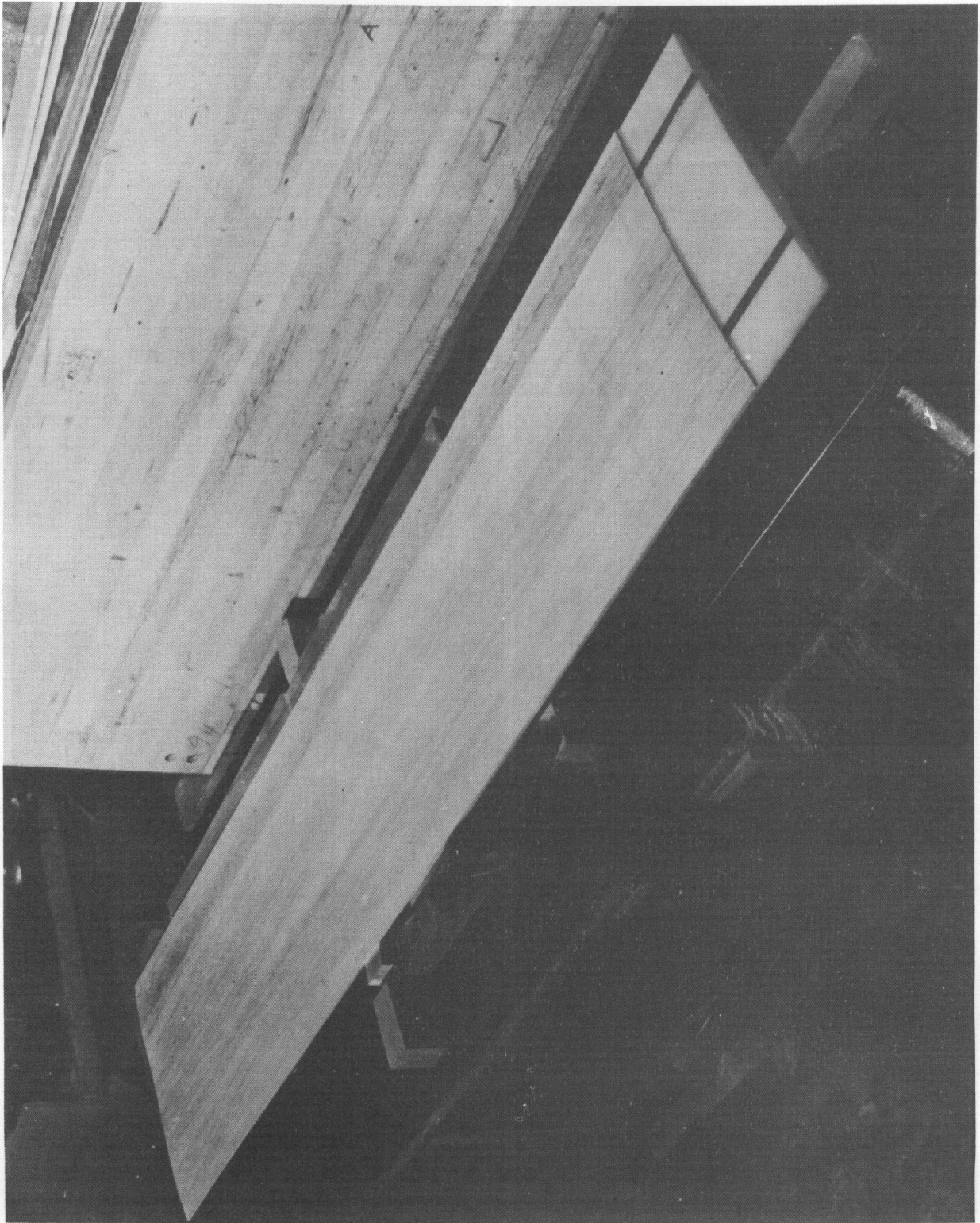


FIGURE 59 AN EXPLODED VIEW OF A COMPOSITE STYROFOAM-BALSA CORE

FIGURE 59 AN EXPLODED VIEW OF A COMPOSITE STYROFOAM-BALSA CORE

CONFIDENTIAL

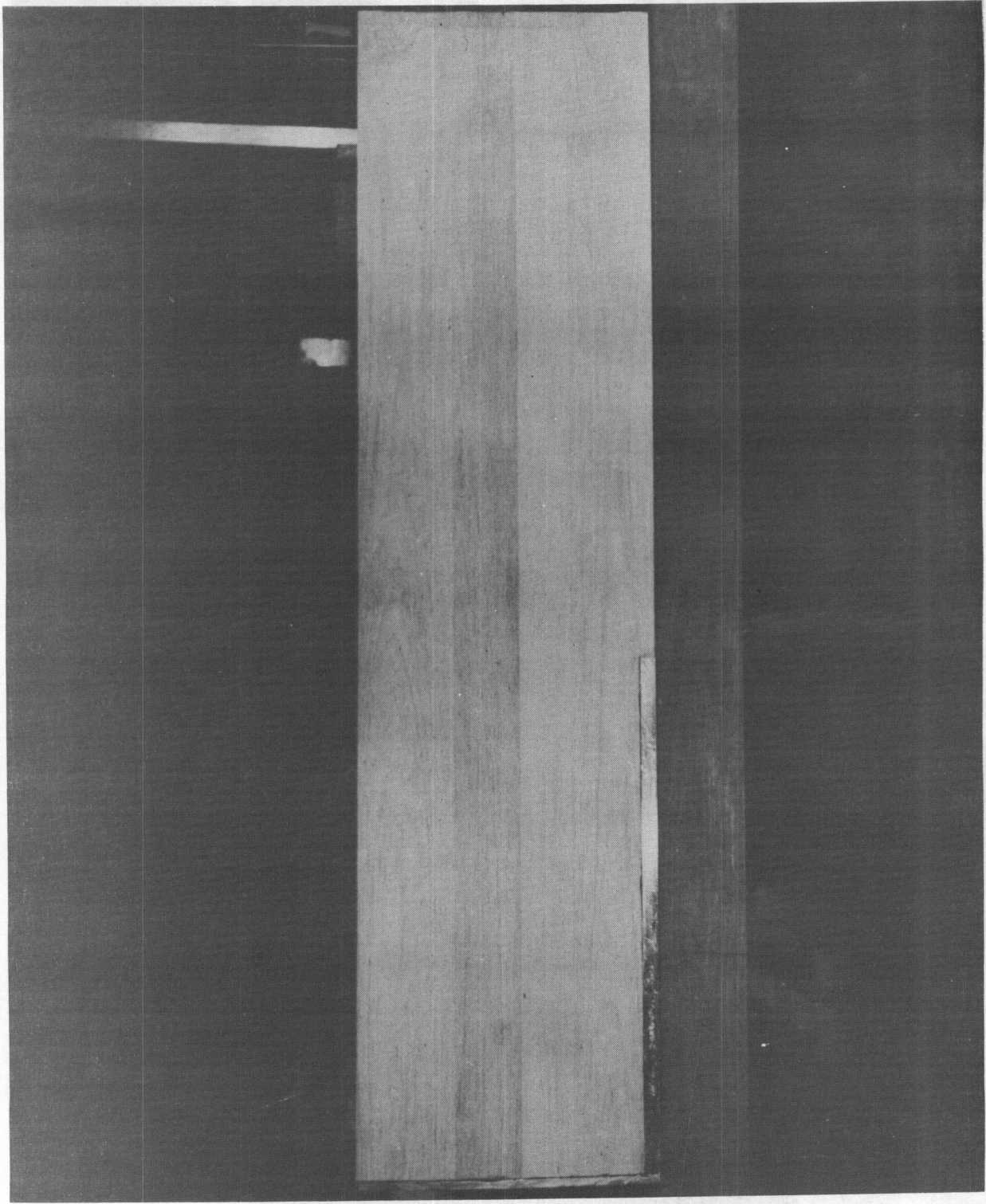


FIGURE 60 A COMPLETED CORE

CONFIDENTIAL

[REDACTED]

is fully discussed in the section describing the flutter lock but briefly it was placed in the wing to correctly ballast the wing against flutter in the modes present when the flutter lock was actuated.

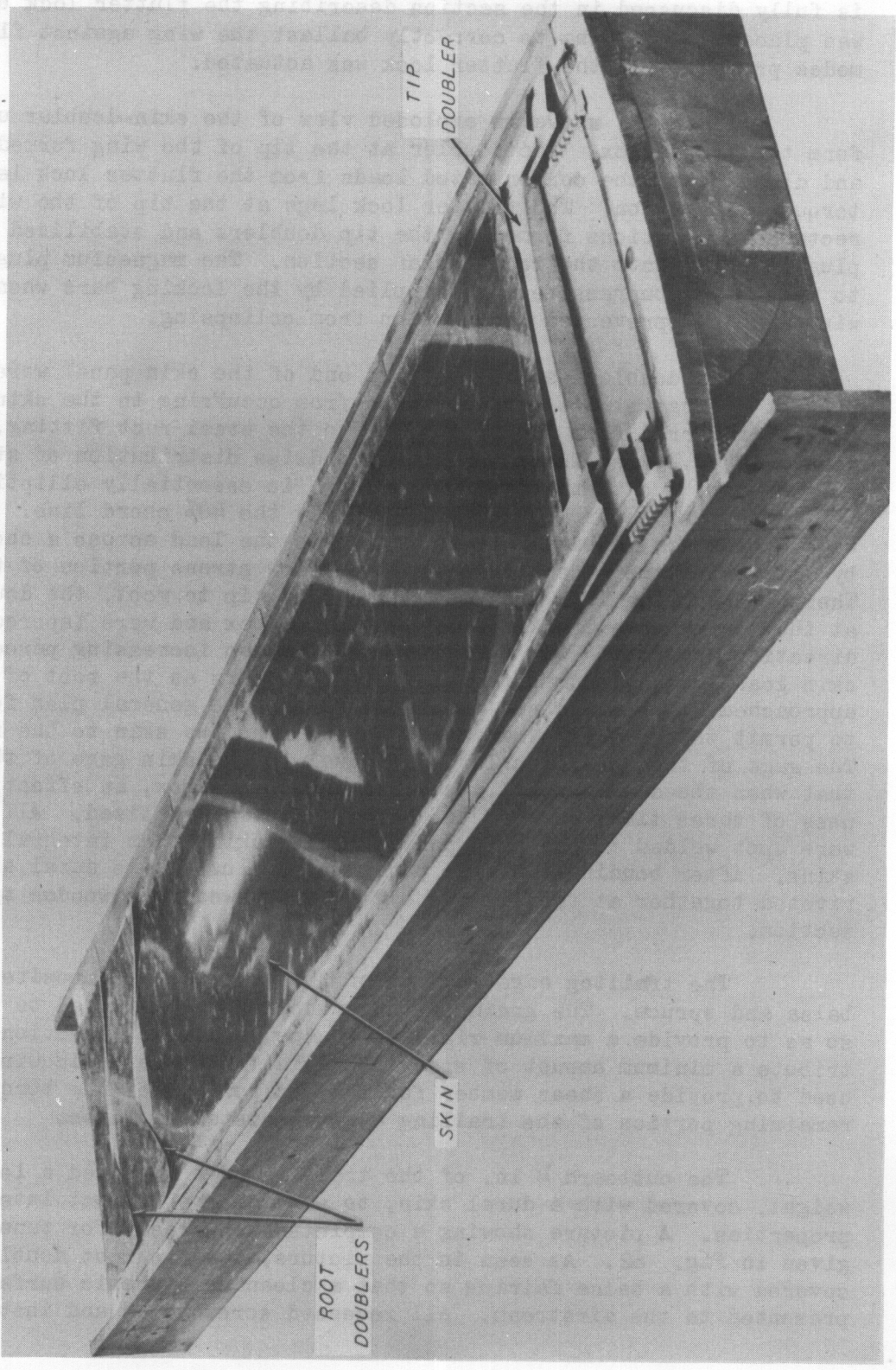
Figure 61 shows an exploded view of the skin-doubler unit used to form the torque box. The doubler at the tip of the wing formed the end rib and distributed the concentrated loads from the flutter lock legs into the torque box section. The flutter lock legs at the tip of the wing were hollow rectangular sections formed by the tip doublers and stabilized by a magnesium plug inserted into the rectangular section. The magnesium plugs were inserted to react the compressive loads applied by the locking bars when clamping the wing and thus prevented the section from collapsing.

The doublers at the inboard end of the skin panel were designed to prevent a large stress concentration from occurring in the skin as the loads were transferred from the torque box to the steel root fitting. This was accomplished by realizing that the chordwise distribution of stress in the skin panels, due to the airfoil contour, is essentially elliptic with the maximum stress occurring at approximately the 40% chord line. The doublers were, therefore, designed to redistribute the load across a chordwise section by increasing the skin thickness at the low stress portion of the torque box. Therefore, moving in a spanwise direction, tip to root, the doublers started at the chordwise extremities of the torque box and were tapered in a chordwise direction toward the 40% chord line so that an increasing percentage of the skin loads would be transferred to the doublers as the root of the wing was approached. Two staggered doublers of the same general plan form were used to permit this orderly transfer of loads from the skin to the root fitting. The gage of the dural doublers was equal to the skin gage of the model so that when the doublers fully covered the torque box, an effective skin thickness of three times that of the normal skin was realized. All doubler units were spot welded to the skin panels, thus making them integral parts of the skins. After bonding the skin panels to the core, the dural sheets were riveted together at the leading edge and screwed to a wooden trailing edge section.

The trailing edge section of the wing was a composite structure of balsa and spruce. The grain of these woods being oriented to run chordwise so as to provide a maximum rigidity in the chordwise direction, but to contribute a minimum amount of spanwise rigidity to the basic wing. Spruce was used to provide a shear member for the aft portion of the torque box and the remaining portion of the trailing edge consisted of balsa.

The outboard 1/4 in. of the trailing edge included a lead ballast weight, covered with a dural skin, to provide the correct integrated mass properties. A picture showing a completed wing ready for tunnel testing is given in Fig. 62. As seen in the picture, the two root doublers have been covered with a balsa fairing so that a clean aerodynamic surface would be presented to the airstream. All recessed screw holes and instrumentation

CONFIDENTIAL



CONFIDENTIAL

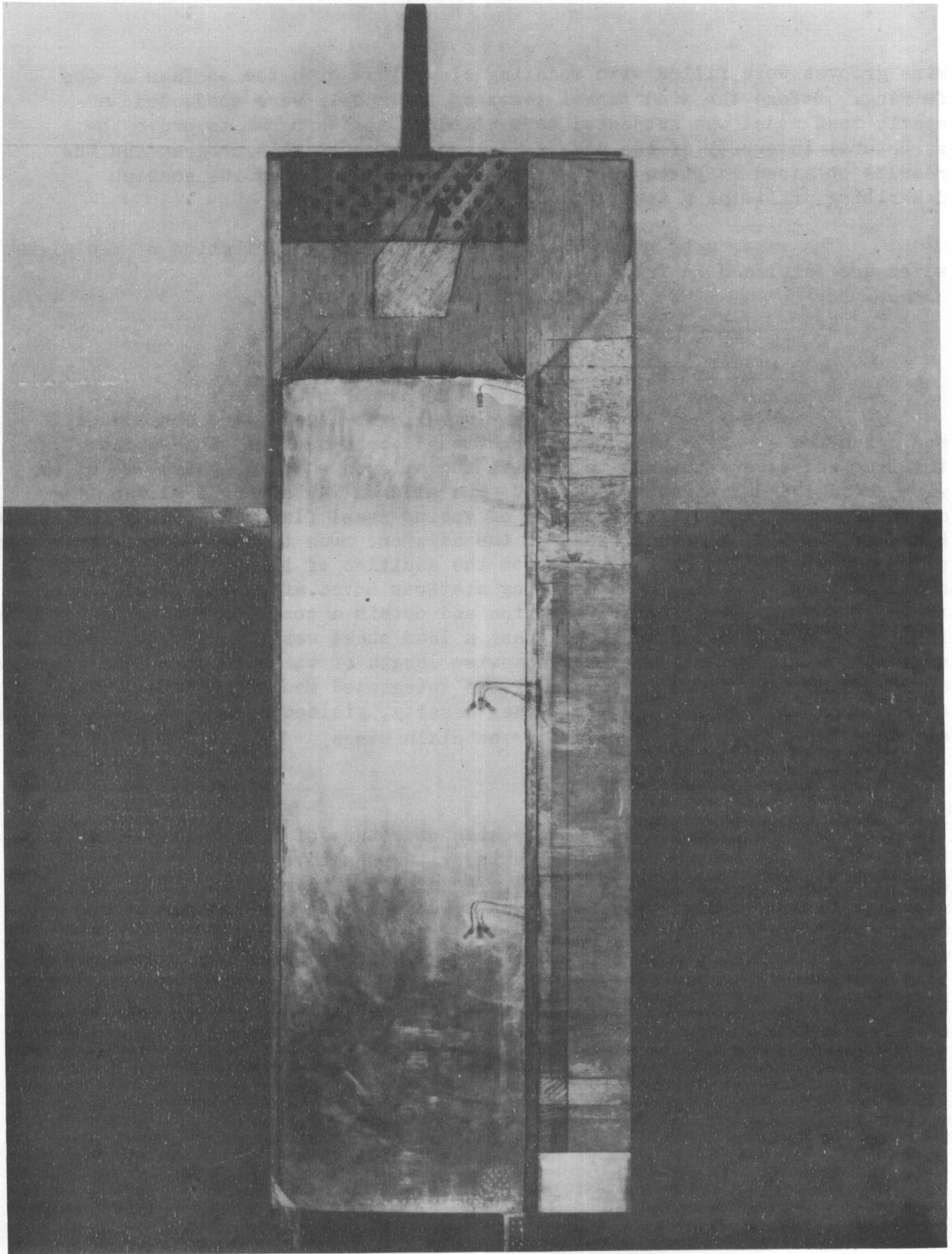


FIGURE 62 A COMPLETED MODEL READY FOR INSTALLATION IN THE TUNNEL

[REDACTED]

wire grooves were filled with modeling clay flush with the surface of the fairing. Before the wind tunnel tests of the models were conducted, a static test model was subjected to a rigorous test program to prove the structural integrity of the model. A description of this program and the results obtained is given in the body of the report under the section describing preliminary tests.

The mass, unbalance, and moment of inertia distribution of the plain wings are tabulated in Table IX, Appendix II.

2. Wing-Aileron Models

(a) Wing Construction

The wings used for the wing-aileron models were obtained by modifying the straight plain wings previously constructed. The wooden trailing edges were cut out to receive the aileron which occupied 20% of the wing chord and 50% of the wing span. The aileron was attached to the wing at three spanwise stations by means of spring steel flexure pivots which provided hinge points at the leading edge of the aileron. Due to the increase in weight at the trailing edge of the wing from the addition of the aileron and attachment fittings, the c.g. of these wing stations moved aft. Therefore, to move the c.g. back to its original position and obtain a constant percentage increase in all the integrated mass properties, a lead sheet was bonded to the leading edge of the wing over the entire spanwise length of the aileron. This produced approximately a 4.5% increase in all the integrated mass properties and, when a comparable change was made in tunnel density, yielded results at the same wing-air mass ratio, μ ; as reported for the plain wings.

(b) Aileron Construction

The aileron was a composite structure of a cellulose acetate (Strux) core and a 0.004 in. dural skin, with associated dural fittings to attach the spring and flexure pivots. An exploded view of the core and fittings is presented in Fig. 63. The 0.004 in. skin was bonded to the Strux core with an epoxy resin (Hysol). In addition, a 0.004 in. doubler was bonded around the nose and fittings to evenly transfer the concentrated loads from the springs and flexure pivots to the skin. A completed aileron is shown in Fig. 64. The non-dimensional mass parameters of the aileron obtained with this construction are:

Ratio of aileron weight to wing weight
per foot of span = 0.74

Aileron radius of gyration in terms of
aileron chord = 0.44

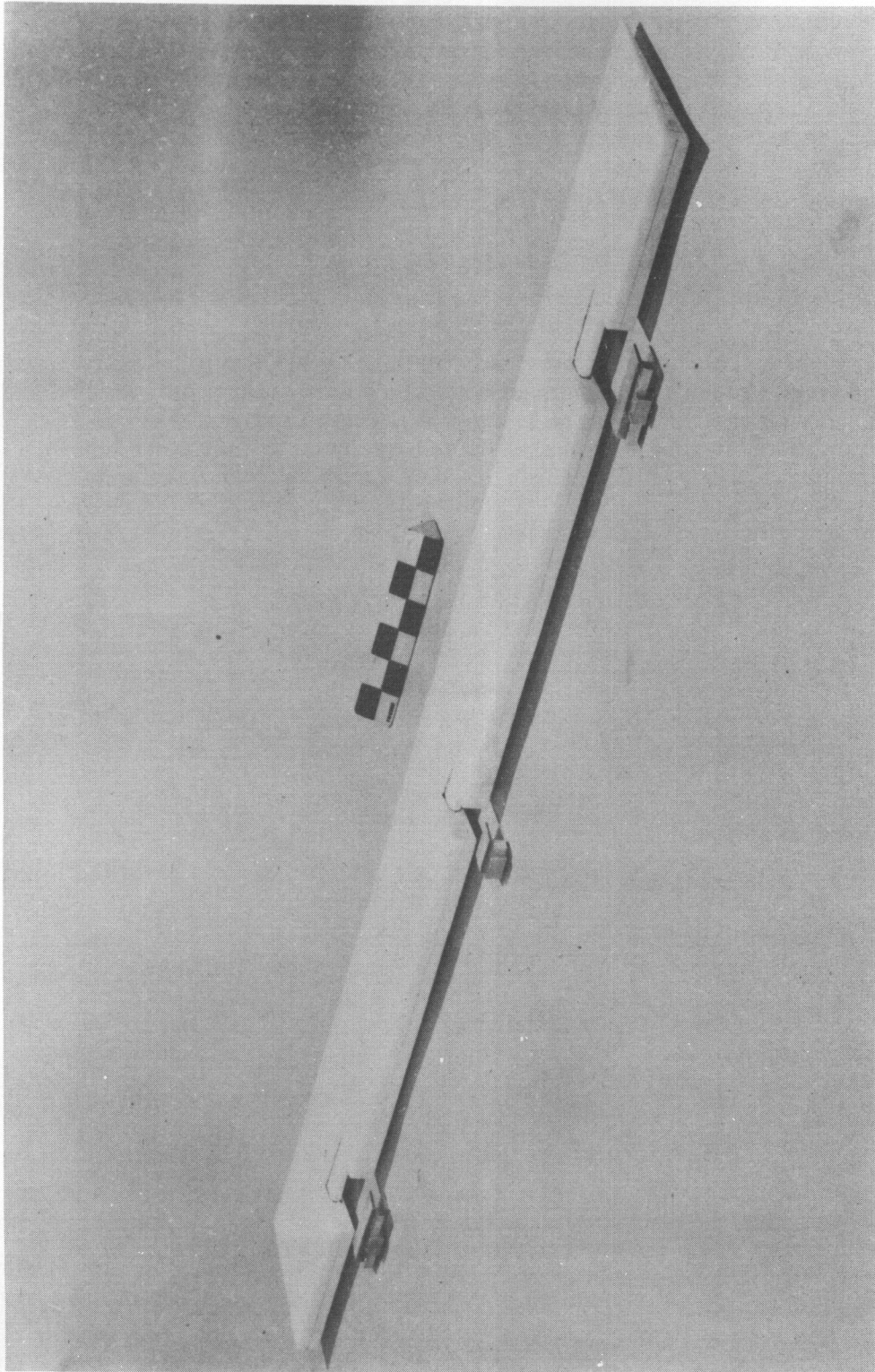


FIGURE 63 AN EXPLODED VIEW OF THE AILERON

~~CONFIDENTIAL~~

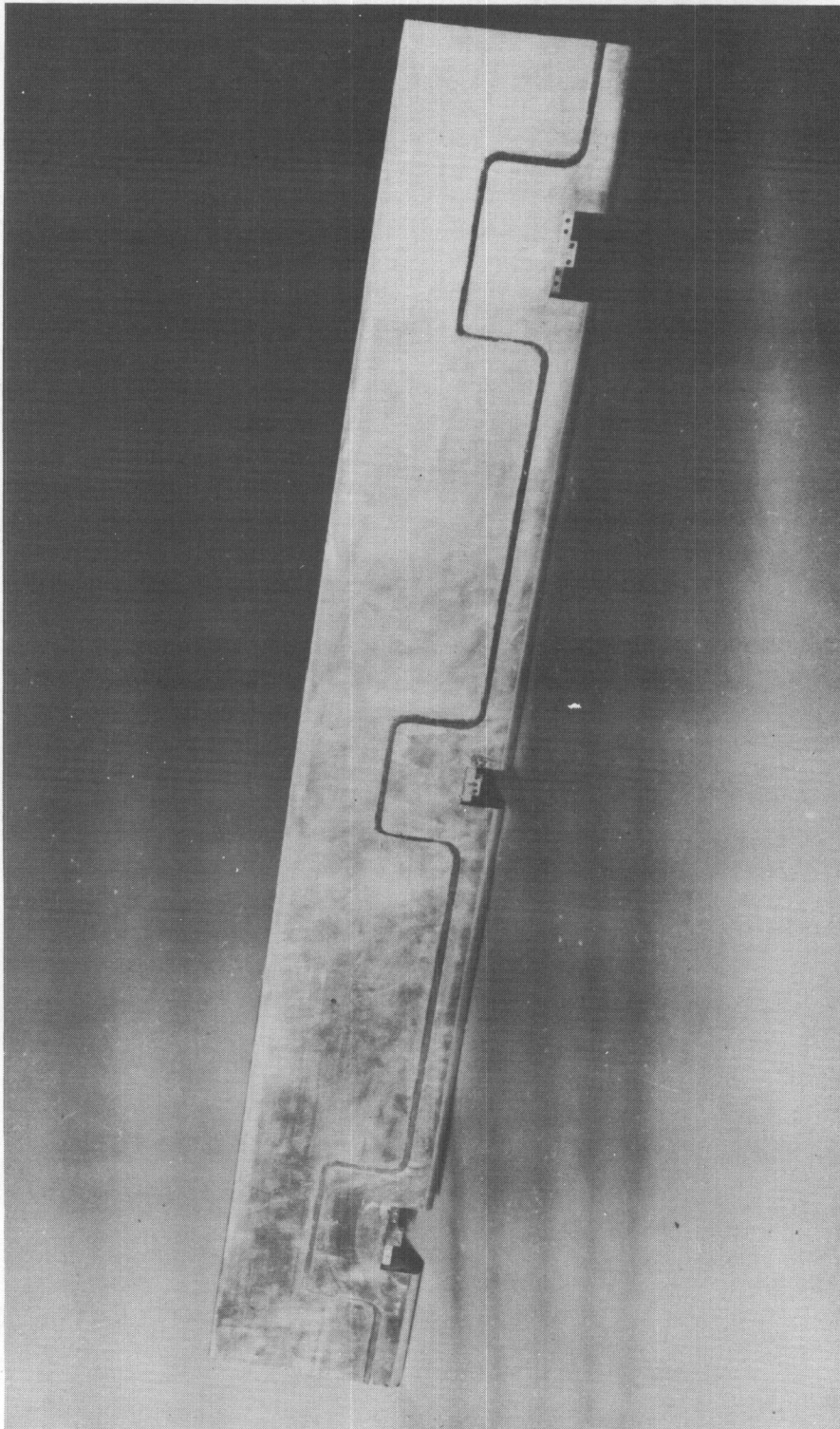


FIGURE 64 A COMPLETE AILERON

~~CONFIDENTIAL~~

[REDACTED]

Aileron c.g. location in terms of aileron chord = .0.33

The weight distribution for the wing-aileron models is given in Table X, Appendix II.

(c) Aileron Frequency System

The rotational frequency of the aileron was controlled by springs which could be changed to give an incremental frequency change. Sets of two springs were used at two flexure points to give the desired frequency. A frequency range between 15 cps and 70 cps was obtained using different combinations of springs. Figure 65 presents a photograph showing the details of one of the flexure-spring mountings. The cover plates, which normally present a smooth contour to the airstream, are removed in this photograph so that the details of the mounting can be seen. The strain gages, mounted on one of the flexures, were used to measure the relative motion between the aileron and wing. Figure 66 shows an aileron installed in a wing with the cover plates in place.

B. Suspension System

The form of the suspension system was dictated primarily by the requirement that a lightweight fuselage with a large pitching moment of inertia be incorporated without introducing the low natural vibratory frequencies which a full-size airplane fuselage also displays. The suspension system was located in a plane parallel to and slightly above the wind tunnel ceiling. The structure designed to meet the above requirements is schematically presented in Fig. 67 for the various types of arrangements used. Figure 68 is a photograph showing all the basic components of the suspension system connected together to form the symmetric end conditions. The suspension system shown in Fig. 68 is basically the same as reported in Ref. 1.

1. Symmetric Root Conditions

In the schematic diagram of Fig. 67, the dashed areas represent fixed structure of the wind tunnel ceiling. The model extends into the paper in a plane perpendicular to the linkage labeled "C". Member "A" is the main load-carrying member of the four-bar linkage and was mounted in large double-row bearings at the fixed end, and carried a table "B" at the free end. The function of member "A" was to support the model, provide the translational degree of freedom by rotating in its bearings, and resist the root aerodynamic and inertial bending moment of the model wings. A pitch lever arm, "D", was fixed to the root fitting of the wing by intermediate structure when the suspension was connected for the symmetric configuration. Arms "E" and "F" provided the fuselage static unbalance and pitching moment of inertia respectively.

CONFIDENTIAL

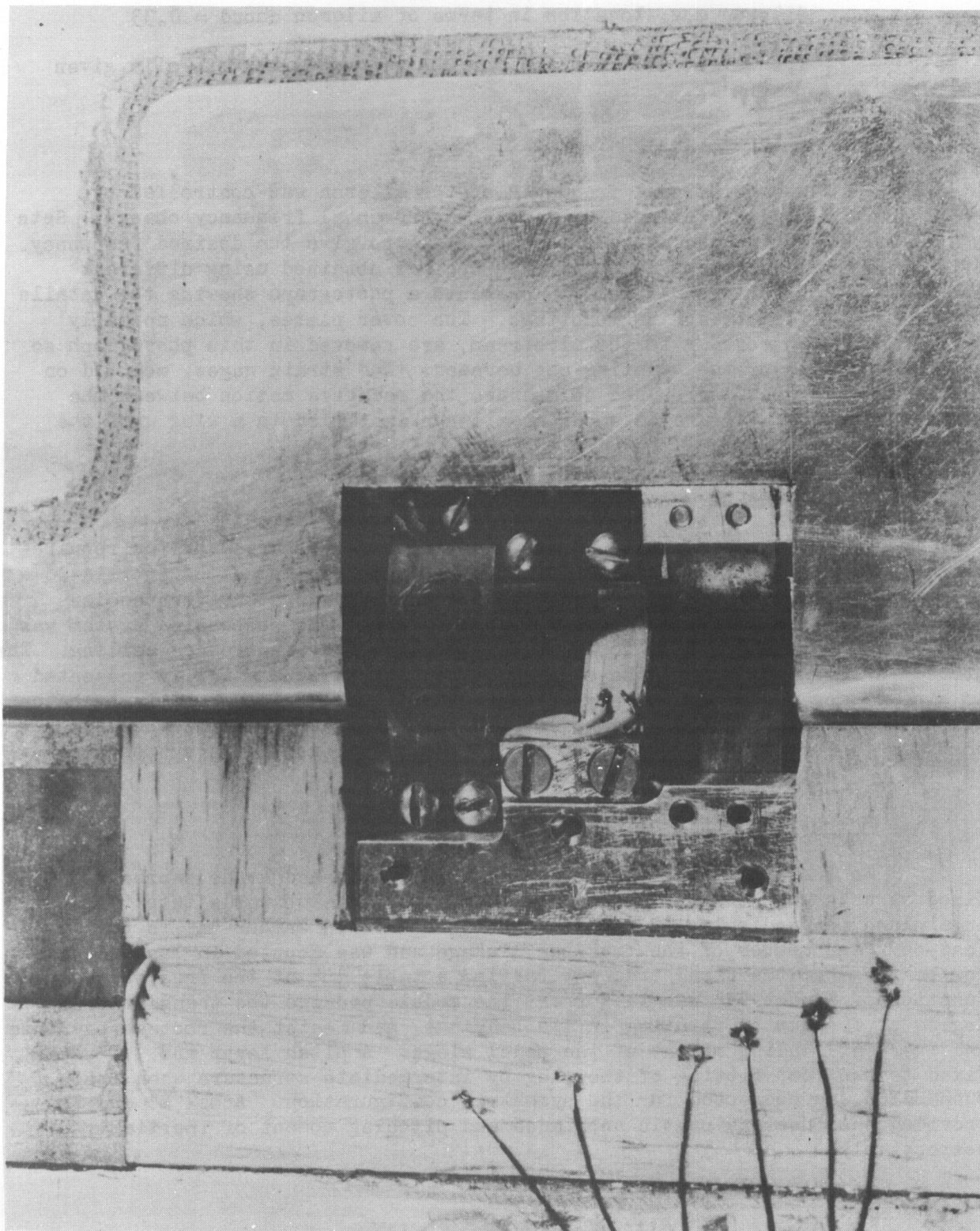


FIGURE 65 DETAILS OF AILERON SPRINGS AND FLEXURE PIVOT

WADC TR 55-334

102

CONFIDENTIAL

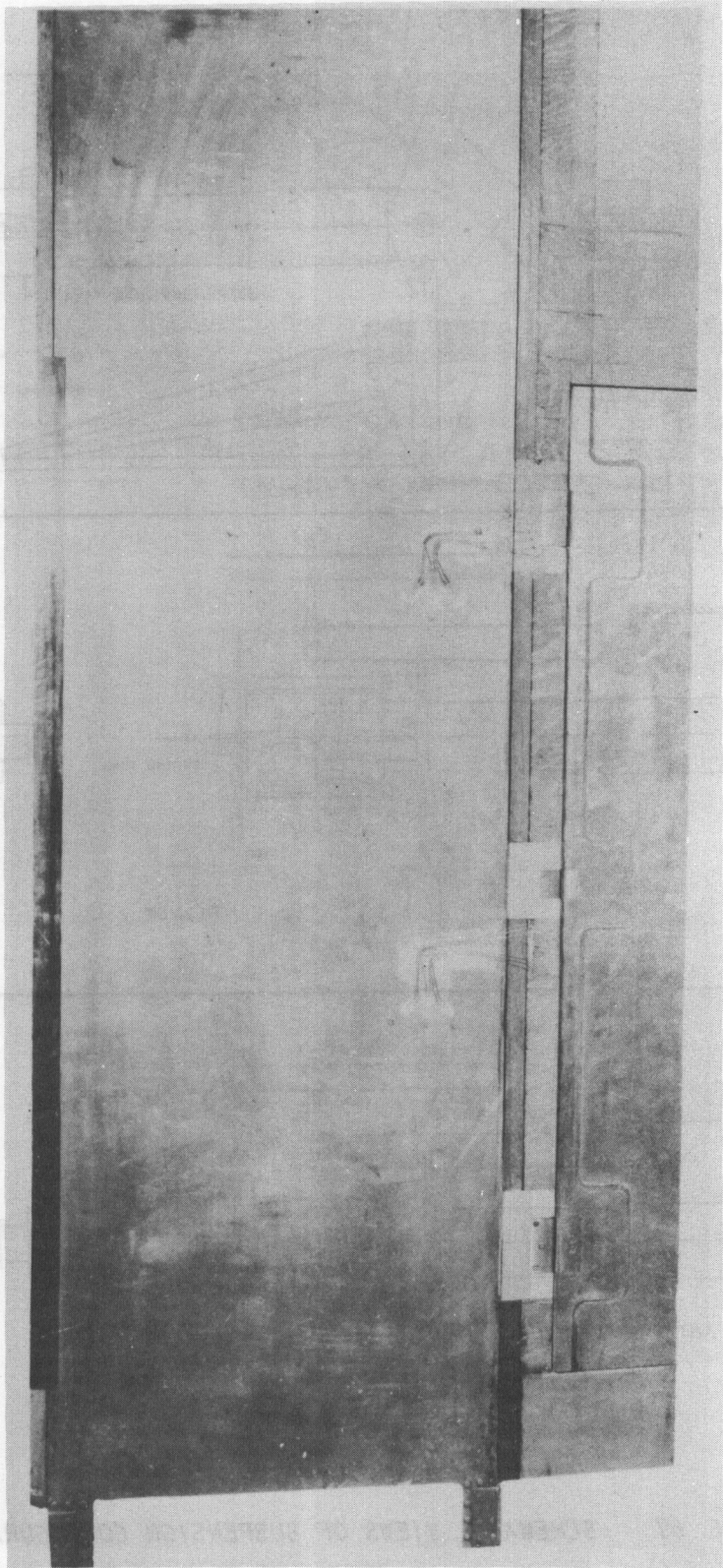


FIGURE 66 A WING-AILERON MODEL

WADC TR 55-334

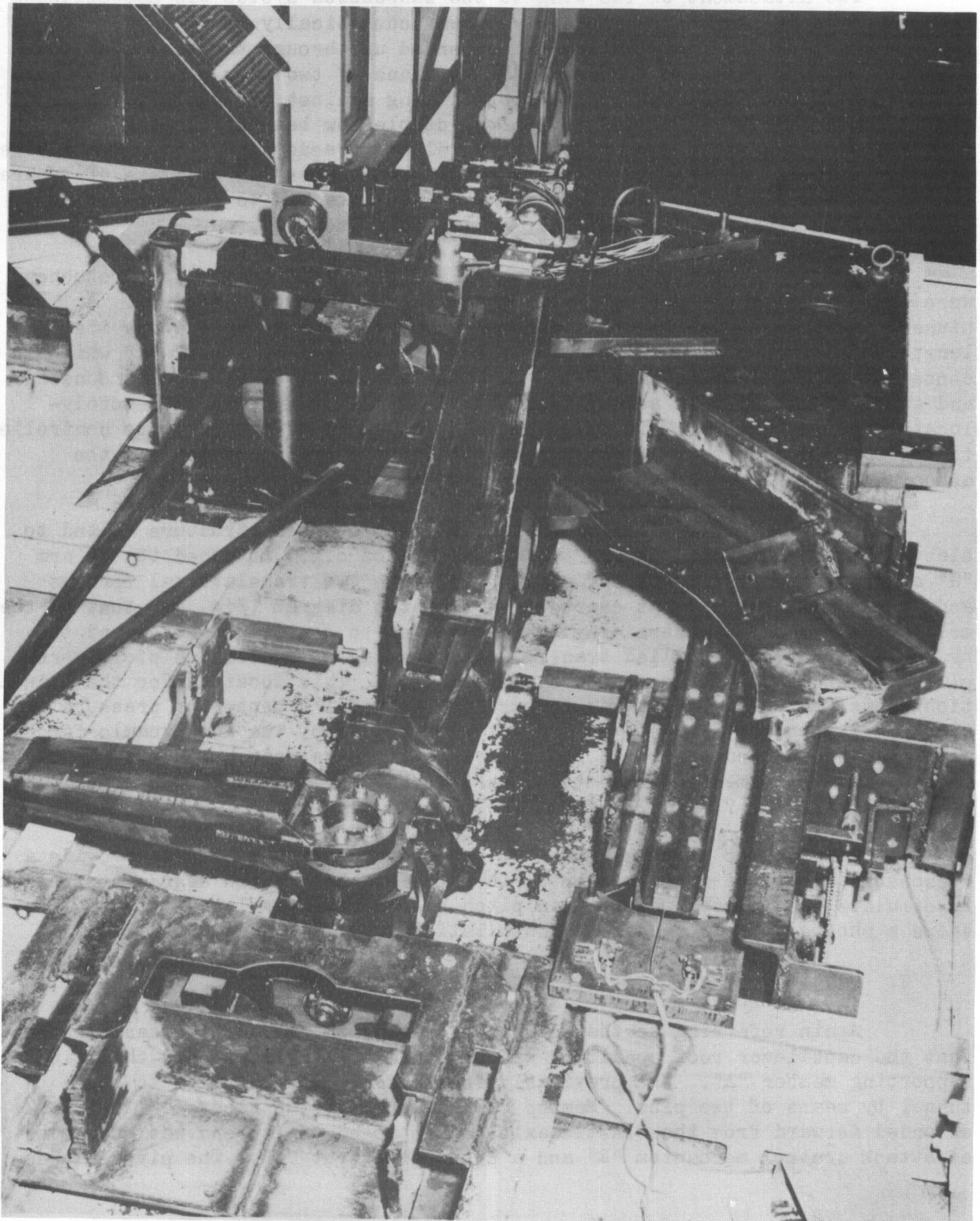


FIGURE 68 PICTURE OF BASIC SUSPENSION SYSTEM

[REDACTED]

The attachment of the wing to the suspension system was accomplished by means of a machined steel assembly shown schematically in Fig. 69. The tapered shaft of the root fitting "L" extended up through the bottom of the assembly and was fastened to sleeve "M" by means of two keys placed 90° apart and also by a nut which forced the root fitting against the matching taper of "M". Sleeve "M" was supported by the two double row bearings labeled "N", thus allowing the wing, root fitting, and sleeve freedom in pitch. The sleeve was also attached to the pitch lever arm "D" and member "G" by means of tapered bushings and bolts. The bearing casing "P" was attached to the supporting member "A" by means of the bearings "R" and roll lock "Q".

The angle of attack of the model and the rigid body pitch frequency were controlled by the spring system shown schematically in Fig. 67. A pinned-pinned beam, labeled "H", had one support point movable along its length which thus changed the spring constant realized by member "J" which is connected to the inertial arm "F". Both the variation of the spring constant and angle of attack were accomplished by electrical means from a remotely-located control panel. This setup allowed the angle of attack to be controlled to 1/1000th of a degree. A photograph showing the spring system and the associated electrical drive motors is presented in Fig. 70.

Member "G" (see Fig. 67 or Fig. 69) was a steel structure bolted to sleeve "M" and extended forward to the suspension c.g. Attached to the arm "G" at the suspension center of gravity were the two translational springs and a hydraulic damper. It can be seen from the diagram (Fig. 67) that as the model translated the restraining springs tended to center the model and the hydraulic strut "K" supplied translational damping. Translation stops were placed to contact the arm at the suspension c.g. This location for the translation stops was chosen as it was forward of the model's center of pressure and, therefore, when the arm came in contact with the stop, the aerodynamic forces developed would tend to rotate the wing into the airstream. Photographs showing the relative placement of the stops, springs, damper, and other equipment are presented in Figs. 71 and 72.

A hydraulic strut attached to the inertia arm was used to provide a reasonable amount of viscous damping in the rigid body pitch degree of freedom to simulate the inherent damping in pitch of a normal airplane. Figure 73 shows a photograph of the damper installation.

2. Cantilever End Condition

Again referring to the schematic drawing in Fig. 67, it can be seen that the cantilever root condition was obtained by utilizing only the main supporting member "A". The previously free end of "A" was fixed to the tunnel by means of two pins. Member "D" attached to the sleeve "M" (Fig. 67) extended forward from the elastic axis and attached to its end was an angle of attack control mechanism "E" and a pneumatic strut "F". The pivoted beam

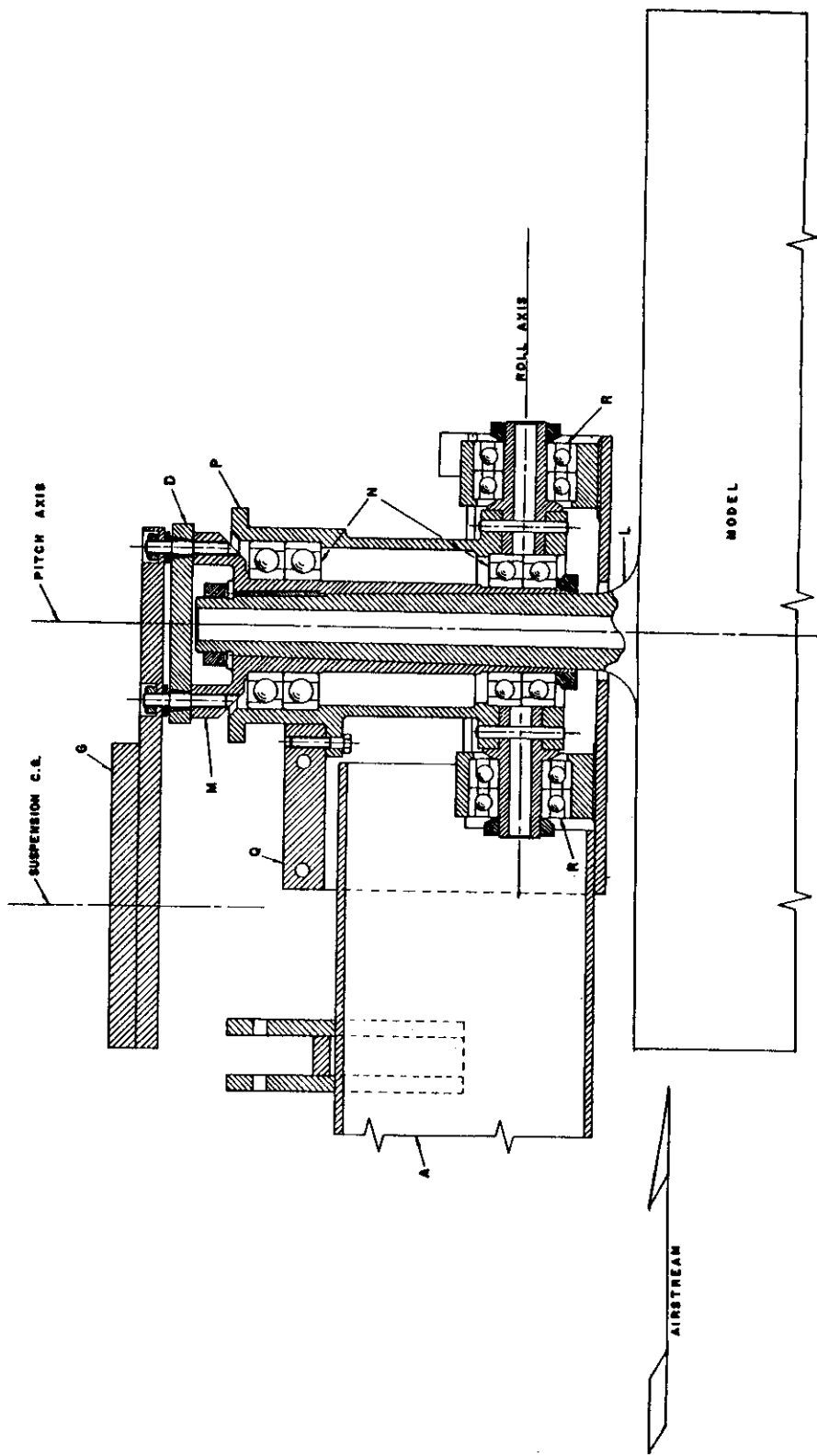


FIGURE 69 CUTAWAY VIEW OF MODEL SUSPENSION HEAD

~~CONFIDENTIAL~~

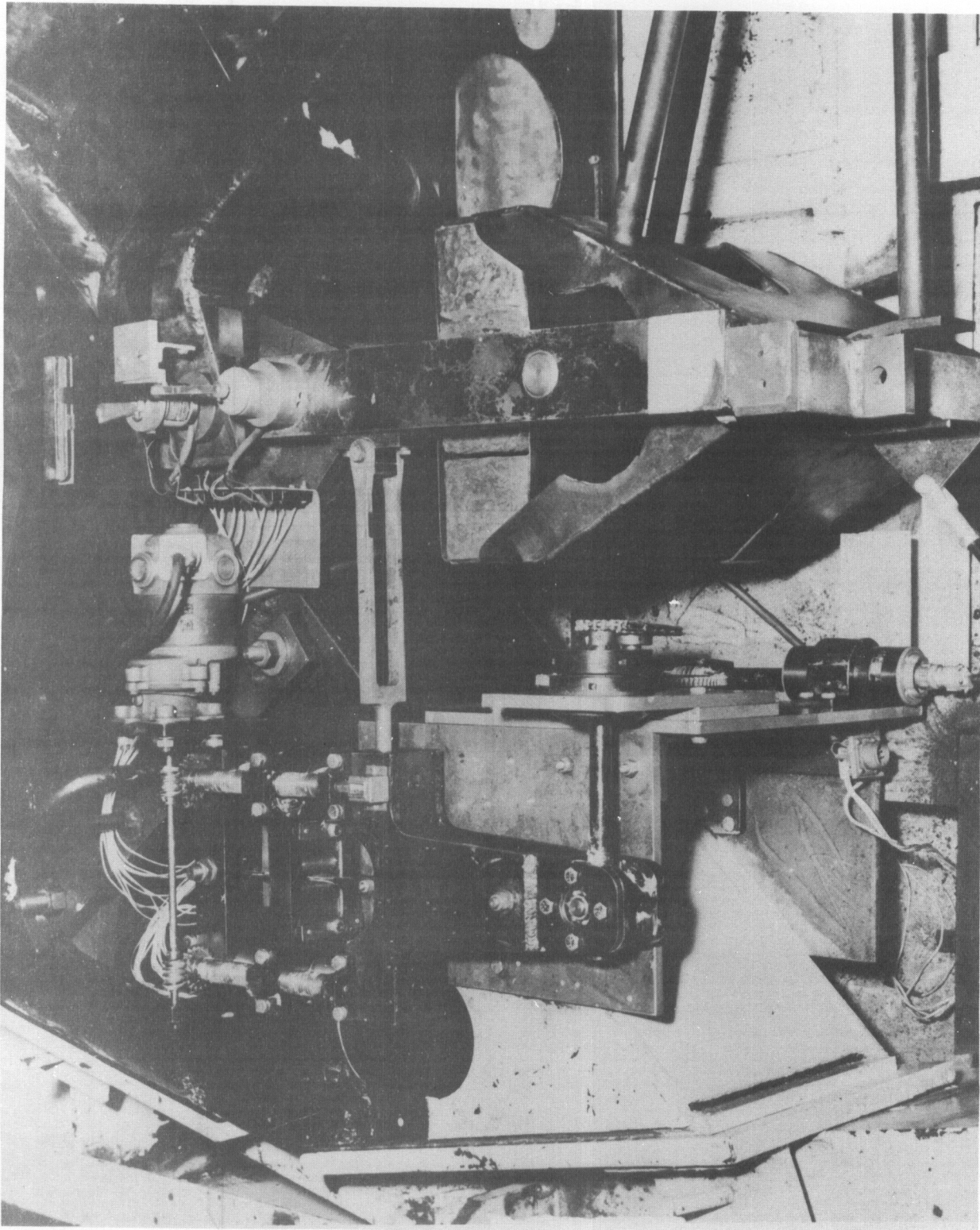


FIGURE 70 SUSPENSION PITCH FREQUENCY SYSTEM AND ANGLE OF ATTACK CONTROL

~~CONFIDENTIAL~~

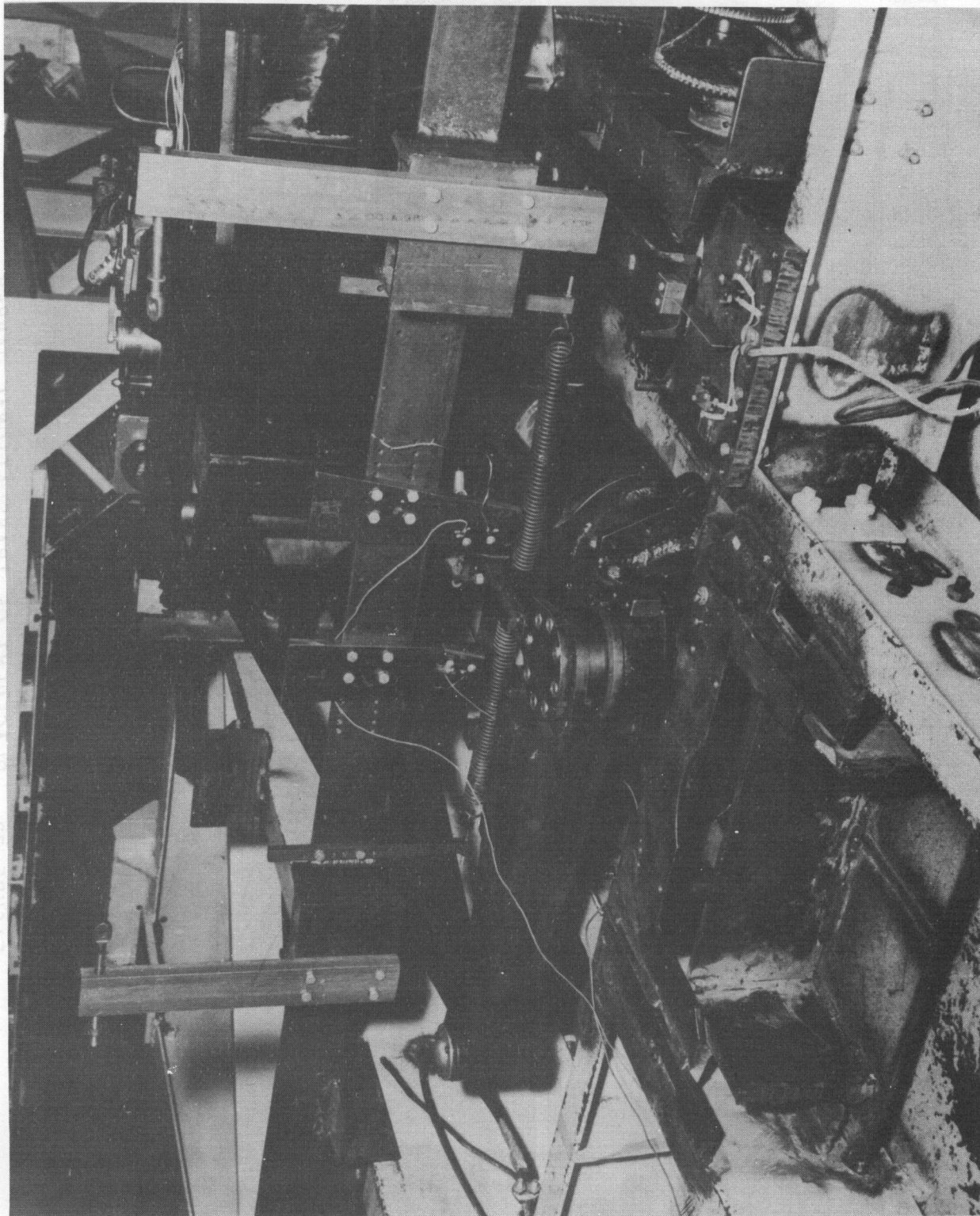


FIGURE 71 PLACEMENT OF TRANSLATIONAL STOPS AND SPRINGS

CONFIDENTIAL

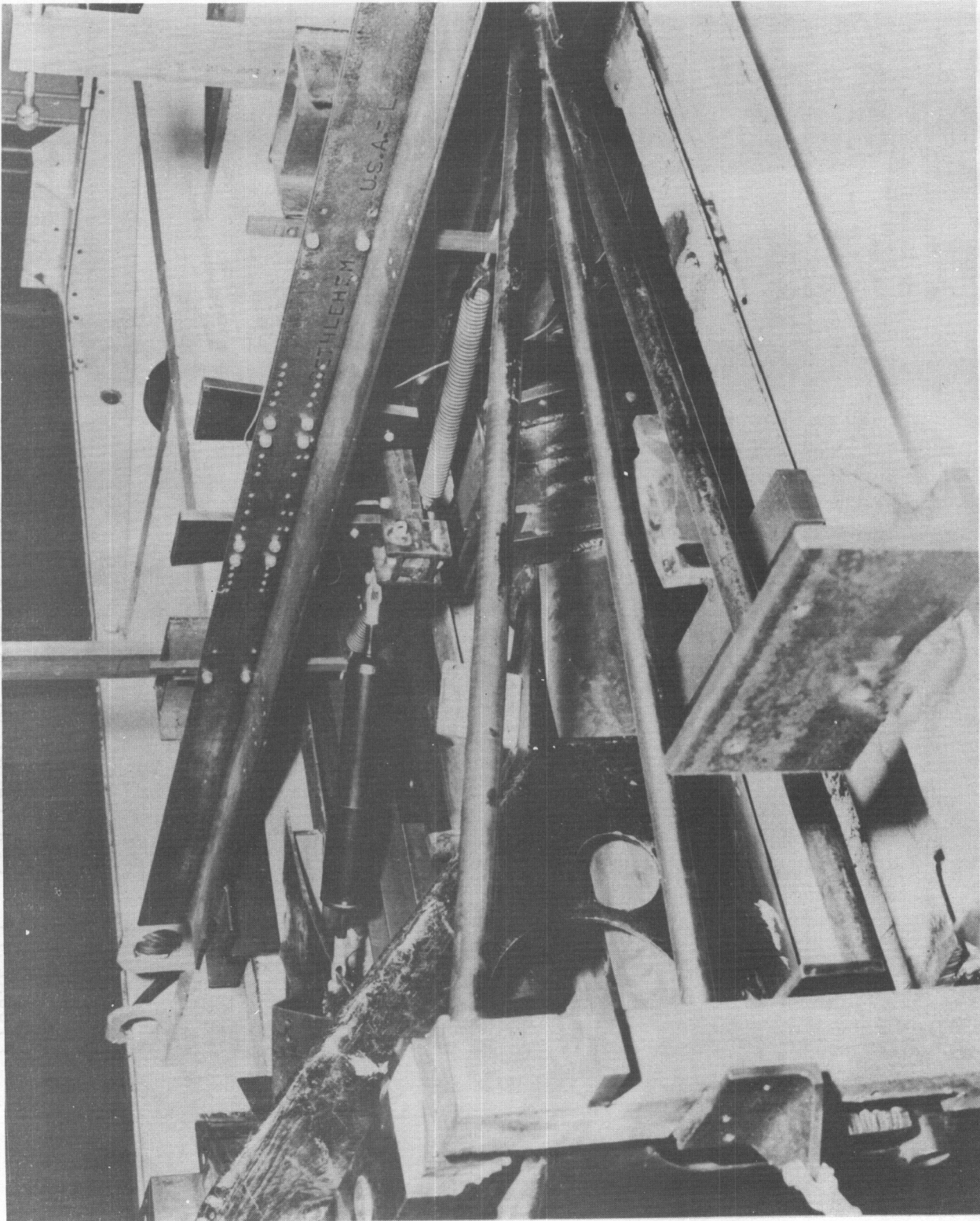


FIGURE 72 PLACEMENT OF TRANSLATIONAL DAMPER

CONFIDENTIAL

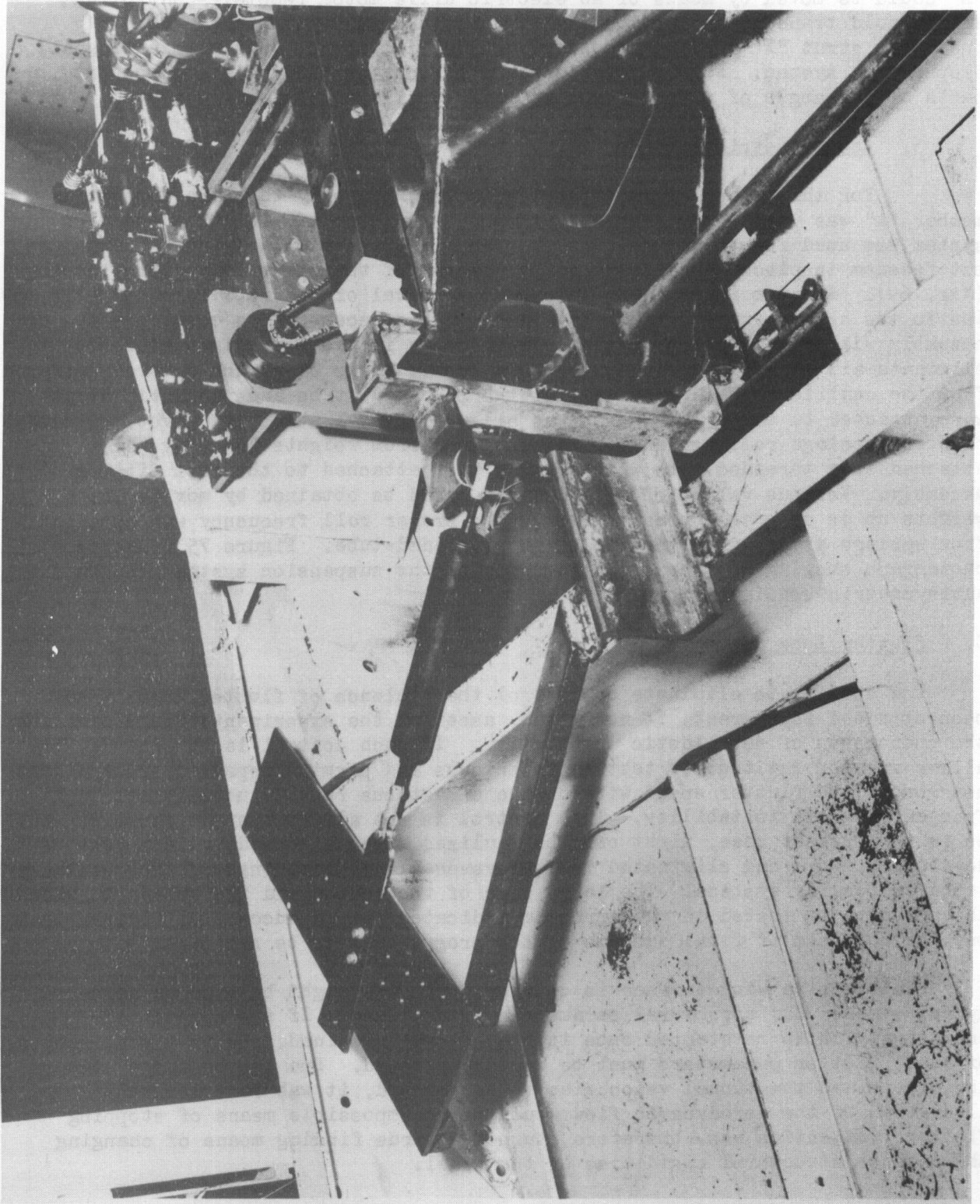


FIGURE 73 INSTALLATION OF PITCH DAMPER

[REDACTED]

"E" could be moved by means of an electric drive motor, remotely-controlled, which would transmit its motion to "D" through a push-pull tube. The pneumatic strut "F" applied a continuous 1800 lb. force, thus eliminating all slop in the system. Figure 74 presents a photograph showing the component parts of the angle of attack mechanism and cantilever suspension system.

3. Antisymmetric Root Conditions

For this case, again referring to Fig. 67, only the main supporting member "A" was used. A different attachment assembly of wing to suspension system was used for this case. The new assembly was similar to the former one but freedom in pitch was eliminated by removal of the sleeve and pitch bearings (Fig. 69). Freedom in roll was allowed by removal of the roll lock "Q" (Fig. 69). Due to the high torsional loads involved, it was necessary to construct the new assembly without the pitch degree of freedom as it was found impossible to eliminate all pitch motion by means of a lock. Angle of attack control differed from the cantilever case only in that the push-pull tube and pneumatic strut were attached to member "A" which was allowed to move about its pivot. Simulation of fuselage rolling inertia was obtained from weights "D" (Fig. 67) attached to a threaded tube which was in turn attached to the root fitting assembly. Various values of roll inertia could be obtained by moving the weights up or down the threaded tube. The proper roll frequency was obtained from springs attached to the top of the threaded tube. Figure 75 presents a photograph showing the various components of the suspension system used in the antisymmetric configuration.

C. Flutter Lock

The ability to eliminate or control the violence of flutter once it has been obtained is a great, if not vital, asset to the experimenter investigating the phenomenon of aeroelastic instability. If such control is obtainable, it allows greater latitude in testing techniques and permits repeated explorations near or at the flutter speed without the disastrous results usually obtained from aeroelastic instability. This control is not always easy to acquire, and, as in the present case, might only be realized after a considerable amount of development work had eliminated the unforeseeable shortcomings of progressively improved locking systems. The large size of the models and the speeds to which they were to be tested in this program indicated that a successful flutter lock must be obtained if final success of the program was to be realized.

Flutter of a wing surface is obtained when the right balance of aerodynamic, mass, and structural parameters is realized. If the aeroelastic instability is to be stopped once it has become sustained, one or a combination of these flutter parameters must be rapidly altered. Due to the large size of the models and the tunnel velocities to be reached, it was reasoned that alteration of the aerodynamic flow would be an impossible means of stopping flutter. Attention was, therefore, turned towards finding means of changing the mass or structural rigidities of the model.

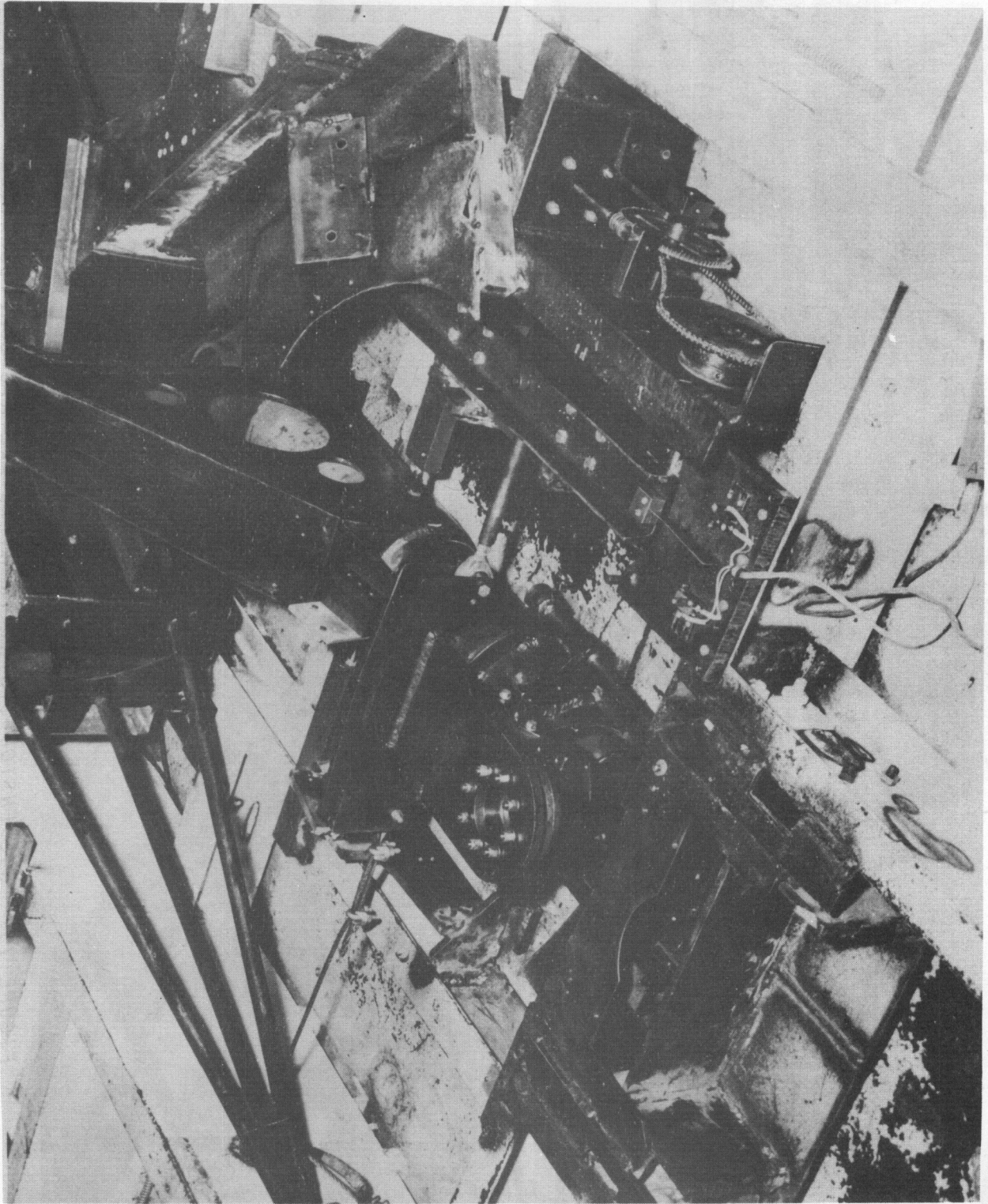


FIGURE 74 SUSPENSION SYSTEM IN CANTILEVER CONFIGURATION

[REDACTED]

FIGURE 75 20268210M 2A21EM IN CIVIL ENGINEER CONSULTATION

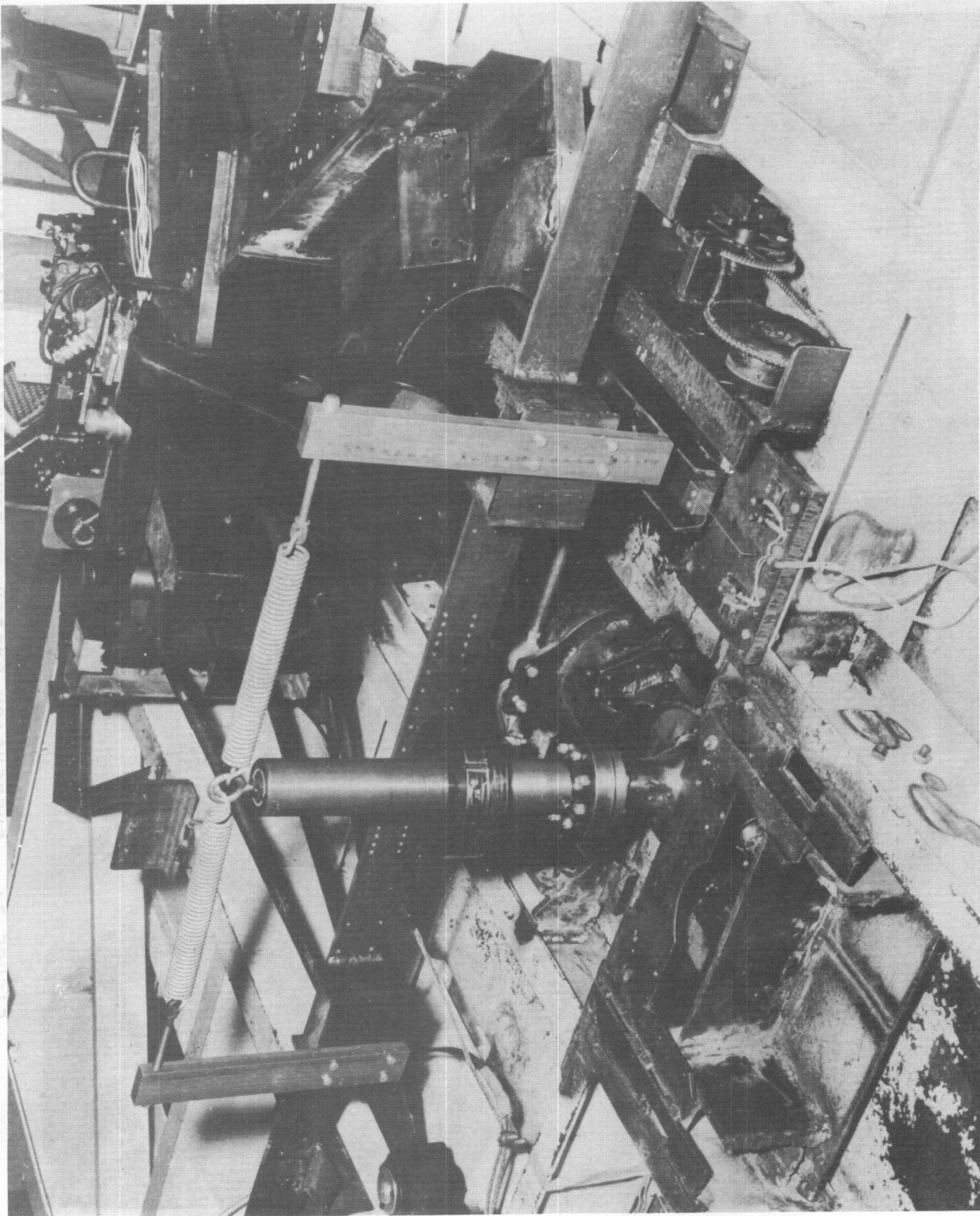


FIGURE 75 SUSPENSION SYSTEM IN ANTISYMMETRIC CONFIGURATION

[REDACTED]

WADC TR 55-334

[REDACTED]

At first, thought was given to changing the mass parameters of the wing. Two means of sufficiently changing the effective mass parameters to stop flutter on the basis of theoretical predictions were devised. These are as follows:

1. Chordwise movement of the ballast weights located at the $3/4$ span position.
2. Spanwise movement of a ballast weight along the leading edge.

The movement of the ballast weight in both cases would have been accomplished by pneumatic means to obtain as rapid a change as possible.

The chordwise shift of ballast weights in the desired system kept the integrated mass constant, reduced the mass coupling by 50%, and raised the torsional frequency $3\frac{1}{2}\%$ due to the reduction in the integrated inertia. The system, while physically obtainable, was discarded due to the weight penalty it imposed upon the wing. However, this system would conceivably be acceptable for a model of an airplane designed to carry concentrated weights in the form of fuel tanks, engine nacelles, or other external stores.


Spanwise movement of a suitable ballast weight eliminated the weight penalty since the weight would be located at the wing root until flutter was obtained and then would be rapidly moved to the tip of the wing. A model incorporating this scheme was constructed and tested to see if sufficiently rapid movement could be obtained to make it practical. The model consisted of a one-inch dural tube into which a $1\frac{1}{2}$ lb. circular steel weight was placed. Rapid movement of the steel ballast weight was done by pneumatic means. Stopping the ballast weight as it reached the wing tip was accomplished by placing a metered opening at the end of the dural tube. Therefore, as the ballast weight was driven towards the wing tip, the air preceding it was compressed and slowed the weight down over its last six inches of travel. Sufficient velocity of the ballast weight was obtained to move it from the root to the tip of the wing (6 ft.) in 0.05 sec.. This system overcame the objection which rejected the chordwise movement of weights. The effective weight during the test, before flutter was obtained, consisted only of a thin-walled dural tube and was, therefore, very small. The system was demonstrated to be sufficiently rapid and it was theoretically proven to stop flutter by sufficiently changing the mass coupling. However, the brake was finally considered not desirable for the present program for the following two reasons:

- (a) For the flutter tests involving the rigid body degrees of freedom, the flutter brake would not stop any rigid body dynamic instability which might occur.
- (b) The rapidity with which the flutter mode would be destroyed by changing the mass parameters was not known.

[REDACTED]

If a reasonable answer could be obtained for the second objection, it appears that this flutter brake would be a desirable flutter lock for flutter models tested only in the cantilever condition.

Since a successful flutter lock design could not be found by changing the aerodynamics or mass properties in the flutter mode, attention was turned to investigating means of varying the structural properties of the models. Changing the internal structural rigidities of the models would stop the classical type of flutter but would not restrain any low frequency dynamic instability involving the rigid body degrees of freedom present in the symmetric or antisymmetric flutter configurations. It was, therefore, decided that an external lock designed to restrain the motion at the tip of the wing when flutter or dynamic instability occurred, was the best means of saving the model from either type of instability. An external lock designed to restrain the tip of the wing is shown installed in Fig. 58, p. 91. As can be seen from the figure, the lock consisted of two steel cables, (3/32 in. in diameter) stretched across the tunnel at two chordwise stations of the wing. Attached to the cables were a large number of circular steel buttons with their circular faces perpendicular to the axis of the cable. Fastened to the tip of the wing were two pylons having a chordwise row of teeth facing downward. When flutter or a dynamic instability occurred, a pneumatic strut mounted on one tunnel wall moved the cables upward and the teeth became engaged in between the buttons. The pneumatic strut was triggered when a pre-set torsional strain level, measured by strain gages attached to the root of the wing, was exceeded. Torsional strain was chosen to monitor the flutter brake for two reasons; (1) calculations indicated that the torsional motion would be predominant in the flutter mode, and (2) it was desired to prevent low frequency buffeting, which produces sizable bending deflections but small torsional deflections, from firing the lock. Drag back of the cables due to air resistance was countered by a remotely-controlled drive motor which moved one end of the cables fore and aft and thus kept the cables properly aligned with respect to the pylons. It was realized that the lock had an undesirable characteristic in that the wing could be locked off-center. However, it was felt that there would be insufficient torsional motion for the wing to be locked with a torsional deflection which might prove destructive, and a bending deflection was not considered to be detrimental, as the wing would just vibrate in bending when the lock was released. During the flutter tests, this lock was automatically applied when the wing was flying at a relatively high speed. At the instant the teeth engaged the buttons, the wing was slightly deflected to one side. When the flutter lock was released, the front cable immediately cleared and the rear cable "hung up" for an instant in the teeth. This aft pivot point (70% chord station), at the wing tip produced an unstable divergence condition and the wing was immediately lost. The failure of the model due to the action of the flutter lock indicated that the following requirements were necessary to successfully lock and unlock the model:

- 
- (a) The model must be locked with zero angle of attack and zero bending deflection.
 - (b) The lock must disengage the wing simultaneously along the chord.

To overcome the objections of the previous locks, a locking system was designed whereby the lock gathered the wing and placed it in a neutral position before clamping. The lock consisted of a pair of endless run-around cables located fore and aft of the flutter model. To a similar point on each run-around cable, a pair of locking bars were attached. Both cables were pneumatically-driven simultaneously, thus bringing the bars together and locking the wing. Due to the rapidity at which the lock operated, approximately 1/32 in. clearance was allowed between the bars and the model when in the clamped condition. This clearance was allotted for over-travel of the locking bars when rapidly closing so that the model and accelerometer pickup mounted at the model tip would not be damaged. The brake in its open position permitted ± 2.0 in. of free bending deflection at the wing tip. During wind tunnel testing, the lock closed while at an airspeed close to the bending-torsion flutter speed expected. As the lock closed, violent oscillations of the wing occurred, opening and then destroying the flutter lock. Flutter of the wing continued for a fraction of a second thereafter before the model was also destroyed. Inspection of the recorded oscillograph trace showed that the flutter frequency was much higher than could be expected from the free cantilever bending-torsion aeroelastic coupling. From the results of the test, it was concluded that the 1/32 in. clearance plus the low ratio of wing clamped torsional rigidity to the free torsional rigidity had allowed a cantilever-free torsion mode to exist along with a cantilever-pinned bending mode while the lock was in a closed position. Flutter analyses using these modes as degrees of freedom indicated that aeroelastic coupling of these modes could produce a flutter speed below that present when the model and lock failed. To overcome these difficulties, the lock was modified to incorporate changes which made it stronger and impossible to open once it had closed. It was also decided to ballast the models so that flutter in the clamped-pinned mode would be eliminated. By proper reballasting this was accomplished without appreciably changing the characteristics of the primary bending-torsion flutter.

A drawing showing all the major components of the flutter lock is presented in Fig. 76. A picture of the lock installed in the wind tunnel is shown in Fig. 77. The small wires running perpendicular to the main cables were used to prevent galloping of the locking cables during the high speed runs.

The lock was constructed as before with two endless run-around cables to which the locking bars were attached to a similar point on each cable. To eliminate the effect of cable drag-back due to air flow, the cables were

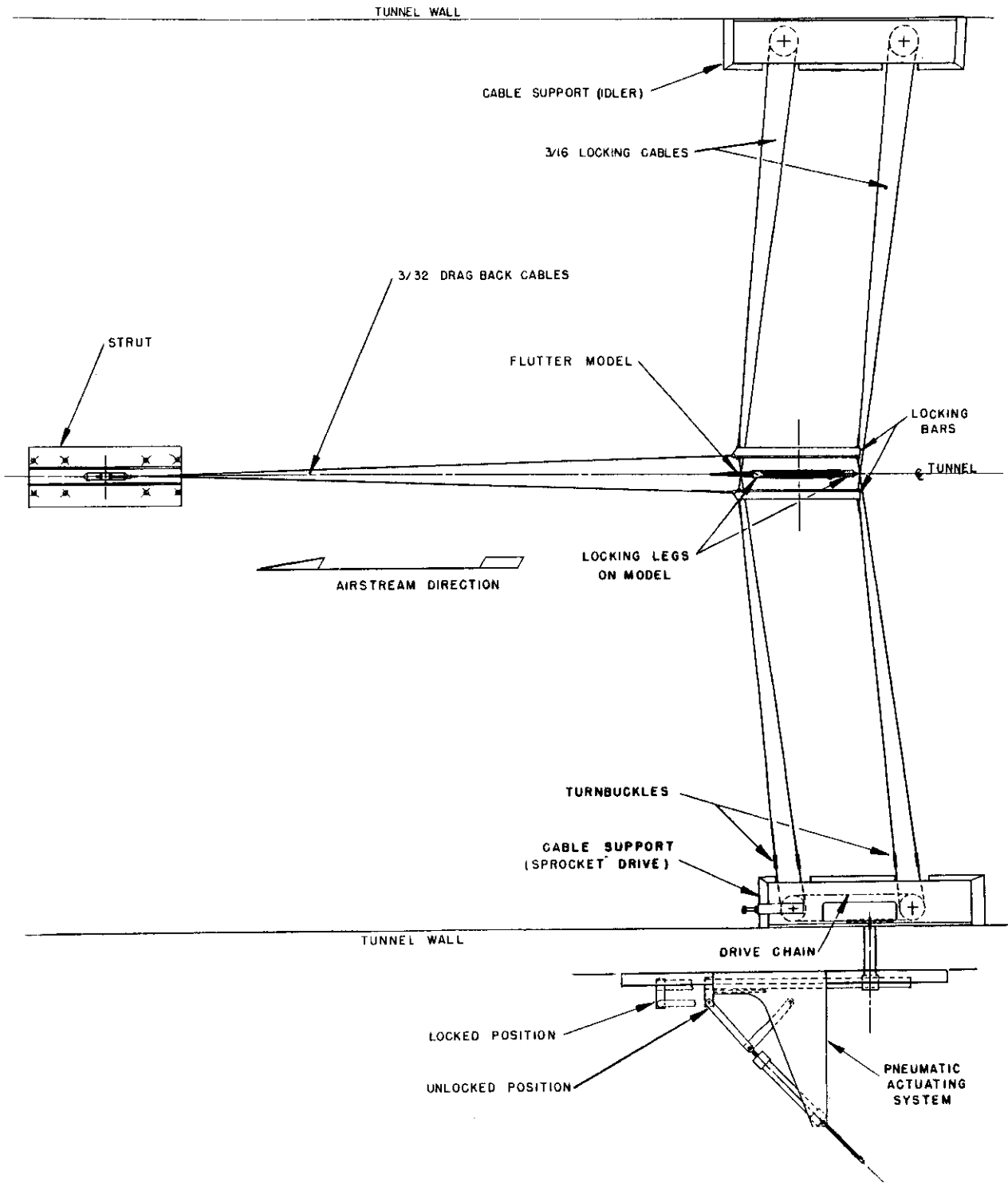


FIGURE 76 FLUTTER LOCK MOUNTED IN TUNNEL



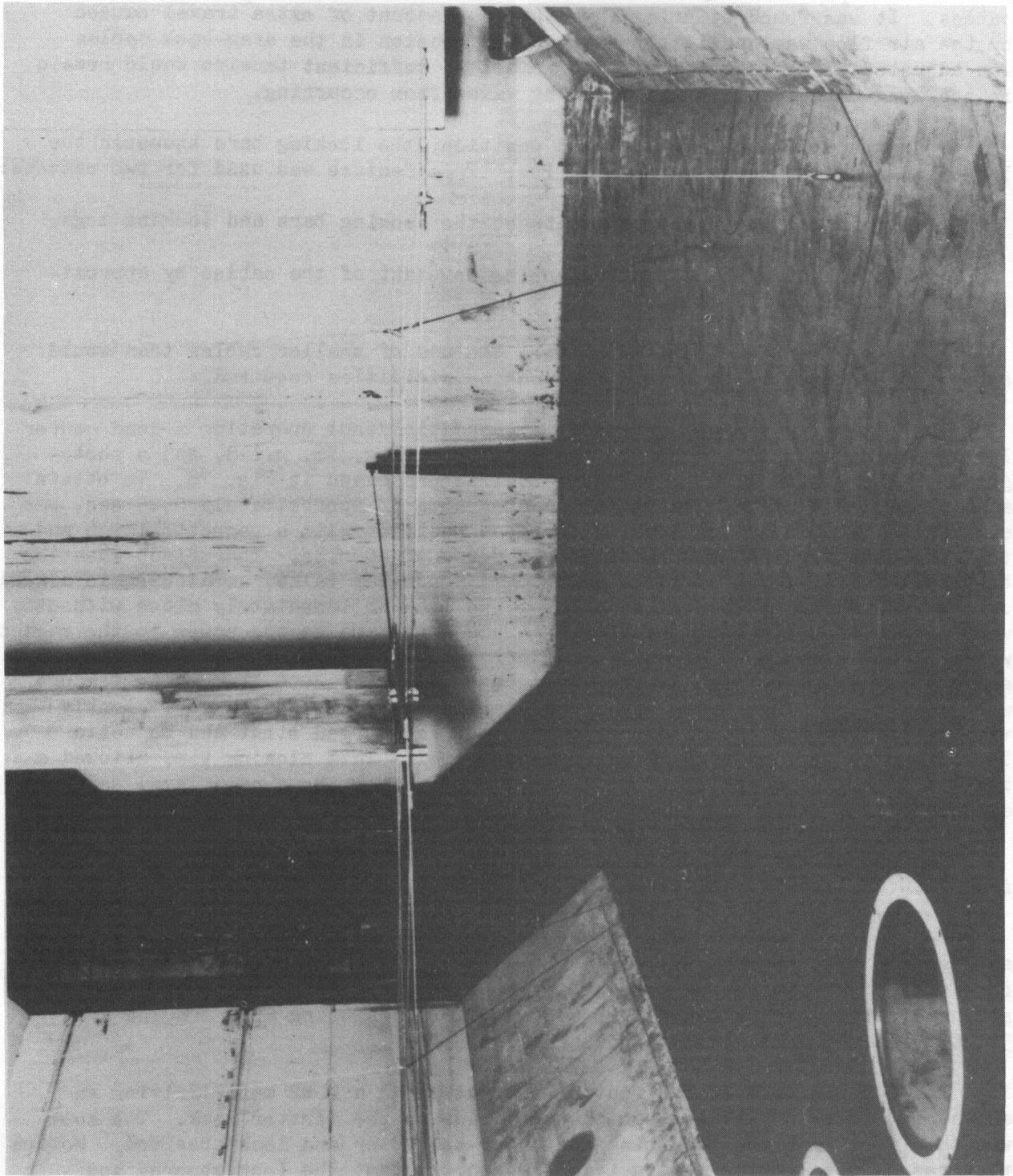


FIGURE 77 PICTURE OF LOCK CLAMPING MODEL IN THE TUNNEL

[REDACTED]

pulled back approximately 8 in. at their center by means of two small drag cables. It was found by doing this that the amount of extra travel caused by the air flow was negligibly small. The tension in the drag-back cables was adjusted so that at the highest velocity, sufficient tension would remain in the drag cables to prevent traveling waves from occurring.

When the lock was in its closed position, the locking bars squeezed the locking legs with approximately 400 lbs. This feature was used for two reasons:

- (1) Elimination of all slop between the locking bars and locking legs.
- (2) Increasing the effective spring constant of the cables by approximately 2-1/2 times.

The attainment of item (2) allowed the use of smaller cables than would otherwise be possible to obtain the locking rigidities required.

The entire system was driven by a pneumatic strut operating a dead center linkage. The system is shown in the drawing of Fig. 76, p.118, and a photograph of the system mounted on the tunnel is presented in Fig. 78. To obtain a minimum closing time, the valve transfer time of approximately 0.05 sec. was eliminated by holding the lock in the open position with a magnetic latch and then pre-charging the strut with an air force of 400 lbs. Therefore, when the torsional strain level of the wing reached a pre-set value, an electronic circuit cut the power to the magnet and allowed the lock to immediately close without waiting for the valves to transfer. At the same time as the power to the magnet was cut, the electronic circuit transferred the pneumatic valves (see Fig. 78), and allowed the air force in the strut to build up to 2000 lbs. This feature was provided to prevent the wing from keeping the lock open if sufficiently violent flutter had occurred. By using the pre-charged strut and magnetic latch, a closing time of 0.07 sec. was obtained. This closing time allowed a maximum of only two cycles of flutter to occur after the strain level had been exceeded.

The amount the wing could move between the locking bars could be changed from ± 1.0 in. to ± 5.0 in. by making suitable changes in the linkage system.

Before the lock was used in the tunnel for a wind tunnel test, a static and dynamic test program was conducted. The static test of the flutter lock consisted of obtaining the bending and torsional rigidity of the lock. The spring constants so obtained were 6000 lbs./in. resisting wing bending and 300,000 lbs. in./rad. resisting wing torsion.

The dynamic test of the flutter lock utilized a 2 HP motor driving an eccentric arm at 13 CPS between the open pads of the flutter lock. The lock was then fired and the resulting motion of the motor and lock observed. Motion pictures of the locking action (Fig. 79) showed that the lock stopped and reversed the direction of the motor in one-quarter of a cycle.

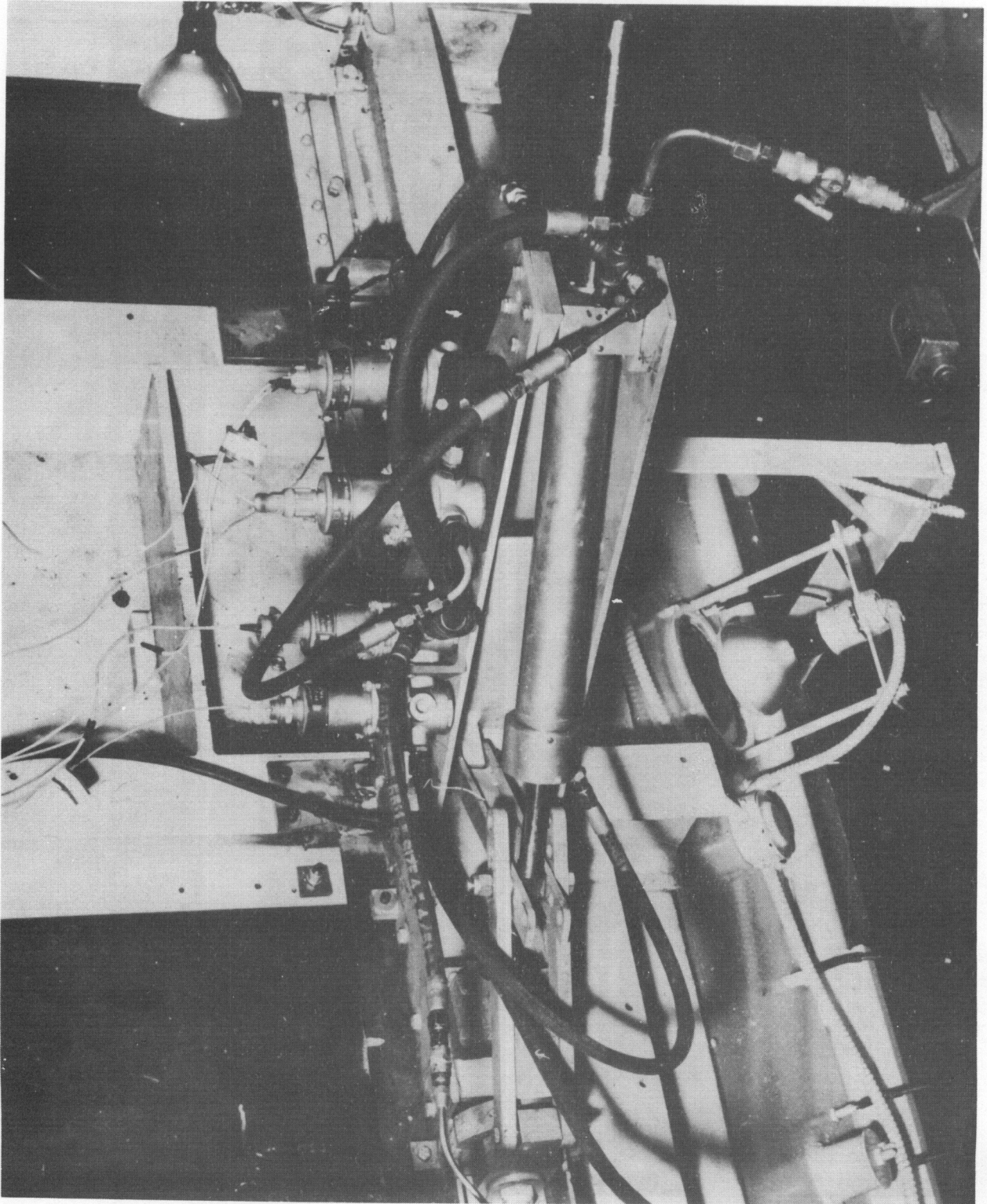


FIGURE 78 PNEUMATIC ACTUATING SYSTEM FOR LOCK



FIGURE 79 MECHANICAL LOCKING SEQUENCE OF FLUTTER BRAKE

FIGURE 79 LOCKING SEQUENCE OF FLUTTER BRAKE

[REDACTED]

APPENDIX II

LISTING OF FLUTTER DETERMINANT ELEMENTS

A. Flutter Determinant

$$\begin{vmatrix} A & B & C & D \\ E & F & G & H \\ I & J & K & L \\ M & N & P & Q \end{vmatrix} = 0$$

Numerical values of the following aerodynamic summations are given in Table XI.

(1) Cantilever Case

$$A = \frac{\sum W h_1^2}{\pi \rho b_r^2 L} \left[1 - \left(\frac{\omega h_1}{\omega} \right)^2 (1 + j g h_1) \right] + \frac{\sum b^2 \Delta x h_1^2}{b_r^2 L} I_h$$

$$B = \frac{\sum S_\alpha h_1 \alpha_1}{\pi \rho b_r^3 L} + \frac{\sum b^3 \Delta x h_1 \alpha_1}{b_r^3 L} \left[L_\alpha - \left(\frac{1}{2} + a \right) I_h \right]$$

$$E = \frac{\sum S_\alpha h_1 \alpha_1}{\pi \rho b_r^3 L} + \frac{\sum b^3 \Delta x h_1 \alpha_1}{b_r^3 L} \left[M_h - \left(\frac{1}{2} + a \right) I_h \right]$$

$$F = \frac{\sum I_\alpha \alpha_1^2}{\pi \rho b_r^4 L} \left[1 - \left(\frac{\omega \alpha_1}{\omega} \right)^2 (1 + j g \alpha_1) \right] + \frac{\sum b^4 \Delta x \alpha_1^2}{b_r^4 L} \left[-\frac{1}{2} \left(\frac{1}{2} + a \right) - L_\alpha \left(\frac{1}{2} + a \right) + M_\alpha + \left(\frac{1}{2} + a \right)^2 I_h \right]$$

$$C = D = G = H = I = J = K = L = M = N = P = Q = 0$$

(2) Antisymmetric Case

$$A = \frac{\sum W h_1^2 + I_R \phi_1^2}{\pi \rho b_r^2 L} \left[1 - \left(\frac{\omega h_1}{\omega} \right)^2 (1 + j g h_1) \right] + \frac{\sum b^2 \Delta x h_1^2}{b_r^2 L} I_h$$

$$B = \frac{\sum S_\alpha h_1 \alpha_1}{\pi \rho b_r^3 L} + \frac{\sum b^3 \Delta x h_1 \alpha_1}{b_r^3 L} \left[L_\alpha - \left(\frac{1}{2} + a \right) I_h \right]$$

$$C = \frac{\sum b^2 \Delta x h_o r h_1}{b_r^2 L} L_h$$

$$E = \frac{\sum S_\alpha h_1 \alpha_1}{\pi \rho b_r^3 L} + \frac{\sum b^3 \Delta x h_1 \alpha_1}{b_r^3 L} \left[M_h - \left(\frac{1}{2} + a \right) L_h \right]$$

$$F = \frac{\sum I_\alpha \alpha_1^2}{\pi \rho b_r^4 L} \left[1 - \left(\frac{\omega \alpha_1}{\omega} \right)^2 (1 + j g_\alpha 1) \right] \\ + \frac{\sum b^4 \Delta x \alpha_1^2}{b_r^4 L} \left[-\frac{1}{2} \left(\frac{1}{2} + a \right) - L_\alpha \left(\frac{1}{2} + a \right) + M_\alpha + \left(\frac{1}{2} + a \right)^2 L_h \right]$$

$$G = \frac{\sum S_\alpha h_o r \alpha_1}{\pi \rho b_r^3 L} + \frac{\sum b^3 \Delta x h_o r \alpha_1}{b_r^3 L} \left[M_h - \left(\frac{1}{2} + a \right) L_h \right]$$

$$I = \frac{\sum b^2 \Delta x h_o r h_1}{b_r^2 L} L_h$$

$$J = \frac{\sum S_\alpha h_o r \alpha_1}{\pi \rho b_r^3 L} + \frac{\sum b^3 \Delta x h_o r \alpha_1}{b_r^3 L} \left[L_\alpha - \left(\frac{1}{2} + a \right) L_h \right]$$

$$K = \frac{\sum W h_o r^2 + I_R \phi_o^2}{\pi \rho b_r^2 L} \left[1 - \left(\frac{\omega h_o r}{\omega} \right)^2 (1 + j g_{h_o}) \right] + \frac{\sum b^2 \Delta x h_o r^2}{b_r^2 L} L_h$$

$$D = H = L = M = N = P = Q = 0$$

(3) Symmetric Case

$$A = \frac{\sum W h_1^2}{\pi \rho b_r^2 L} \left[1 - \left(\frac{\omega h_1}{\omega} \right)^2 (1 + j g_{h_1}) \right] + \frac{\sum b^2 \Delta x h_1^2}{b_r^2 L} L_h$$

$$B = \frac{\sum S_\alpha h_1 \alpha_1}{\pi \rho b_r^3 L} + \frac{\sum b^3 \Delta x h_1 \alpha_1}{b_r^3 L} \left[L_\alpha - \left(\frac{1}{2} + a \right) L_h \right]$$

$$C = \frac{\sum b^2 \Delta x h_o t h_1}{b_r^2 L} L_h$$

$$D = \frac{\sum S_\alpha h_1 \alpha_o}{\pi \rho b_r^3 L} + \frac{\sum b^3 \Delta x h_1 \alpha_o}{b_r^3 L} \left[L_\alpha - \left(\frac{1}{2} + a \right) L_h \right]$$

$$E = \frac{\sum S_{\alpha} h_1 \alpha_1}{\pi \rho b_r^3 L} + \frac{\sum b^3 \Delta x h_1 \alpha_1}{b_r^3 L} \left[M_h - \left(\frac{1}{2} + a\right) L_h \right]$$

$$F = \frac{\sum I_{\alpha} \alpha_1^2}{\pi \rho b_r^4 L} \left[1 - \left(\frac{\omega b_1}{\omega}\right)^2 (1 + jg\alpha_1) \right] \\ + \frac{\sum b^4 \Delta x \alpha_1^2}{b_r^4 L} \left[-\frac{1}{2} \left(\frac{1}{2} + a\right) - L_{\alpha} \left(\frac{1}{2} + a\right) + M_{\alpha} + \left(\frac{1}{2} + a\right)^2 L_h \right]$$

$$G = \frac{\sum S_{\alpha} h_{ot} \alpha_1}{\pi \rho b_r^3 L} + \frac{\sum b^3 \Delta x h_{ot} \alpha_1}{b_r^3 L} \left[M_h - \left(\frac{1}{2} + a\right) L_h \right]$$

$$H = \frac{\sum b^4 \Delta x \alpha_o \alpha_1}{b_r^4 L} \left[-\frac{1}{2} \left(\frac{1}{2} + a\right) - \left(\frac{1}{2} + a\right) L_{\alpha} + M_{\alpha} + \left(\frac{1}{2} + a\right)^2 L_h \right]$$

$$I = \frac{\sum b^2 \Delta x h_{ot} h_1}{b_r^2 L} L_h$$

$$J = \frac{\sum S_{\alpha} h_{ot} \alpha_1}{\pi \rho b_r^3 L} + \frac{\sum b^3 \Delta x h_{ot} \alpha_1}{b_r^3 L} \left[L_{\alpha} - \left(\frac{1}{2} + a\right) L_h \right]$$

$$K = \frac{\sum W h_{ot}^2}{\pi \rho b_r^2 L} \left[1 - \left(\frac{\omega h_{ot}}{\omega}\right)^2 (1 + jgh_o) \right] + \frac{\sum b^2 \Delta x h_{ot}^2}{b_r^2 L} L_h$$

$$L = \frac{\sum S_{\alpha} h_{ot} \alpha_o}{\pi \rho b_r^3 L} + \frac{\sum b^3 \Delta x h_{ot} \alpha_o}{b_r^3 L} \left[L_{\alpha} - \left(\frac{1}{2} + a\right) L_h \right]$$

$$M = \frac{\sum S_{\alpha} h_1 \alpha_o}{\pi \rho b_r^3 L} + \frac{\sum b^3 \Delta x h_1 \alpha_o}{b_r^3 L} \left[M_h - \left(\frac{1}{2} + a\right) L_h \right]$$

$$N = \frac{\sum b^4 \Delta x \alpha_o \alpha_1}{b_r^4 L} \left[-\left(\frac{1}{2} + a\right) L_{\alpha} + M_{\alpha} + \left(\frac{1}{2} + a\right)^2 L_h - \frac{1}{2} \left(\frac{1}{2} + a\right) \right]$$

$$P = \frac{\sum S_{\alpha} h_{ot} \alpha_o}{\pi \rho b_r^3 L} + \frac{\sum b^3 \Delta x h_{ot} \alpha_o}{b_r^3 L} \left[M_h - \left(\frac{1}{2} + a\right) L_h \right]$$

$$Q = \frac{\sum I_{\alpha} \alpha_0^2}{\pi \rho b_r^4 L} \left[1 - \left(\frac{\omega_{\alpha 0}}{\omega} \right)^2 (1 + jg_{\alpha 0}) \right] + \frac{\sum b^4 \Delta x \alpha_0^2}{b_r^4 L} \left[-\frac{1}{2} \left(\frac{1}{2} + a \right) - \left(\frac{1}{2} + a \right) L_{\alpha} + M_{\alpha} + \left(\frac{1}{2} + a \right)^2 L_h \right]$$

(4) Aileron Case

$$A = \frac{\sum W h_1^2}{\pi \rho b_r^2 L} \left[1 - \left(\frac{\omega_{h_1}}{\omega} \right)^2 (1 + jg_{h_1}) \right] + \frac{\sum b^2 \Delta x h_1^2}{b_r^2 L} L_h$$

$$B = \frac{\sum S_{\alpha} h_1 \alpha_1}{\pi \rho b_r^3 L} + \frac{\sum b^3 \Delta x h_1 \alpha_1}{b_r^3 L} \left[L_{\alpha} - \left(\frac{1}{2} + a \right) L_h \right]$$

$$C = \frac{\sum b^2 \Delta x h_1 h_2}{b_r^2 L} L_h$$

$$D = \frac{\sum S_{\beta} h_1 \beta}{\pi \rho b_r^3 L} + \frac{\sum b^3 \Delta x h_1 \beta}{b_r^3 L} L_{\beta}$$

$$E = \frac{\sum S_{\alpha} h_1 \alpha_1}{\pi \rho b_r^3 L} + \frac{\sum b^3 \Delta x h_1 \alpha_1}{b_r^3 L} \left[M_h - \left(\frac{1}{2} + a \right) L_h \right]$$

$$F = \frac{\sum I_{\alpha} \alpha_1^2}{\pi \rho b_r^4 L} \left[1 - \left(\frac{\omega_{\alpha 1}}{\omega} \right)^2 (1 + jg_{\alpha 1}) \right] + \frac{\sum b^4 \Delta x \alpha_1^2}{b_r^4 L} \left[-\frac{1}{2} \left(\frac{1}{2} + a \right) - L_{\alpha} \left(\frac{1}{2} + a \right) + M_{\alpha} + \left(\frac{1}{2} + a \right)^2 L_h \right]$$

$$G = \frac{\sum S_{\alpha} h_2 \alpha_1}{\pi \rho b_r^3 L} + \frac{\sum b^3 \Delta x h_2 \alpha_1}{b_r^3 L} \left[M_h - \left(\frac{1}{2} + a \right) L_h \right]$$

$$H = \frac{\sum [I_{\beta} + b(c-a)S_{\beta}] \alpha_1 \beta}{\pi \rho b_r^4 L} + \frac{\sum b^4 \Delta x \alpha_1 \beta}{b_r^4 L} \left[M_{\beta} - \left(\frac{1}{2} + a \right) L_{\beta} \right]$$

$$I = \frac{\sum b^2 \Delta x h_1 h_2}{b_r^2 L} L_h$$

$$J = \frac{\sum S_{\alpha} h_2 \alpha_1}{\pi \rho b_r^3 L} + \frac{\sum b^3 \Delta x h_2 \alpha_1}{b_r^3 L} \left[L_{\alpha} - \left(\frac{1}{2} + a \right) L_h \right]$$

$$K = \frac{\sum W h_2^2}{\pi \rho b_r^2 L} \left[1 - \left(\frac{\omega h_2}{\omega} \right)^2 (1 + j g h_2) \right] + \frac{\sum b^2 \Delta x h_2^2}{b_r^2 L} I_h$$

$$L = \frac{\sum S_\beta h_2 \beta}{\pi \rho b_r^3 L} + \frac{\sum b^3 \Delta x h_2 \beta}{b_r^3 L} I_\beta$$

$$M = \frac{\sum S_\beta h_1 \beta}{\pi \rho b_r^3 L} + \frac{\sum b^3 \Delta x h_1 \beta}{b_r^3 L} T_h$$

$$N = \frac{\sum [I_\beta + b(c-a)S_\beta] \alpha_1 \beta}{\pi \rho b_r^4 L} + \frac{\sum b^4 \Delta x \alpha_1 \beta}{b_r^4 L} \left[T_\alpha - \left(\frac{1}{2} + a \right) T_h \right]$$

$$P = \frac{\sum S_\beta h_2 \beta}{\pi \rho b_r^3 L} + \frac{\sum b^3 \Delta x h_2 \beta}{b_r^3 L} T_h$$

$$Q = \frac{\sum I_\beta \beta^2}{\pi \rho b_r^4 L} \left[1 - \left(\frac{\omega \beta}{\omega} \right)^2 (1 + j g \beta) \right] + \frac{\sum b^4 \Delta x \beta^2}{b_r^4 L} T_\beta$$

TABLE VII

COMPARISON SUMMARY OF CALCULATED
AND EXPERIMENTAL VIBRATION RESULTS

PLAIN WINGS

Model	Root Condition	Calculated Uncoupled Freq.(CPS)			First Coupled Mode Freq.(CPS)		Second Coupled Mode Freq.(CPS)		Third Coupled Mode Freq.(CPS)	
		First Bend.	First Tors.	Second Bend.	Calc.	Meas.	Calc.	Meas.	Calc.	Meas.
0.65	Cantilever	7.3	33.0	35.0	7.3	7.3	30.7	31.2	40.8	39.2
0.75	Cantilever	8.5	41.0	40.0	8.5	8.5	36.5	36.9	48.2	44.8
0.85	Cantilever	9.1	45.0	43.0	9.1	8.9	38.9	38.1	50.8	48.4
0.65	Symmetric	7.5	33.2	36.0	7.5	7.6	31.2	31.3	41.3	39.0
0.75	Symmetric	8.9	41.0	40.0	8.9	8.9	37.4	38.3	48.1	45.5
0.85	Symmetric	9.5	45.0	43.0	9.5	9.5	39.4	40.0	52.1	47.5
0.65	Antisymmetric	16.9	32.9	40.0	16.7	17.1	34.2	33.9	41.4	41.8
0.75	Antisymmetric	20.0	41.0	50.0	19.6	19.8	41.1	41.7	47.7	45.3
0.85	Antisymmetric	21.3	45.0	51.0	21.1	21.4	43.5	45.0	49.1	48.0

TABLE VII (CONT.)

WING-AILERON MODEL

Model	Root Condition	Calculated Uncoupled Mode Frequencies (CPS)					Aileron
		First Bending	First Torsion	Second Bending	Second Torsion	Third Bending	
0.65	Cantilever	7.2	32.5	34.0	70.0	88.0	33.1
0.65	Cantilever	7.2	32.5	34.0	70.0	88.0	47.9

Model	Root Condition	Coupled Mode Frequencies (CPS)									
		First Mode		Second Mode		Third Mode		Fourth Mode		Fifth Mode	
		Calc.	Meas.	Calc.	Meas.	Calc.	Meas.	Calc.	Meas.	Calc.	Meas.
0.65	Cantilever	7.2	7.2	29.5	29.4	32.5	32.1	43.0	41.0	---	---
0.65	Cantilever	7.2	7.2	30.0	29.7	37.9	36.1	52.1	50.0	68.6	70.0

TABLE VIII

COMPARISON OF CALCULATED
AND EXPERIMENTAL FLUTTER RESULTS

Model	Root Condition	Flutter Speed-mpg		Flutter Freq.-CPS		$\frac{V}{b\Omega}$		$\frac{V}{b\omega}$		Density ρ (slugs) ft. 3	Method of Analysis****
		Calc.	Exp.	Calc.	Exp.	Calc.	Exp.	Calc.	Exp.		
0.65	Cantilever	472	{ 493* 532** 566 }	18.7	22.0	5.90	5.25	3.34	3.47	0.001127	A
0.65	Cantilever	430		15.4	17.0	6.55	7.25	3.05	3.81	0.001127	B
0.65	Cantilever	594		15.4		9.00		4.20		0.001127	C
0.65	Cantilever	556		20.8		6.25		3.93		0.001127	D
0.65	Cantilever	540		18.1		6.97	6.95	3.82	3.95	0.000850	A
0.75	Cantilever	600	{ 592* 639*** 695 }	21.9	22.0	6.40	6.78	3.42	3.37	0.001138	A
0.75	Cantilever	676		22.1	15.0	7.14	9.71	3.85	3.64	0.000830	A
0.85	Cantilever	655	{ 652* 706*** }	24.7	27.0	6.20	5.64	3.40	3.38	0.001120	A
0.85	Cantilever	645		23.4		6.45		3.35		0.001120	E
0.85	Cantilever	740		23.0		7.50		3.84	3.66	0.000830	A
0.65	Symmetric	481	{ 523 584 663 }	18.7	22.0	6.00	5.55	3.38	3.68	0.001120	A
0.75	Symmetric	590		23.3	26.0	5.90	5.25	3.36	3.33	0.001130	A
0.85	Symmetric	665		25.0	28.0	6.20	5.52	3.45	3.44	0.001100	A
0.65	Antisymmetric	467	{ 502 }	19.6	16.0	5.55	7.32	3.30	3.56	0.001139	A
0.65	Antisymmetric	438		18.3		5.60		3.10		0.001139	B
0.65	Antisymmetric	565		22.0		6.00		4.00		0.001139	C
0.75	Antisymmetric	583	613	24.3	19.0	5.60	7.51	3.32	3.49	0.001131	A
0.85	Antisymmetric	651	654	26.7	21.0	5.70	7.26	3.38	3.39	0.001114	A

* Mild flutter

** Violent flutter

*** Speed reached without flutter

**** A - Incompressible, Infinite AR (Ref. 3)

B - Compressible, Infinite AR (Refs. 4 and 6)

C - Incompressible, Finite AR (Ref. 8)

D - Incompressible, Finite AR (Refs. 6 and 7)

E - Includes effects of second bending (Ref. 3)

TABLE IX

MASS PROPERTIES OF VARIOUS PLAIN WING MODELS

Station (in)	M = 0.65 Model			M = 0.75 Model			M = 0.85 Model		
	Weight (lbs) W	Unbalance (lbs-in) S_{α}	Inertia (lbs-in ²) I_{α}	Weight (lbs) W	Unbalance (lbs-in) S_{α}	Inertia (lbs-in ²) I_{α}	Weight (lbs) W	Unbalance (lbs-in) S_{α}	Inertia (lbs-in ²) I_{α}
72	1.609	+ 9.490	156.201	1.565	+ 9.297	145.622	1.643	+ 9.077	150.889
66	2.825	+ 5.161	125.762	2.665	+ 4.630	119.711	2.712	+ 4.495	120.316
54*	2.631	+ 2.583	92.197	2.519	+ 2.615	93.281	2.528	+ 2.261	91.361
42*	2.642	+ 2.714	93.021	2.530	+ 2.709	94.076	2.559	+ 2.355	92.156
30	4.990	-16.008	256.687	4.877	-15.705	254.736	4.956	-16.414	256.327
18	5.370	-14.770	280.994	4.965	-16.180	256.667	5.105	-16.885	260.355
6	23.323	- 1.398	164.301	24.064	- 2.454	177.762	24.641	- 2.906	197.928

Fuselage weight = 130 lbs
 Fuselage pitch inertia = 92,000 lbs-in²
 Fuselage unbalance = -830 lbs-in
 Fuselage roll inertia = 6400 lbs-in²

*Basic unballasted sections of wing.

TABLE IX (CONT.)

INTEGRATED MASS PROPERTIES OF VARIOUS PLAIN MODELS

CANTILEVER ROOT CONDITION

Model	$\sum Wh_1^2$	$\sum S_\alpha h_1 \alpha_1$	$\sum I_\alpha \alpha_1^2$
0.65	5.4878	14.004	466.78
0.75	5.3905	13.048	485.93
0.85	5.5568	12.175	483.28

SYMMETRIC ROOT CONDITION

Model	$\sum Wh_1^2$	$\sum S_\alpha h_1 \alpha_1$	$\sum I_\alpha \alpha_1^2$
0.65	5.5859	14.114	468.20
0.75	5.4600	13.259	487.45
0.85	5.6514	12.527	484.95

ANTISYMMETRIC CONDITION

Model	$\sum Wh_1^2 + I_R \phi_1^2$	$\sum S_\alpha h_1 \alpha_1$	$\sum I_\alpha \alpha_1^2$
0.65	11.6610	17.985	466.78
0.75	11.7940	17.831	485.93
0.85	11.9670	17.555	483.28

TABLE X
 MASS PROPERTIES OF VARIOUS WING-AILERON MODELS

Station (in)	M = 0.65 Model			M = 0.75 Model			M = 0.85 Model		
	Weight (lbs) W	Unbalance (lbs-in) S_{α}	Inertia (lbs-in ²) I_{α}	Weight (lbs) W	Unbalance (lbs-in) S_{α}	Inertia (lbs-in ²) I_{α}	Weight (lbs) W	Unbalance (lbs-in) S_{α}	Inertia (lbs-in ²) I_{α}
72	1.6092	+ 9.4897	156.20	1.5654	+ 9.2974	145.62	1.6427	+ 9.0769	150.89
66	3.0000	+ 5.7679	137.22	2.8400	+ 5.2362	131.17	2.8871	+ 5.1016	131.78
54	2.7895	+ 2.6021	101.40	2.6777	+ 2.6347	102.49	2.6859	+ 2.2806	100.57
42	2.8130	+ 2.8397	103.18	2.7010	+ 2.8342	104.24	2.7292	+ 2.4801	102.31
30	5.1017	-15.4910	264.28	4.9884	-15.1880	262.34	5.0680	-15.8970	263.92
18	5.3704	-14.7700	280.99	4.9646	-16.1800	256.67	5.1046	-16.8850	260.35
6	23.3230	- 1.3978	164.30	24.0640	- 2.4539	177.76	24.6410	- 2.9062	197.93

INTEGRATED MASS PROPERTIES OF VARIOUS WING-AILERON MODELS

Model	Wh_1^2	$S_{\alpha} h_1^2 \rho_1$	$I_{\alpha} \rho_1^2$	$S_{\rho} h_1 \rho_1^3$	$S_{\rho} h_2 \rho_2^3$	$S_{\rho} h_3 \rho_3^3$	$[I_{\rho} + b(c-a)S_{\rho}] \alpha_1 \rho_1$	$[I_{\rho} + b(c-a)S_{\rho}] \alpha_2 \rho_2$	$I_{\rho} \rho^2$
0.65	5.7118	14.636	492.14	0.50578	-0.38542	-0.48443	8.8061	-1.4237	2.604
0.75	5.6105	13.637	512.33	---	---	---	---	---	---
0.85	5.7836	12.724	528.98	---	---	---	---	---	---

TABLE XI

NUMERICAL VALUES OF AERODYNAMIC SUMMATIONS

Model	Root Condition	$\frac{\sum b^2 \Delta x h_1^2}{b_r^2 L}$	$\frac{\sum b^3 \Delta x h_1 \alpha_1}{b_r^3 L}$	$\frac{\sum b^4 \Delta x \alpha_1^2}{b_r^4 L}$	$\frac{\sum b^3 \Delta x h_0 \alpha_1}{b_r^3 L}$	$\frac{\sum b^2 \Delta x h_0^2}{b_r^2 L}$	$\frac{\sum b^2 \Delta x h_0 h_1}{b_r^2 L}$	$\frac{\sum b^4 \Delta x \alpha_0 \alpha_1}{b_r^4 L}$	$\frac{\sum b^3 \Delta x h_1 \alpha_0}{b_r^3 L}$
0.65	Cantilever	0.2286	0.2957	0.4061					
0.75	Cantilever	0.2360	0.3105	0.4401					
0.85	Cantilever	0.2380	0.3102	0.4329					
0.65	Antisymmetric	0.1595	0.0914	0.4061	0.3559	0.3134	0.0924		
0.75	Antisymmetric	0.1516	0.1043	0.4401	0.3804	0.3134	0.1067		
0.85	Antisymmetric	0.1537	0.1052	0.4329	0.3663	0.3134	0.1131		
0.65	Symmetric	0.2147	0.2821	0.4035	0.5534		0.3325	0.5534	0.3325
0.75	Symmetric	0.2218	0.2947	0.4373	0.5912		0.3443	0.5912	0.3443
0.85	Symmetric	0.2235	0.2942	0.4299	0.5875		0.3470	0.5875	0.3470

Aileron Model	$\frac{\sum b^2 \Delta x h_1 h_2}{b_r^2 L}$	$\frac{\sum b^3 \Delta x h_1 \alpha_1}{b_r^3 L}$	$\frac{\sum b^4 \Delta x \alpha_1^2}{b_r^4 L}$	$\frac{\sum b^4 \Delta x \alpha_1 \rho}{b_r^4 L}$	$\frac{\sum b^3 \Delta x h_2 \alpha_1}{b_r^3 L}$	$\frac{\sum b^4 \Delta x \rho^2}{b_r^4 L}$	$\frac{\sum b^3 \Delta x h_2 \beta}{b_r^3 L}$	$\frac{\sum b^3 \Delta x h_1 \rho}{b_r^3 L}$	$\frac{\sum b^2 \Delta x h_2^2}{b_r^2 L}$
0.65	-0.0672	0.2284	0.4082	0.3930	-0.1800	0.5000	-0.2352	0.2777	0.4010